Списък на статии по показател група Г

Публикации в издания Q1:

1. Kolev, S.K., Petkov, P.S., **Rangelov, M.A.**, Trifonov, D.V., Milenov, T.I., Vayssilov, G.N.. Interaction of Na+, K+, Mg2+and Ca2+counter cations with RNA. Metallomics, 10(5), 2018, DOI:10.1039/c8mt00043c, 659-678. ISI IF:3.975

2. Mavrova, A. Ts., Dimov, S., Yancheva, D., **Rangelov, M.**, Wesselinova, D., Tsenov, J. A.. Synthesis, anticancer activity and photostability of novel 3-ethyl-2-mercapto-thieno[2,3-d]pyrimidin-4(3H)-ones. Eur. J. Med. Chem., 123, Elsevier, 2016, ISSN:0223-5234, DOI:DOI: 10.1016/j.ejmech.2016.07.022., 69-79. ISI IF:3.902

3. Kolev, S, Petkov, PS, **Rangelov, M,** Vayssilov, GN. Ab Initio Molecular Dynamics of Na+ and Mg2+ Countercations at the Backbone of RNA in Water Solution. ACS CHEMICAL BIOLOGY, 8, 7, AMER CHEMICAL SOC, 2013, DOI:10.1021/cb300463h, 1576-1589. ISI IF:5.331

4. Smelcerovic, A., **Rangelov, M.**, Smelcerovic, Z., Veljkovic, A., Cherneva, E., Yancheva, D., Nikolic, G.M., Petronijevic, Z., Kocic, G.. Two 6-(propan-2-yl)-4-methyl-morpholine-2,5-diones as new nonpurine xanthine oxidase inhibitors and anti-inflammatory agents. Food Chem. Toxicol., 55, 2013, 493-497. ISI IF:3.977

5. Kolev, S, Petkov P, **Rangelov M.**, Vayssilov GN. Density Functional Study of Hydrogen Bond Formation between Methanol and Organic Molecules Containing Cl, F, NH2, OH, and COOH Functional Groups. J. Phys. Chem. A,, 115, 48, 2011, DOI:10.1021/jp204313f, 14054-14068. ISI IF:2.732

6. Bayryamov SG, **Rangelov M**, Mladjova AP, Yomtova V, Petkov DD. Unambiguous Evidence for Efficient Chemical Catalysis of Adenosine Ester Aminolysis by Its 2‘/3‘-OH. JOURNAL OF THE AMERICAN CHEMICAL SOCIETY, 129, 18, AMER CHEMICAL SOC, 2007, DOI:10.1021/ja068447g, 5790-5791. ISI IF:7.885

Публикации в издания Q2:

1. Zlateva, B., Dumanov, B., **Rangelov M.**. Applications of soil phosphate analysis for identification of activity areas at Doschkere, SE Bulgaria. Comptes rendus de l'Académie bulgare des Sciences, 71, 6, 2018, ISSN:1310-1331, DOI:DOI:10.7546/CRABS.2018.06.04, 751-756. ISI IF:0.27

2. Bayryamov, S. G., Vassilev, N. G., **Rangelov, M. A.**, Mladjova, A. P., Petkov, P. P.. Design and synthesis of substrates for model ribosomal reactions. Peptide & Proteine Letters, 16, 4, 2009, DOI:https://doi.org/10.2174/092986609787848009, 392-401. ISI IF:1.069

Публикации в издания Q4:

1. **Rangelov M.**, Todorova N, Tsacheva I. In silico investigation of single-chain variable fragment (scFv) antibody, structurally similar to native C1q globular heads.. Bulgarian Chemical Communications, 49, Special Issue E, 2017, ISSN:ISSN:0324-1130, 50-53. ISI IF:0.238

2. Zlateva B., **Rangelov M.**. Chemical analysis of organic residues found in hellenistic time amphorae from se bulgaria. Journal of Applied Spectroscopy, 82, 2, Springer New York LLC, 2015, ISSN:00219037, DOI:10.1007/s10812-015-0089-9, 221-227. ISI IF:0.476

3. Šmelcerović, Ž., **Rangelov, M.**, Cherneva, E., Kocić, G., Stojanović, S., Jevtović-Stoimenov, T., Petronijević, Ž., Yancheva, D.. Inhibition mechanism and molecular modelling studies of interactions of 6-(propan-2-yl)-3-methyl-morpholine-2,5-dione to xanthine oxidase. Bulg. Chem. Commun., 47, 2015, 783-787. ISI IF:0.349

Публикувана глава от книга или колективна монография:

1. Todorova N., Alyomov S., Chiotoroiu B. C., Fach B., Osadchaya T., **Rangelov M.**, Salihoglu B., Vasilev V.. World Seas: An Environmental Evaluation, Black Sea Chapter 8. 1, Elsevier, 2018, ISBN:ISBN:978-0-12-8050682, DOI:https://doi.org/10.1016/B978-0-12-805068-2.00011-5, 17, 209-226

J|A|C|S
COMMUNICATIONS

Published on Web 04/13/2007

Unambiguous Evidence for Efficient Chemical Catalysis of Adenosine Ester Aminolysis by Its 2′/3′-OH

Stanislav G. Bayryamov, Miroslav A. Rangelov, Aneta P. Mladjova, Vihra Yomtova, and Dimiter D. Petkov*

Laboratory of BioCatalysis, Institute of Organic Chemistry, Bulgarian Academy of Sciences, Sofia 1113, Bulgaria

Received November 24, 2006; E-mail: dd5kov@orgchm.bas.bg

Peptide bond formation by alkyl ester aminolysis is a very slow reaction and requires a proton transfer catalyst in order to proceed at a measurable rate.[1] As a three-molecular reaction, it involves a large entropy loss which accounts for the extremely slow rates. During protein biosynthesis,[2] this entropy problem is solved by binding of the two substrates and the catalyst in a proper configuration, which transforms the slow three-molecular reaction into a very fast intracomplex one. This could mean that the ribosome provides favorable configurational entropy for efficient catalysis by the proton transfer catalyst—the 3′-terminal adenosine 2′-OH of the peptidyl tRNA. The verification of this hypothesis requires studies of both the ribosome and model systems. The current mechanistic proposals are dominated by the idea of the ribosome being a template for entropic activation only without providing acid−base catalytic groups.[3] Here, we report on computational and experimental studies of intramolecular aminolysis reactions, catalyzed by a vicinal OH group. They were designed as model reactions (Chart 1) of the ribosome intracomplex aminolysis in order to find support for the crucial role of the 3′-terminal adenosine 2′-OH of the peptidyl tRNA as acid−base catalyst in the ribosome peptidyl transfer.

Quite recently[4] we reported a computational study of the mechanism and energetics of the simplest model of the reaction naturally catalyzed by the ribosome—the ammonolysis of 1-*O*-formyl 1,2-ethanediol **1** (Chart 1). The favored pathway predicted by calculations is a stepwise addition/elimination in which addition and elimination are coupled with *syn*-2-OH-assisted proton shuttling to maintain the neutrality of the tetrahedral intermediate formed. The model substrate **1** is designed to possess enantiotopic rather than diastereotopic re and si faces of the ester carbonyl and the amine attack produces R and S transition states/tetrahedral intermediates with the same energy and mirror-image structures. To model the intramolecularity of the ribosome aminolysis reaction, we now study the aminolysis of 1-*O*-*δ*-aminovaleryl 1,2-ethanediol **2**, in which the NH_2 group is an integral part of the substrate and attacks the pro-S face of the ester carbonyl (Chart 1) as does probably α-NH_2 of the aminoacyl tRNA during the ribosome reaction.[3d] The calculations were performed at the B3LYP level with the 6-31G(d,p) basis set.[4]

Our reference reaction is the ammonolysis of 1-*O*-formyl 1,2-ethanediol with an anti-oriented 2-OH **1a** (Chart 1), in which neither 2-OH nor *δ*-NH_2 can exert a proximity effect. The calculated reduction of the activation Gibbs free energy of the reference reaction $\Delta\Delta G^*$, caused by the proximity effects in the addition and elimination transition states **TS1** and **TS2** of the stepwise mechanism, is shown in Table 1. The design of the substrates allows us to calculate the individual contribution to $\Delta\Delta G^*$ of (a) the intramolecular attack of *syn*-*δ*-NH_2 **2a**, (b) the intramolecular catalysis by *syn*-2-OH **1b**, and (c) the combined action of *syn*-2-OH and *syn*-*δ*-NH_2 **2b** (Chart 1).

Chart 1

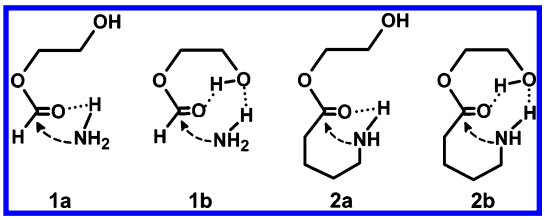


Table 1. Calculated Reduction of ΔG^*, ΔH^*, and $T\Delta S^*$ of the Reference Aminolysis Reaction **1a** by an Intramolecular Pro-S Attack of *syn*-*δ*-NH_2 (**2a**), an Intramolecular Participation of *syn*-2-OH (**1b**), and Their Combined Effect (**2b**), Associated with the First, Second, and Rate-Determining Transition States **TS1**, **TS2**, and **RDTS**

	TS1			TS2			RDTS		
	$\Delta\Delta G^*$	$\Delta\Delta H^*$	$T\Delta\Delta S^*$	$\Delta\Delta G^*$	$\Delta\Delta H^*$	$T\Delta\Delta S^*$	$\Delta\Delta G^*$	$\Delta\Delta H^*$	$T\Delta\Delta S^*$
1a	0	0	0	0	0	0	0	0	0
2a	6.5	−1.0	−7.5	11.0	3.3	−7.7	6.5	−1.0	−7.5
1b	22.5	26.3	3.8	8.1	10.2	2.1	15.9	17.5	1.6
2b	32.8	29.2	−3.6	16.9	11.8	−5.1	24.7	19.1	−5.6

Characteristically, in the first transition state **TS1**, the reduction of $\Delta\Delta G^*$ induced by *syn*-OH catalysis (22.5 kcal/mol for **1b**) is more than three times larger than the reduction caused by the intramolecularity of the *δ*-NH_2 attack (6.5 kcal/mol for **2a**). The combined proximity effect of the two groups is synergistic (32.8 kcal/mol for **2b**). On the contrary, the proximity effect of *syn*-*δ*-NH_2 in the second transition state **TS2** is even higher than that of *syn*-2-OH, and their combined effect is almost additive (Table 1).

Thus, the calculated variations in $\Delta\Delta G^*$ match the effect of the transition state proton transfer geometry,[4] suggesting a domination of *syn*-2-OH proton shuttling catalysis in the acceleration of the aminolysis. This conclusion is supported by the variation of the calculated enthalpic and entropic contributions $\Delta\Delta H^*$ and $T\Delta\Delta S^*$ (Table 1). Actually, the entropic contribution in both the first and second transition states of **2a** aminolysis exceeds the enthalpic contribution due to the unfavorable direct proton transfer in the absence of the *syn*-OH assistance.[4] On the contrary, the enthalpic contribution to the reduction of the free energy of the two transition states in **1b** and **2b** is 2−6 times larger than the entropic contribution (Table 1) due to the effective *syn*-2-OH-assisted proton shuttling.[4] Therefore, the driving force for the acceleration of the model aminolysis reaction is the proton shuttling catalysis by *syn*-2-OH.

The experimental determination of ΔH^* and ΔS^* requires dissection of ΔG^* into enthalpy and entropy contributions. However, this cannot be done for ΔG^* determined in aqueous solutions because of the enthalpy−entropy compensation in water:[5] the measured values contain contributions from ΔH_{sol} and ΔS_{sol} that cancel out in ΔG^* but may obscure measured ΔH^* and ΔS^*. On

10.1021/ja068447g CCC: $37.00 © 2007 American Chemical Society

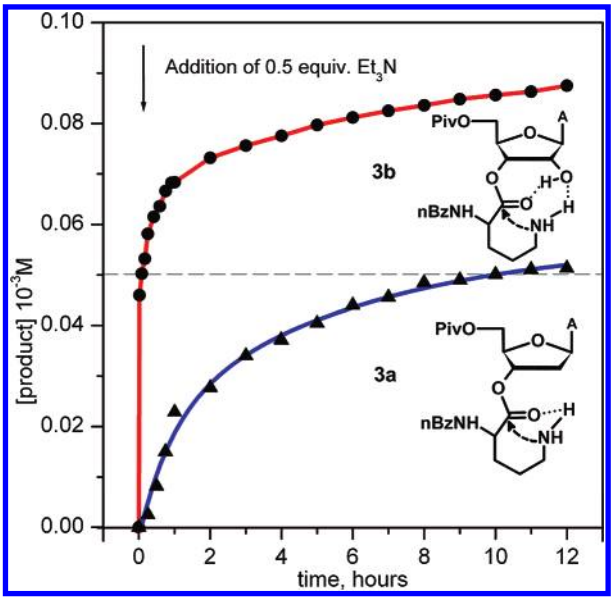


Figure 1. Time course of the intramolecular aminolysis (lactamization) in acetonitrile at 25 °C of 0.1 mmol trifluoroacetate of 2′/3′-*O*-(α-*N*-*p*-nitrobenzoyl ornithinyl) 5′-*O*-pivaloyl adenosine **3b** and deoxyadenosine **3a** to α-*N*-*p*-nitrobenzoyl cyclic ornithine after addition of 1/2 equiv of Et_3N.

the basis of such experimental data, the ribosome has been considered as an entropy trap.[3a] On the other hand, the computer simulation approaches predict a larger contribution of the solvation entropy ΔS_{sol} than of the solute configurational entropy ΔS_{prox} considered here. The authors, however, do not mention the ratio of the corresponding enthalpic contributions, ΔH_{sol} and ΔH_{prox}.[6b]

The acceleration of the overall aminolysis reaction is associated with the decrease in the activation energy of the rate-limiting transition state $\Delta\Delta G^*$ (Table 1). The difference between the values for intramolecular aminolysis of 1-*O*-δ-aminovaleryl 1,2-ethanediol with (**2b**) and without (**2a**) participation of 2-OH is 18.2 kcal/mol, which corresponds to a more than billion-fold (2.2×10^{13}) rate acceleration. In order to check this prediction of the theory, we prepared 2′/3′-*O*-(α-*N*-*p*-nitrobenzoyl-L-ornithinyl) 5′-*O*-pivaloyl adenosine **3b** and its 2′-deoxy analogue **3a** and studied the time course of their intramolecular aminolysis to the corresponding δ-lactam (α-*N*-*p*-nitrobenzoyl cyclic L-ornithine) in the polar organic solvent acetonitrile. After the addition of 1/2 equiv of Et_3N to 0.1 mmol of trifluoroacetate of the adenosine ester **3b**, an initial "burst" formation of ca. 0.05 mmol of cyclic L-ornithine, followed by a much slower release, was observed (Figure 1). The biphasic nature of the time course suggests the occurrence of two consecutive reactions, the first one being that of the free base δ-NH_2 and the second that of its trifluoroacetate salt. Under the same conditions, however, only slow aminolysis by δ-NH_2 is registered in the case of the deoxy analogue **3a**. The estimated minimal rate constant ratio of the aminolysis of adenosine and deoxyadenosine ester is ca. 3600.[7] Therefore, while the lactamization of the adenosine ester **3b** is instantaneous (the reaction being over during the mixing of the reagents and its quenching in the analytical sample (10 s)), that of the deoxyadenosine ester **3a** is not over until 10 h (Figure 1). Since the only difference in the substrates is the presence or not of the 2′-OH, the observed dramatic acceleration in the case of the adenosine ester can only be attributed to the catalysis by the 2′-OH group. To the best of our knowledge, this is the first unequivocal experimental evidence for efficient chemical catalysis of adenosine ester aminolysis by its 2′-OH group in a nonribosomal reaction.

The dramatic difference in the aminolysis rate of the adenosine and deoxyadenosine esters approaches the large difference in reactivity of peptidyl tRNA and its 2′-deoxy mutant in the ribosome fragment reaction.[8] The parallel change in the reactivity of the model and ribosome reaction, however, do not necessarily imply that the ribosome provides a microenvironment resembling that of a polar aprotic solvent. However, as established by molecular dynamic simulation studies,[6] enzymes and particularly the ribosome use preorganized polar electrostatic environment to catalyze the corresponding reactions. The observed time course of our bioorganic model reactions indicates that the non-hydrogen-bonding polar organic solvent acetonitrile is the simplest model of the ribosome polar electrostatic environment of the rate-limiting transition state.

After the formation of the ribosome−substrate complex, each of the ribosome substrates becomes an integral part of the ribosome and the participation of substrate acid−base groups in the catalytic process is possible. This reminds us of the formation of a holoenzyme from an apoenzyme and coenzyme, the latter being the ribosome and peptidyl tRNA, respectively. Recent studies of ribosome−substrate crystal structures[3d] reveal that the 2′-OH of the peptidyl tRNA 3′-terminal adenosine hydrogen bonds to aminoacyl tRNA α-NH_2 and is the only functional group positioned to act as a general base. The deleterious effect of its removal on ribosome catalysis[9] and the dramatic change in the aminolysis rate after deletion of the adenosine 2′-OH observed here strongly support its significant catalytic role in substrate-assisted ribosome catalysis.

Acknowledgment. Supported by grants from the National research Fund of Bulgaria (grants X-1001 and X-1517). We thank I.G. Pojarlieff for helpful and stimulating discussions.

Supporting Information Available: Computational details and data, synthesis and characterization of the substrates, and description of the kinetic experiments. This material is available free of charge via the Internet at http://pubs.acs.org.

References

(1) Satterthwait, A. C.; Jencks, W. P. *J. Am. Chem. Soc.* **1974**, *96*, 7018−7031.
(2) Wilson, D. N.; Nierhaus, K. N. *Angew. Chem., Int. Ed.* **2003**, *42*, 3464−3486.
(3) (a) Sievers, A.; Beringer, M.; Rodnina, M. V.; Wolfenden, R. *Proc. Natl. Acad. Sci. U.S.A.* **2004**, *117*, 7897−7901. (b) Youngman, E. M.; Brunelle, J. L.; Kochniak, A. B.; Green, R. *Cell* **2004**, *117*, 589−599. (c) Changalov, M. M.; Ivanova, G. D.; Rangelov, M. A.; Acharia, P.; Acharia, S.; Minakawa, N.; Foldesi, A.; Stoineva, I. B.; Yomtova, V. M.; Roussev, C. D.; Matsuda, A.; Chattopadhyaya, J.; Petkov, D. D. *ChemBioChem* **2005**, *6*, 972−977. (d) Martin Schmeiling, T.; Huang, K. S.; Kitchen, D. E.; Strobel, S. A.; Steitz, T. A. *Mol. Cell* **2005**, *20*, 437−448. (e) Rodnina, M.; Beringer, M.; Wintermeyer, W. *Quart. Rev. Biophys.* **2006**, *39*, 203−225. (f) Changalov, M. M.; Petkov, D. D. *Tetrahedron Lett.* **2007**, *48*, 2381−2384.
(4) Rangelov, M. A.; Vayssilov, G.; Yomtova, V. M.; Petkov, D. D. *J. Am. Chem. Soc.* **2006**, *128*, 4964−4965 and details are found in the Supporting Information.
(5) Dunitz, J. D. *Chem. Biol.* **1995**, *2*, 709−712.
(6) (a) Trobo, S.; Aqvist, J. *Proc. Natl. Acad. Sci. U.S.A.* **2005**, *102*, 12395−12400. (b) Sharma, P. K.; Xiang, Y.; Kato, M.; Warshel, A. *Biochemistry* **2005**, *44*, 11307−11314. (c) Warshel, A. *J. Biol. Chem.* **1995**, *273*, 27035−27038.
(7) The estimation is found under Supporting Information.
(8) Chinali, G.; Sprinzl, M.; Parmeggiani, A.; Cramer, F. *Biochemistry* **1974**, *13*, 3001−3010.
(9) (a) Hecht, S. *Tetrahedron* **1977**, *33*, 1671−1696. (b) Weinger, J. S.; Parnell, K. M.; Dorner, S.; Green, R.; Strobel, S. A. *Nat. Struct. Mol. Biol.* **2004**, *11*, 1101−1106.

JA068447G

Design and Synthesis of Substrates for Model Ribosomal Reactions

Stanislav G. Bayryamov[1,*], Nikolay G. Vassilev[2], Miroslav A. Rangelov[1], Aneta P. Mladjova[1] and Dimiter D. Petkov[1]

[1]*Laboratory of BioCatalysis, Institute of Organic Chemistry, Bulgarian Academy of Sciences, Sofia 1113, Bulgaria;* [2]*Laboratory of Nuclear Magnetic Resonance, Institute of Organic Chemistry, Bulgarian Academy of Sciences, Sofia 1113, Bulgaria*

Abstract: 2'/3'-O-[Bz(NO_2)-Orn(Boc)]-5'-O-Piv-Ado (**1**) and its deoxy analog: 3'-O-[Bz(NO_2)-Orn(Boc)]-5'-O-Piv-2'-dAdo (**2**) were designed and synthesized as substrates for the model ribosome reaction we used to demonstrate the crucial role of A76 2'-OH of peptidyl-tRNA in the rate acceleration of peptide bond formation during protein biosynthesis.

Keywords: Design, peptide synthesis, nucleoside synthesis, ribosome catalysis.

1. INTRODUCTION

The biosynthesis of proteins proceeds on the cell organelle ribosome. Understanding the chemical mechanism of peptide bond formation and how it is accelerated by the ribosome is of fundamental interest to biochemistry and chemical biology. Nowadays there are two main working hypotheses in the study of the ribosome catalytic mechanism:

1) In the first hypothesis the acceleration is a result of a favorable entropy effect, i.e. the proximity of peptidyl-tRNA and aminoacyl-tRNA in the ribosome peptidyl transfer center plays an important role in the dramatic rate accelleration of the aminolysis of peptidyl-tRNA and the ribosome acts as an entropy trap [1].

2) According to the second hypothesis the dramatic acceleration of peptide bond synthesis in the ribosome reaction can be attributed to an enthalpy effect. It is supposed that the catalytic groups play a crucial role in the overall process [2]. The point mutations and mutation analyses of many universally conserved nucleotides demonstrated that the base modifications in ribosomal RNAs: A-2486 (A-2451), U2506, U2585 and A2602 in the innermost layer of the active site of the large subunit of the ribosome have a limited, but no lethal influence on the rate of peptide bond synthesis [3]. They are pivotal for peptide release, while the nucleotides of the outer shell are responsible for promoting peptide bond formation. This direct the attention toward the participation of the ribosomal substrate groups in the catalytic act, i.e. the contribution of the substrate-assisted catalysis. Our preliminary experiments showed that even if any effect of the nucleobase A76 of peptidyl-tRNA exists, it is not significant [4]. On the other hand, the inactivation of the peptidyl tRNA as substrate when its 2'-OH in 3'-terminal adenosine A76 is deleted presumes its crucial participation in the catalysis by the ribosome. For instance, substitution of the 3'-terminal adenosine 2'-OH of the genuine peptidyl tRNA by 2'-H or 2'-F gives rise to a more than 1 000 000-fold rate decrease [5]. Therefore, it is supposed, that the main contribution to the overall catalysis of peptide bond formation on the ribosome is due to the catalytic action of the 3'-terminal A76 2'-OH of peptidyl tRNA.

Although the presence of a 2'-OH in the 3'-terminal adenosine of peptidyl tRNA has long been known to be crucial for protein biosynthesis, the nature (mechanism) of its rate-enhancement effect is still not clearly understood. To reveal the mechanism, by which the presence of 2'-OH in the 3'-terminal adenosine of peptidyl tRNA plays a crucial role in protein biosynthesis, it is necessary to reduce the supramolecular complexity to a simpler model reactions. The approaches of chemical biology and bioorganic chemistry allow the use of these methods, employing substrate mimics – analogues of macromolecules, reaction centres and transition states, for proving the mechanisms of biosynthetic reactions. Thus, the catalytic role of A76 2'-OH of the peptidyl-tRNA in ribosome catalysis reamains to be demonstrated experimentally.

In previous paper [6] we reported computational studies of the mechanism and energetics of the ammonolysis of 1-O-formyl 1,2-ethanediol and predicted a stepwise addition/elimination pathway in which the reaction is much slower without participation of a *syn*-oriented 2-OH-group, the latter providing a favourable transition state proton transfer geometry [6].

It was predicted and proved that *syn*-2-OH-assisted proton shuttling maintains the neutrality of the tetrahedral intermediate formed. We also studied in the previous paper the aminolysis (lactamization) of 1-O-δ-amino-valeryl 1.2-ethanediol in which the attacking amino group is an integral part of the substrate, by the methods of computational chemistry, and the calculations were performed at the B3LYP level with 6-31G(d,p) basis set [7]. It was predicted that the enthalpic contribution in the reduction of the free energy of the two transition states of substrates is 2-6 times larger than the entropic contribution because of the effective *syn*-2-OH-assisted proton shuttling catalysis. Therefore, the driving

*Address correspondence to this author at the Laboratory of BioCatalysis, Institute of Organic Chemistry, Bulgrian Academy of Sciences, Acad. Bonchev Str., bld. 9, 1113 Sofia, Bulgaria;
E-mail: stanly_chem2002@yahoo.com

0929-8665/09 $55.00+.00 © 2009 Bentham Science Publishers Ltd.

force for the acceleration of the model aminolysis reaction is the proton shuttling catalysis by the *syn*-oriented-2-OH group. The difference between the values for intramolecular aminolysis of 1-O-δ-aminovaleryl 1,2-ethanediol with and whithout participation of the 2-OH group is 18.2 kcal/mol, which corresponds to a more than a billion-fold ($2.2x10^{13}$) rate acceleration. To prove this prediction we studied the time course of aminolysis (lactamization) of 2'/3'-O-(α-N-p-nitrobenzoyl-L-ornithinyl) 5'-O-pivaloyl adenosine (1') and 3'-O-(α-N-p-nitrobenzoyl-L-ornithinyl) 5'-O-pivaloyl 2'-deoxy adenosine (2') to the corresponding δ-lactam (3-(p-nitrobenzoylamino) piperidine-2-on, α-N-p-nitrobenzoyl-cyclo-L-ornithine) and 5'-O-pivaloyl adenosine or 5'-O-pivaloyl 2'-deoxy adenosine in the polar aprotic organic solvent acetonitrile [7]. While the lactamization of 2'/3'-O-(α-N-p-nitrobenzoyl-L-ornithinyl) 5'-O-pivaloyl adenosine (1') is instantaneous, the lactamization of 3'-O-(α-N-p-nitrobenzoyl-L-ornithinyl) 5'-O-pivaloyl 2'-deoxy adenosine (2') to the corresponding δ-lactam (3-(p-nitrobenzoylamino) piperidine-2-on and 5'-O-pivaloyl 2'-deoxy adenosine takes more than 10 hours. Since the difference between the two substrates is only in the presence of 2'-OH group in 2'/3'-O-(α-N-p-nitrobenzoyl-L-ornithinyl) 5'-O-pivaloyl adenosine (1'), the observed dramatic difference in their reactivity (ca. 3600 times) can be attributed to the effective 2'-OH-assisted proton shuttling catalysis. Thus we have studied the important (essential) role of the vicinal *cis*-2-OH group of the diol monoester system and A76 2'-OH in peptidyl-tRNA as an important catalytic unit. This is the first unambiguous experimental evidence for the effective chemical catalysis by the *cis*-vicinal diol system of the adenosine ester aminolysis [7].

In this work we describe in details the design and the synthesis of 2'/3'-O-(α-N-p-nitrobenzoyl-δ-N-(Boc)-L-ornithinyl) 5'-O-pivaloyl adenosine (2'/3'-O-[Bz(NO_2)-Orn (Boc)]-5'-O-Piv-Ado) (**1**) and 3'-O-(α-N-p-nitrobenzoyl-δ-N-(Boc)-L-ornithinyl) 5'-O-pivaloyl 2'-deoxy adenosine (3'-O-[Bz(NO_2)-Orn(Boc)]-5'-O-Piv-2'-dAdo) (**2**) as substrates for model ribosomal reactions with which we carried out the kinethic studies.

2. EXPERIMENTAL

General Procedures, Methods and Materials

All reagents and solvents were purchased and used without further purification. Reverse phase HPLC analyses were performed on a Waters Liquid Chromatograph equipped with an absorbance detector model 441 set at 280 nm and a column Nucleosil 100-5C_{18} (12.5 cm x4.6 mm) for analytical runs. ^{1}H and ^{13}C NMR spectra were recorded in DMSO-d6 at 20^{o}C on a Bruker Avance II+ 600MHz spectrometer using BBO or TBI probeheads. Chemical shifts are expressed in ppm and coupling constants in Hz. The precise assignments of the ^{1}H and ^{13}C NMR spectra were accomplished by measurement of 2D homonuclear correlation (COSY), DEPT-135 and 2D inverse detected heteronuclear (C–H) correlations (HSQC and HMBC). Chemical shifts are reported in δ (ppm). The analysis of first order multiplets in ^{1}H NMR spectra was speed up by the use of FAFOMA program [8].

3. SYNTHESIS

3.1. Synthesis of Bz(NO_2)-Orn(Boc)-OCH_2CN

The procedure on cyanomethylation of Bz(NO_2)-Orn (Boc)-OH includes reaction of the aminoacyl derivative with $ClCH_2CN$ at room temperature and different solutions, which vary from polar aprotic to hydrophobic. To a solution of 0.289g (0.759 mmol) of Bz(NO_2)-Orn(Boc)-OH in DMF were added 2 equiv. - 0.211ml (1.518 mmol) triethylamine in ice cold bath. After 10 minutes 2 equiv. – 0.096 ml (1.518 mmol) of chloroacetonitrile were added to the reaction mixture. The temperature of the reaction was left to reach room t^{0}C and was left overnight. It was then evaporated under reduced pressure and dissolved in ethylacetate. The organic phase was washed three times with 0.5N HCl, brine, a saturated solution (10%) of $NaHCO_3$ and again with brine. Finally the organic phase was dried over sodium sulfate and evaporated to dryness in vacuo. Yield -0.262g (87%). Rf = 0.545 (CH_2Cl_2 : CH_3OH – 9 : 1). M.p. 78^{0}C.

^{1}H NMR: δ = 1.365(s, 9H, CH_3), 1.46-1.55(m, 2H, 4-CH_2), 1.76-1.88(m, 2H, 3-CH_2), 2.94-2.98(m, 2H, 5-CH_2), 4.50-4.54(m, 1H, 2-CH), 5.046(s, 2H, OCH_2), 6.844(t, J=5.7 Hz, 1H, 5-CH_2N<u>H</u>), 8.109(d, J=8.8 Hz, 2H, 3-CH and 5-CH), 8.351(d, J=8.8 Hz, 2H, 2-CH and 6-CH), 9.230(d, J=7.1 Hz, 1H, 2-CHN<u>H</u>).

^{13}C NMR: δ = 25.97(4-CH_2), 27.29(3-CH_2), 28.19(CH_3), 39.97(5-CH_2), 49.44(OCH_2), 52.41(2-CH), 77.42(C), 115.72 (CN), 123.57(3-CH and 5-CH), 128.96(2-CH and 6-CH), 138.94(1-C), 149.21(4-C), 155.56(NHCOO), 156.12 (NH CO), 170.94(COOC).

3.2. Synthesis of 2',3'-O-Isopropylidene Adenosine

To 2.67 g (10 mmol) of adenosine and 2.30g (12 mmol) p-toluene sulfonat monohydrate were added 25 ml of 2,2'-dimethoxy propane at 20^{0}C. After 12 hours the reaction mixture was neutralized with 1N solution of sodium methylate. After that it was concentrated under vacuo and the solid residue was dissolved in H_2O. The water phase was extracted several times with CH_2Cl_2. The combined organic phase was extracted once with a saturated solution of NaCl, dried over anhydrous Na_2SO_4 and evaporated under reduced pressure in vacuo. (The other possible way of purification of the final product was the extraction of the solid residue after neutralization and evaporation of the reaction mixture with hot $CHCl_3$ (5x10 ml). The combined organic phase was filtered through Hyflo-Supercel, dried over anhydrous Na_2SO_4 and then evaporated in vacuo). Yield - 2.432 g (82%). Rf = 0.289 (CH_2Cl_2 : CH_3OH – 8 : 2). M.p. 219^{o}C (216-217^{o}C [9], 220^{o}C [10]).

^{1}H NMR: δ = 1.322(s, 3H) and 1.542(s, 3H, CH_3), 3.510 (td, J=5.2, 11.7 Hz, 1H) and 3.559(td, J=4.8, 11.7 Hz, 1H, 5`-CH_2), 4.210(dt, J=2.6, 4.8 Hz, 1H, 4'-H), 4.959(dd, J=2.4, 6.1 Hz, 1H, 3'-H), 5.263(t, J=5.6 Hz, 1H, OH), 5.336(dd, J=3.1, 6.1 Hz, 1H, 2'-H), 6.114(d, J=3.1 Hz, 1H, 1'-H), 7.365(bs, 2H, NH_2), 8.149(s, 1H, 2-H), 8.341(s, 1H, 8-H).

^{13}C NMR: δ = 25.14(CH_3), 27.04(CH_3), 61.53(5`-$CH_2$), 81.31(3`-CH), 83.15(2`-CH), 86.28(4`-CH), 89.56(1`-CH), 113.01(C), 119.04(5-C), 139.66(8-CH), 148.75(4-C), 152.61 (2-CH), 156.10(6-C).

3.3. Synthesis of 2',3'-O-Isopropylidene Adenosine (II)

To a solution of 2.67 g (10 mmol) of adenosine in 5ml acetone and 5ml MeOH in ice cold bath were added droppwise 1.47g (15 mmol) of H_2SO_4 dissolved in 5ml acetone. The reaction mixture was allowed to stand for 24 hours at ambient temperature and then the pH was slowly adjusted to 7-8 with a solution of NaOMe in MeOH or solution of 10% $NaHCO_3$ in H_2O (5% Na_2CO_3). The solvents of the reaction mixture were distilled off in vacuo and it was dissolved in H_2O. The water phase was extracted several times with CH_2Cl_2. The combined organic phase was extracted 3 times with a saturated solution of $NaHCO_3$, and 3 times with brine, dried over anhydrous sodium sulfate and evaporated under reduced pressure. (The final product may also be purified by trituration of the solid residue after neutralization and evaporation of the reaction mixture with hot $CHCl_3$. The combined organic phase was then filtered through Hyflo-Supercel, dried over anhydrous sodium sulfate and then evaporated to dryness in vacuo). Yield - 2.669 g (90%). Rf = 0.289 (CH_2Cl_2 : CH_3OH – 8 : 2). M.p. 220^{o}C.

^{1}H NMR: δ = 1.322(s, 3H) and 1.542(s, 3H, CH_3), 3.510(td, J=5.2, 11.7 Hz, 1H) and 3.559(td, J=4.8, 11.7 Hz, 1H, 5`-CH_2), 4.210(dt, J=2.6, 4.8 Hz, 1H, 4'-H), 4.959(dd, J=2.4, 6.1 Hz, 1H, 3'-H), 5.263(t, J=5.6 Hz, 1H, OH), 5.336(dd, J=3.1, 6.1 Hz, 1H, 2'-H), 6.114(d, J=3.1 Hz, 1H, 1'-H), 7.365(bs, 2H, NH_2), 8.149(s, 1H, 2-H), 8.341(s, 1H, 8-H).

^{13}C NMR: δ = 25.14(CH_3), 27.04(CH_3), 61.53(5`-$CH_2$), 81.31(3`-CH), 83.15(2`-CH), 86.28(4`-CH), 89.56(1`-CH), 113.01(C), 119.04(5-C), 139.66(8-CH), 148.75(4-C), 152.61 (2-CH), 156.10(6-C).

3.4. Synthesis of 5'-O-Piv-Ado

The procedure of pivaloylation was carried out according to the method of Fromageot *et al.* with some modifications [10]. To a solution of 1 g (3.289 mmol) of 2',3'-O-isopropylidene adenosine in 10 ml pyridine were added 0.607 ml pyvaloyl chloride (1.5 equiv., 4.934 mmol) in ice cold bath. After that the reaction was allowed to stand overnight at room temperature, stopped with 3 ml EtOH for 1 hour at ambient temperature and was then concentrated in vacuo. The remaining residue was coevaporated several times with a solution of H_2O - EtOH (1 : 1) and dissolved in 10 ml (90%) HCOOH at 20^{0}C. Under these conditions only the 2',3'-O-isopropylidene group was cleaved. After 18 hours it was concentrated for several hours at reduced pressure in vacuo before 30^{0}C, dissolved in H_2O, saturated with NaCl (brine) and CH_2Cl_2 and neutralized with 1N KOH or with solution of sodium or potassium methylate in methanol. The H_2O-phase was extracted several times with CH_2Cl_2 and the combined organic phases were washed once with brine, dried over Na_2SO_4 and evaporated in vacuo. The content of the crude product thus obtained from organic and water phases was summary - 5'-O-Piv-Ado : N^6,5'-O-di-Piv-Ado : N^6-Piv-Ado in the following proportions - (72%: 15%: 3%)[1] and residual quantity of unreacted starting substrate Ado - (10%). To obtain the pure 5'-O-Piv-Ado it was necessary to:

1) evaporate the CH_2Cl_2 in organic phase and dissolve the crude product in CH_3COOH : H_2O (90% : 10%) or 80% HCOOH in H_2O and to maintain the reaction under reflux for 3-4 hours. Under these conditions only N^6-Piv-group was removed from N^6,5'-O-di-Piv-Ado without deprotection of 5'-O-Pivaloyl group in N^6,5'-O-di-Piv-Ado and 5'-O-Piv-Ado. After the N^6-Piv-group was removed the reaction mixture was evaporated to dryness in vacuo, dissolved in H_2O and neutralized to pH - 7 with 1N KOH. The water phase was extracted several times with CH_2Cl_2 and the combined organic phase was extracted once with brine, dried over Na_2SO_4 and evaporated to dryness in vacuo.

2) To the water phase was added CH_3COOH to reach 80 - 90% of acid according to the water. The reaction mixture was heated under reflux for 2-3 hours, then evaporated to dryness in vacuo and neutralized with N KOH. Under these conditions only N^6-Piv-group was removed from N^6-Piv-Ado without deprotection of 5'-O-Pivaloyl group in 5'-O-Piv-Ado. The water phase was extracted several times with CH_2Cl_2 and the combined organic phase was extracted once with brine, dried over Na_2SO_4 and evaporated to dryness in vacuo. Another possible way to obtain the pure product after deprotection of N^6-Piv-group in acid conditions, neutralization of the H_2O-phase with N KOH and evaporation of the reaction mixture was to pass the crude product through silicagel column in CH_2Cl_2 : Hexane (8 : 2) or CH_2Cl_2 : Acetone (7 : 3), CH_2Cl_2 : Acetone (1 : 1). Yield - 1.005 g (87%), (13% recovering of Ado). Rf - 0.325 (CH_2Cl_2 : CH_3OH – 9 : 1). M.p.161-163^{0}C.

^{1}H NMR: δ = 1.108(s, 9H, CH_3), 4.072(dt, J=4.0, 5.3 Hz, 1H, 4`-CH), 4.184(dd, J=5.7, 12.0 Hz, 1H) and 4.303(dd, J=3.9, 12.0 Hz, 1H, 5`-CH_2), 4.264(pseudo q, J=5.3 Hz, 1H, 3`-CH), 4.662(pseudo q, J=5.3 Hz, 1H, 2`-CH) 5.372(d, J=5.6 Hz, 1H, 3`-OH), 5.593(d, J=5.7 Hz, 1H, 2`-OH), 5.894(d, J=4.7 Hz, 1H, 1`-CH), 7.315(s, 2H, NH_2), 8.138(s, 1H, 2-CH), 8.284(s, 1H, 8-CH).

^{13}C NMR: δ = 26.77(CH_3), 38.20(C), 63.68(5`-$CH_2$), 70.00(3`-CH), 72.80(2`-CH), 81.24(4`-CH), 87.78(1`-CH), 119.12(5-C), 139.63(8-C), 149.22(4-C) 152.65(2-CH), 156.05(6-C), 177.28(C=O).

3.5. Synthesis of 5'-O-Piv-Ado (II)

To a solution of 1g (3.289 mmol) of 2',3'-O-isopropylidene adenosine in 10 ml pyridine and 1 ml of triethylamine were added 0.486 ml pyvaloyl chloride (1.2 equiv., 3.947 mmol) at room temperature. After that the reaction was allowed to stand overnight at room temperature, stopped with 3 ml EtOH for 1 hour at ambient temperature and then concentrated in vacuo. The remaining residue was coevaporated several times with H_2O-EtOH (1 : 1) and dissolved in 10 ml 80% HCOOH (90% CH_3COOH). The reaction mixture was heated under reflux for 2-3 hours and evaporated to dryness in vacuo. After solubilization of the crude product in water and neutralization with 1N KOH the H_2O-phase was extracted several times with CH_2Cl_2 and the combined organic phase was washed once with brine, dried over Na_2SO_4 and evaporated to dryness in vacuo. The com-

[1] On the other hand the distribution of the individual products (components) in CH_2Cl_2 phase were: 5'-O-Piv-Ado (40%) : N^6,5'-O-di-Piv-Ado (15%), and in the H_2O-phase were: 5'-O-Piv-Ado (32%) : N^6-Piv-Ado (3%) : Ado (10%).

bined brine and H_2O - phase were evaporated and the crude product was passed through a silicagel column in CH_2Cl_2 : Hexane (8 : 2) or CH_2Cl_2 : Acetone (7 : 3), CH_2Cl_2 : Acetone (1 : 1). Yield - 0.947 g (82%), (18% recovering of Ado). Rf - 0.325 (CH_2Cl_2 : CH_3OH – 9 : 1). M.p. 162-163^{0}C.

^{1}H NMR: δ = 1.108(s, 9H, CH_3), 4.072(dt, J=4.0, 5.3 Hz, 1H, 4`-CH), 4.184(dd, J=5.7, 12.0 Hz, 1H) and 4.303(dd, J=3.9, 12.0 Hz, 1H, 5`-CH_2), 4.264(pseudo q, J=5.3 Hz, 1H, 3`-CH), 4.662(pseudo q, J=5.3 Hz, 1H, 2`-CH) 5.372(d, J=5.6 Hz, 1H, 3`-OH), 5.593(d, J=5.7 Hz, 1H, 2`-OH), 5.894(d, J=4.7 Hz, 1H, 1`-CH), 7.315(s, 2H, NH_2), 8.138(s, 1H, 2-CH), 8.284(s, 1H, 8-CH).

^{13}C NMR: δ = 26.77(CH_3), 38.20(C), 63.68(5`-$CH_2$), 70.00(3`-CH), 72.80(2`-CH), 81.24(4`-CH), 87.78(1`-CH), 119.12(5-C), 139.63(8-C), 149.22(4-C) 152.65(2-CH), 156.05(6-C), 177.28(C=O).

3.6. Synthesis of 5'-O-Piv-2'-dAdo

To a solution of 0.502 g (2 mmol) of anhydrous 2'-dAdo or 0.538 g (2 mmol) of 2'-dAdo.H_2O in pyridine were added slowly dropwise 0.417 ml triethylamine and 0.369 ml (3 mmol) pivaloyl chloride in ice cold bath and after 10 min. it was allowed to stand overnight at room temperature. After the reaction was completed (TLC), to the solution were added 3ml. EtOH for 1 hour, then it was evaporated under reduced pressure, coevaporated several times with H_2O - EtOH (1 : 1), with dry CH_3CN and passed through a silicagel column in CH_2Cl_2 : Hexane (8 : 2) or CH_2Cl_2 : Acetone (7 : 3), CH_2Cl_2 : Acetone (6 : 4). Oil. Yield - 0.436g (65%). Rf - 0.360 (CH_2Cl_2 : CH_3OH – 9 : 1).

^{1}H NMR: δ = 1.271(s, 9H, CH_3), 2.336(ddd, J=4.4, 6.7, 13.4 Hz, 1H) and 2.775(td, J=6.6, 13.4 Hz, 1H, 2'-H), 4.14(m, 1H) and 4.256(dd, J=4.5, 11.8 Hz, 1H, 5'-H), 3.987(td, J=4.2, 5.8 Hz, 1H, 4'-H), 4.479(dq, J=4.2, 6.2 Hz, 1H, 3'-H), 5.497(d, J=4.3 Hz, 1H, 3'-OH), 6.335(d, J=6.7 Hz, 1H, 1'-H), 7.292(bs, 2H, NH_2), 8.132(s, 1H, 2-H), 8.273(s, 1H, 8-H).

^{13}C NMR: δ = 26.75(CH_3), 38.15(C), 38.40(2`-CH), 63.77(5`-CH_2), 70.34(3`-CH), 83.19(1`-CH), 83.85(4`-CH), 119.13(5-C), 139.36(8-CH), 148.97(4-C), 152.55(2-C), 156.01(6-C), 177.24(C=O).

3.7. Synthesis of 3'-O-[Bz(NO_2)-Orn(Boc)]-5'-O-Piv-2'-dAdo (2)

To 0.1 g (0.298 mmol) 5'-O-Piv-2'-dAdo in dry DMF were added 0.15 g (0.358 mmol) of Bz(NO_2)-Orn(Boc)-OCH_2CN at room temperature. After that 44.6 µl (0.298 mmol) of DBU were added and the reaction mixture was allowed to stand for 12 hours at ambient temperature. After the reaction was completed (TLC, HPLC), 0.09 g (0.536 mmol, 1.8 equiv. according to DBU) of nitrobenzoic acid were added and allowed to stand for 1 hour at 25^{0}C to stopping of the reaction. Then the reaction mixture was evaporated to dryness in vacuo and passed through a column in CH_2Cl_2 : Acetone (6 : 4) or (7 : 3). Oil. Yield - 0.114 g (55%). Rf - 0.380 (CH_2Cl_2 : CH_3OH – 9 : 1).

^{1}H NMR: δ = 1.103(s, 9H, CH_3), 1.363(s, 9H, CH_3), 1.54(m, 2H, 4-CH_2), 1.82(m, 1H) and 1.88(m, 1H, 3-CH_2), 2.552(ddd, J=2.3, 6.1, 14.1 Hz, 1H) and 3.182(m, 1H, 2`-$CH_2$), 2.96-3.00(m, 2H, 5-$CH_2$), 4.21(m, 1H, 4`-CH), 4.26(m, 2H, 5`-$CH_2$), 4.468(ddd, J=5.0, 7.0, 9.5 Hz, 1H, 2-CH), 5.343(td, J=2.3, 8.6 Hz, 1H, 3`-CH), 6.345(dd, J=6.3, 8.0 Hz, 1H, 1`-CH), 6.857(t, J=5.5 Hz, 1H, 5-CH_2N<u>H</u>), 7.338(s, 2H, NH_2), 8.122(d, J=8.9 Hz, 2H, 3-CH and 5-CH), 8.136(s, 1H, 2-CH), 8.318(s, 1H, 8-CH), 8.351(d, J=8.9 Hz, 2H, 2-CH and 6-CH), 9.206(d, J=6.8 Hz, 1H, 2-CHN<u>H</u>).

^{13}C NMR: δ = 26.12(4-CH_2), 26.70(CH_3), 27.43(3-CH_2), 28.19(CH_3), 35.14(2`-$CH_2$), 38.16(C), 39.25(5-$CH_2$), 52.91 (2-CH), 63.20(5`-CH_2), 74.78(3`-CH), 81.28(4`-CH), 77.42 (C), 83.44(1`-CH), 119.14(5-C), 123.56(3-CH and 5-CH), 128.99(2-CH and 6-CH), 139.24(i-C), 139.32(8-C), 149.07(4-C), 149.16(p-C), 152.61(2-CH), 155.57(NHCOO), 156.05(6-C), 165.30(NHCO), 171.28(3'-COOC), 177.10(5'-OC=O).

3.8. Synthesis of 2'/3'-O-[Bz(NO_2)-Orn(Boc)]-5'-O-Piv-Ado (1)

To 0.12 g (0.342 mmol) of 5'-O-Piv-Ado in DMF were added 0.12 g (0.284 mmol) of Bz(NO_2)-Orn(Boc)-OCH_2CN and 0.476 ml (3.423 mmol, 10 equiv. towards the 5'-O-Piv-Ado) of triethylamine. The reaction mixture was allowed to stand for 72 hours at room temperature after that it was evaporated to dryness in vacuo and passed through a silicagel column in CH_2Cl_2 : Acetone (5 : 5). Oil. Yield - 0.138g (68%). Rf - 0.375 (CH_2Cl_2 : CH_3OH – 9 : 1).

^{1}H NMR: δ = 1.122(s, 9H, CH_3), 1.364(s, 9H, CH_3), 1.55(m, 2H, 4-CH_2), 1.84(M, 1H) and 1.93(m, 1H, 3-CH_2), 2.96-3.00(m, 2H, 5-CH_2), 4.24(m, 1H, 4`-CH), 4.33(m, 2H, 5`-CH_2), 4.618(ddd, J=4.9, 7.6, 9.8 Hz, 1H, 2-CH), 5.087(dt, J=5.3, 6.4 Hz, 1H, 2`-CH) 5.374(dd, J=3.1, 5.3 Hz, 1H, 3`-CH), 5.918(d, J=6.4 Hz, 1H, 1`-CH), 5.933(d, J=6.4 Hz, 1H, 2`-OH), 6.847(t, J=5.5 Hz, 1H, 5-CH_2N<u>H</u>), 7.377(s, 2H, NH_2), 8.120(d, J=8.9 Hz, 2H, 3-CH and 5-CH), 8.142(s, 1H, 2-CH), 8.339(s, 1H, 8-CH), 8.353(d, J=8.9 Hz, 2H, 2-CH and 6-CH), 9.156(d, J=7.6 Hz, 1H, 2-CHN<u>H</u>).

^{13}C NMR: δ = 26.22(4-CH_2), 26.71(CH_3), 27.60(3-CH_2), 28.20(CH_3), 38.16(C), 38.19(5-CH_2), 52.76(2-CH), 63.00(5`-$CH_2$), 70.62(2`-CH), 72.82(3`-CH), 77.42(C), 79.15(4`-CH), 87.11(1`-CH), 119.12(5-C), 123.53(3-CH and 5-CH), 129.00 (2-CH and 6-CH), 139.46(i-C), 139.64(8-C), 149.12(4-C), 149.36(p-C), 152.65(2-CH), 155.56(NHCOO), 156.04(6-C), 165.28(NHCO), 170.87(3'-COOC), 177.11(5'-OC=O).

3.9. Synthesis of Bz(NO_2)-C-Orn

To a solution of 0.198 g (0.5 mmol) of Bz(NO_2)-Orn(Boc)-OCH_3 in 2 ml CH_2Cl_2 were added 2 ml of solution of 50% TFA in CH_2Cl_2 at ambient temperature. After 1 hour the reaction was completed (TLC) and the solution evaporated in vacuo, coevaporated several times with CH_2Cl_2 to avoid unnecessary trifluoracetic acid. 0.205 g (0.5 mmol) of Bz(NO_2)-Orn-OCH_3.TFA were dissolved in 5 ml MeOH and the solution was allowed to stand in oil bath and reflux condenser at 50^{0}C. After that 0.104 ml (0.75 mmol) of triethylamine were added to the reaction mixture and it was allowed to stand for 3-4 hours at 50^{0}C. After the reaction was completed (TLC) it was evaporated in vacuo to remove the solvent and coevaporated several times with 3 ml MeOH on

each evaporation. The crude product was dissolved in CH_2Cl_2 and washed several times with $NaHCO_3$, water, 0.5N HCl and again water. After the organic phase was dried over Na_2SO_4 and was evaporated to dryness in vacuo. Yield - 0.119 g (90%). Rf = 0.185 (CH_2Cl_2 : CH_3OH : NH_3 – 9 : 1 : 1).

^{1}H NMR: δ = 1.78-1.86(m, 3H, 5-CH_2 and ax-4-CH_2), 2.00-2.03(m, 1H, eq-4-CH_2), 3.17-3.19(m, 2H, 6-CH), 4.39(m, 1H, 3-CH), 8.086(d, J=8.8 Hz, 2H, 2-CH and 6-CH), 8.333(d, J=8.8 Hz, 2H, 3-CH and 5-CH), 8.993(d, J=8.3 Hz, NHCO).

^{13}C NMR: δ = 21.22(5-CH_2), 27.48(4-CH_2), 41.13(6-CH_2), 49.57(3-CH), 123.53(2-CH and 6-CH), 128.71(2-CH and 6-CH), 139.86(i-C), 148.96(p-C), 164.11(NHCO), 169.34(cyclo-CONH).

3.10. General Procedure for Deprotection of 3'/2'-O-[Bz(NO_2)-Orn(Boc)]-5'-O-Piv-Ado (1) and 3'-O-[Bz(NO_2)-Orn(Boc)]-5'-O-Piv-2'-dAdo (2) with trifluoroacetic acid [7, 11].

To a solution of 2'/3'-O-[Bz(NO_2)-Orn(Boc)]-5'-O-Piv-Ado and 3'-O-[Bz(NO_2)-Orn(Boc)]-5'-O-Piv-2'-dAdo in 5 ml dichlorometane were added 5 ml 30% solution of trifluoroacetic acid in dichlormetane at room temperature. After an hour the reaction mixture was evaporated under vacuo and coevaporated with dry acetonitrile and finally with diethyl ether. The trifluoroacetate salts of model substrates were obtained as solids which were hygroscopic.

3'/2'-O-[Bz(NO_2)-Orn]-5'-O-Piv-Ado.TFA (**1"**). ^{1}H NMR: δ = 1.108(s, 9H, CH_3), 1.68(m, 2H, 4-CH_2), 1.86(m, 1H) and 2.00(m, 1H, 3-CH_2), 2.84(m, 2H, 5-CH_2), 4.18-4.34(m, 2H, 5`-$CH_2$), 4.29(m, 1H, 4`-CH), 4.666(ddd, J=4.7, 7.8, 10.3 Hz, 1H, 2-CH), 5.018(t, J=5.9 Hz, 1H, 2`-CH), 5.367(dd, J=3.1, 5.4 Hz, 1H, 3`-CH), 5.940(d, J=6.4 Hz, 1H, 1`-CH), 7.74(bs, 2H, NH_2), 7.77(bs, 2H, NH_2), 8.104(d, J=8.9 Hz, 2H, 3-CH and 5-CH), 8.289(s, 1H, 2-CH), 8.478(s, 1H, 8-CH), 8.347(d, J=8.9 Hz, 2H, 2-CH and 6-CH), 9.233(d, J=7.8 Hz, 1H, 2-CHN<u>H</u>).

^{13}C NMR: δ = 24.11(4-CH_2), 26.91(CH_3), 27.50(3-CH_2), 38.40(C), 38.62(5-CH_2), 63.19(5`-$CH_2$), 71.28(2`-CH), 73.01 (3`-CH), 75.69(C), 79.62(4`-CH), 87.44(1`-CH), 116.7 (<u>C</u>F_3 COO^-), 119.20(5-C), 123.69(3-CH and 5-CH), 128.93 (2-CH and 6-CH), 139.16(i-C), 139.53(8-C), 149.12(4-C), 149.37 (p-C), 149.43(2-CH), 153.68(6-C), 158.62 (CF_3<u>C</u>OO^-), 165.24(NHCO), 170.66(3'-COOC), 177.56(5'-OC=O).

3'-O-[Bz(NO_2)-Orn]-5'-O-Piv-2'-dAdo.TFA (**2"**). ^{1}H NMR: δ = 1.105(s, 9H, CH_3), 1.55(m, 2H, 4-CH_2), 1.84(m, 1H) and 1.93(m, 1H, 3-CH_2), 2.61(m, 2H, 2`-$CH_2$), 2.80(m, 2H, 5-$CH_2$), 4.22(m, 1H, 4`-CH), 4.36(m, 2H, 5`-$CH_2$), 4.85(m, 1H, 2-CH), 5.28(m, 1H, 3`-CH), 5.97(d, J=6.4 Hz, 1H, 1`-CH), 7.380(s, 2H, NH_2), 8.100(d, J=8.9 Hz, 2H, 3-CH and 5-CH), 8.485(s, 1H, 2-CH), 8.507(s, 1H, 8-CH), 8.297(d, J=8.9 Hz, 2H, 2-CH and 6-CH), 8.993(d, J=7.7 Hz, 1H, 2-CHN<u>H</u>).

^{13}C NMR: δ = 26.22(4-CH_2), 25.69(CH_3), 27.33(3-CH_2), 37.73(2`-$CH_2$), 38.17(C), 38.30(5-$CH_2$), 62.34(5`-CH_2), 75.44(3`-CH), 78.35(4`-CH), 83.76(1`-CH), 119.43(5-C), 123.81(3-CH and 5-CH), 129.29(2-CH and 6-CH), 139.16(i-C), 139.84(8-C), 149.11(4-C), 149.41(p-C), 152.40(2-CH), 156.13(6-C), 165.34(NHCO), 170.59(3'-COOC), 176.59(5'-OC=O).

4. DISCUSSION

4.1. Design of the Substrates

2'/3'-O-(α-N-p-nitrobenzoyl-L-ornithinyl) 5'-O-pivaloyl adenosine (**1**) and its deoxy analog (**2**) were designed to be soluble in organic solvents (hydrophobic protecting group pivaloyl (Piv) and p-nitrobenzoyl (nBz) groups as well as functionalized with a chromophoric group (p-nitrobenzoyl (nBz) group) to possess a suitable signal for HPLC monitoring and finally with a protecting group (pivaloyl (Piv) group) that survives the cleavage of the temporary protecting group t-butyloxycarbonyl (Boc) group (Fig. **1**).

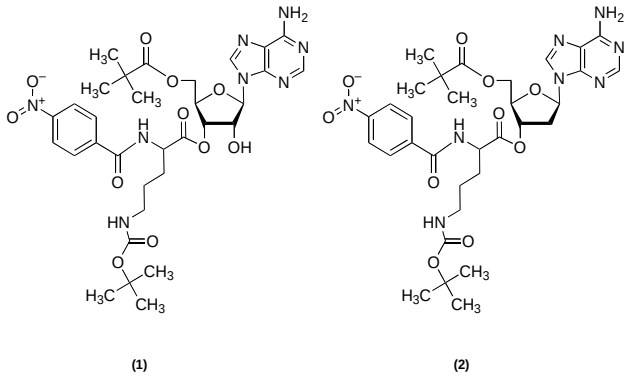


Figure 1. Design of 2'/3'-O-[Bz(NO_2)-Orn(Boc)]-5'-O-Piv-Ado (**1**) and 3'-O-[Bz(NO_2)-Orn(Boc)]-5'-O-Piv-2'-dAdo (**2**).

Our previous attempts to synthesize substrates for model ribosomal reactions were unsuccessful because of the many requirements and difficulties in choising suitable protecting groups for the different functionalities of the molecules, and the synthesis of the model compounds.

First, ornithine was chosen as an amino acid because it possesses N^{δ}-amino group as side functionality to mimic the intracomplex reaction of the attack of an α-amino group of aminoacyl tRNA on the 3'-ester carbonyl carbon atom of peptidyl tRNA during the peptidyl transferase reaction on the ribosome. The N^{α}-amino group of the amino acid compound had to be protected with a permanent protection (nBz), that survives all procedures of the synthesis and deprotection of other groups, that mimics the increasing peptide chain in the peptidyl tRNA and that possesses a chromophoric group to allow an appropriate signal for HPLC monitoring of the reaction. The N^{δ}-amino group of the amino acid was protected with a Boc-group to avoid unwanted side reactions during the aminoacylation of the nucleoside component under base conditions. It also had to be an acid-labile group to allow the deprotection of N^{δ}-amino group at the last stage of synthesis of the model substrates, immediatelly before the kinetic measurement experiments.

Second, pivaloyl (trimethyl acetyl) protecting group in 5'-O-pivaloylated adenosine (5'-O-Piv-Ado) and its 2'-deoxy analog was chosen as a hydrophobic group for permanent protection of 5'-OH group in the nucleoside compounds. The pivaloyl protection mimics the ribonucleotide chain of tRNA, bind to the A76 of the 3'-OH end of the pep-

tidyl tRNA, and it survives all procedures of the synthesis. It is hydrophobic, mimics tRNA and allows the model substrates to be soluble in aprotic organic media (CH_3CN) in which the experiments were carried out. Previous attempts to employ trityl (Trt)-group as a protection for 5'-OH-group of the nucleoside were unsuccessful, because of the acid lability of this group rather, than Boc-protection under the conditions of deprotection of N^{δ}-(Boc)-amino group of ornithine in the model substrates before the kinetic experiments. Pivaloyl (Piv) (trimethylacetyl) protecting group seemed the most suitable, which was stable under these conditions. It is exclusively stable under acid conditions and survives under basic conditions. It is selectively cleaved by tetrabutylammonium hydroxide.

The only difference between the two substrates is the presence of the 2'-OH-group in the 2'/3'-O-(α-N-p-nitrobenzoyl-L-ornithinyl) 5'-O-pivaloyl adenosine (**1**) and its lack in the 2'-deoxy analog (**2**).

4.2. Synthesis of the Substrates

For the successful synthesis of 2'/3'-O-(α-N-p-nitrobenzoyl-δ-N-(Boc)-L-ornithinyl) 5'-O-pivaloyl adenosine (**1**) and 3'-O-(α-N-p-nitrobenzoyl-δ-N-(Boc)-L-ornithinyl) 5'-O-pivaloyl 2'-deoxy adenosine (**2**) (Fig. **2**), the general and efficient route of Robertson *et al.* for chemical aminoacylation of nucleosides and nucleotides with cyanomethyl esters of amino acids was employed with some modifications [4, 7, 12]. The cyanomethyl esters of N-protected amino acids are known from classical peptide synthesis to be midly activated, requiring about (ca) 24-48 hours for complete coupling [13, 14], but they are suitable reagents for the aminoacylation of nucleosides [4, 12].

The model substrates **1** and **2** contain nucleoside and amino acid parts.

It was first necessary to synthesize adenosine and 2'-deoxyadenosine derivatives with protected 5'-OH group to avoid unwanted side reactions and making these compounds more soluble in aprotic organic solvents. We used pivaloyl (2,2,2-trimethyl acetyl) group as a bulk and hydrophobic protection group which is stable under acid and base conditions and is selectively cleaved upon treatment with tetrabutylammonium hydroxide. The 5'-O-pivaloyl adenosine was synthesized after the protection of 2',3'-OH groups with 2,2-dimethoxy propane and reaction of 2',3'-O-isopropylidene adenosine with 1.2 equivalents of pivaloyl chloride in pyridine [10]. The reaction of protection of 2',3'-OH groups of adenosine was carried out using two different procedures. The first procedure includes using 2,2-dimethoxy propane as reagent for introducing of the isopropylidene protecting group, and p-toluenesulfonic acid as catalyst. The second procedure was carried out employing a mixture of acetone/CH_3OH as solvents and at the same time as reagents for isopropylidene protection. H_2SO_4 was used as acid catalyst. The yield in this procedure was higher than in the former reaction. Moreover the reaction product obtained, was with high purity and low cost, because of the inexpensive reagents for introducing the isopropylidene protection. To the best of our knowledge this is the first method for introduction of the isopropylidene group using a mixture of acetone/CH_3OH as solvents and at the same time as reagents for isopropylidene protection, and H_2SO_4 as catalyst. In both procedures the reaction temperature was about 25^0C. For the successful synthesis of adenosine and 2'-deoxyadenosine derivatives with pivaloyl protected 5'-OH group we used the strategy of

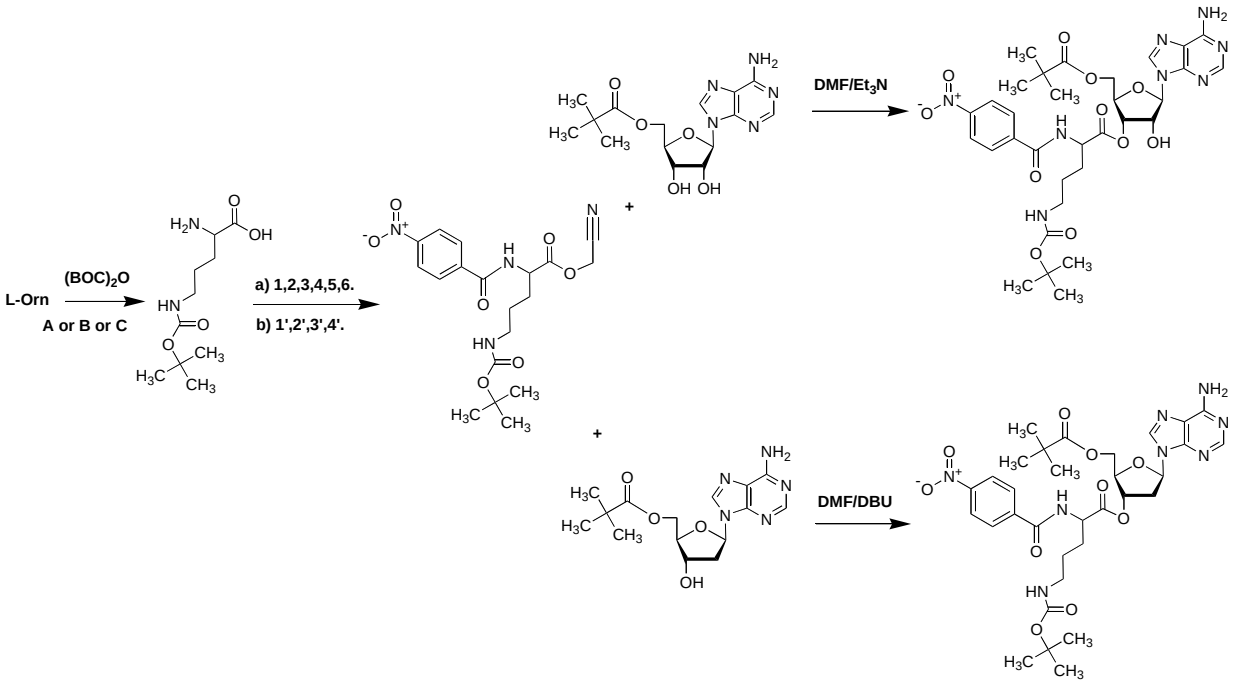


Figure2. Reaction pathways for synthesis of **1** and **2**. 1N NaOH, MeOH[15, 16]; **B.** $CuSO_4$, KOH, MeOH [17, 18]; **C.** $CuCO_3$, $NaHCO_3$, acetone [19]. **Patway a) 1**: Fmoc-ONSu, $NaHCO_3$, acetone [20, 21]; **2**: CH_2N_2, Et_2O; **3:** piperidine or 10% Et_2N/DMF**; 4:** $Bz(NO_2)$-Cl, $CHCl_3$, $NaHCO_3$, **5:** 1N NaOH, MeOH; 6: $ClCH_2CN$, DMF, Et_3N [4], [12]. **Patway b) 1':** trimethyl ortoformate, $NaHSO_4$, MeOH; **2':** $Bz(NO_2)$-Cl, CH_2Cl_2, Et_3N; **3':** 1N NaOH, MeOH; **4':** $ClCH_2CN$, DMF, Et_3N [4], [12].

Fromageot *et al.* [10] again with our modifications in the purification procedure, which we believe may find wide application in the synthetical nucleoside chemistry. The 5'OH-protected adenosine and 2'-deoxyadenosine derivatives were synthesized as shown in Fig. (**3**). Two different reaction conditions were used to synthesize the 5'-O-Piv adenosine. When we carried out the reaction in 0^0C in the beginning, and after 30 min. at room temperature, the yields were higher, than carrying at ambient temperature at the all time.

The synthesis of 5'-O-pivaloyl 2'-deoxy adenosine was carried out without preliminary protection of 3'-OH group of 2'-deoxy adenosine moiety with 1.2 equivalents of pivaloyl chloride. The 5'-OH group was selectively acylated and the co-products were removed by silicagel column chromatography.

The aminoacyl component was protected employing orthogonal type of protection of amino acids, having side functional groups. Protection of α-NH_2 goup with p-nitrobenzoyl group allows monitoring of the reaction by HPLC. δ-NH_2 group was protected with Boc-protecting group and the carboxyl group of the amino acid was activated as a cyanomethyl ester, allowing its coupling with 5'-O-protected nucleosides by the reaction of transesterification for aminoacylation of nucleosides.

Bz(NO_2)-Orn(Boc)-OCH_3 was synthesized as a precursor of a mildly activated cyanomethyl ester. It was needed because of the very low yields and long reaction time of nitrobenzoylation of H-Orn(Boc)-OH with Bz(NO_2)-Cl under standard Shotten-Baumann conditions, probably due to the low solubility of the Boc-amino acid in CH_2Cl_2 ($CHCl_3$). When we tried to obain Bz(NO_2)-Orn(Boc)-OH according to the procedure of nitrobenzoylation of Orn(Boc)-OH with N-hydroxysuccinimide or cyanomethyl activated esters of p-nitrobenzoic acid the yields were also unsatisfactory due to the very low reactivity of this reagents (sterically hindered). H-Orn(Boc)-OCH_3 is much more soluble, the reaction with Bz(NO_2)-Cl proceeds within 2-3 hours and the yields were higher.

Two different pathways for the synthesis of methyl ester of α-N-p-nitrobenzoyl-δ-N-(Boc)-L-ornithine were used [22].

Finally the 5'-O-Piv-2'-dAdo and 5'-O-Piv-Ado were aminoacylated with Bz(NO_2)-Orn(Boc)-OCH_2CN in DMF, using sterically hindered non nucleophyllic tertiary bases as catalysts to obtain 3'-O-[Bz(NO_2)-Orn(Boc)]-5'-O-Piv-2'-dAdo (**2**) and 2'/3'-O-[Bz(NO_2)-Orn(Boc)]-5'-O-Piv-Ado (**1**) [4, 7, 12]. In the case of ornithinylation of 5'-O-Piv-2'-dAdo DBU was used (Fig. **4**), and in the reaction with 5'-O-Piv-Ado as a base component was employed triethylamine [4, 7] (Fig. **5**).

Cleaving of the Boc-protection of 3'-O-[Bz(NO_2)-Orn(Boc)]-5'-O-Piv-2'-dAdo (**2**) and 2'/3'-O-[Bz(NO_2)-Orn(Boc)]-5'-O-Piv-Ado (**1**) leads to their trifluoroacetate salts: 3'-O-[Bz(NO_2)-Orn]-5'-O-Piv-2'-dAdo.TFA (**2"**) and 2'/3'-O-[Bz(NO_2)-Orn]-5'-O-Piv-Ado.TFA (**1"**) immediatelly before the kinetic experiments with these substrates (Fig. **6**). Because of the large size and many functionalities in these substrates they were susceptible to strong reaction conditions (TFA, HCl in dioxane). Therefore the Boc-group in these substrates was removed using 15% solution of TFA in CH_2Cl_2 for 3-4 hours (TLC) at room temperature.

Moreover, α-N-p-nitrobenzoyl-cyclo-L-Ornithine (α-N-Bz(NO_2)-C-Orn, δ-lactam, 3-(p-nitrobenzoylamino) piperidine-2-on) was prepared as an internal standard for properly monitoring of the products with HPLC (α-N-Bz(NO_2)-C-Orn and 5'-O-Piv-2'-dAdo or 5'-O-Piv-Ado) during the model reactions of cyclization of 3'-O-[Bz(NO_2)-Orn]-5'-O-Piv-2'-dAdo.TFA (**2"**) and 2'/3'-O-[Bz(NO_2)-Orn]-5'-O-Piv-Ado.TFA (**1"**). For this purpose Bz(NO_2)-Orn-OCH_3.TFA was synthesized by deprotection of Bz(NO_2)-Orn(Boc)-OCH_3 in TFA:CH_2Cl_2 – 25%:75% at room temperature for 3-4 hours and incubation of its salt- Bz(NO_2)-Orn-OCH_3.TFA in methanol and 3 equiv. triethylamine at 50^0C for 2-3 hours. Under these conditions pure α-N-Bz(NO_2)-C-Orn was obtained without further purification.

CONCLUSION

The two compounds: 2'/3'-O-[Bz(NO_2)-Orn(Boc)]-5'-O-Piv-Ado (**1**) and 3'-O-[Bz(NO_2)-Orn(Boc)]-5'-O-Piv-2'-dAdo (**2**) were designed and synthesized as substrates for the

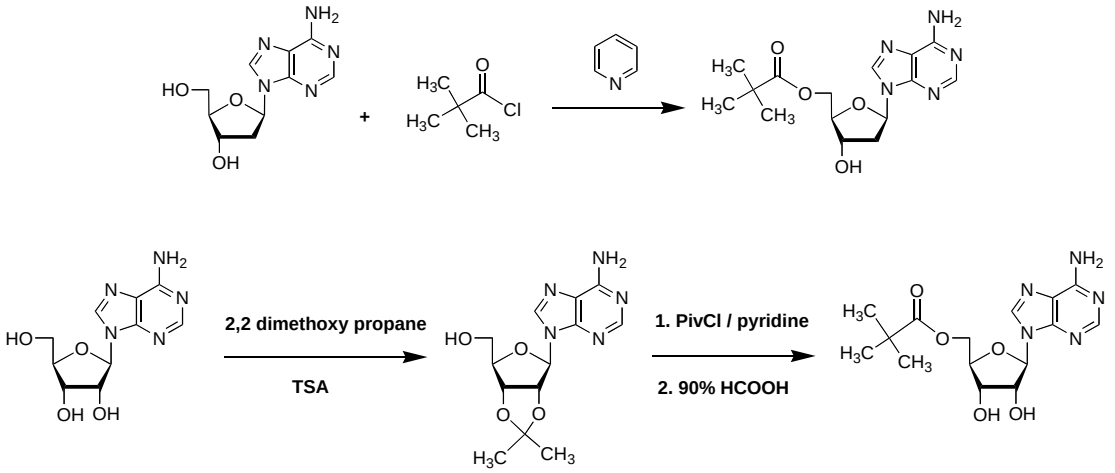


Figure 3. Scheme of the synthesis of 5'-O-pivaloyl adenosine and its 2'-deoxy analog.

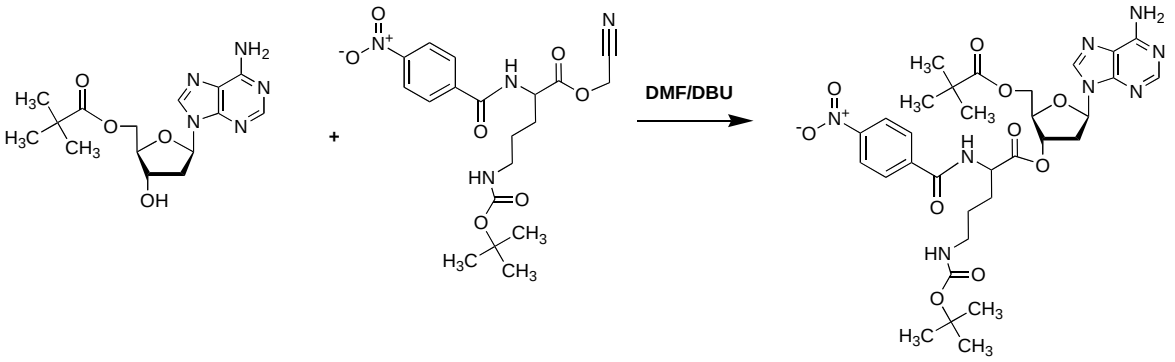


Figure 4. Synthesis of 3'-O-[Bz(NO_2)-Orn(Boc)]-5'-O-Piv-2'dAdo (**2**) by aminoacylation of 5'-O-Piv 2'dAdo with Bz(NO_2)-Orn(BOC)-OCH_2CN.

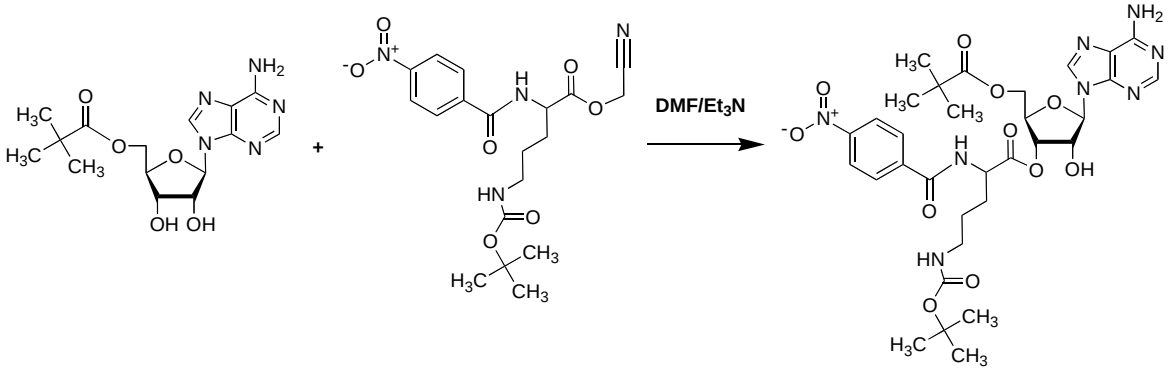


Figure 5. Synthesis of 2'/3'-O-[Bz(NO_2)-Orn(Boc)]-5'-O-Piv-Ado (**1**) by aminoacylation of 5'-O-Piv Ado with Bz(NO_2)-Orn(Boc)-OCH_2CN.

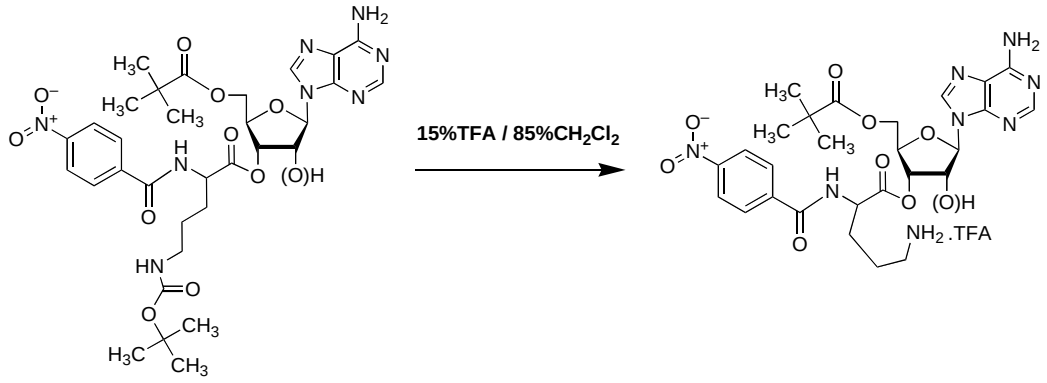


Figure 6. Cleaving of BOC-protection from **1** and **2**.

model ribosomal reactions, using precisely selected strategy of combination of protecting groups and methods for peptide, nucleoside and nucleotide synthesis. In another paper we have carried out model ribosomal reactions with these substrates and proved the essential role of cis-vicinal 2-OH-group in 1,2-diol monoester aminolysis, and the crucial role of A76 2'-OH of peptidyl-tRNA in the rate acceleration of peptide bond formation (Fig. **7**) by deprotection of δ-N-Boc-groups of **1** and **2** in aminoacyl (ornithinyl) moiety with TFA and employing in our model ribosomal reactions.

On the other hand the synthesis of these model substrates and the kinetic experiments opens a strategy for the preparation of a new class substrate inhibitors of translation. The 2'/3'-O-[Bz(NO_2)-Orn(Boc)]-5'-O-Piv-Ado, (2'/3'-O-[Orn]-5'-O-Piv-Ado.2TFA) and its macromolecule $tRNA^{aa}$ analog may be employed as potencial anticancer drugs, potencial blockers of the elongation step of protein biosynthesis.

ACKNOWLEDGEMENTS

The financial support by the National Research Fund of Bulgaria (grants X-1517 and X-1408, and for the purchase of Bruker Avance II+ 600 NMR spectrometer in the framework of the Program "Promotion of the Research Potential through Unique Scientific Equipment" – Project UNA-17/2005) is gratefully acknowledged.

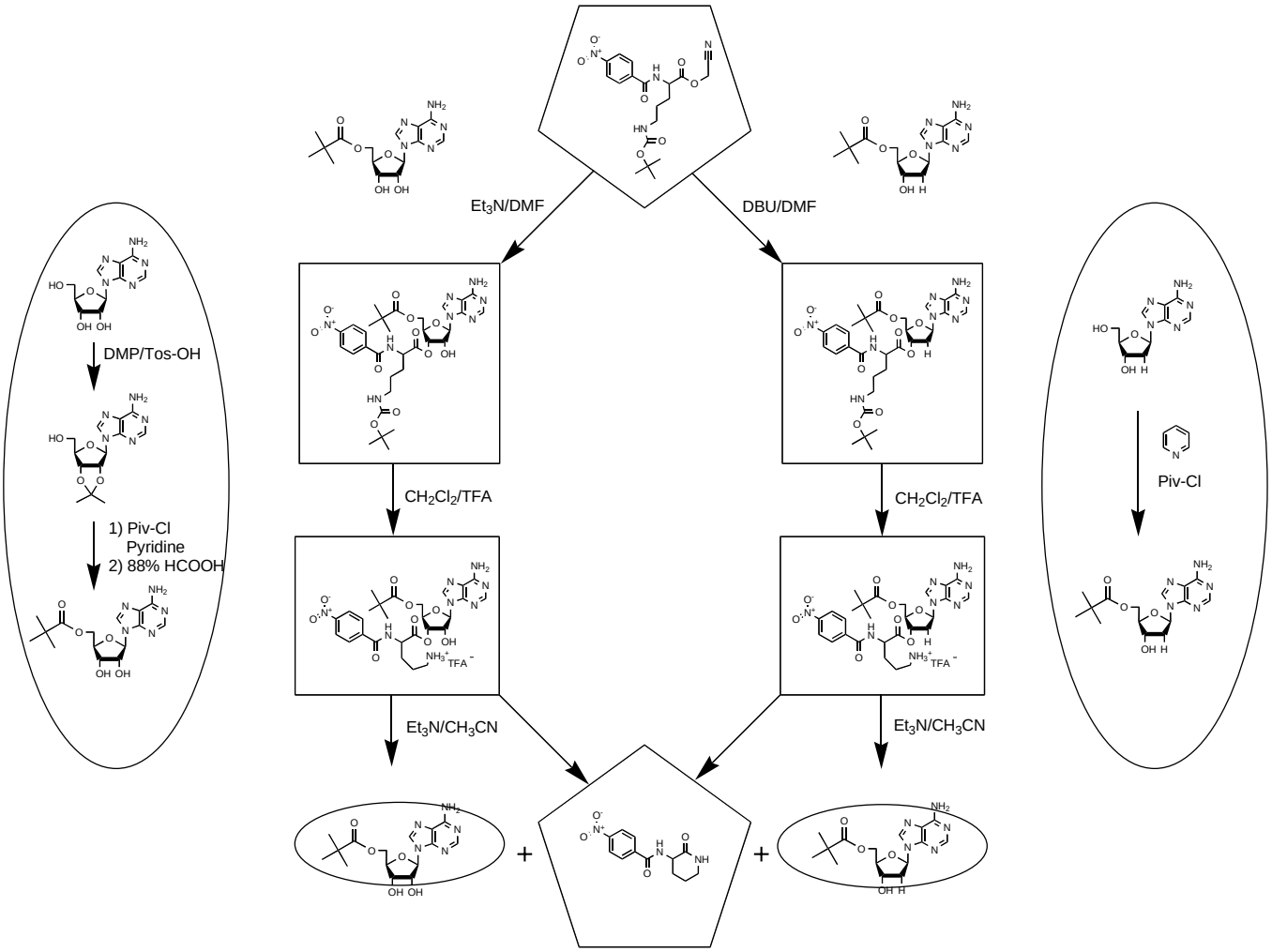


Figure 7. Schematic presentation of the synthetic pathways for the preparation of bioorganic models and their cyclization (intramolecular aminolysis, lactamization).

LIST OF ABBREVIATIONS

Ado	=	Adenosine
BBO	=	Broadband observe
Boc	=	Tret-butyloxycarbonyl
Bz	=	Benzoyl
Bz(NO_2)	=	p-Nitro-Benzoyl
COSY	=	Correlation Spectroscopy
dAdo	=	2'-Deoxy-Adenosine
DBU	=	1, 8-Diazabicyclo-[5, 4, 0]-undec-7-ene
DEPT-135	=	Distortionless Enhanced Polarization Transfer using a 135 degree decoupler pulse
DMF	=	Dimethylformamide
Et_3N	=	Triethylamine
HMBC	=	Heteronuclear Multiple Bond Correlation
HPLC	=	High Performance Liquid Chromatography
HSQC	=	Heteronuclear Single Quantum Correlation
IR	=	Infrared spectroscopy
NMR	=	Nuclear Magnetic Resonance
Orn	=	Ornithine
Piv	=	Pivaloyl (trimethyl acetyl)
RNA	=	Ribonucleic acid
TBI	=	Triple broadband inverse
TFA	=	Trifluoroacetic acid
tRNA	=	Transfer Ribonucleic acid
$tRNA^{aa}$	=	Aminoacyl transfer Ribonucleic acid
TLC	=	Thin layer chromatography

REFERENCES

[1] Sievers, A.; Beringer, M.; Rodnina, M.V.; Wolfenden, R. The ribosome as an entropy trap. *Proc. Natl. Acad. Sci. USA*, **2004**, *101*(21), 7897-7901.

[2] Rodnina, M.V.; Beringer, M.; Wintermeyer, W. Mechanism of Peptide Bond Formation on the Ribosome. *Q. Rev. Biophy.*, **2006**, *39*(3), 203-225.

[3] Youngman, E.M.; Brunelle J.L.; Kochaniak, A.B.; Green, R. The active site of the ribosome is composed of two layers of conserved

nucleotides with distinct roles in peptide bond formation and peptide release. *Cell*, **2004**, *117*(5), 589-599.

[4] Changalov, M.M.; Ivanova, G.D.; Rangelov, M.A.; Acharia, P.; Acharia, S.; Minakawa, N.; Foldesi, A.; Stoineva, I.B.; Yomtova, V.M.; Roussev, C.D.; Matsuda, A.; Chattopadhyaya, J.; Petkov, D.D. 2'/3'-O-peptidyl Adenosine as a General Base Catalyst of its Own External Peptidyl Transfer: Implications for the Ribosome Catalytic Mechanism. *ChemBioChem*., **2005**, *6*(6), 992-996.

[5] Weinger, J.S.; Parnell, K.M.; Dorner, S.; Green, R.; Strobel, S.A. Substrate-assisted catalysis of peptide bond formation by the ribosome. *Nat. Struct. Mol. Biol*., **2004**, *11*, 1101-1106.

[6] Rangelov, M.A.; Vayssilov, G.; Yomtova, V.M.; Petkov, D.D. The syn-Oriented 2-OH Provides a Favorable Proton Transfer Geometry in 1,2-Diol Monoester Aminolysis: Implications for the Ribosome Mechanism. *J. Am. Chem. Soc*., **2006**, *128*(15), 4964-4965.

[7] Bayryamov, S.G.; Rangelov, M.A.; Mladjova, A.P.; Yomtova, V.M.; Petkov, D.D. Unambiguous evidence for efficient chemical catalysis of adenosine ester aminolysis by its 2′/3′-OH. *J. Amer. Chem. Soc.*, **2007**, *129*(18), 5790-5791.

[8] Vassilev, N. Fully automatic first-order multiplet analysis (FAFOMA). *Bulg. Chem. Commun*., **2005**, *37*(4), 256-259.

[9] Hampton, A. Nucleotides. II. A New Procedure for the Conversion of Ribonucleosides to 2′,3′-*O*-Isopropylidene Derivatives. *J. Amer. Chem. Soc.*, **1961**, *83*(17), 3640-3645.

[10] Fromageot, H.P.M.; Griffin, B.E.; Reese, C.B.; Sulston, J.E. The synthesis of oligoribonucleotides—III: Monoacrylation of ribonucleosides and derivatives *via* orthoester exchange. *Tetrahedron*, **1967**, *23*(5), 2315-2331.

[11] Kappeler, H.; Schwyzer, R. Synthese eines Heptapeptides mit starker CRF-Wirkung. *Helv. Chim. Acta*, **1960**, *43*(6), 1453-1459.

[12] Robertson, S.A.; Ellman, J.A.; Schultz, P.G. A General and Efficient Route for Chemical Aminoacylation of Transfer RNAs. *J. Am. Chem. Soc*., **1991**, *113*(7), 2722-2729.

[13] Schwizer, R.; Iselin, B.; Rittel, W.; Sieber, P. Synthesen zyklischer Polypeptide. c-Tetraglycyl und c-Hexaglycyl. Über aktivierte Ester VII. *Helv. Chim. Acta*, **1956**, *39*(3), 872-883.

[14] Bodanszky, M. In *The peptides*; Gross, E., Meienhofer, J., Ed.; Academic Press Inc.; New York, San Francisco, London, **1979**, Vol. *1*, pp. 105-196.

[15] Scallenberg, E.E.; Calvin, M. Ethyl Thioltrifluoroacetate as an Acetylating Agent with Particular Reference to Peptide Synthesis. *J. Am. Chem. Soc*., **1955**, *77*(10), 2779-2783.

[16] Greenstein, G.P.; Winitz, M. In *Chemistry of The Amino Acids*; Wiley and Sons, New York, **1961**, pp. 915.

[17] Bodanszky, M.; Bodanszky, A. *The Practice of Peptide Synthesis*; Akademie-Verlag: Berlin, **1985**.

[18] Wunsch, E.; Fries, G.; Zwick, A. Beiträge zur Peptidsynthese, V. Darstellung und peptidsynthetische Verwendung von *O*-Benzyl-L-tyrosin. *Chem. Ber*., **1958**, *91*(3), 542-547.

[19] Roeske, R.; Stewart, F.H.S.; Stedman, R.J.; du Vigneaud, V. Synthesis of a Protected Tetrapeptide Amide Containing the Carboxyl Terminal Sequence of Lysine-Vasopressin. *J. Am. Chem. Soc*., **1956**, *78*(22), 5883-5887.

[20] Paquet, A. Introduction of 9-fluorenylmethyloxycarbonyl, trichloroethoxycarbonyl, and benzyloxycarbonyl amine protecting groups into O-unprotected hydroxyamino acids using succinimidyl carbonates. *Can. J. Chem*., **1982**, *60*(8), 976-980.

[21] Sigler, G.F.; Fuller, W.D.; Chaturvedi, N.C.; Goodman, M.; Verlander, M. Formation of oligopeptides during the synthesis of 9-fluorenylmethyloxycarbonyl amino acid derivatives. *Biopolymers*, **1983**, *22*(10), 2157-2162.

[22] Bayryamov, S.G.; Vassilev, N.G, (unpublished results).

Received: August 26, 2008 Revised: September 25, 2008 Accepted: November 03, 2008

THE JOURNAL OF PHYSICAL CHEMISTRY A

ARTICLE

pubs.acs.org/JPCA

Density Functional Study of Hydrogen Bond Formation between Methanol and Organic Molecules Containing Cl, F, NH_2, OH, and COOH Functional Groups

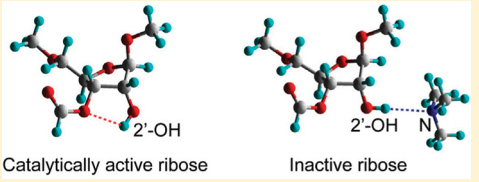
Stefan K. Kolev,[†] Petko St. Petkov,[†] Miroslav A. Rangelov,[‡] and Georgi N. Vayssilov*[,†]

[†]Faculty of Chemistry, University of Sofia, Boulevard James Bouchier 1, 1126 Sofia, Bulgaria

[‡]Laboratory of BioCatalysis, Institute of Organic Chemistry, Bulgarian Academy of Sciences, Str. Acad. G. Bontchev, Bl. 9, 1113 Sofia, Bulgaria

Supporting Information

ABSTRACT: Various hydrogen-bonded complexes of methanol with different proton accepting and proton donating molecules containing Cl, F, NH_2, OH, OR, and COOH functional groups have been modeled using DFT with hybrid B3LYP and M05-2X functionals. The latter functional was found to provide more accurate estimates of the structural and thermodynamic parameters of the complexes of halides, amines, and alcohols. The characteristics of these complexes are influenced not only by the principle hydrogen bond of the methanol OH with the proton acceptor heteroatom, but also by additional hydrogen bonds of a C−H moiety with methanol oxygen as a proton acceptor. The contribution of the former hydrogen bond in the total binding enthalpy increases in the order chlorides < fluorides < alcohols < amines, while the contribution of the second type of hydrogen bond increases in the reverse order. A general correlation was found between the binding enthalpy of the complex and the electrostatic potential at the hydrogen center participating in the formation of the hydrogen bond. The calculated binding enthalpies of different complexes were used to clarify which functional groups can potentially form a hydrogen bond to the 2′-OH hydroxyl group in ribose, which is strong enough to block it from participation in the intramolecular catalytic activation of the peptide bond synthesis. Such blocking could result in inhibition of the protein biosynthesis in the living cell if the corresponding group is delivered as a part of a drug molecule in the vicinity of the active site in the ribosome. According to our results, such activity can be accomplished by secondary or tertiary amines, alkoxy groups, deprotonated carboxyl groups, and aliphatic fluorides, but not by the other modeled functional groups.



1. INTRODUCTION

Hydrogen bonding is one of the most important types of interaction determining properties and functioning of both natural and artificial systems from water to advanced materials and living organisms.[1−6] Formation of hydrogen bonds is exclusively used by the nature for arrangement of the structure of various biomolecules, molecular recognition, directing of biochemical processes, and so on. Based on the knowledge on the active centers of key biomolecules (as enzymes, peptides, or nucleic acids), the hydrogen bonding ability of different functional groups is also used as a tool in the selective binding of drugs to their targets.[3] In addition to the increasing the interaction between or within molecules, formation of hydrogen bonds can influence the reactivity of different active sites or can even change the reaction mechanism of chemical or biochemical processes.[6−9]

Various hydrogen-bonded complexes of methanol with different proton accepting and proton donating molecules have been studied both experimentally and computationally. Appropriate references for the present study are the complexes in the gas phase because they are not affected by their surroundings (solvent in solution or other molecules in solids). The structure of such complexes was investigated by microwave spectroscopy or rotationally resolved laser-induced fluorescence spectroscopy.[10−14] Formation and the properties of the complexes are often studied with different methods of the vibrational spectroscopy: infrared (IR), Raman,[15−21] jet FTIR,[22−24] jet Raman,[22] IR cavity ringdown spectroscopy,[25] IR-depletion spectroscopy,[26,27] and so on. Most often, the red shift of the stretching OH vibrations are followed, but in some cases, also low frequency vibrational modes have been measured by spectral hole burning[28] and disperse fluorescence spectroscopy.[28,29] The stability of the complexes of methanol with different amines, phenol, methanol, and so on have been determined by thermodynamic measurements,[19,30] IR,[19−21] NMR,[31] or TOF mass spectrometry with laser excitation.[32] In some of the studies the structural parameters, vibrational frequencies, and binding energies, measured experimentally, were supplemented by simulations with computational methods at different levels HF, DFT, MP2, MP4, and CI.[16,18,22,24,25,33−39] Where appropriate, we compared our results with those reported previously.

In the present study, we analyze structural and energetic features, electron density distribution, and vibrational frequencies of various hydrogen-bonded complexes containing methanol

Received: May 9, 2011
Revised: September 11, 2011
Published: October 12, 2011

ACS Publications © 2011 American Chemical Society

as a model of an aliphatic hydroxyl group in organic or bioorganic compounds as alcohols, polyols, carbohydrates, nucleic acids, and so on. As proton acceptor groups, we considered Cl, F, NH_2, OH, and COOH. To account for the possibility for formation of a second weak hydrogen bond C−H···O between the methanol oxygen atom and the organic moiety, for each functional group we considered a series of compounds with different aliphatic and aromatic substituents. In addition to the information for the individual modeled complexes, the present study can be helpful in the clarification of various local, intra-, and intermolecular interactions in larger systems based on formation of hydrogen bonds.

One of the various examples for the importance of hydrogen bonding is the influence of the vicinal 2′-OH group in ribose on the elementary step in the peptide bond formation in the ribosome, which is common for the protein biosynthesis in all living cells. The participation of this vicinal OH group in the proton transfer accompanying the process is found to reduce the energy barrier of the reaction by about 70 kJ/mol, leading to 10^9 orders of magnitude acceleration of the process.[40] Thus, the vicinal 2′-OH in the ribose has crucial importance for peptide bond formation that can be used as a specific target in the design of drugs controlling/inhibiting the protein biosynthesis in the living cells. Such function is accomplished by various types of antibiotics that target different parts of the ribosome: the peptidyl transferase center, the protein exit tunnel, and several mobile elements that provide the dynamics required for protein biosynthesis.[41,42] Because methanol can be considered as a simplified model of the 2′-hydroxyl group in ribose, we can use the results from the present calculations to help find an alternative way of inhibiting protein biosynthesis by clarification of the type of proton acceptor functional groups that can potentially block via a hydrogen bond the 2′-OH hydroxyl group in ribose and, thus, can inhibit the protein biosynthesis if it can be delivered as a part of a drug molecule in the vicinity of the active site in the ribosome.

2. COMPUTATIONAL DETAILS

The computational modeling was performed with the density functional method. All calculations were accomplished with the Gaussian 09 package.[43] For DFT calculations, we used two hybrid functionals, B3LYP[44−46] and M05-2X.[47] The latter functional was recommended for modeling of system in which weak dispersion interactions are important.[48] The formation of the hydrogen bond of the OH group of methanol with organic molecules containing Cl, F, NH_2, OH, and COOH functional groups was modeled. In each series we considered compounds with different hydrocarbon parts: methyl (Me), ethyl (Et), propyl (Pr), isopropyl (iPr), cyclohexyl (Chex), and phenyl (Ph). In some series, we included additional compounds to compare the results with available experimental data (as complexes of methanol with water, dimethyl and diethyl ethers, etc.).

To find the most stable structures of the complexes, we started the optimization of their geometries from different initial orientations and different conformations of the interacting molecules. For example, the most stable conformers obtained in optimization of diethylamine and triethylamine starting from various initial structures correspond to the most stable structures in C_s and C_3 symmetry, respectively, derived from experimental data.[49] To clarify the contributions of different types of possible hydrogen bonds of methanol acting only as proton donor and acceptor, for methyl-substituted halides, amines, and alcohols, we performed additional calculations with a fixed linear orientation of the desired hydrogen bond O−H···X or C−H···O-(MeOH) and compared the results with those from unconstrained optimization. In the following we reported as hydrogen bonds only the bonds with interatomic distances H···X (X = N, O, F, Cl) lower than the sum of the van der Waals radii of the two atoms:[50] 275, 272, 267, and 295 pm for N, O, F, and Cl, respectively.

For all calculations we used the 6-311++G(2df,2pd) basis set. For both DFT functionals we performed the geometry optimization with accounting for the BSSE correction at each optimization step, as suggested previously[51,52] (the final BSSE correction energies are reported in Table S1 of the Supporting Information). For comparison, for methyl, ethyl, and phenyl amines, alcohols, and halides, we also optimized the structures of the complexes with MP2 method using the same basis set.

Harmonic vibrational frequencies and Zero Point Energy Corrections (ZPE) were calculated for the optimized complexes and for the nonbonded molecules. None of the fully optimized complexes has imaginary frequencies. The procedure for correcting the calculated frequencies is described in section 3.2. It is based on the scaling coefficients reported earlier, 0.955 for B3LYP and 0.936 for M05-2X,[53] and comparison of the results obtained here with available experimental data for hydrogen-bonded complexes of methanol.

The binding energies of the complexes, BE, were calculated according to the scheme

$$\mathrm{BE} = E_C^{\mathrm{BSSE,ZPE}} - (E_{M1}^{\mathrm{ZPE}} + E_{\mathrm{MeOH}}^{\mathrm{ZPE}}) \quad (1)$$

where $E_C^{\mathrm{BSSE,ZPE}}$ is the electronic energy of the complex corrected for BSSE and ZPE, and E_{M1}^{ZPE} and $E_{\mathrm{MeOH}}^{\mathrm{ZPE}}$ are the electronic energies of the isolated molecules and isolated methanol corrected for the ZPE. The obtained BE values were used to calculate the enthalpy, ΔH, and Gibbs free energy, ΔG, for formation of the complexes. In addition to the calculated electronic energy, BSSE, and ZPE, in calculation of the enthalpy change, ΔH, we took into account the thermal populations of vibrational, rotational, and translational energies. The entropy change, ΔS, included the calculated translational, rotational and vibrational contributions to the entropy. All energy values in the present work are in kJ/mol and the thermodynamic characteristics are calculated at T = 298 K.

Atomic charges of the free molecules and complexes were estimated using Mulliken,[54] Chelpg[55] and NBO[56] schemes as implemented in Gaussian 09, but only NBO charges are reported in the paper. The electrostatic potential at nuclei (EPN), defined for nuclei Y as[57,58]

$$V_Y \equiv V(R_Y) = \sum_{A \neq Y} \frac{Z_A}{|R_Y - R_A|} - \int \frac{\rho(r')}{|R_Y - r'|} \mathrm{d}r' \quad (2)$$

was also evaluated. In the equation, Z_A is the charge on nucleus A with radius-vector R_A, $\rho(r)$ is the electronic density function of the respective molecule as obtained from quantum chemical calculations, and r' is a dummy integration variable. The equation is written in atomic units and contains a summation over all atomic nuclei, treated as positive point charges as well as integration over the continuous distribution of the electronic charge.

Table 1. Structural Data (Distances in pm, Angles in Degrees), and ΔH (in kJ/mol) for Formation of the Complexes of Methanol with R−NH_2, R−OH, ROR, and Water Molecules

	B3LYP				M05-2X				MP2			
H bond acceptor	HB1	Δ(OH)[a]	<OHX	ΔH	HB1	Δ(OH)[a]	<OHX	ΔH	HB1	Δ(OH)[a]	<OHX	ΔH
$MeNH_2$	194	1.6	172	−19.6	193	1.5	165	−23.1	193	1.5	169	−22.7
Me_2NH	193	1.8	172	−19.1	190	1.6	161	−25.3	185	1.9	168	−24.7
Me_3N	193	1.8	172	−17.8	189	1.8	178	−24.6	183	2.2	180	−25.4
$EtNH_2$	194	1.7	173	−19.7	195	1.4	167	−22.7	188	1.7	169	−22.7
Et_2NH	193	1.9	172	−19.1	187	1.9	167	−28.7	182	2.2	173	
Et_3N	200	1.7	169	−13.9	188	2.1	173	−25.9	185	2.4	172	
$PrNH_2$	194	1.7	173	−19.8	193	1.5	166	−23.5				
$iPrNH_2$	194	1.7	172	−20.2	193	1.6	167	−23.7				
$ChexNH_2$	195	1.7	175	−19.6	194	1.6	171	−25.9				
$PhNH_2$	206	1.0	166	−11.0	211	0.6	165	−17.7	203	0.9	167	
$MeNH_2$[b]	224	0.0	154	−3.3	226	0.0	135	−9.0	220	0.0	136	−8.3
$PhNH_2$[b]	210	0.0	172	−8.3	213	0.0	147	−15.7	210	0.1	146	
MeOH	194	0.8	175	−12.9	197	0.6	151	−16.9	193	0.7	169	−15.4
EtOH	194	0.8	174	−13.2	195	0.7	171	−18.8	188	0.9	173	−16.8
PrOH	194	0.8	176	−13.4	196	0.6	153	−17.3				
iPrOH	193	0.9	172	−14.2	193	0.8	162	−19.4				
ChexOH	194	0.9	174	−13.8	193	0.8	170	−19.6				
PhOH	204	0.4	169	−7.2	207	0.4	154	−14.0	199	0.5	161	
PhOH[b]	186	0.1	172	−18.9	188	0.1	163	−25.7	182	0.2	164	−24.0
Me_2O	193	0.8	177	−12.3	194	0.8	155	−16.8	185	1.0	175	−16.0
Et_2O	195	0.9	175	−11.8	191	0.8	174	−21.3	183	1.1	180	
H_2O	198	0.7	174	−11.6	198	0.6	179	−13.8	194	0.6	178	−12.0
H_2O[b]	193	0.1	173	−13.4	194	0.0	159	−16.8	189	0.1	167	−14.4

[a] Elongation of the OH distance in the complex compared to the distance in the free methanol molecule, which is calculated at 96.0, 95.6, and 95.8 pm at B3LYP, M05-2X, and MP2 levels, respectively. [b] Complex with methanol as acceptor of the hydrogen bond.

3. RESULTS AND DISCUSSION

The results for the modeled complexes with compounds containing different functional groups are reported and discussed in three groups due to the similarities in the bonding in the complexes: (i) amines and alcohols, (ii) halogen derivatives (fluorides and chlorides), and (iii) carboxylic acids. First we present the structural features of the complexes and their stability. The vibrational frequencies and electron density distribution in the complexes are discussed briefly in sections 3.2 and 3.3, respectively, and some general trends and correlations for the modeled complexes are highlighted. Finally, using the calculated binding enthalpies, we analyze the applicability of the different functional groups in blocking the 2′-OH of ribose. In various places we compare the obtained results with previous experimental or computational data.

3.1. Structure and Stability of the Complexes. *Complexes with Amines, Alcohols, and Ethers.* As expected, the binding of methanol to amines, alcohols, and ethers is determined mainly by the hydrogen bond between the heteroatom (nitrogen or oxygen) and the proton from the OH group of the methanol molecule. The pertinent structural information is reported in Table 1 and structures of some of these complexes are shown in Figure 1a−f. The optimized structures of all studied complexes at M05-2X level of theory are presented in Figure S2 of the Supporting Information.

The hydrogen bond length d(HB1), reported as the distance between the proton from the methanol OH group and the proton acceptor heteroatom, in the primary aliphatic amines calculated with B3LYP and M05-2X functionals is 194 ± 1 pm. Due to the lower basicity of aniline compared to the aliphatic amines, the d(HB1) in the corresponding complex is calculated notably longer, 206 and 211 pm for B3LYP and M05-2X. The values of d(HB1) for the aliphatic alcohols calculated with B3LYP and M05-2X functionals are very similar, 194 ± 1 and 195 ± 2 pm, respectively. The hydrogen bond to the phenol oxygen is notably longer, 204 and 207 pm for B3LYP and M05-2X. Due to higher acidity of the phenol, we optimized the complex MeOH−PhOH also with methanol as the proton acceptor and obtained a notably shorter hydrogen bond, 186−188 pm. In most cases, the d(HB1) obtained after optimization with the MP2 method are shorter than those obtained with the DFT method by 3−9 pm.

The length of the hydrogen bonds in the optimized complexes of methanol with secondary or tertiary amines (methyl or ethyl) and with dimethyl or diethyl ethers essentially fall into the intervals obtained for the primary amines and alcohols, respectively. Only the complex with triethyl amine calculated at the B3LYP level features a somewhat longer hydrogen bond, 200 pm.

The angle of the hydrogen bond, <O−H···X (X = N, O) depends to some extent on the functional employed in the calculations: for amines it varies in the intervals 166−175° (B3LYP) and 161−178° (M05-2X), and for alcohols, phenols, and ethers it varies in the intervals 169−177° (B3LYP) and 151−174° (M05-2X). Obviously, the intervals obtained with the

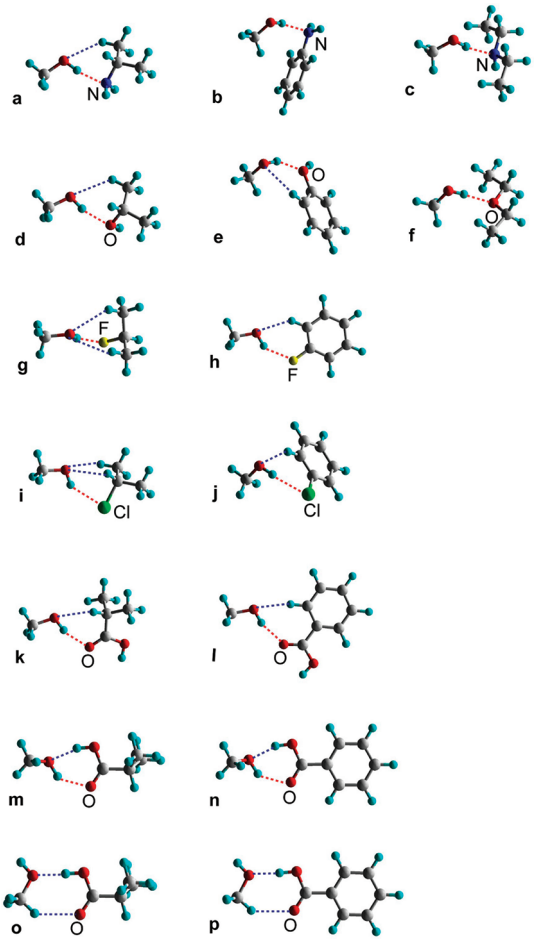


Figure 1. Examples of optimized structures (at M05-2X level) of the complexes of methanol bound via hydrogen bonds with amines (a−c), alcohols (d, e), ether (f), fluorides (g, h), chlorides (i, j), and carboxylic acids: complexes types A (k, l), B (m, n), and C (o, p).

M05-2X functional are larger, likely due to the ability of this functional to better account for formation of additional weak C−H···O bonds from the methanol oxygen atom and hydrogen from the hydrocarbon part of the other molecule in the complex. These additional interactions distort the structure of the complex from the optimal <O−H···X angle (around 180°).

According to the calculated enthalpies of formation, ΔH (see Table 1), all modeled complexes of methanol with amines, alcohols, and ethers are stable. The ΔH values calculated with M05-2X functional are higher (in absolute value) than those calculated with the B3LYP functional, by 2−12 kJ/mol as the difference is highest for di- and triethyl amines and diethyl ether. As expected, the enthalpies of formation of the complex with aliphatic amines, −23 to −29 kJ/mol (M05-2X), are higher than those for complexes with alcohols or ethers, −17 to −21 kJ/mol. The binding of methanol as proton donor to aniline or phenol is weaker, −18 and −14 kJ/mol (M05-2X), respectively. On the other hand, ΔH for the complex MeOH−PhOH with methanol as proton acceptor is −26 kJ/mol, by 12 kJ/mol more stable than the complex with methanol as proton donor. The lower stability of the latter complex agrees with longer HB1 distance in this case. The ΔH values calculated with the MP2 method for methyl and ethyl derivatives are slightly lower (in absolute values) than the values obtained with M05-2X functional: by 0.0−0.7 kJ/mol for amines and 0.8−2.0 kJ/mol for alcohols and ethers.

Table 2. Comparison of the Optimized and Experimentally Derived (Refs 11, 12, and 13) Structural Parameters (Distances in pm, Angles in Degrees) for the Complexes MeOH−Me_3N and MeOH−$PhNH_2$[a]

complex		experiment	B3LYP	M05-2X	MP2
MeOH−MeOH	$d_{O\cdots H}$	196 ± 2	194	197	193
MeOH−Me_3N	$d_{N\cdots H}$	192 ± 5	193	189	183
	<NHO	179.3 ± 5	171.9	178.1	179.5
MeOH−$PhNH_2$	d_{N-O}	303	301	305	298
	<CNO	94.9	124.1	89.2	90.1

[a] The optimized structures are shown in Figure S2c,j of SI.

Complexes MeOH−$MeNH_2$ and MeOH−$PhNH_2$, where the proton donor is the primary amine group and methanol acts as acceptor of the hydrogen bond (see Figure S2k,l of SI) were also studied. The first complex has lower stability by 14 kJ/mol (M05-2X) than the complex with methanol as proton donor. The enthalpy difference in the second case (MeOH−$PhNH_2$ complexes) is just 2 kJ/mol, because of the lower basicity of aniline compared to methylamine. This determines the preferable formation of methanol−alkylamine complexes, where methanol is the proton donor, while for methanol−arylamine complexes, both methanol and amine could act as proton donors.

For comparison, we modeled the complex of methanol (either as proton donor or proton acceptor) with water. In agreement with the experimental data,[10,27] the complex with the water molecule as proton donor is found to be more stable but only by about 3 kJ/mol (see Table 1).

For some of the compounds, the optimized structures of the complexes and the calculated interaction enthalpies can be compared with available experimental data. For example, the structures of methanol−methanol,[11] methanol−trimethylamine,[12] and methanol−aniline[13] complexes have been experimentally studied by microwave spectroscopy. The comparison with the experimental distances (Table 2) suggested that both functionals (B3LYP and M05-2X) provide accurate estimates of the characteristic distances: for the hydrogen bond lengths in MeOH−MeOH and MeOH−Me_3N complexes, the calculated values fall into the experimental error margins;[11,12] and for the N−O distance in MeOH−$PhNH_2$,[13] the deviation of the calculated values from the experiment is only ±2 pm, that is, ±0.7%. The experimentally determined symmetry group of the complex methanol−trimethylamine fits to the optimized structures of the complex both with B3LYP and M05-2X. The two functionals, however, behave differently in the reproduction of the experimental values of the characteristic angles. For both complexes, MeOH−Me_3N and MeOH−$PhNH_2$, the calculations with M05-2X functional yield in <NHO or <CNO angles differing from the experiment by only 1−5°. On the other hand, the <CNO angle in complex methanol−aniline optimized using the B3LYP functional is by about 30° higher than the values from experiment or from M05-2X calculations. This difference origin from the different orientation of the methyl group of methanol in the two optimized structures: in the M05-2X structure (Figure 1b), the CH_3 group interacts weakly with the benzene ring, while in the B3LYP structure, this group is far from the ring because the latter functional does not account for the dispersion interactions. The interatomic distances and angles for the complexes

optimized with the MP2 method fit well to the experimental values (Table 2).

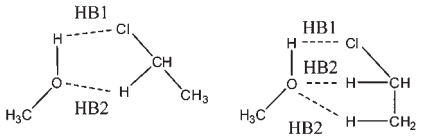
The experimental and calculated enthalpies for formation of the hydrogen-bonded complexes, ΔH, are presented in Table 3. The enthalpies determined with the M05-2X functional fall in the experimental interval for 6 of 8 complexes; as for two of the complexes, the difference between the calculated values and the center of the experimental interval is at most 0.3 kJ/mol. Larger deviations from the experiment are observed for complexes with the two tertiary amines, Me_3N and Et_3N, where the calculated values are by 4.3 and 5.5 kJ/mol lower than the center of the experimental interval. The comparison with the experiment suggests that ΔH values calculated with the B3LYP functional are systematically underestimated, and for none of the complexes, the ΔH value determined with the latter functional falls in the experimental error margins. Particularly large are the differences in ΔH for the complexes of the two tertiary amines, 11−17 kJ/mol. For five complexes, also values from the MP2 calculations are available; they fit at the lower border of the experimental intervals (Table 3), except for Me_3N, where the enthalpy is underestimated similar to M05-2X results. The values, calculated for methyl and ethyl amines with the B3LYP method, are very close to the results of Kone et al.[34] obtained with the same method but with a larger basis set, aug-cc-pVTZ. The MP2/aug-cc-pVTZ calculations reported in the same paper resulted in higher ΔH for the complexes of methanol with Me_3N and Et_3N, in agreement with the experiment.

Table 3. Experimental and Calculated Enthalpies (in kJ/mol) for Formation of Complexes of Methanol with Different Proton Acceptor Molecules

H acceptor	ΔH[a]	ΔH(B3LYP)	ΔH(M05-2X)	ΔH(MP2)
$MeNH_2$	−23.4 ± 1.0[b]	−19.6	−23.1	−22.7
Me_2NH	−25.9 ± 1.0[b]	−19.1	−25.3	−24.7
Me_3N	−28.9 ± 1.0[b]	−17.8	−24.6	−25.4
Et_2NH	−28.0[b]	−19.1	−28.7	
Et_3N	−31.4 ± 2.0[b]	−13.9	−25.9	
MeOH	−17.4 ± 2.1[c]	−12.9	−16.9	−15.4
Et_2O	−19.7 ± 2.9[d]	−11.8	−21.3	
PhOH[f]	−25.6 ± 0.8[e]	−18.9	−25.7	−24.0

[a] Experimental values. [b] Ref 30. [c] Ref 31. [d] Ref 20. [e] Ref 32. [f] Complex with methanol as acceptor of the hydrogen bond.

Scheme 1



Complexes with Alkyl or Aryl Halides. The complexes with fluorides and chlorides, R−X, feature two types of hydrogen bonds (Figure 1g−j and Scheme 1): the regular hydrogen bond with the OH group of methanol as proton donor and the halogen of RX as proton acceptor (denoted as HB1), and a hydrogen bond with a C−H moiety of the alkyl or aryl halide as proton donor and the oxygen atom from the methanol molecule as proton acceptor (denoted as HB2). The second type of hydrogen bonds, C−H···X, where X is an electronegative heteroatom, can play an important role in determining the geometry of hydrogen bonded complexes with halogenated hydrocarbons, as it was shown for the $CHCl_3\cdots NH_3$ complex.[59]

Selected structural information for the complexes with alkyl and aryl halides is presented in Table 4. The length of the regular hydrogen bond HB1 for the complexes with alkyl fluorides calculated with B3LYP and M05-2X functionals is in the region 203 ± 3 pm, while the hydrogen bond in the complex MeOH−PhF is by about 10 pm longer, 213−218 pm. The two functionals give, however, a different number of additional

Table 4. Structural Data for the Complexes of Methanol with Alkyl and Aryl Halides (Distances in pm, Angles in Degrees, and Enthalpy in kJ/mol)

	B3LYP						M05-2X						MP2					
	Δ(OH)[a]	HB1	HB2	<OHX	NBO[c]	ΔH	Δ(OH)[a]	HB1	HB2	<OHX	NBO[c]	ΔH	Δ(OH)[a]	HB1	HB2	<OHX	NBO[c]	ΔH
MeF	0.3	206		149		−6.4	0.3	205	253	142	0.179	−10.9	0.3	208	261	144	0.152	−8.9
EtF	0.3	203		157		−7.4	0.4	202	269[b]	144	0.228[b]	−12.9	0.4	196	263[b]	150	0.201[b]	−10.6
PrF	0.3	203		158		−7.4	0.4	202	271[b]	144	0.221[b]	−12.5						
iPrF	0.4	202		159		−8.1	0.4	200	265[b]	153	0.227[b]	−14.6						
ChexF	0.4	200		162		−8.1	0.4	200	270[b]	149	0.231[b]	−12.5						
PhF	0.2	218	255[b]	148	0.240[b]	−4.1	0.2	213	242[b]	146	0.255[b]	−9.2	0.2	207	236[b]	150	0.235[b]	
MeCl	0.3	258	254	139	0.224	−4.7	0.3	253	241	137	0.232	−9.8	0.3	253	245	140	0.207	−8.6
EtCl	0.3	253	263	145	0.215	−5.1	0.4	248	263	141	0.220	−11.9	0.4	239	269	146	0.189	−10.2
									272[b]		0.225[b]				268[b]		0.198[b]	
PrCl	0.4	252	270	146	0.213	−5.2	0.4	249	259	141	0.219	−12.3						
iPrCl	0.4	249		153		−5.4	0.4	247	265	143	0.217	−11.6						
									271[b]		0.230[b]							
ChexCl	0.4	250		155		−5.4	0.4	247	262	145	0.219	−11.2						
									271[b]		0.229[b]							
PhCl	0.2	265	248[b]	149	0.240[b]	−2.5	0.2	267	243[b]	138	0.249[b]	−9.7	0.2	254		164		

[a] Elongation of the OH distance in the complex compared to the distance in the free methanol molecule, which is calculated at 96.0, 95.6, and 95.8 pm at B3LYP, M05-2X, and MP2 levels, respectively. [b] The C−H moiety in the halide, which acts as proton donor for this hydrogen bond is not at the α-C atom but with a carbon atom neighboring to the C−X group. [c] NBO charge of the hydrogen atom that forms HB2.

dx.doi.org/10.1021/jp204313f |J. Phys. Chem. A 2011, 115, 14054–14068

Table 5. Binding Energies (in kJ/mol) and Hydrogen Bonds Lengths, HB1 and HB2 (in pm), of the Complexes with One Type of Hydrogen Bond, HB1 or HB2, Obtained with Constrained Geometry Optimization[a]

	B3LYP			M05-2X			MP2		
	BE[b]	HB1	HB2	BE[b]	HB1	HB2	BE[b]	HB1	HB2
$MeNH_2$	−20.3	194		−24.0	193		−23.5	193	
HB1	−19.8	194		−24.0	194		−22.5	189	
HB2	0.0		269	−1.4		254	−2.1		247
MeOH	−14.2	194		−18.1	197		−16.9	193	
HB1	−13.9	193		−18.1	193		−16.1	188	
HB2	−0.3		259	−2.8		250	−2.2		244
PhOH	−9.5	204		−16.0	207				
HB1	−9.3	201		−14.3	199				
HB2	−0.9		249	−3.9		238			
MeF	−8.4	206		−12.7	205	253	−10.8	208	261
HB1	−6.1	208		−8.6	203		−6.8	203	
HB2	−2.6		249	−4.4		244	−4.4		240
PhF	−6.7	218		−11.9	213	242			
HB1	−3.5	215		−6.0	210				
HB2	−3.2		240	−5.9		234			
MeCl	−7.0	258		−11.9	253	241	−10.8	253	245
HB1	−0.6	318[c]		−2.1	279		−2.1	271	
HB2	−3.5		241	−6.4		235	−5.7		231
PhCl	−5.4	265		−12.0	267	243			
HB1	−0.1	342[c]		−1.4	284				
HB2	−3.0		242	−6.2		233			

[a] For comparison, the characteristics of the corresponding complexes obtained without constraints are provided. [b] The binding energy (BE) corresponds to the ZPE and BSSE corrected electronic energy. [c] The distance cannot be considered as bonding since it is longer than the sum of the van der Waals radii.

hydrogen bonds, with the C−H bond of the alkyl/aryl fluoride as proton donor (HB2). While the B3LYP functional suggests such a bond only for PhF (at 255 pm), the structures optimized with the M05-2X functional have such hydrogen bonds not only in this complex (at 242 pm), but also in the complexes with the aliphatic fluorides, although at longer distances, 253−271 pm.

Due to the larger vdW radius (by 28 pm) and the lower basicity of Cl compared to F, the length of the hydrogen bond type HB1 for the complexes with alkyl chlorides are longer than those for corresponding fluorides in average by 50 (B3LYP) or 47 pm (M05-2X) to 249−258 and 247−253 pm, respectively. The hydrogen bonding distance for the complex with phenyl chloride, 265−267 pm, is again longer than for the complexes with aliphatic chlorides. The additional hydrogen bonds type HB2 for alkyl chlorides, 241−265 pm, are calculated somewhat shorter than those for fluorides obtained with the M05-2X functional. Note, however, that for alkyl chlorides such HB2 bonds appear also in the structures optimized with the B3LYP functional at distances of 254−270 pm. The distance of HB2 for the complex with PhCl is among the shortest distances for this type of hydrogen bond, 248 (B3LYP) and 243 pm (M05-2X).

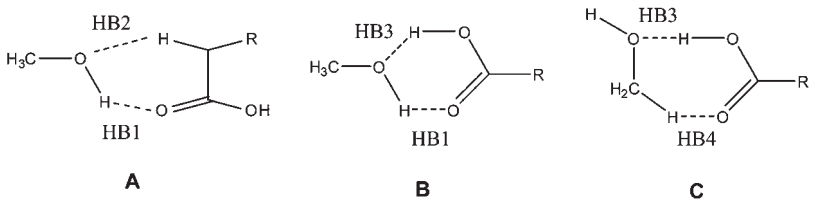
Due to the formation of additional hydrogen bonds, of HB2 type, in the complexes with alkyl and aryl halides, the angle of the hydrogen bond type HB1, <O−H···X (X = F, Cl) deviates stronger from the optimal angle for the hydrogen bond (180°), than in the complexes with amines, alcohols, or ethers. For fluorides, this angle varies in the regions 148−162° (B3LYP) and 142−153° (M05-2X), and for chlorides, the regions of the optimized values with B3LYP and M05-2X functionals are 139−155° and 137−145°, respectively.

The structural features of the complexes of methanol with fluorides and chlorides described above are also in agreement with the results from the optimization of the complexes with MeX, EtX, and PhX performed at the MP2 level. The individual hydrogen bonding distances differ from M05-2X results by 3−9 pm for fluorides and 0−13 pm for chlorides.

The enthalpies for formation of the alkyl halides (Table 4) calculated with B3LYP functional are by 4−7 kJ/mol lower (in absolute value) than those obtained with the M05-2X functional. The binding of the complexes with alkyl chlorides, −10 to −12 kJ/mol (M05-2X), is somewhat weaker than the complexes with alkyl fluorides, −11 to −15 kJ/mol (M05-2X), which in turn are less stable than the complexes of methanol with amines, alcohols, and ethers reported above. The complexes of methanol with the aromatic halides, PhF and PhCl, are the least stable among the modeled ones, −9.2 and −9.7 kJ/mol, respectively. The ΔH values for methyl and ethyl halides calculated with MP2 method (Table 4) are by about 2.0 kJ/mol lower (in absolute value) than the corresponding binding enthalpies obtained with DFT using M05-2X functional.

Estimation of the Contributions of the Different Hydrogen Bonds in Formation of the Complexes. To estimate the contributions of the different types of hydrogen bonds (HB1 and HB2) in the formation of the complexes, we performed restricted optimization of the complexes of methanol with $MeNH_2$, MeOH, MeF, PhF, MeCl, and PhCl. The initial geometries of these complexes are arranged to provide formation of only one

Scheme 2



hydrogen bond between the interacting molecules with an angle for the hydrogen bond, <O−H···X or <C−H···O, of 179° (essentially the optimal). These angles (see Table S10 of SI) are kept fixed during the geometry optimization (the optimized structures of these complexes are shown in Figure S1 of SI). The analysis in this section is based on the results obtained at the M05-2X level. For comparison, these calculations were also performed at the B3LYP and MP2 levels.

The results for the binding energies of the complexes and the hydrogen bond lengths are presented in Table 5. It is clearly seen that crucial contribution in the bonding for the complexes of methanol with $MeNH_2$ and MeOH is provided by HB1; the BE of the completely optimized complexes is equal to the BE for the complexes obtained with constrained optimization with HB1. The complexes only with the second type of hydrogen bond, HB2, are rather unstable: −1.4 kJ/mol for the amine and −2.8 kJ/mol for methanol. In the complex MeOH−MeF, the contribution of HB1 in the BE of the complex decreases to −8.6 kJ/mol, while the contribution of HB2 increases to −4.4 kJ/mol, that is, the binding via the second hydrogen bond represents 35% of the total BE of the complex (−12.7 kJ/mol). Comparing the calculated values for the complexes with $MeNH_2$, MeOH, and MeF (Table 5), one can conclude that the sums of BE of the structures with individual hydrogen bonds are higher than the BE of the corresponding complexes optimized without geometry constraints. This suggests that the optimized structure of the unconstrained complex cannot provide such a location of the interacting centers that is optimal for formation of both types of hydrogen bonds. However, the calculated differences are small: −1.4, −2.8, and −0.3 kJ/mol for the complex with $MeNH_2$, MeOH, and MeF.

For MeCl, the complex with HB2 is found more stable, BE = −6.4 kJ/mol, than the complex with HB1, BE = −2.1 kJ/mol. Thus, the contribution of the two types of hydrogen bonds in the BE of the MeOH−MeCl complex is reverse, compared to the complexes with the other functional groups described above. An additional peculiarity of this complex is the synergic effect of the two hydrogen bonds: the BE of the complex optimized without geometry constraints is by 3.4 kJ/mol higher (in absolute value) than the sums of BE of the structures with individual hydrogen bonds. The formation of each of the bonds causes the polarization of the OH group in methanol and H−C−Cl moiety in methyl chloride and, thus, strengthening of the other hydrogen bond.

For the complex MeOH−PhF, HB1 and HB2 are almost equally strong, while for the complex MeOH−PhCl, HB2 is much stronger. This is determined by two factors: (i) the participation of the electron pair of the halogen in $n-\pi$ conjugation with the aromatic ring, which partially reduces the electron density of the halogen; and (ii) stronger polarization of the aromatic C−H bonds compared to aliphatic ones due to sp^2 hybridization of the C atom. Thus, for PhF the calculated binding energies of HB1 and HB2 are −6.0 and −5.9 kJ/mol, respectively. For PhCl the HB2 completely dominates the bonding with −6.2 kJ/mol, while the BE of HB1 is calculated as only −1.4 kJ/mol.

In summary of this section, the total binding energies of the complexes decreases along the series R−NH_2 > R−OH > R−*F* > R−Cl, following the decrease of the strength of HB1. In the same order increases the strength of HB2. Although the latter increase cannot compensate the weakening of HB1, the HB2 hydrogen bond has an increasing influence on the optimal structure of the complex. Thus, the binding of the complexes of methanol with $MeNH_2$ or MeOH is determined mainly by HB1, while HB2 dominates in the complexes with chlorides.

Complexes with Carboxylic Acids. We modeled three different structures of the complexes of methanol with carboxylic acids, which include four types of hydrogen bonds (see Figure 1k−p and Scheme 2): (i) HB1 between the hydrogen atom from the methanol OH group and the carbonyl oxygen atom of the carboxylic acid; (ii) HB2 between the C−H moiety of the carboxylic acid as proton donor and the oxygen atom from the methanol molecule as proton acceptor; (iii) HB3 between the proton from the carboxylic acid and the oxygen atom of the methanol molecule; and (iv) HB4 between a hydrogen atom of the methanol CH_3 group and carbonyl oxygen atom of the carboxylic acid. The first type of modeled complexes, type A, includes HB1 and HB2 types of bonds. They form six atomic cycles. The complexes B and C feature three types of hydrogen bonds, HB1 + HB3 and HB3 + HB4, respectively, and form six atomic or seven atomic cycles (Scheme 2).

Following the decrease of the acidity of the three proton donor groups COOH < O−H < C−H, the hydrogen bond length increases in the order HB3 < HB1 < HB2 and HB4 (Table 6). The optimized values depend slightly on the exchange-correlation functional employed in the calculations, for the B3LYP functional, the hydrogen bond distances are around 178, 194−200, 245−270, and 254 pm, for HB3, HB1, HB2, and HB4, respectively; the corresponding values calculated with the M05-2X functional are in most cases similar, 176, 195−199, 234−257, and 245 pm. For HB1 bond length the lower value corresponds to complex type A, while the higher value is for complexes type B, where HB3 is the dominant hydrogen bond. HB2 type hydrogen bond is presented only in complex type A; it is relatively short only for the complex MeOH−PhCOOH, 245 and 234 pm for B3LYP and M05-2X functional, respectively. Due to the presence of both HB3 and HB1 hydrogen bonds, the type B complexes are the most stable (with ΔH of about −35 and −42 kJ/mol for B3LYP and M05-2X, respectively). They are followed by complexes type C (about −24 and −31 kJ/mol for B3LYP and M05-2X), and the least stable are the type A complexes, which have HB1 and HB2 bonds (about −15 and −21 kJ/mol for B3LYP and M05-2X). Similar to the results for the complexes with other compounds described above, the

Table 6. Structural Data for the Complexes of Methanol with Carboxylic Acids (Distances in pm, Angles in Degrees, and Enthalpy in kJ/mol)[a]

	B3LYP					M05-2X				
	HB1	HB2	HB3	HB4	ΔH	HB1	HB2	HB3	HB4	ΔH
MeCOOH(A)	197	252			−14.8	196	241			−20.4
EtCOOH(A)	195	270			−14.8	195	257			−21.5
PrCOOH(A)	195	270			−15.4	196	254			−22.6
iPrCOOH(A)	195	264			−14.6	195	257			−20.7
ChexCOOH(A)	194	264			−14.9	196	254			−21.3
PhCOOH(A)	195	245[b]			−13.7	195	234[b]			−18.8
MeCOOH(B)	200		178		−32.2	199		177		−39.2
EtCOOH(B)	199		179		−36.5	199		177		−44.8
PrCOOH(B)	199		179		−35.4	199		177		−42.8
iPrCOOH(B)	198		178		−32.4	198		177		−40.2
ChexCOOH(B)	198		178		−32.1	198		177		−39.4
PhCOOH(B)	199		177		−32.8	199		175		−40.6
MeCOOH(C)			178	255	−24.2			178	246	−30.5
EtCOOH(C)			178	254	−24.0			178	246	−30.8
PrCOOH(C)			178	254	−23.8			178	245	−30.7
iPrCOOH(C)			178	254	−23.9			178	245	−30.7
ChexCOOH(C)			178	254	−23.4			178	245	−29.7
PhCOOH(C)			177	254	−24.5			176	246	−31.7

[a] For the notation of the different type of complexes and hydrogen bonds see Figure 1k−p and Scheme 2. [b] The C−H moiety, which acts as proton donor for this hydrogen bond is at the ortho position in the aromatic ring.

stability of the complexes is calculated higher with the M05-2X functional than with the B3LYP.

3.2. Vibrational Frequencies of Methanol in the Modeled Complexes. The vibrational frequencies of methanol in the optimized complexes were calculated with both DFT functionals and with MP2 for methyl and ethyl derivatives. We focus in particular on the changes in the stretching vibrations of the methanol OH group after formation of hydrogen bonds. Following the standard procedure for correcting the calculated values both for the anharmonicity and the error of the computational method, all calculated harmonic frequency values are scaled, ν_{sc}, using the coefficients reported in the literature: 0.955 for B3LYP,[53] 0.936 for M05-2X,[53] and 0.945 for MP2.[53] This scaling works well for the stretching frequency of the OH group of the free methanol: ν_{sc} = 3677, 3693, and 3693 cm^{-1} for B3LYP, M05-2X, and MP2 calculations, while the experimental value is ν_{exp} = 3686 cm^{-1},[24] that is, the error for B3LYP, M05-2X, and MP2 methods is 9, −7, and −7 cm^{-1}, respectively. If we apply the same approach to the stretching OH frequency of MeOH in the complexes (which is red-shifted toward lower frequencies due to formation of the hydrogen bond),[60] we can compare the computationally derived values with available experimental data (see Table 7). Such a comparison is presented in Figure 2a, where one can see small deviations of the scaled computational values from the experimental ones when the OH frequency shift is small, while the difference increases with increasing of the red shift, that is, the slopes of the plotted lines for the scaled frequencies obtained with both functionals and with MP2 method differ from one. This observation suggests that for both functionals the uniform scaling coefficient for the whole range of red-shifted OH frequencies is not adequate, as already reported for some individual complexes modeled either with DFT or with MP2 method.[22,24] This difference may originate from (i) exaggeration of the elongation of the OH bond in methanol due to hydrogen bonding; (ii) different performance of the computational methods when the O−H distance close and far from the optimized value in the free molecule; or (iii) different influence of the hydrogen bond formation on the harmonic and the anharmonic component of the OH vibrational frequency.[22] Thus, for the calculated corrected frequencies ν_{corr} to be compared with the experimental values, in addition to the standard scaling of the principle stretching OH frequency of the free MeOH, we applied additional scaling factor acting only

Table 7. Comparison of the Experimental Stretching OH Vibrational Frequencies ν_{exp} (in cm^{-1}) of Methanol in Different Complexes with Computational Values Obtained by Scaling ν_{sc} and Corrected According to eq 3, ν_{corr}

	experiment	B3LYP		M05-2X		MP2	
	ν_{exp}	ν_{sc}	ν_{corr}	ν_{sc}	ν_{corr}	ν_{sc}	ν_{corr}
free	3686[a]	3677	3677	3693	3693	3693	3693
$MeNH_2$	3443[b]	3361	3417	3371	3436	3400	3437
Me_2NH	3393[b]	3329	3391	3326	3400	3310	3358
Me_3N	3376,[b] 3358[c]	3322	3386	3278	3362	3262	3316
$EtNH_2$	3436[b]	3357	3414	3383	3445	3366	3407
Et_2NH	3361[b]	3311	3377	3261	3348		
Et_3N	3313[b,d]	3334	3396	3225	3320		
MeOH	3575,[a] 3574[e]	3531	3557	3584	3606	3566	3582
EtOH	3556[a]	3523	3550	3543	3573	3531	3552
Et_2O	3558[f]	3515	3545	3520	3555		
PhF	3663,[g] 3666[g]	3655	3659	3644	3654		

[a] Ref 24. [b] Ref 17. [c] Ref 18. [d] Ref 21. [e] Ref 25. [f] Ref 20. [g] Ref 26.

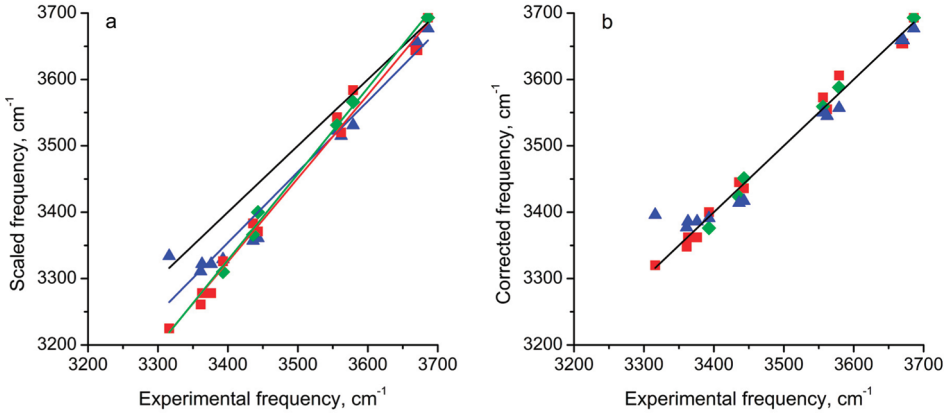


Figure 2. Correlation between calculated stretching OH frequencies of methanol in series of modeled complexes (triangles, B3LYP; squares, M05-2X; rhombus, MP2) and corresponding experimental values (black line; see Table 7). (a) Calculated frequencies scaled uniformly by the scaling factors of the used DFT functionals reported in ref 53. (b) Calculated frequencies corrected with additional factor for the shift due to formation of hydrogen bond following eq 3; the correlation coefficients of the linear fits are: 0.946, 0.990, and 0.955 for B3LYP, M05-2X, and MP2, respectively.

Table 8. Computationally Derived Frequency Shifts Corrected According to eq 3, ν_{corr} (in cm^{-1}), and Calculated Infrared Intensities[a] (in km/mol) of the Methanol OH Group Stretching Vibrations in the Modeled Complexes

	B3LYP		M05-2X			B3LYP		M05-2X	
complex	$\Delta\nu_{corr}$	int	$\Delta\nu_{corr}$	int	complex	$\Delta\nu_{corr}$	int	$\Delta\nu_{corr}$	int
$MeNH_2$	259	799	257	754	MeCOOH(A)	111	453	120	462
$EtNH_2$	262	927	248	778	EtCOOH(A)	121	488	129	448
$PrNH_2$	264	951	256	868	PrCOOH(A)	123	479	133	424
$iPrNH_2$	273	906	280	840	iPrCOOH(A)	118	511	129	454
$ChexNH_2$	274	803	281	664	ChexCOOH(A)	123	506	134	425
$PhNH_2$	158	695	115	320	PhCOOH(A)	99	476	103	461
Me_2NH	285	945	293	809					
Et_2NH	300	864	345	921					
Me_3N	291	997	331	1074					
Et_3N	281	751	373	967					
MeOH	120	500	87	275	MeCOOH(B)	151	412	151	394
EtOH	126	497	120	428	EtCOOH(B)	152	444	154	411
PrOH	124	586	91	282	PrCOOH(B)	153	464	155	433
iPrOH	134	568	133	481	iPrCOOH(B)	162	466	159	432
ChexOH	133	521	140	441	ChexCOOH(B)	165	509	162	464
PhOH	61	356	62	215	PhCOOH(B)	156	529	147	456
PhOH[b]	5	50	23	71					
Me_2O	126	545	130	439					
Et_2O	132	481	138	498					
MeF	34	176	51	169	MeCOOH(C)	−8	46	16	68
EtF	41	210	58	182	EtCOOH(C)	−9	45	11	68
PrF	42	219	59	178	PrCOOH(C)	−8	45	−1	67
iPrF	46	224	65	213	iPrCOOH(C)	−8	46	−3	67
ChexF	48	288	63	221	ChexCOOH(C)	−9	45	0	67
PhF	18	131	39	152	PhCOOH(C)	−9	47	15	70
MeCl	34	176	60	160					
EtCl	41	210	69	174					
PrCl	42	219	67	176					
iPrCl	46	224	71	197					
ChexCl	48	288	74	194					
PhCl	18	131	34	81					

[a] The calculated intensity of the OH mode in free MeOH is 30 and 49 cm^{-1} for B3LYP and M05-2X, respectively. [b] Complex with methanol as acceptor of the hydrogen bond.

on the frequency shift:

$$\nu_{corr} = \nu_{calc}(\text{MeOH}) \times \alpha + [\nu_{calc}(\text{MeOH—RX}) - \nu_{calc}(\text{MeOH})] \times \beta \quad (3)$$

with the following values of the coefficients: α(B3LYP) = 0.955,[53] α(M05-2X) = 0.936,[53] α(MP2) = 0.945,[53] β(B3LYP) = 0.783, β(M05-2X) = 0.747, and β(MP2) = 0.826 (this work). The correlation of the experimental values with the calculated frequencies corrected according to eq 3 with additional factor for the shift due to formation of hydrogen bond is shown in Figure 2b. As it can be seen, the correlation between experimental values and the computationally derived values for both B3LYP and M05-2X functionals is very good with the slope of the trend line equal to 1.000 for the whole region of stretching OH frequencies.

The computationally derived frequency shifts (after the correction procedure described above) of the methanol OH group in the modeled complexes are reported in Table 8. Since the frequencies obtained with M05-2X functional seems to approach closer the experimental values, only these values are commented below. As expected, the stretching frequency shift $\Delta\nu_{corr}$ of the methanol OH group in the complexes correlates with its bond length. Thus, the red shift of the OH frequency for complexes with monoalkyl amines, 248−281 cm^{-1}, as absolute value is higher than the shift for the complexes with alcohols, 87−140 cm^{-1}. Similarly the red shifts for the di- and trialkyl amines, 293−373 cm^{-1}, are higher compared to the complexes with ethers, 130−138 cm^{-1}. Halide derivatives feature even lower red shift, 51−65 and 60−74 in cm^{-1} for aliphatic fluorides and chlorides, and the shifts of the corresponding aromatic derivatives are twice smaller, 39 and 34 cm^{-1}.

In the complexes (type A) of methanol as proton donor with carboxylic acid, the frequency red shift is 103−134 cm^{-1}, similar to that in the complexes with alcohols and ethers. The complexes type B feature somewhat stronger red shift of the methanol OH frequency, 147−162 cm^{-1}, due to the synergetic effect of the stronger hydrogen bonding with carboxylic group where MeOH is simultaneously proton donor and proton acceptor. The OH frequency shift is calculated close to zero, at most 16 cm^{-1}, in the complexes of type C, because in these complexes, the OH group of methanol participates only as a proton acceptor.

Considering all series of complexes the intensities of infrared absorption roughly correlate with the stretching frequency red shift $\Delta\nu_{corr}$ (Figure 3). Thus, the lowest IR absorption intensities are observed in the phenyl substituted complexes: $PhNH_2$, PhOH, PhF, and PhCl (Table 8). In the cases of carboxylic acids complexes, the values of IR intensities in each series A, B, and C are relatively close, about 430 ± 35 km/mol for complexes A and B. The lowest values, about 67 km/mol, are observed in complexes type C, where the methanol OH group is not proton donor.

3.3. Analysis of the Electron Density Distribution in the Modeled Complexes. Various computational studies suggest that electrostatics plays an important role in hydrogen bonds formation.[58−64] To estimate these effects in the modeled complexes, we calculated Mulliken, ChelpG and NBO charges and electrostatic potential at nuclei (EPN) of the interacting atoms (see Tables S3−S9 of the Supporting Information). Due to the weak electronic effect of the alkyl substituent in the aliphatic compounds, the variation of the alkyl chain hardly changes the proton acceptor properties of the hydrogen bond accepting atom, N, O, F, or Cl. The variations of the calculated NBO changes (from M05-2X calculations) within the series are

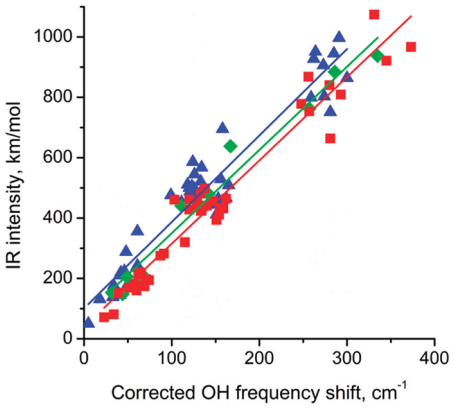


Figure 3. Correlation between the calculated infrared intensities of the stretching OH vibration of methanol in the modeled complexes vs the corrected calculated frequency shift of the same band (triangles, B3LYP; squares, M05-2X; rhombus, MP2). The equations and correlation coefficients of the line fits are: $y = 3.02x + 80$ ($R^2 = 0.92$), $y = 2.76x + 39$ ($R^2 = 0.94$), and $y = 2.76x + 75$ ($R^2 = 0.97$) for B3LYP, M05-2X, and MP2, respectively.

0.01−0.02 e, and that of the EPN at the proton acceptor atom are in the region 0.10−0.37 eV (for N and F, respectively). After formation of the complex with MeOH, a minor increase of the negative charge on the proton acceptor atoms is observed, −0.01 to −0.03 e, which is accompanied by a small increase of the positive change on the methanol proton by 0.01−0.04 e for halides and amines, respectively. The calculated total change of the methanol molecule in the complexes is −0.01 to −0.04 e, that is, the formation of hydrogen bond essentially does not involve charge transfer.

We checked for possible correlations of the different electronic characteristics with the calculated enthalpy of formation or the binding energy of the complexes (Figure 4a−c). Relevant correlation was found between the enthalpy or BE and the shift of the EPN at the hydrogen center participating in the formation of a hydrogen bond. Figure 4a shows this correlation for the completely optimized complexes (blue rhombus) with MeOH as proton donor for amines, alcohols, fluorides, and chlorides. Such correlation is observed only when complexes with all different proton acceptors are considered, while it is not valid within each individual series. Figure 4a shows also the same correlation for the complexes with fixed orientation of the HB1 hydrogen bond (magenta squares) for the complexes with $MeNH_2$, MeOH, MeF, MeCl, PhF, and PhCl. The two correlations are very close in the amine region because, in this case, the binding in the complex is accomplished exclusively by the HB1 hydrogen bond. However, the two correlations deviate notably for halides, where HB2 bond contributes substantially to the binding in the complex, as described in section 3.1 above.

Analogous correlation between BE and the EPN(H) value can be observed also for the formation of the complexes with fixed orientation via HB2 hydrogen bond (red triangles in Figure 4b). Note, however, that the correlation plots for the HB1 and HB2 hydrogen bonds have the opposite slops: for HB1 the calculated BE increases (in absolute value) when the EPN(H) becomes more negative, while for the HB2 the binding is stronger for less negative EPN(H). The reason for this difference is the different type of the hydrogen center participating in the formation of the hydrogen bond and the way in which the electronegative

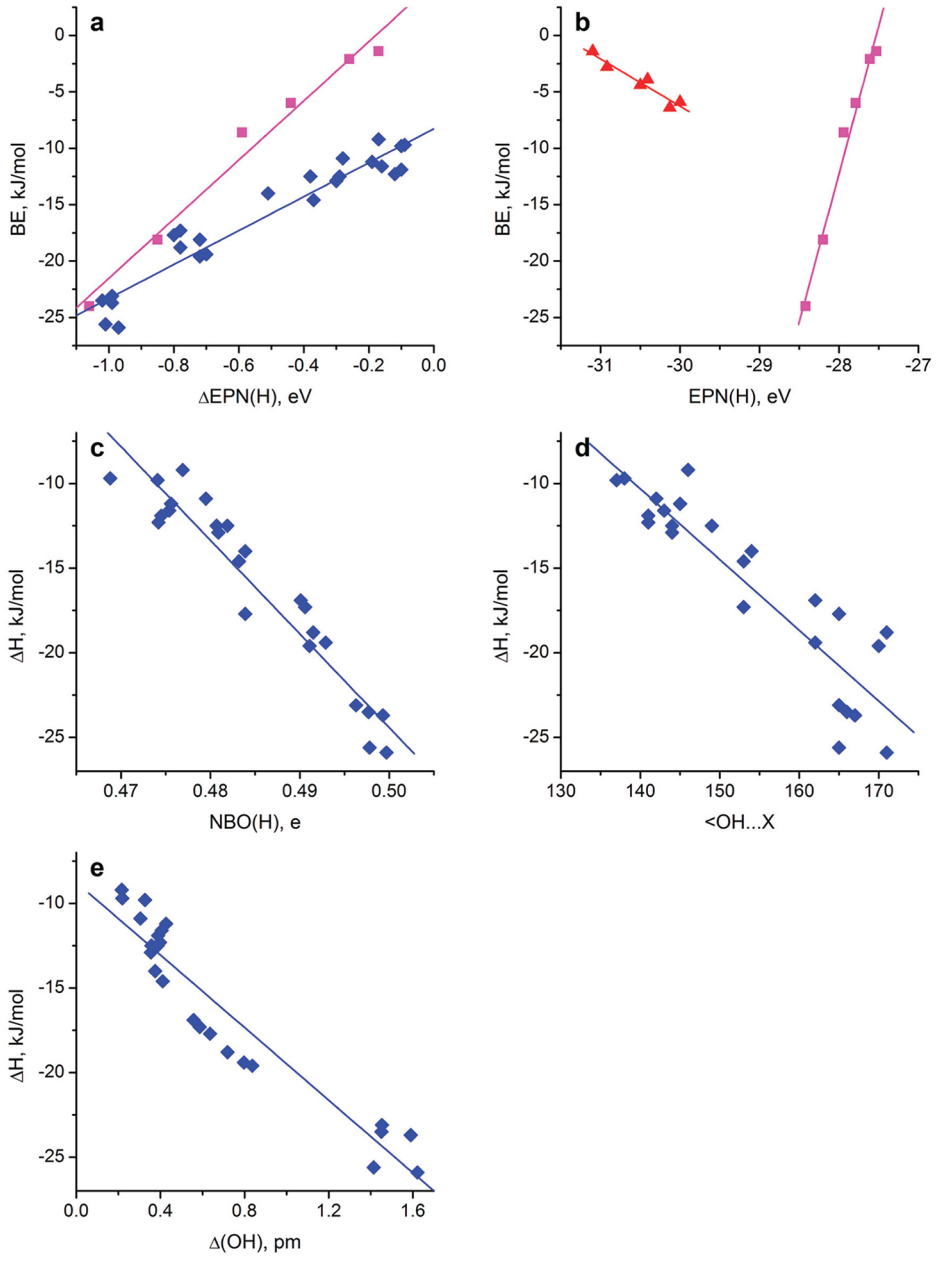


Figure 4. Correlation between the calculated enthalpies ΔH or BE for formation of hydrogen bonds and (a) electrostatic potential at nuclei for hydrogen centers, EPN, participating in hydrogen bonds for optimized structures (blue rhombus, $R^2 = 0.922$) and structures with fixed orientation for formation of HB1 bonds (magenta squares, $R^2 = 0.980$); (b) EPN for hydrogen centers participating in HB1 (magenta squares, $R^2 = 0.980$) and HB2 (red triangles, $R^2 = 0.988$) hydrogen bonds; (c) NBO charges of the methanol protons for optimized structures ($R^2 = 0.920$); (d) the optimized angle for formation of hydrogen bond <OH···X ($R^2 = 0.826$); and (e) the elongation of the O−H distance with respect to methanol in the gas phase ($R^2 = 0.880$).

heteroatom (N, O, F, or Cl) affects its charge. In HB1 hydrogen bonds the proton is from the polar and polarizable O−H group and the heteroatom acts as proton acceptor center inducing additional polarization via its electrostatic field. Depending on the proton acceptor atom (see Figure 5), the NBO charge on the H atom increases by 0.002 to 0.038 e and the EPN(H) decreases by −0.17 to −1.06 eV (for both characteristics the former and the latter value correspond to Cl and NH_2, respectively). In HB2 the hydrogen center is from the less polar and more "electronically rigid" C−H fragment and the heteroatom (from the same molecule) affects the formation of the hydrogen bond with methanol oxygen center via intramolecular charge distribution. This interaction of H with oxygen from methanol responsible for the formation of HB2 hydrogen bond results in essentially constant changes in the electronic characteristics of H in all proton donor molecules (MeX or PhX, X = NH_2, OH, F, Cl), NBO charge increases by 0.03 e and the EPN(H) decreases by 0.50 to 0.60 ev (Figure 5).

Calculated binding enthalpy of the complexes is found to correlate also with two structural characteristics of the complexes in which methanol is proton donor: the optimized angle for formation of hydrogen bond <OH···X (Figure 4d) and the

dx.doi.org/10.1021/jp204313f |J. Phys. Chem. A 2011, 115, 14054–14068

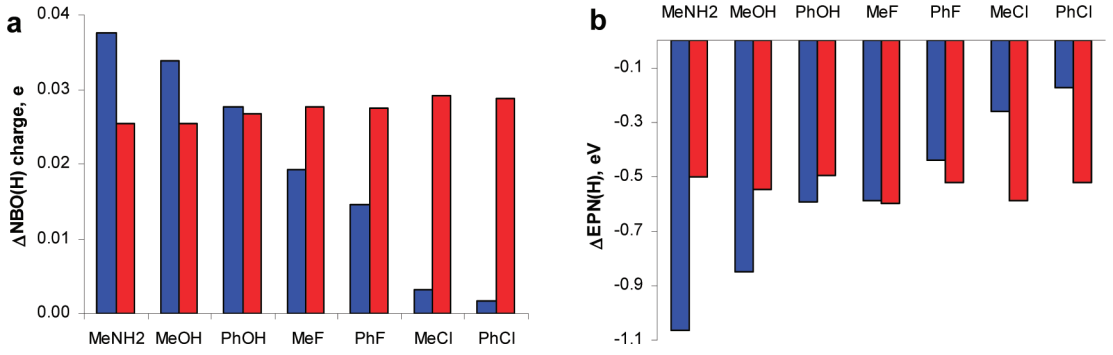


Figure 5. Changes in the calculated NBO charge (a) and electrostatic potential at the nuclei (b) for hydrogen centers participating in hydrogen bonds type HB1 (blue bars) and HB2 (red bars).

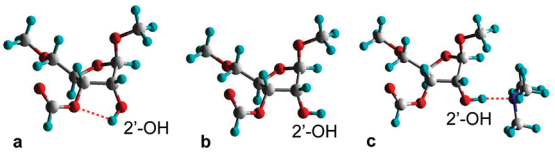


Figure 6. 3′-Formyl-1′,5′-dimethyl ribose, model for tRNA in ribosome, bound to polypeptide chain during protein biosynthesis: (a) 2′-OH group participating in intramolecular hydrogen bonding; (b) the molecule without the intramolecular hydrogen bond; (c) the molecule bound to trimethylamine via 2′-OH···N hydrogen bond.

elongation of the O−H distance in the methanol (Figure 4e). Due to the low correlation coefficients ($R^2 < 0.9$), both correlations can be considered as trends. Nevertheless, they highlight the connection between the hydrogen bond angle and the O−H bond elongation and the stability of the complexes.

3.4. Implications for the Influence of Proton Acceptor Groups on Protein Biosynthesis. As mentioned in the Introduction, the obtained results can be used to have a hint which of the considered functional groups can preferentially form hydrogen bond with the 2′-OH hydroxyl group in ribose as proton donor, thus, preventing formation of the intramolecular hydrogen bond with 3′-oxygen in the ribose moiety. Because the latter hydrogen bond was found to be crucial for facilitation of the proton transfer accompanying the protein biosynthesis,[7,40] the blocking of the 2′-OH via a side hydrogen bond will result in inhibiting the protein biosynthesis in the ribosome if the corresponding proton acceptor group can be delivered (e.g., as a part of a drug molecule) in the vicinity of the active site. In a previous study[65] it was shown that the presence of a proton donor group in the vicinity of the 2′-OH can only facilitate the protein biosynthesis since the hydrogen bond to 2′-OH as the proton acceptor lowers the activation barrier of the rate limiting step of the reaction by up to 30 kJ/mol, depending on the location of the side group. Thus, the only way to inhibit the protein biosynthesis via blocking the vicinal 2′-OH from participation in the process is a hydrogen bond to a side proton accepting group, which is stronger than the intramolecular hydrogen bond.

We estimated the preference for formation of the hydrogen bond with the modeled functional groups by comparing the corresponding ΔH values with the enthalpy of formation of the intramolecular hydrogen bond in ribose, calculated to be −5.0 and −10.3 kJ/mol for B3LYP and M05-2X functionals, respectively. These values are calculated as ΔH difference between the two conformers of the model molecule, formylated ribose, with (Figure 6a) or without (Figure 6b) intramolecular hydrogen bond.

Because the M05-2X functional was found to provide better accuracy in reproduction of the experimental enthalpies (see section 3.1), here we compare only the enthalpy values obtained with this functional. All modeled aliphatic amines, alcohols, and ethers form stronger hydrogen bonds as proton acceptors ($\Delta H = -22.7 \div -28.7, -16.9 \div -19.6, -16.8 \div -21.3$ kJ/mol, respectively) than the intramolecular hydrogen bond in ribose. As mentioned above, the calculated ΔH values for $PhNH_2$ and PhOH are lower than that of the corresponding aliphatic derivatives but the binding is still sufficiently stronger than the intramolecular hydrogen bond. The OH group in phenol, however, was found to form a stronger hydrogen bond as proton donor and methanol oxygen as proton acceptor, that is, phenolic OH can act as activator but not as inhibitor of the process. To estimate the preference for formation of a side hydrogen bond with 2′-OH as proton donor or as proton acceptor with the other (aliphatic) hydroxyl derivatives we should compare (i) the binding enthalpy of the side hydrogen bond with 2′-OH as proton donor, with (ii) the sum of the binding enthalpies of the side hydrogen bond with 2′-OH as proton acceptor and ΔH of the intramolecular hydrogen bond. Because in these complexes both groups participating in the formation of the side hydrogen bond are aliphatic OH groups, the additional stabilization due to the intramolecular hydrogen bond in the case will give preference by about 10 kJ/mol to the complex in which the side OH groups is proton donor and 2′-OH is proton acceptor. By this reason a side hydroxyl group (both phenolic and alcoholic) can act only as activator but not as inhibitor of the protein biosynthesis in the ribosome. Similar to alcohols, primary and secondary amines could act as proton donors. In the case of phenylamine, the reverse hydrogen-bonded system with 2′-OH as proton acceptor is more stable by about 8 kJ/mol than the system with the aromatic amine as proton acceptor. In the case of primary aliphatic amines (calculated for methylamine), the energy difference is about 14 kJ/mol in favor of the system, where the amine acts as proton acceptor, and for the secondary aliphatic amines this preference is 16−19 kJ/mol. The formation of the intramolecular hydrogen bond in the ribose, which can be accomplished when these amines are proton donors, reduces this preference by 10 kJ/mol, but the preference remains still sufficient large, which allows us to conclude that secondary aliphatic amines should be able to form complexes in which 2′-OH of the ribose is proton donor and in this way they are able to inhibit protein

biosynthesis. With tertiary amine and ether (methoxy or ethoxy) groups reverse hydrogen bonds with 2′-OH as proton acceptor cannot be formed, thus these groups can efficiently block formation of the intramolecular hydrogen bond and inhibit the process. For comparison we optimized a complex with a hydrogen bond between ribose 2′-OH group and trimethylamine (Figure 6c). Indeed, according to the calculated enthalpy this structure is by 25.4 kJ/mol more stable that the ribose with intramolecular hydrogen bond and a distant trimethylamine molecule.

Ethyl, propyl and cyclohexyl fluorides participate in slightly stronger hydrogen bonds than the intramolecular hydrogen bond in the ribose; the enthalpy difference is only 2.2 to 4.3 kJ/mol. The hydrogen bonds with MeF and PhF are, however, weaker. The strength of the hydrogen bonds with chlorides as proton acceptors is lower that of the intramolecular hydrogen bond since the "reverse" hydrogen bond (denoted above as HB2) also contributes in the total binding enthalpy of the complexes.

In the energetically preferred way of hydrogen bonding of methanol hydroxyl with the carboxyl group MeOH acts as proton acceptor (complexes type 2), thus such groups can not block the 2′-OH of the ribose from participating in the intramolecular hydrogen bond (Figure 6a). However, since a deprotonated carboxyl group has no acidic proton, such group can form the desired hydrogen bond with methanol OH group as proton donor.

In summary, only secondary or tertiary aliphatic amines, alkoxy groups, deprotonated carboxyl groups and some aliphatic fluorides can prevent 2′-OH group in the ribose from participation in the intramolecular hydrogen bond. By this reason we can conclude that such groups in vicinity of the reaction center will be able to inhibit the process of protein biosynthesis. If such groups, appropriately positioned, are attached to molecules targeting specifically prokaryotic ribosomes, the obtained compounds can be used as antimicrobial drugs. After the initial selection performed here, the effect of the appropriate functional groups on the process could be checked with elaborate models of the protein bond formation center in the ribosome as those employed earlier.[7,66]

4. CONCLUSIONS

In the present study various hydrogen bonded complexes of methanol with different proton accepting and proton donating molecules have been investigated using quantum chemical methods (DFT with M05-2X exchange-correlation functional), recommended for modeling of system in which weak dispersion interactions are important. The modeling suggested that the binding of methanol to amines, alcohols, and ethers is determined mainly by the hydrogen bond between the heteroatom (nitrogen or oxygen) and the proton from the OH group of the methanol molecule (denoted as HB1). The complexes with fluorides and chlorides, R−X, feature two types of hydrogen bonds, HB1 and a hydrogen bond with methanol oxygen atom as proton acceptor and C−H group from the halide as proton donor (denoted as HB2). Due to the formation of such additional hydrogen bonds in these complexes, the angle of the hydrogen bond type HB1, deviates stronger from the optimal angle for the hydrogen bond (180°), than in the complexes with amines, alcohols, or ethers.

The total enthalpy of the complexes studied here decreases along the series R−NH_2 > R−OH > R−F > R−Cl, when R is aliphatic group. The complexes with the corresponding aromatic compounds have lower stability in each series. In the order R−NH_2, R−OH, R−F, R−Cl the strength of HB1 decreases while the strength of HB2 increase, although this increase cannot compensate the weakening of HB1. Thus, the binding enthalpy of the complexes of methanol with amines, alcohols and ethers has the main contribution from HB1 hydrogen bond, while the contribution of HB2 is higher in the complexes of methanol with chlorides.

Three different structures of the complexes of methanol with carboxylic acids were modeled. The most stabile complexes, with enthalpy of formation ΔH about −42 kJ/mol, have two types of hydrogen bonds, HB3 (with carboxyl group as proton donor and methanol oxygen as proton acceptor) and HB1. The calculated Gibbs free energies of formation of the complexes with all types of organic molecules suggest that the complexes are unstable at room temperature with exception of the complexes of MeOH with EtCOOH, PrCOOH, and iPrCOOH with the structure described above.

The harmonic vibrational frequencies and the corresponding IR intensities of the OH group in MeOH were also simulated. The standard scaling procedure, using coefficients acting on the calculated vibrational frequency works well for the stretching frequency of the free methanol. However, if we apply the same approach to the stretching OH frequency of methanol in the complexes the scaled values differ considerably from the experimental ones. These differences increase with increasing the frequency red shift. This observation suggests that for both employed DFT functionals (M05-2X and B3LYP) the uniform scaling coefficient for the whole range of red-shifted OH frequencies is not adequate. To avoid this deficiency of the standard scheme in addition to the standard scaling of the principle stretching OH frequency of the free MeOH, we applied additional scaling factors acting only on the frequency shift (0.783 for B3LYP, 0.747 for M05-2X, and 0.826 for MP2). These new corrected calculated frequencies ν_{corr} compare well with the experimental values with maximal deviation for M05-2X functional of ± 19 cm^{-1} (which is only 0.5% of the value).

Relevant correlation was found between the enthalpy and the EPN at the hydrogen center participating in the formation of hydrogen bond. Such correlation is observed only when complexes with all different proton acceptors are considered, while it is not valid within each individual series. Due to the weak electronic effect of the alkyl substituent in the aliphatic compounds, the variation of the alkyl chain hardly changes the properties of the hydrogen bond accepting atom. The variations of the calculated NBO changes on the heteroatoms (from M05-2X calculations) within the series are 0.01 to 0.02 e, and those of the EPN are 0.10 to 0.37 eV (for N and F, respectively).

The enthalpy of formation of the intramolecular hydrogen bond between the 2′-OH group as proton donor and the 3′-oxygen atom of the formylated ribose is calculated to be −10.3 kJ/mol. Using this value, we compared different ways of formation of intermolecular and intramolecular hydrogen bonds with particular attention on formation of the intermolecular hydrogen bond of the 2′-OH as proton donor with a side proton acceptor group because only in such case the 2′-OH will not participate in the intramolecular hydrogen bond. In the latter case, the process of the protein biosynthesis in the ribosome will be inhibited. On the base of such an analysis we concluded that secondary or tertiary amines, alkoxy groups, deprotonated carboxyl groups, and some aliphatic fluorides in the vicinity of the active center can prevent participation of the 2′-OH group in the intramolecular

hydrogen bond and thus will be able to inhibit the protein biosynthesis. The other modeled functional groups are not able to accomplish such inhibition. These results could be helpful in developing new types of antimicrobial drugs after addition of the appropriate functional groups to molecules targeting specifically prokaryotic ribosomes.

■ ASSOCIATED CONTENT

Supporting Information. Table with the values of the BSSE corrections; Table with the calculated Gibbs free energies of formation of the complexes; Tables with electrostatic properties of different atoms in the isolated molecules and in the complexes; Table with the geometry restrictions, used during geometry optimization for complexes with fixed HB1 and HB2; Figures with the completely optimized and with partially restricted structures of all studied complexes at M05-2X level of theory. This material is available free of charge via the Internet at http://pubs.acs.org.

■ AUTHOR INFORMATION

Corresponding Author
*E-mail: gnv@chem.uni-sofia.bg.

■ ACKNOWLEDGMENT

Financial support from the Bulgarian National Research Fund (grants DO 02-133/2008 and DCVP 02/1) is gratefully acknowledged. We thank the FP7 project BeyondEverest.

■ REFERENCES

(1) (a) Iglev, H.; Schmeisser, M.; Simeonidis, K.; Thaller, A.; Laubereau, A. *Nature* **2006**, *439*, 183–186. (b) Pandelov, S.; Pilles, B. M.; Werhahn, J. C.; Iglev, H *J. Phys. Chem. A* **2009**, *113*, 10184–10188.
(2) Mele, F.; Mineva, T.; Russo, N.; Toscano, M. *Theor. Chim. Acta* **1995**, *91*, 169–177.
(3) Testa, B.; van de Waterbeemd, H.; Folkers, G.; Guy, R. *Pharmacokinetic Optimization in Drug Research: Biological, Physicochemical, and Computational Strategies*; Wiley: Zurich, Switzerland, 2001.
(4) Sijbesma, R. P.; Beijer, F. H.; Brinsveld, L.; Folmer, B. J. B.; Hirschberg, J. J. K. K.; Lange, R. F. M.; Lowe, J. K. L.; Meijer, E. W. *Science* **1997**, *278*, 1601–1604.
(5) Aakeröy, C. B.; Beatty, A. M.; Leinen, D. S.; Lorimer, K. R. *Chem. Commun.* **2000**, 935–936.
(6) Hynes, J. T., Klinman, J. P., Limbach, H.-H., Schowen, R. L., Eds. *Hydrogen Transfer Reactions*; Wiley-VCH: Weinheim, 2007.
(7) Wallin, G.; Åqvist, J. *Proc. Natl. Acad. Sci. U.S.A.* **2010**, *107*, 1888–1893.
(8) Yang, W.; Drueckhammer, D. G. *Org. Lett.* **2000**, *2*, 4133–4136.
(9) Jin, L.; Wu, Y.; Kim, C.; Xue, Y. *J. Mol. Struct.* **2010**, *942*, 137–144.
(10) Stockman, P. A.; Blake, G. A.; Lovas, F. J.; Suenram, R. D. *J. Chem. Phys.* **1997**, *107*, 3782–3790.
(11) Lovas, F. J.; Hartwig, H. *J. Mol. Spectrosc.* **1997**, *185*, 98–109.
(12) Tan, X.-Q.; Ioannou, I. I.; Foltz, K. B.; Kuczkowski, R. L. *J. Mol. Spectrosc.* **1996**, *177*, 181–193.
(13) Haeckel, M.; Stahl, W. *J. Mol. Spectrosc.* **1999**, *198*, 263–277.
(14) Schmitt, M.; Küpper, J.; Spangenberg, D.; Westphal, A. *Chem. Phys.* **2000**, *254*, 349–361.
(15) Bartlome, R.; Rey, J. M.; Sigrist, M. W. *Anal. Chem.* **2008**, *80*, 5334–5341.
(16) Ohno, K.; Shimoaka, T.; Akai, N.; Katsumoto, Y. *J. Phys. Chem. A* **2008**, *112*, 7342–7348.
(17) Hussein, M. A.; Millen, D. J. *J. Chem. Soc., Faraday Trans. 2* **1974**, *70*, 685–692.
(18) Howard, D. L.; Kjaergaard, H. G. *J. Phys. Chem. A* **2006**, *110*, 9597–9601.
(19) Fild, M.; Swiniarski, M. F.; Holmes, R. R. *Inorg. Chem.* **1970**, *9*, 839–843.
(20) Inskeep, R. G.; Dickson, F. E.; Kelliher, J. M. *J. Mol. Spectrosc.* **1960**, *4*, 477–479.
(21) Hirano, E.; Kozima, K. *Bull. Chem. Soc. Jpn.* **1966**, *39*, 1216–1220.
(22) Larsen, R. W.; Zielke, Ph.; Suhm, M. A. *J. Chem. Phys.* **2007**, *126*, 194307–18.
(23) Cezard, C.; Rice, C. A.; Suhm, M. A. *J. Phys. Chem. A* **2006**, *110*, 9839–9848.
(24) Emmeluth, C.; Dyczmons, V.; Suhm, M. A. *J. Phys. Chem. A* **2006**, *110*, 2906–2915.
(25) Provencal, R. A.; Paul, J. B.; Roth, K.; Chapo, C.; Casaes, R. N.; Saykally, R. J.; Tschumper, G. S.; Schaefer, H. F., III *J. Chem. Phys.* **1999**, *110*, 4258–4267.
(26) Djafari, S.; Barth, H.−D.; Buchhold, K.; Brutschy, B. *J. Chem. Phys.* **1997**, *107*, 10573–10581.
(27) Huisken, F.; Stemmler, M. *Chem. Phys. Lett.* **1991**, *180*, 332–338.
(28) Schmitt, M.; Müller, H.; Henrichs, U.; Gerhards, M.; Perl, W.; Deusen, Ch.; Kleinermanns, K. *J. Chem. Phys.* **1995**, *103*, 584–594.
(29) Abe, H.; Mikami, N.; Ito, M.; Udagawa, Y. *J. Phys. Chem.* **1982**, *86*, 2567–2569.
(30) Millen, D. J.; Mines, G. W. *J. Chem. Soc., Faraday Trans. 2* **1974**, *70*, 693–699.
(31) Clague, A. D. H.; Govil, G.; Bernstein, H. J. *Can. J. Chem.* **1969**, *47*, 625–629.
(32) Courty, A.; Mons, M.; Dimicoli, I.; Piuzzi, F.; Brenner, V.; Millie, Ph. *J. Phys. Chem. A* **1998**, *102*, 4890–4898.
(33) Küpper, J.; Westphal, A.; Schmitt, M. *Chem. Phys.* **2001**, *263*, 41–53.
(34) Kone, M.; Illien, B.; Graton, J.; Laurence, Ch. *J. Phys. Chem. A* **2005**, *109*, 11907–11913.
(35) Bjerkeseth, L. H.; Bakke, J. M.; Uggerud, E. *J. Mol. Struct.* **2001**, *567 − 568*, 319–338.
(36) Westphal, A.; Jacoby, Ch.; Ratzer, Ch.; Reichelt, A.; Schmitt, M. *Phys. Chem. Chem. Phys.* **2003**, *5*, 4114–4122.
(37) Fileti, E. E.; Canuto, S. *Int. J. Quantum Chem.* **2005**, *102*, 554–564.
(38) Jovan Jose, K. V.; Gadre, Sh. R.; Sundararajan, K.; Viswanathan, K. S. *J. Chem. Phys.* **2007**, *127*, 104501–10.
(39) Sedlak, R.; Hobza, P.; Patwari, G. N. *J. Phys. Chem. A* **2009**, *113*, 6620–6625.
(40) (a) Rangelov, M. A.; Vayssilov, G. N.; Yomtova, V. M.; Petkov, D. D. *J. Am. Chem. Soc.* **2006**, *128*, 4964–4965. (b) Rangelov, M. A.; Petrova, G. P.; Yomtova, V. M.; Vayssilov, G. N. *J. Org. Chem.* **2010**, *75*, 6782–6792.
(41) Yonath, A. *Annu. Rev. Biochem.* **2005**, *74*, 649–679.
(42) Dunkle, J. A.; Xiong, L.; Mankin, A. S.; Cate, J. H. D. *Proc. Natl. Acad. Sci. U.S.A.* **2010**, *107*, 17152–17157.
(43) Frisch, M. J.; Trucks, G. W.; Schlegel, H. B.; Scuseria, G. E.; Robb, M. A.; Cheeseman, J. R.; Scalmani, G.; Barone, V.; Mennucci, B.; Petersson, G. A.; Nakatsuji, H.; Caricato, M.; Li, X.; Hratchian, H. P.; Izmaylov, A. F.; Bloino, J.; Zheng, G.; Sonnenberg, J. L.; Hada, M.; Ehara, M.; Toyota, K.; Fukuda, R.; Hasegawa, J.; Ishida, M.; Nakajima, T.; Honda, Y.; Kitao, O.; Nakai, H.; Vreven, T.; Montgomery, J. A.; Jr., Peralta, J. E.; Ogliaro, F.; Bearpark, M.; Heyd, J. J.; Brothers, E.; Kudin, K. N.; Staroverov, V. N.; Kobayashi, R.; Normand, J.; Raghavachari, K.; Rendell, A.; Burant, J. C.; Iyengar, S. S.; Tomasi, J.; Cossi, M.; Rega, N.; Millam, J. M.; Klene, M.; Knox, J. E.; Cross, J. B.; Bakken, V.; Adamo, C.; Jaramillo, J.; Gomperts, R.; Stratmann, R. E.; Yazyev, O.; Austin, A. J.;Cammi, R.; Pomelli, C.; Ochterski, J. W.; Martin, R. L.; Morokuma, K.; Zakrzewski, V. G.; Voth, G. A.; Salvador, P.; Dannenberg, J. J.; Dapprich, S.; Daniels, A. D.;Farkas, O.; Foresman, J. B.; Ortiz, J. V.;

Cioslowski, J.; Fox, D. J. *Gaussian 09*, Revision A.02; Gaussian, Inc.: Wallingford, CT, 2009.
(44) Lee, Ch.; Yang, W.; Parr, R. G. *Phys. Rev. B* **1988**, *37*, 785–789.
(45) Becke, A. D. *Phys. Rev. A* **1988**, *38*, 3098–3100.
(46) Stephens, P. J.; Devlin, F. J.; Chabalowski, C. F.; Frisch, M. J. *J. Phys. Chem.* **1994**, *98*, 11623–11627.
(47) Zhao, Y.; Schultz, N. E.; Truhlar, D. G. *J. Chem. Theory Comput.* **2006**, *2*, 364–382.
(48) Hohenstein, E. G.; Chill, S. T.; Sherrill, C. D. *J. Chem. Theory Comput.* **2008**, *4*, 1996–2000.
(49) Takeuchi, H.; Kojima, T.; Egawa, T.; Konaka, S. *J. Phys. Chem.* **1992**, *96*, 4389–4396.
(50) Bondi, A. *J. Phys. Chem.* **1964**, *68*, 441–451.
(51) Plumley, J. A.; Dannenberg, J. J. *J. Comput. Chem.* **2011**, *32*, 1519–1527.
(52) Daza, M. C.; Dobado, J. A.; Molina, J. M. *J. Chem. Phys.* **1999**, *110*, 11806–11813.
(53) (a) Database of Frequency Scaling Factors for Electronic Structure Methods; http://comp.chem.umn.edu/freqscale/version3b1.htm, Zheng, J.; Alecu, I. M.; Lynch, B. J.; Zhao, Y.; Truhlar D. G., 2011. (b) Alecu, I. M.; Zheng, J.; Zhao, Y.; Truhlar, D. G. *J. Chem. Theory Comput.* **2010**, *6*, 2872–2887.
(54) Mulliken, R. S. *J. Chem. Phys.* **1955**, *23*, 1833–1840.
(55) Breneman, C. M.; Wiberg, K. B. *J. Comput. Chem.* **1990**, *11*, 361–373.
(56) Reed, A. E.; Curtiss, L. A.; Weinhold, F. *Chem. Rev.* **1988**, *88*, 899–926.
(57) Politzer, P., Truhlar, D. G., Eds. *Chemical Applications of Atomic and Molecular Electrostatic Potentials*; Plenum Press: New York, 1981.
(58) Kollman, P.; McKelvey, J.; Johansson, A; Rothenberg, S. *J. Am. Chem. Soc.* **1975**, *97*, 955–965.
(59) Hippler, M.; Hesse, S.; Suhm, M. A. *Phys. Chem. Chem. Phys.* **2010**, *12*, 13555–13565.
(60) Vayssilov, G. N.; Lercher, J. A.; Rösch, N. *J. Phys. Chem. B* **2000**, *104*, 8614–8623.
(61) Dimitrova, V.; Ilieva, S.; Galabov, B. *J. Phys. Chem. A* **2002**, *106*, 11801–11805.
(62) Galabov, B.; Bobadova−Parvanova, P.; Ilieva, S.; Dimitrova, V. *J. Mol. Struct.: THEOCHEM* **2003**, *630*, 101–112.
(63) Kenny, P. W. *J. Chem. Soc., Perkin Trans.* **1994**, *2*, 199–202.
(64) Platts, J. A. *Phys. Chem. Chem. Phys.* **2000**, *2*, 973–980.
(65) Rangelov, M. A.; Petrova, G. P.; Yomtova, V. M.; Vayssilov, G. N. *J. Mol. Graph. Model.* **2011**, DOI: 10.1016/j.jmgm.2011.05.004.
(66) Trobro, S.; Åqvist, J. *Proc. Natl. Acad. Sci. U.S.A.* **2005**, *102*, 12395–12400.

ACS chemical biology

Articles

pubs.acs.org/acschemicalbiology

Ab Initio Molecular Dynamics of Na^+ and Mg^{2+} Countercations at the Backbone of RNA in Water Solution

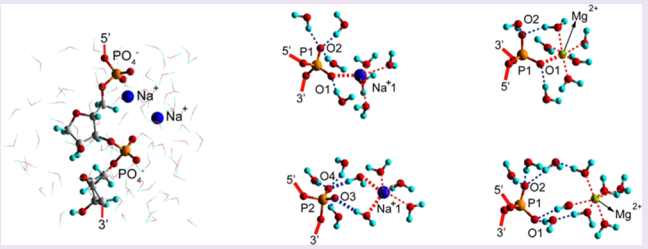
Stefan Kolev,[†] Petko St. Petkov,[†] Miroslav Rangelov,[‡] and Georgi N. Vayssilov*[,†]

[†]Faculty of Chemistry and Pharmacy, University of Sofia, Boulevard James Bouchier 1, 1126 Sofia, Bulgaria

[‡]Laboratory of BioCatalysis, Institute of Organic Chemistry, Bulgarian Academy of Sciences, Str. Acad. G. Bontchev, Bl. 9, 1113 Sofia, Bulgaria

Supporting Information

ABSTRACT: The interactions between sodium or magnesium ions and phosphate groups of the RNA backbone represented as dinucleotide fragments in water solution have been studied using ab initio Born−Oppenheimer molecular dynamics. All systems have been simulated at 300 and 320 K. Sodium ions have mobility higher than that of the magnesium ions and readily change their position with respect to the phosphate groups, from directly bonded to completely solvated state, with a rough estimate of the lifetime of bonded Na^+ of about 20−30 ps. The coordination number of the sodium ions frequently changes in irregular intervals ranging from several femtoseconds to about 10 ps with the most frequently encountered coordination number five, followed by six. The magnesium ion is stable both as directly bonded to an oxygen atom from the phosphate group and completely solvated by water. In both states the Mg^{2+} ion has exactly six oxygen atoms in the first coordination shell; moreover, during the whole simulation of more than 100 ps no exchange of ligand in the first coordination shells has been observed. Solvation of the terminal phosphate oxygen atoms by water molecules forming hydrogen bonds in different locations of the ions is also discussed. The stability of the system containing sodium ions essentially does not depend on the position of the ions with respect to the phosphate groups.



Metal ions (Na^+, K^+, Mg^{2+}, Ca^{2+}) play important roles in the stability, folding, and functioning of nucleic acids.[1,2] Their presence is essential for the structural integrity of the chromosomes of different living cells, including mammalian.[3,4] These ions help maintain the spatial configuration of DNA[5,6] and RNA[7,8] not only by neutralizing the negative charges of the phosphate groups but also mediation by some of them of the interactions between parts of the macromolecules. Metal ions stabilize the tertiary structure of RNA in the ribosome[9,10] and the ribozymes[11−14] or directly participate in the interactions between different components of the ribozymes. Metal ions could also be used as doping agents to alter the electronic properties of nucleic acids in order to create new materials for the photonics and electronics [15]

The interactions between metal ions and various DNA and RNA sequences have been experimentally studied employing various techniques. The preferred binding sites of monovalent and divalent metal ions in solution and crystal phase have been explored by NMR[5,6,8,16−18] and vibrational spectroscopy methods including IR[19,20] and Raman[21−26] spectroscopy. The interactions between the ions and phosphate groups have been analyzed by measuring symmetric and asymmetric PO_4^- vibrations. The assignment of the vibrational frequencies for this analysis was based on the vibrational spectra of low molecular weight phosphoric acid esters.[27−29] Low frequency vibrations, arising from the presence of alkali ions near the phosphate groups of DNA, are also studied.[30] The locations of the ions in crystal phase may be determined by X-ray crystallography,[5,6,9,10,31−35] but often their positions are not clear due to irregular location of the cations and difficulties in distinguishing them from the water molecules.[5] An additional complication comes from the fact that the structure of the biomolecules in the crystalline phase differs from that in solution. The experimental results obtained in solution more closely match the biological systems, but the methods, applied in these studies (NMR, IPR, vibrational spectroscopy) give only indirect information for the interactions and the structural information derived by them is to a large extent qualitative.

To complement this deficiency of the available experimental methods, theoretical approaches, including classical molecular dynamics[36−38] and Monte Carlo methods,[39] are also used to study interactions of metal ions with nucleic acids. While these methods are very powerful for modeling dynamics of biomolecules as proteins, DNA, or RNA, the description of the local interactions in these methods is predetermined by the parametrization of the applied force field. Such local interactions are properly described with quantum chemical methods, although they are restricted by the size of the modeled system. The first-principles approaches based on quantum chemical methods intrinsically account for all types of

Received: August 31, 2012
Accepted: May 5, 2013
Published: May 5, 2013

 © 2013 American Chemical Society

Table 1. Data from Dynamical Simulations[a]

cation[b]	temp (K)	period (ps)	M−O1 (pm)	M−O (pm)	% N[c]	comment
Na^+1	300	1−18	235	235	19/**61**/20/0	Na^+1 bonded to O1
Na^+2			665	235	9/**79**/12/0[d]	Na^+2 solvated
Na^+1	300	18−66	455	235	2/**88**/8/1	Na^+1 solvated
Na^+2			645	235		Na^+2 solvated
Na^+1	300	66−95	255	245	1/32/**52**/15	Na^+1 bonded to O1
Na^+2			645	245		Na^+2 solvated
Na^+1	300	95−104	355	235	1/**81**/18/0	Na^+1 solvated
Na^+2			665	235		Na^+2 solvated
Na^+1	320	104−125	455	245	3/**82**/14/1	Na^+1 solvated
Na^+2			665	235	3/**78**/19/0[d]	Na^+2 solvated
Mg^{2+} bonded	300	1−61	205	215	0/0/**100**/0	Mg^{2+} bonded to O1
Mg^{2+} bonded	320	61−140	205	215	0/0/**100**/0	Mg^{2+} bonded to O1
Mg^{2+} solvated	300	1−61	465−565	215	0/0/**100**/0	Mg^{2+} solvated
Mg^{2+} solvated	320	61−140	425	215	0/0/**100**/0	Mg^{2+} solvated

[a]Including the temperature used; period; distances (peaks of the RDF) between the cations, O1 oxygen atom, and the oxygen atoms from the first coordination shell; and percents of time during which the ion coordinates different numbers of oxygen atoms, % N. [b]For notation of the atoms see Figure 1 and the description in the text. [c]The numbers a/b/c/d in the column denote the percentage of time in the corresponding simulation period during which the coordination number of the ion is 4, 5, 6, and 7, respectively. The highest value is in bold. [d]For Na^+2 the values are calculated for the whole periods of simulation at 300 and 320 K, 1−104 and 104−125 ps.

interactions between the atoms, ions, molecules, or functional groups in the system as electrostatic interaction, electron transfer (including variation of the charge of the species during simulation), mutual polarization, Pauli repulsion, electron exchange and correlation. Some of these interactions are included in the classical potentials for MD simulations. Since the parameters of these potentials are derived to reproduce certain properties of the systems to be modeled, they cannot necessarily provide correct results for other systems or for other properties (for a recent example see ref 40). Since the quantum chemical methods are derived from first principles, they as such are not system-specific and can be used to simulate different properties or characteristics of the system without special parametrization. For this reason quantum chemical calculations are often used as targets in derivation of the parameters of classical potentials or for evaluation of their accuracy with respect to certain properties.[41] A detailed discussion of the advantages, disadvantages and typical applications of the classical, quantum mechanical and hybrid quantum mechanical-molecular mechanical (QM/MM) methods for simulations of RNA is provided in the recent paper of Ditzler et al.[42]

The application of quantum chemical methods has so far been limited to optimization of the structure of RNA fragments with Na^+ and Mg^{2+} ions in gas phase or water modeled as continuum[43] as well as using QM/MM schemes.[42,44] On the basis of cluster calculations using a continuum solvent model, it was suggested that both sodium and magnesium ions have affinity for binding to the phosphate groups of RNA, although the affinity of Mg^{2+} is higher by about 116 kJ/mol, assuming that Mg^{2+} is bonded to two phosphate groups while the Na^+ binds only to the one.[43] In order to understand the complexity of the interactions, in addition to looking at a local minimum, one could simulate the evolution of the system by ab initio molecular dynamics. Such type of modeling has been used to describe the behavior of the metal ions in different systems such as in water solution of carbonates,[45] but ab initio MD simulations of the interaction of metal cations with RNA or DNA fragments has not been reported so far.

In the present paper we report ab initio molecular dynamic simulation of sodium or magnesium ions in the vicinity of the backbone fragment of a nucleic acid in water solution. The model system includes two phosphate groups and two ribose moieties compensated by two sodium or one magnesium cation. The whole system is solvated in 106 or 110 water molecules for the model systems with two Na^+ ions or one Mg^{2+}, respectively. With these calculations we were able to clarify the actual location and mobility of these cations with respect to the phosphate groups of the backbone in water and to shed light on the picoseconds dynamic of the system up to 125 ps. We have shown that sodium cation is very mobile and moves between the first and second coordination sphere of the phosphate in periods of ca. 30 ps, while magnesium ion keeps its coordination sphere rather strong (no exchange of the ligands in its first coordination shell is observed) and does not move notably with respect to the phosphate.

RESULTS AND DISCUSSION

Dynamics of the Sodium-Containing Systems. *Mobility of the Sodium Ions.* First we report the results from the ab initio molecular dynamics simulation related to the interactions of sodium ions with the phosphate groups from RNA backbone. The length of the simulation is in total 125 ps. In Table 1, the summary of the conditions and duration of all performed simulations is presented. During the first 104 ps, the temperature (thermostat) is adjusted to 300 K, while in the last 21 ps the temperature is set at 320 K in order to speed up the dynamics of the system.

After 1 ps (necessary for thermal equilibration to 300 ± 20 K), both sodium ions stay close to their initial positions: one of the Na^+ ions (denoted as Na^+1, Figure 1b,c) is directly *bonded* to an oxygen atom (O1) from the phosphate group (P1), while the other Na^+ ion (Na^+2) interacts with one of the phosphate groups via one water molecule and is denoted as *solvated* in water (Figure 1b,c). The Na^+1 ion remains coordinated directly to the O1 atom until the 18th ps of the simulation. The radial distribution function (RDF) for the Na^+1−O1 distance during the 1−18 ps period, presented in Figure 2a, has a maximum at 235 pm, which indicates a direct contact between the sodium ion and the oxygen atom from the phosphate group. The solvation of the Na^+1 ion begins after the 18th ps. The Na^+1−

dx.doi.org/10.1021/cb300463h | ACS Chem. Biol. 2013, 8, 1576−1589

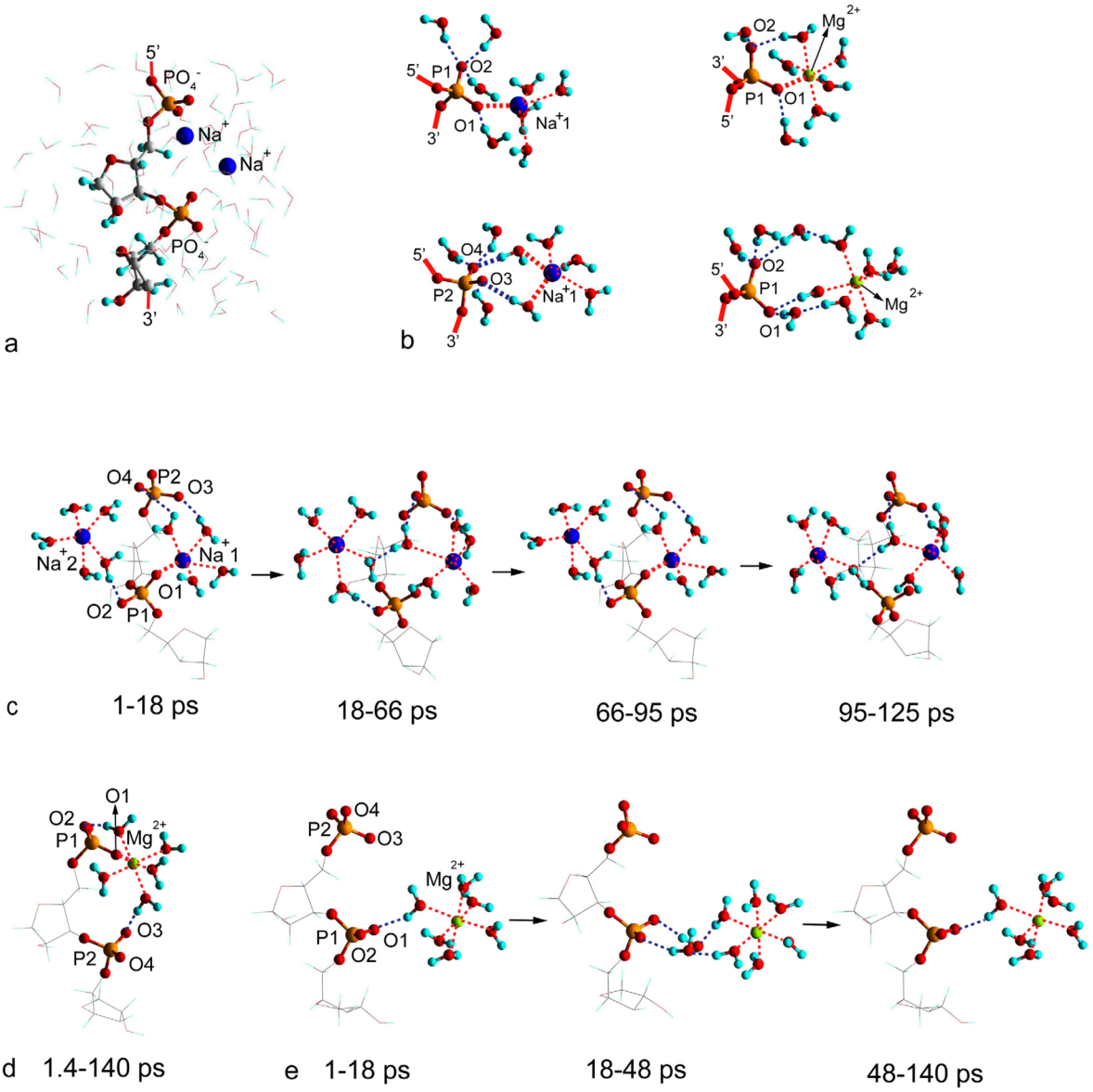


Figure 1. Selected snapshots from the simulations: (a) the simulation box with the RNA backbone model and two sodium ions (water molecules are shown only as lines); (b) water molecules solvating P1 or P2 phosphate groups and the countercations in bonded and solvated state; (c) sodium ions in different time periods; (d) bonded magnesium ion; and (e) solvated magnesium ion in different time periods.

O1 radial distribution function for the 18th to the 66th ps simulation time (Figure 2a) has several small maxima and corresponds to the process of the movement of sodium ion into the solution without direct contact with the phosphate oxygen atom. The final maximum is at 455 pm, indicating indirect interaction of the Na^+1 ion with the oxygen atoms from the phosphate group through two water molecules. After this period the Na^+1 ion is bonded again to the O1 oxygen atom for about 30 ps (from the 66th to 95th ps) with Na^+1−O1 RDF maximum of 255 pm. After the 95th ps the ion again starts transition to the solution and in the period 104−125 ps (simulated at 320 K) is already completely solvated. The maxima of the RDF (Na^+1−O1) for the periods 95−104 ps and 104−125 ps are 335 and 455 pm, respectively. The continuous time evolution of the Na^+1−O1 distance is presented in Figure 2a, and snapshots typical for the consecutive periods are shown in Figure 1c.

It should be noted that the Na^+ ion coordinates to the phosphate group in a monodentate manner, as observed for Na^+1 ion in the periods 1−18 ps and 66−95 ps, remaining in a close contact with only one oxygen atom from the phosphate group, Figure 1b. The second terminal oxygen atom of the phosphate group, O2, remains in these periods at more than 100 pm farther from the cation than O1. This can be seen from the maxima of the RDF for Na^+1−O2 distances in the time periods 1−18 ps and 66−95 ps, 405 and 385 pm, respectively (Figure 2c,d).

When Na^+1 ion is not directly bonded to O1, it interacts with each one of the O1 and O2 phosphate oxygen atoms via two water molecules. During the major part of the simulation (5−125 ps), Na^+1 interacts with the terminal oxygen atoms of the distant phosphate group, O3 and O4, via a single water molecule from the first coordination shell of Na^+1 ion, forming an eight-membered cycle, Figure 1b.

dx.doi.org/10.1021/cb300463h | ACS Chem. Biol. 2013, 8, 1576−1589

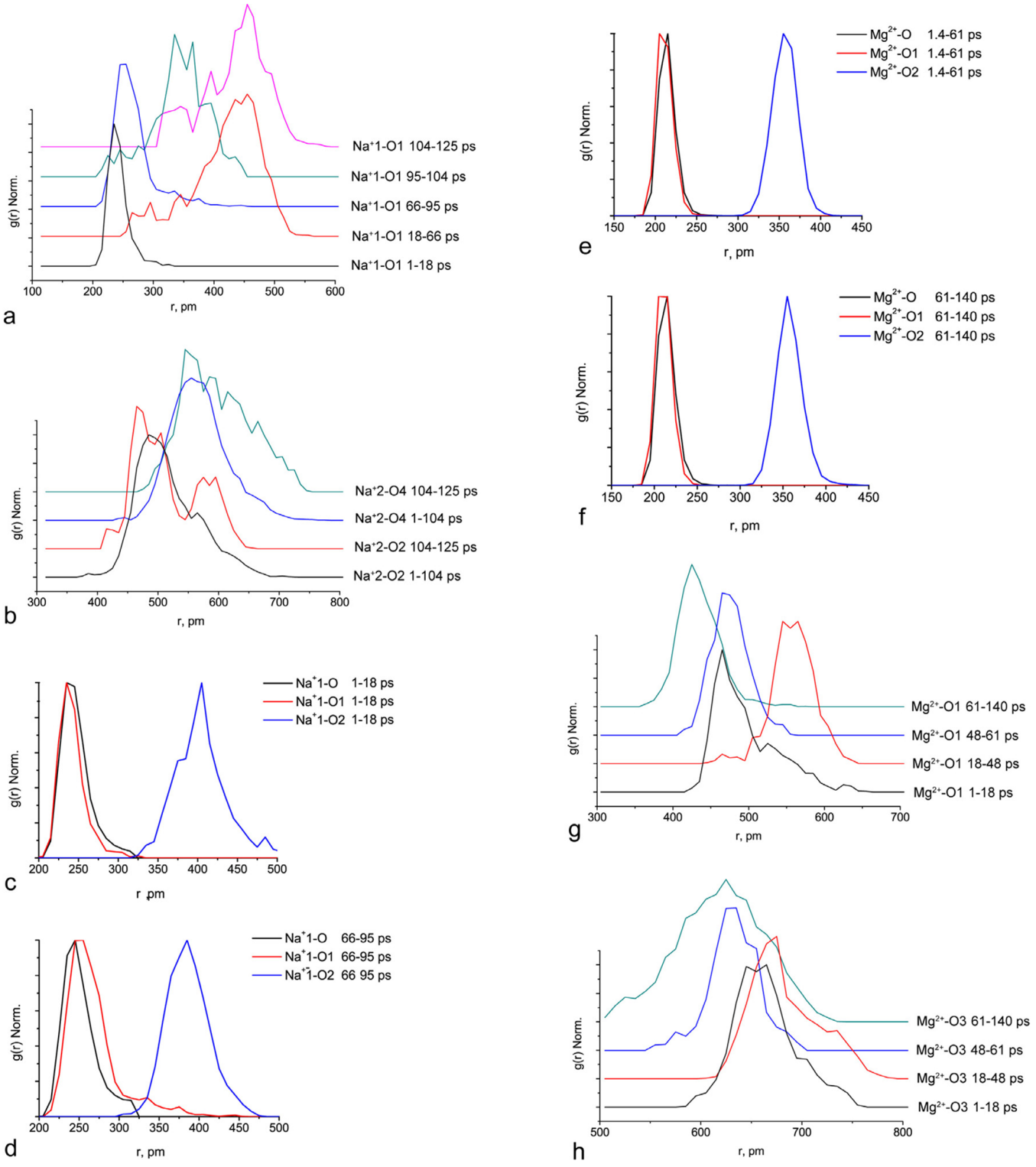


Figure 2. Radial distribution functions, RDF, of various species: (a) Na^+1 and (b) Na^+2 ions to the nearest O center from a phosphate group in different time intervals of the simulations. (c, d) Na^+1 to all O centers and to O1 and O2 centers of P1 phosphate group in the periods when this cation is bonded, 1−18 ps (c) and 66−95 ps (d). (e, f) Bonded Mg^{2+} ion to all O centers and to O1 and O2 centers of P1 phosphate group in the periods simulated at 300 K (e) and at 320 K (f). (g, h) Solvated Mg^{2+} ion to O1 (g) and O3 (h) centers of P1 and P2 phosphate groups in different simulation periods at 300 K (1−61 ps) and at 320 K (61−140 ps). For notation of the atoms see Figure 1 and the description in the text.

The second sodium ion Na^+2 remains completely solvated during the whole simulation time, 1−125 ps. The time evolution of the Na^+2−O2 distance is presented in Figure 2b. The closest phosphate oxygen atom to Na^+2 is O2, followed by O4, which is farther by about 100 pm during the simulation (also shown in Figure 1c). Na^+2 interacts with O2 through a single water molecule during the initial period of the simulations, 1−24 ps. During the 24−37 ps period, Na^+2 interacts with O2 through two water molecules and, during the 37−120 ps period, again through a single water molecule.

dx.doi.org/10.1021/cb300463h | ACS Chem. Biol. 2013, 8, 1576−1589

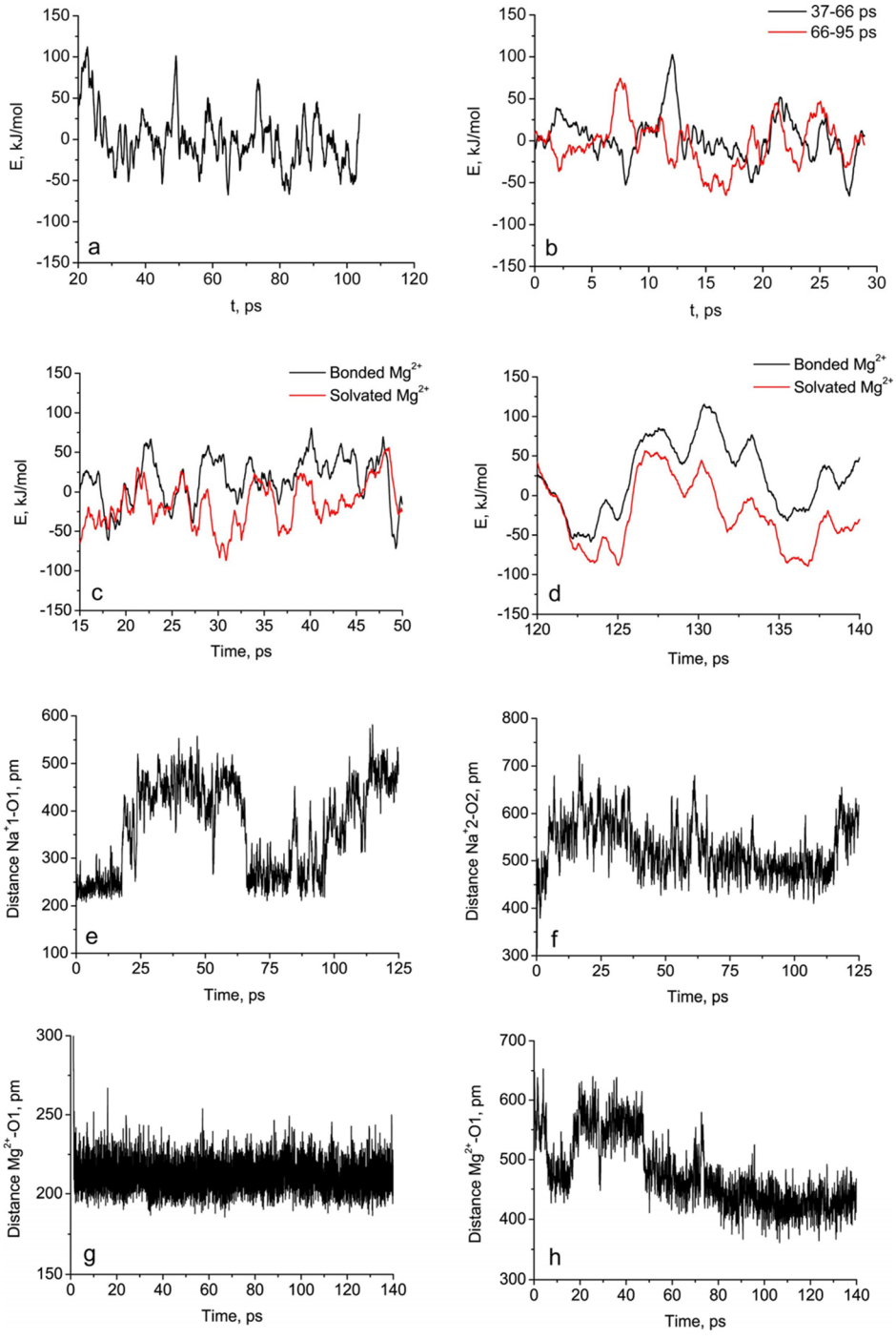


Figure 3. (a) Variation of the potential energy of the simulated system with two sodium cations for the interval 20−104 ps, simulated at 300 K, and (b) comparison of the variations in the potential energy for the periods 37−66 ps (solvated Na^+1) and 66−95 ps (bonded Na^+1). The values are averaged over 1000 points. Zero energy corresponds to the average value for the whole period 20−104 ps, −2193.71634 hartree. (c, d) Variation of the potential energy of the simulated systems with bonded and solvated magnesium cation for the intervals 15−50 ps at 300 K (c) and 120−140 ps at 320K (d). The values are averaged over 1000 points. Zero energy for panel c is −2169.04305 hartree, which is the mean value between the average values for the bonded and for the solvated Mg^{2+} in the 15−50 ps period. Zero energy for panel d is −2169.04721 hartree, which is the mean value between the average values for the bonded and for the solvated Mg^{2+} in the 120−140 ps periods. (e−h) Variation of the distance between the metal cation and the oxygen center from phosphate group closest to it for Na^+1 (e) and Na^+2 (f) ions in the simulation with two sodium ions and for Mg^{2+} in the simulations with bonded (g) and solvated (h) magnesium ion.

During the last 5 ps of the simulation Na^+2 interacts with O2 through two water molecules. The maximum at around 475 pm (Figure 2b) indicates interaction through a single water molecule, and the peak around 575 pm indicates interaction via two water molecules.

Energy of the System. Potential energy of the system with two sodium cations for the period 20−104 ps is presented in Figure 3a. To improve visibility the plot is smoothed by averaging at every 1000 points of the simulation. It should be noted that local minima and maxima of the potential energy do

dx.doi.org/10.1021/cb300463h | *ACS Chem. Biol.* 2013, 8, 1576−1589

Table 2. Characteristics of the First and Second Peaks in the RDF for the Interatomic Distances between Na^+1, Na^+2, and Mg^{2+} Ions and All Oxygen or Hydrogen Atoms in the System for Different Time Periods

distance/period[a]	first peak				second peak			
	start	maximum	end	integral	start	maximum	end	integral
2 Na^+ ions								
Na^+1–O/1–18	205	235	315	5.0	315	445	535	23.7
Na^+1–O/18–66	205	235	325	5.1	325	435	515	20.8
Na^+1–O/66–95	205	245	315	5.8	315			
Na^+1–O/104–125	205	245	315	5.1	315	445	515	21.2
Na^+1–H/1–18	215	295						
Na^+1–H/18–66	225	295	355	12.0	355			
Na^+1–H/66–95	215	295	395	16.1	395	495	535	36.4
Na^+1–H/104–125	215	295	375	14.6	375			
Na^+2–O/1–104	205	235	325	5.1	325	445		
Na^+2–O/104–125	205	235	325	5.2	325	435		
Na^+2–H/1–104	215	295	385	14.5	385	495	565	48.1
Na^+2–H /104–125	215	295	385	14.5	385	485		
Mg^{2+} bonded								
Mg^{2+}–O/1.4–61	185	215	295	6.0	295	415	495	20.2
Mg^{2+}–O/61–140	185	215	305	6.0	305	425	505	20.8
Mg^{2+}–H/1.4–61	215	275	365	12.5	365	485		
Mg^{2+}–H/61–140	225	275	375	12.6	375	495		
Mg^{2+} solvated								
Mg^{2+}–O/1–18	185	215	285	5.9	285	425	505	21.3
Mg^{2+}–O/18–48	185	215	305	6.0	305	425	515	23.0
Mg^{2+}–O/48–61	185	215	275	6.0	275	435	505	21.5
Mg^{2+}–O/61–140	185	215	285	6.0	285	425	485	19.1
Mg^{2+}–H/1–18	225	275	345	12.4	345	475		
Mg^{2+}–H/18–48	225	275	325	12.5	325	465		
Mg^{2+}–H/48–61	235	275	325	12.6	325	475		
Mg^{2+}–H/61–140	225	275	345	12.6	345	485		

[a]For notation of the atoms see Figure 1 and the description in the text.

not correlate with some specific position of the metal ions with respect to the phosphate groups but to a large extent reflect the variation of the arrangement of the water molecules in the system since potential energy variations of the same order of magnitude are observed in simulation of bulk water.

To compare the energy of the two distinct positions of the sodium ion Na^+1, bonded to the phosphate oxygen atom O1 and solvated, the potential energies of the corresponding periods 37–66 ps and 66–95 ps (both periods include 29 ps simulation) are plotted in Figure 3b. The average value of the potential energy during the 66–95 ps period, when the Na^+1 ion is directly bonded to the O1 phosphate oxygen atom, is by 6 kJ/mol lower than that for the period with solvated Na^+1 ion. Having in mind the large variations in the potential energy of the system, the energy difference of 6 kJ/mol can be considered as negligible for the studied systems and could be attributed to minimal variations in the arrangement of the water molecules. So, both locations of the sodium cation can be considered energetically equivalent, and the energy of the system does not depend strongly on the position of the sodium ions toward the phosphate groups, being directly bonded or interacting through a water molecule.

Solvation Shell of the Sodium Ions. The radial distribution functions of the distances between Na^+1 and Na^+2 ions and all oxygen and hydrogen atoms in the system with two sodium cations are presented in Figures S1 and S2 of the Supporting Information and in Table 2, along with the coordination numbers $n(r)$ obtained from the integral of the RDF.

We will start with the Na^+2 ion, which is solvated during the whole simulation, 1–125 ps. Its first solvation shell has Na^+2–O distances between 205 and 325 pm, with a maximum at 235 pm, indicating the most probable distance between the ion and the oxygen atoms from the surrounding water molecules. The RDF value at the first minimum, 325 pm, does not reach zero, which indicates a poorly defined first coordination shell.[46] The coordination number for the first coordination shell is 5.10 and 5.22 for the periods 1–104 ps and 104–125 ps, respectively, suggesting the solvation of sodium ion by 5 water molecules, but states at which the sodium ion is solvated by 4 or 6 water molecules can also be observed during the simulation.

For the Na^+1 ion, which is bonded to the phosphate oxygen atom O1 during the periods 1–18 ps and 66–95 ps of the simulation, the first coordination shell begins at 205 pm and ends at 315–325 pm, with a maximum within the interval 235–245 pm and the integrated value corresponding to about 5 oxygen atoms participating in the first coordination shell of the sodium ion, oxygen atoms from water molecules and one oxygen atom from the phosphate group (Table 2). An exception is the period 66–95 ps in which sodium ion has 6 oxygen atoms in the first coordination shell, 5 water molecules and one oxygen atom from the phosphate group. The second maximum of the RDF for Na^+1–O distance appears at 435–445 pm, and the integrated value suggests that the second coordination shell of the sodium ion contains 13 water molecules. It should be noted that during the whole simulation (1–125 ps) the oxygen atoms from the ribose do not contribute to either the first or the second coordination shell

dx.doi.org/10.1021/cb300463h | ACS Chem. Biol. 2013, 8, 1576–1589

of the sodium ion Na^+1, but the ribose moiety occupies some space in vicinity of the Na^+1 ion, which for the solvated ion is occupied by water molecules.

The characteristic minima and maxima in the RDF of the Na^+1−H distances, see Figure S1 of the Supporting Information, are similar to those for the Na^+2−H distance (Supplementary Figure S2), but the integrated values $n(r)$ include some hydrogen atoms from the ribose and depend on the proximity of Na^+1 ion to the dinucleotide. The integral of the second maximum, about 36.4, includes, beside water molecules, 4 hydrogen atoms from the ribose. Thus, one can estimate that in addition to the 13 water molecules in the second coordination shell (estimated from Na^+1−O RDF, see previous paragraph) in this area fall 6 hydrogen atoms from neighboring H_2O molecules forming hydrogen bonds.

In order to compare the interaction of the sodium ion Na^+1 with the oxygen atoms O1 and O2 from the phosphate group and from the water molecules, we present the radial distribution functions between Na^+1 and O1 and O2 and between Na^+1 and all oxygen atoms in the system except O1 and O2 denoted as Na^+1−O (Figure 2c,d) for the periods when Na^+1 is bonded to the phosphate group. For the period 1−18 ps, both maxima are located at 235 pm, indicating equal average distances between the sodium ion and the oxygen atoms from water molecules or O1 from the phosphate group. For the period 66−95 ps, the average Na^+1−O1 distance is somewhat longer, 245−255 pm, due to coordination of two proton-donating water molecules at O1 atom for this period (see below). Na^+1−O2 distance is spread in a wider interval with maxima at 410 and 390 pm.

Solvation Shell of the Phosphate Oxygen Atoms. The radial distribution functions On−H, where On represents terminal oxygen atoms of the phosphate moieties, O1, O2, O3, and O4, and H represents all hydrogen atoms in the system with the exception of the hydrogen atoms from the dinucleotide, are used to assess the hydration of the phosphate oxygen atoms that are not bonded to the alkyl residue (Figure S3 of the Supporting Information and Table 3). The first hydration shell around O1 starts at 145 pm (1−104 ps) or 135 pm for the 104−125 ps (at 320 K) periods with the most probable distance O1−H of 175 pm, except for the 66−95 ps period, where it is longer by 10 pm at 185 pm. During the 1−18 ps period one water molecule ($n(r)$ = 0.96) is hydrogen bonded to the O1 atom in addition to the Na^+1 cation coordinated to it, while for the second period with bonded Na^+1 cation, 66−95 ps, two water molecules are coordinated to O1 ($n(r)$ = 1.94), although at somewhat longer distance. During the periods with solvated Na^+1 cation, 18−66 ps (at 300 K) and 104−125 ps (320 K), the integrated values of the first peak are 1.78 and 1.58, corresponding to two water molecules hydrogen bonded most of the time to the phosphate oxygen atom as the $n(r)$ value at 320 K is by 0.2 lower than the value obtained at 300 K, i.e., the hydration of this O atom is reduced with the increasing of the temperature.

The O2−H, O3−H, and O4−H radial distribution functions start at about 125 pm, and their maxima are at 175 pm, which suggests formation of strong hydrogen bonds as should be expected since these oxygen centers are formally negatively charged. The first minima, about 245 pm, are clearly distinguished, suggesting a well ordered first hydration shell, similarly to the O1−H RDF. For O2 and O4 the $n(r)$ values clearly suggest three water molecules hydrogen bonded to the phosphate oxygen atoms, whereas for O3, the value is close to two hydrogen bonded water molecules, similarly to the O1 oxygen atom described above. The reason for this difference is the 5′-CH_2 groups of the two ribose moieties that remain close to O1 and O3 centers, at about 260 pm, and prevent the approach of the third water molecule to these negatively charged oxygen centers. The other two oxygen atoms, O2 and O4, are farther from the ribose and are able to coordinate three water molecules. The influence of the temperature on the hydration for the two groups of oxygen atoms, as estimated by $n(r)$, is different: the $n(r)$ for O1 and O3 decreases by 0.2 when the temperature increases by 20 K, while for O2 and O4 $n(r)$ increases or remains unchanged, respectively.

Table 3. Characteristics of the First Peak in the RDF for the Interatomic Distances between Different Oxygen Centers of the Two Phosphate Groups and Hydrogen Atoms in the System for Different Time Periods

	first peak			
distance/period[a]	start	maximum	end	integral
2 Na^+ ions				
O1−H/1−18	145	175	235	1.0
O1−H/18−66	145	175	265	1.8
O1−H/66−95	145	185	245	1.9
O1−H/104−125	135	175	255	1.6
O2−H/1−104	125	175	245	2.8
O2−H/104−125	145	175	245	3.0
O3−H/1−104	135	175	245	2.2
O3−H/104−125	125	165	245	2.0
O4−H/1−104	125	175	255	2.9
O4−H/104−125	125	175	245	2.9
Mg^{2+} bonded				
O1−H/1.4−61	145	185	235	1.0
O1−H/61−140	135	185	235	0.9
O2−H/1.4−61	135	175	255	2.1
O2−H/61−140	135	175	255	2.1
O3−H/1.4−61	135	175	265	2.3
O3−H/61−140	135	175	255	2.0
O4−H/1.4−61	125	175	245	2.9
O4−H/61−140	135	175	265	3.2
Mg^{2+} solvated				
O1−H/1−61	135	175	245	2.1
O1−H/61−140	135	175	245	2.1
O2−H/1−61	135	175	265	2.9
O2−H/61−140	125	175	255	3.0
O3−H/1−61	135	175	255	2.9
O3−H/61−140	135	175	245	2.6
O4−H/1−61	135	175	255	2.4
O4−H/61−140	145	175	255	2.6

[a]For notation of the atoms see Figure 1 and the description in the text.

During the simulation all water molecules that form hydrogen bonds with the phosphate oxygen atoms participate with only one of their hydrogen atoms as a donor of the hydrogen bond, as presented in Figure 1b. The dynamic behavior of the water molecules coordinated to the terminal phosphate oxygen atoms is not uniform: the fastest exchange of the water molecules forming hydrogen bonds to the phosphate oxygen atoms occurs for 20−30 ps, while some of the water molecules remain bonded to the oxygen atoms during the whole simulation of 125 ps.

Dynamics of the System with Directly Bonded Magnesium Ion. *Solvation Shell of the Directly Bonded Magnesium Ion.* Initially, in this simulation the magnesium ion

dx.doi.org/10.1021/cb300463h | ACS Chem. Biol. 2013, 8, 1576−1589

was placed in the space between the two phosphate groups, at a distance of about 450 pm from both phosphorus atoms. After 1.4 ps, the Mg^{2+} ion is directly bonded to the O1 oxygen atom from the P1 phosphate group (Figure 1b). The magnesium ion remains bonded to O1 during the whole simulation: 1.4−61 ps at 300 K and 61−140 ps at 320 K (Figure 1d). According to the RDFs for the Mg^{2+}−O1 distance (Figure 2e,f), the most probable distance between the magnesium ion and the oxygen atom O1 is 205 pm both at 300 K (1.4−61 ps) and at 320 K (61−140 ps). The magnesium ion binds to the phosphate group in a monodentate manner, remaining in direct contact with only the O1 oxygen atom, while the Mg^{2+}−O2 distance (Figure 2e,f) remains around 355 pm. The magnesium ion interacts with O2 and O3 through single water molecules (see Figure 1d).

The radial distribution functions Mg^{2+}−O (Figure 2e,f) clearly indicate that the first coordination shell of the Mg^{2+} ion is well-defined, at variance from the coordination shell of the sodium ion. The integrated values at the first peak for both periods are exactly equal to 6.00 (Table 2 and Figure S4 of the Supporting Information), indicating 6 oxygen centers bonded to the magnesium ion, five of which from water molecules and one from the O1 oxygen atom from the phosphate group. The peak maximum is located at 215 pm, longer by 10 pm than the Mg^{2+}−O1 distance, likely due to stronger electrostatic attraction between the Mg^{2+} ion and the negatively charged phosphate O1 center. The second maximum of the Mg^{2+}−O RDF is located at 415 pm (1.4−61 ps at 300 K) and 425 pm (61−140 ps at 320 K), and n(r) values correspond to 9 or 10 water molecules (taking into account the oxygen atoms from the backbone) in the second coordination shell of the Mg^{2+} ion at 300 and 320 K, respectively. The Mg^{2+}−H radial distribution functions (Figure S4 of the Supporting Information and Table 2) suggest the same number of water molecules in the first coordination sphere of the cation. At variance from Na^+, for Mg^{2+} hydrogen atoms from the ribose moiety do not participate in the second coordination sphere.

Solvation Shell of the Phosphate Oxygen Atoms. The analysis of the solvation of the O1, O2, O3, and O4 oxygen atoms from the P1 and P2 phosphate groups is based on the corresponding On−H RDFs including all hydrogen atoms in the system with the exception of the hydrogen atoms from the dinucleotide (Figure S5 of the Supporting Information and Table 3). The first hydration shell around O1, which is directly bonded to the Mg^{2+} ion, contains about one water molecule during the whole simulation, and the most probable length of the hydrogen bond O1−H is 185 pm.

For the other three phosphate oxygen atoms, O2, O,3 and O4, the most probable length of the hydrogen bonds with the water molecules is 175 pm, shorter by 10 pm than O1−H. The integral of the first peak corresponds to two water molecules hydrogen bonded to O2 and O3 oxygen atoms during the whole simulation, while for the O4−H radial distribution functions, the n(r) values are 2.86 (1.4−61 ps) and 3.21 (61−140 ps), corresponding to about three hydrogen bonded water molecules. Thus, as expected, the O1 oxygen atom, which is in direct contact with the Mg^{2+} ion, coordinates fewer water molecules (one) than the other phosphate oxygen atoms, which are hydrogen bonded to 2 or 3 water molecules. The main difference from the solvation of the phosphate oxygen atoms in the presence of bonded Na^+ is the reduction of the number of water molecules in the O2 coordination shell likely due to blocking of the space around O2 center by the rigid $Mg^{2+}(H_2O)_5$ moiety.

Dynamics of the System with Solvated Magnesium Ion. *Solvation Shell of the Solvated Magnesium Ion.* In this simulation the magnesium ion was initially solvated by water molecules at about 500 pm from the O1 oxygen atom from the phosphate group P1 interacting with it through a single water molecule (Figure 1e) and remains solvated during the whole simulation (1−140 ps). In the initial period, 1−18 ps, the magnesium ion interacts with O1 via a single water molecule (Figure 1e) with a Mg^{2+}−O1 distance of 465 pm and interacts with O2 and O3 oxygen atoms through two water molecules. During the period 18−48 ps, the Mg^{2+} ion moves away and interacts with O1 and O2 atoms through two water molecules with Mg^{2+}−O1 distance of 565 pm, 100 pm longer than in the previous position (Figure 2g). After the 48th ps of the simulation, the Mg^{2+} ion moves back, closer to the O1 oxygen atom, and interacts with it through a single water molecule with Mg^{2+}−O1 distance of 465 pm, as in the first period. During this period the magnesium ion interacts with O2 and O3 through 2 water molecules. In the last period of the simulation, 61−140 ps, run at 320 K, the Mg^{2+} ion interacts with the O1 oxygen atom through a single water molecule with Mg^{2+}−O1 distance of 425 pm, shorter by 40 pm than the distance for the analogous position at 300 K (periods 1−18 and 48−61 ps).

Similarly to the magnesium ion bonded to the phosphate group, the first coordination shell of the solvated magnesium ion has an RDF maximum of 215 pm and contains exactly 6 oxygen atoms (Table 2, Figure S6 of the Supporting Information) all belonging to water molecules. The second maxima of the Mg^{2+}−O RDF are located at about 425 pm for all simulation periods, but the amount of water molecules in the second coordination shell differs in different periods: it is 17 when magnesium ion interacts with the phosphate oxygen atoms through 2 water molecules, and decreases to 14 for Mg^{2+} interacting through single water molecule since part of the solvation shell is replaced by the phosphate oxygen atoms. The simulation at 320 K (61−140 ps) resulted in a further decrease of the number of water molecules in the second coordination shell of Mg^{2+} ion to 12. The Mg^{2+}−H RDFs with first and second maxima at 275 pm and 465−485 pm suggest similar number of water molecules in the first and second coordination shell of the cation as the Mg^{2+}−O distances.

Solvation Shell of the Phosphate Oxygen Atoms in the System with Solvated Magnesium Ion. For all oxygen atoms O1, O2, O3, O4 the first coordination shell, consisting of water molecules, hydrogen bonded to the phosphate oxygen atoms, begins at about 135 pm (Table 3, Figure S7 of the Supporting Information). Similarly to the phosphate oxygen atoms (nonbonded to Mg^{2+} ion) from the previous simulation, the most probable length of the O···H hydrogen bond is 175 pm. In average five water molecules are coordinated to the two terminal oxygen atoms of each phosphate group. For P1 group O1 and O2 centers have most of the time two and three coordinated water molecules, due to variation of the position of the ribose five-atomic ring with respect to these centers. The ribose is oriented on the side of O1 at the distance of 350 pm, which is responsible for the lower coordination number of O1. The number of water molecules hydrogen bonded to O3 and O4 oxygen centers varies between 2.9 and 2.4 during the first 61 ps of the simulation. The O4 oxygen atom is closer to the 3′ hydrogen atom from the ribose by 10 pm than the O3 to the 5′ hydrogen atom, the nearest hydrogen atoms (245 and 255 pm

dx.doi.org/10.1021/cb300463h | ACS Chem. Biol. 2013, 8, 1576−1589

mean distances), which may explain the slightly lower coordination number of O4. During the last period of the simulation, 61−140 ps, when both O3 and O4 oxygen atoms coordinate the mean number of 2.6 water molecules, no structural differences between the O3 and O4 neighboring structures are observed.

Energy of the Systems with Magnesium Ions. The variations of the potential energy of the systems with directly bonded or solvated magnesium ions are presented in Figure 3c,d. The potential energies are plotted from the 15th to the 50th ps (300 K), corresponding to the period when the solvated Mg^{2+} interacts with O1 through 2 water molecules, and the 120−140 ps period (320 K), the last 20 ps of the simulation, when Mg^{2+} interacts with O1 through 1 water molecule. During both periods no energy drift is observed. Like in the simulation with sodium ions, local minima and maxima of the potential energy do not correlate with the position of the metal ions with respect to the phosphate groups but likely reflect the arrangement of the water molecules in the system.

Comparison between Sodium and Magnesium Ions. *Solvation of the Sodium and Magnesium Ions.* During the whole simulation (both at 300 and 320 K) both directly bonded and completely solvated magnesium ions have exactly 6 oxygen atoms in their first coordination shell. Moreover, the ligands are strongly coordinated to magnesium cation, and no exchange of water molecule or phosphate oxygen atom occurs in the first coordination shells during the whole simulations.

On the other hand sodium ions readily exchange water molecules between the first and second coordination shells and change coordination numbers. During the simulation sodium ions coordinate 4−7 oxygen atoms from water molecules or phosphate groups. The rapid changing of the coordination number for the Na^+ ions is evident in Figure 4, where coordination number for Na^+1 and Na^+2 ions is plotted against time for the last 21 ps of the simulations and for the Na^+1 the 66−95 ps period, when the ion is directly bonded to the phosphate group (Na−O distance cutoff is 320 pm).

Water molecules from "bulk" solution participate in the exchange between the coordination shells, while water molecules hydrogen bonded to phosphate groups are much less mobile. For this reason, water molecules from the first coordination shell of the sodium ions that form hydrogen bonds with phosphate oxygen centers are not frequently exchanged.

The variation of the coordination numbers of the sodium cation can be also followed as the fractions of time (in percents) during which the ion coordinates different numbers of oxygen atoms (Table 1). During the whole simulations the most frequently encountered coordination number for the sodium ions is five (with 61−88% for the Na^+1 ion in different time intervals and 78−79% for the Na^+2 ion), followed by coordination number six. Exception is the 66−95 ps period, when the Na^+1 ion is directly bonded to the O1 phosphate oxygen atom, when the most frequently encountered coordination number is six (with 52%), followed by five and seven. No clear influence of the temperature on the coordination number is observed.

Comparison with Experimental and Previous Computational Results. In some cases the positions of the metal ions, Na^+ or Mg^{2+}, with respect to the phosphate groups of RNA backbone have been determined by X-ray crystallography.[9,32] Since Na^+ is particularly difficult to be identified in the nucleic acid X-ray crystal structures,[5,34] we present only an example of

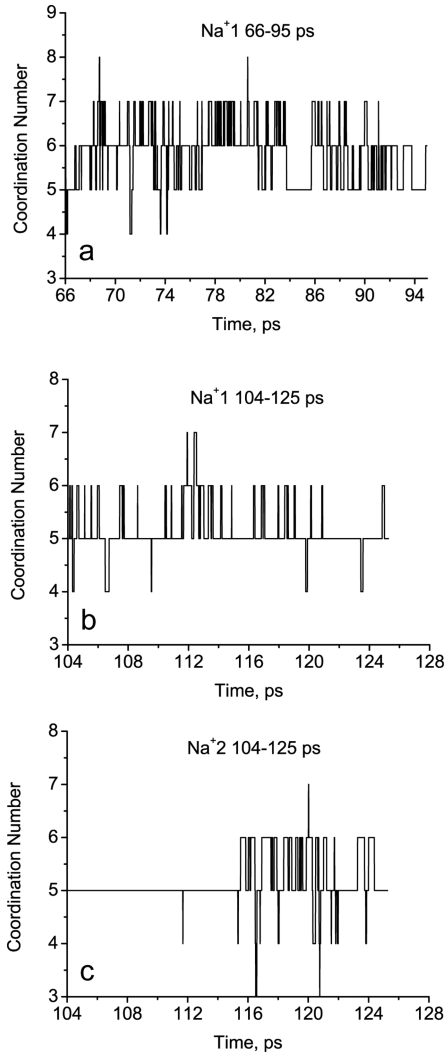


Figure 4. Variation of coordination number of Na^+1 and Na^+2 cations in selected simulation periods.

sodium ion, directly bonded to a phosphate group, see Supplementary Figure S8a (Na^+ ion number 315 from PDB 2OJ0 from ref 31 with resolution 260 pm). The distance between the ion and the oxygen atom from the phosphate group is 245 pm, which is in agreement with the typical Na^+1−O1 distance found in our simulations, 235−255 pm.

In the PDB files from the crystallographic data, magnesium ions are observed either directly bonded to the phosphate groups or interacting through water molecules.[9,32,33] The Mg^{2+}−O(P) distance for the magnesium ions interacting directly with phosphate oxygen atoms in the large ribosomal subunit is estimated by Klein et al.[9] to be shorter than 240 pm. According to the data reported by Subirana et al.[34] the average Mg^{2+}−O(P) distance to phosphate oxygen atoms (averaged over Mg^{2+} ions in a sample studied at very high resolution, 89−120 pm) is 203 pm, which is very close to the corresponding average distance derived from our ab initio MD simulations. An example of such position of magnesium ion is presented in Supplementary Figure S8b (Mg^{2+} ion number 200 from PDB 354D from ref 33 with 150 pm resolution) with Mg^{2+}−O(P) distance of 205 pm. The Mg^{2+}−O(P) distances when the phosphate oxygen atoms and the Mg^{2+} ion are separated by one water molecule may vary by a large interval (Figure 2h). An

dx.doi.org/10.1021/cb300463h | ACS Chem. Biol. 2013, 8, 1576−1589

example for such location observed experimentally is shown in Supplementary Figure S8c (Mg^{2+} ion number 201 from PDB 354D from ref 33) with Mg^{2+}−O(P) distance of 466 pm, close to the average value from our simulation for the analogous location of the magnesium ion (Figure 1e).

Using geometry optimization approach with a DFT method Petrov et al.[43] reported interatomic distances very similar to the optimal values obtained in our calculations. The calculated distances Mg^{2+}−O(P) were about 200 pm and Mg^{2+}−O(Water) about 215 pm; Na^+−O(P) about 235 pm and Na^+−O(Water) about 245 pm. Note that in their calculations the RNA fragment forms a chelate complex with the magnesium ion with two neighboring phosphate groups coordinated to it.

We also compared the results from the ab initio MD simulation with classical MD simulation of dinucleotide with sodium or magnesium ions (at 300 K) using CHARMM and AMBER force fields. For Na^+ the optimal Na^+−O distance to the oxygen atoms from the phosphate and water molecules in the classical MD simulation with AMBER is the same as the distance in the ab initio MD, 235 pm. However, the location of the cation differs (Figure S9 of the Supporting Information). In the classical MD most of the time Na^+ ion is located close to both terminal oxygen atoms of one of the phosphate groups (O1 and O2), while in the ab initio MD only one of these oxygen atoms enters in the first coordination shell of the cation and a bidentate complex is not observed. The simulation with CHARMM resulted in monodentate location of Na^+ with respect to the phosphate group, but the Na^+−O(P) distances are around 215 pm (Supplementary Figure S10a,b), shorter by 20 pm than in the ab initio MD. Similarly to the ab initio MD, in the classical MD simulations we also observed mobility of one of the Na^+ ions (Supplementary Figures S9a, S10a) although for different duration; it moves away from the phosphate oxygen in the periods 40−49 ps (AMBER) and 44−49 ps (CHARMM).

The classical MD simulation for magnesium ion resulted in very similar position of the cation with respect to the phosphate group, monodentate coordination (Supplementary Figures S9b, S10c). However, the maximal values of the RDF for Mg^{2+}−O distances were found to be 10−30 pm shorter than those in ab initio simulation of bonded Mg^{2+} ion: Mg^{2+}−O1 to the oxygen atom from the phosphate is 175 pm (CHARMM) and 185 pm (AMBER), and Mg^{2+}−O(w) to the oxygen atoms from the water molecules is 195 pm both with CHARMM and AMBER (Figure S10c).

Effect of Temperature. Since our simulations are performed at two temperatures, 300 and 320 K, we may compare some characteristics of the systems obtained at these temperatures. The first maxima of the Na^+−O and Mg^{2+}−O RDF are located essentially at the same distances for the two temperatures (see Table 1). The coordination numbers for magnesium are also the same, exactly six. A small increase of the average coordination number of the solvated sodium ion with the temperature is observed. At 300 K it is 5.03 and at 320 K it is 5.16, due to the increase of the time in which the cation is six coordinated (see Figure S11e of the Supporting Information). Although this difference is rather small, it follows the general trend for increase of the average number of ligands in the first solvation shell of Na^+ in water with the temperature, observed in separate simulation: when the temperature increases from 303 to 353 K, the sodium coordination number increases by 0.39.

The mobility of the cations at different temperature can be estimated by the difference between the minimal and maximal values of the root-mean-square deviation (RMSD) of their position for certain simulation period. In Supplementary Figure S11a−d we present the variations of RMSD for Na^+ and Mg^{2+} ions during the simulations. ΔRMSD values for magnesium and solvated sodium ions (Table S1 of the Supporting Information) are higher for the simulations at 320 K, which indicates higher mobility of the Na^+ and Mg^{2+} ions at the higher temperature.

Vibrational Analysis of the Phosphate Groups in the Modeled Systems. Complete vibrational analysis of the studied systems explicitly including also the water molecules has been performed for the cations (Na^+ or Mg^{2+}) in solution or directly bonded to the phosphate groups. We summarize here only the symmetric ν_s and asymmetric ν_{as} vibrations of the phosphate groups (Figure 5 and Supplementary Table S4), since they are

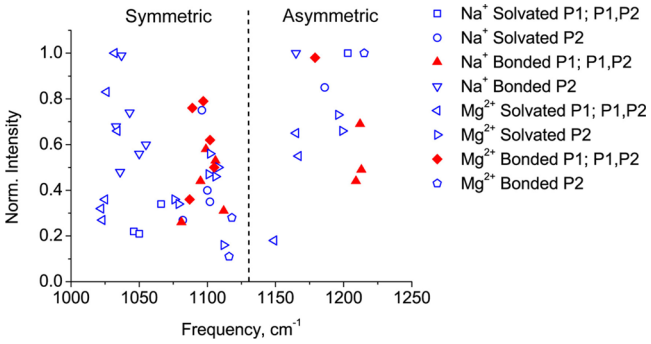


Figure 5. Calculated frequencies of the symmetric and asymmetric phosphate groups' vibrations and their normalized intensities. The filled red symbols correspond to vibrations of a phosphate group with countercation bonded to it, and the empty blue symbols correspond to vibrations of a phosphate group surrounded only by water molecules without a countercation bonded to its oxygen centers.

considered depending on the positions of the metal ions. As the frequencies of these vibrations depend also on the phosphate groups conformations,[47,48] we present the conformations of the structures used for vibrational analysis (Table S2 of the Supporting Information). During the simulations (Supplementary Table S3) one of the phosphate groups (P1 in the systems with 2 Na^+ and with solvated Mg^{2+}, and P2 in the system with bonded Mg^{2+}) remains always in gauche−gauche (gg) conformation, which was reported to be slightly more stable that the trans−gauche (tg) conformation for phosphate esters.[47,48] The conformation of the other phosphate group changes irregularly between tg and tt as the 3′ end remains always in trans configuration.

The frequencies of the symmetric vibration ν_s of the phosphate groups that are not directly bonded to metal ions appear in two regions, a lower frequency region around 1035 cm^{-1} and a higher frequency region around 1100 cm^{-1}, which can be compared to the experimental vibrational frequencies measured in different samples around 1023−1040 cm^{-1} and 1072−1115 cm^{-1}.[49] All frequencies for ν_s bands of the phosphate groups bonded to a Mg^{2+} or Na^+ ion are located only in the higher frequency region around 1100 cm^{-1}. The asymmetric frequencies are observed in the 1150−1215 cm^{-1} region, but no clear correlation between their values and the positions of metal ions was observed. These results suggest that the bands for symmetric vibrations of the phosphate groups can be used experimentally for determination of the position of the

dx.doi.org/10.1021/cb300463h | ACS Chem. Biol. 2013, 8, 1576−1589

sodium or magnesium ion with respect to the phosphate moieties, in the absence of a directly bonded countercation both low and high symmetric frequency bands will appear, while in presence of a countercation directly bonded to it the lower frequency band will disappear and the intensity of the high frequency band is expected to increase.

Similar trends have been experimentally observed by Raman spectroscopy of RNA crystals in water medium, complemented by XRD measurments.[24] The ν_s frequency of the RNA phosphate groups in NaCl solution was measured 1100 cm^{-1}, while after addition of Mg^{2+} ions in the solution a band at 1117 cm^{-1} (by 17 cm^{-1} higher than the initial value) is evident. Although the exact values of the vibrational frequencies cannot be reproduced precisely with this computational method and model, the observed experimental trend suggests that the sodium ions are staying mainly in hydrated form in the solution and phosphate groups did not interact directly with the counterion. On the other hand, magnesium ions are directly bonded to the phosphate groups in solvated RNA for long times that correspond to the high frequency band of the symmetric vibrations. The direct bonding of Mg^{2+} ions to the phosphate groups was confirmed by XRD measurement.[24] It should be noted these experimental data are obtained with double stranded RNA, while our calculated value correspond to the backbone of single stranded RNA.

In the previous quantum chemical simulations of the vibrational frequencies of the phosphate group in some model compounds the solvation of the phosphate and the metal ion was taken into account by a continuum solvation models and partially by explicit water molecules.[48,49] Although our model system is more realistic since it includes explicitly the complete first and second solvation shells of both metal ions and the phosphate moieties, the calculated characteristic vibrational frequencies cannot be used for direct comparison with the experiment by several reasons: (i) typical error of the computational method; (ii) anharmonicity of the vibrations; (iii) variation of the local arrangement of the water molecules solvating the phosphate oxygen atoms in the real solution resulting in broadening of the experimental bands; (iv) influence of the conformations of the phosphate groups,[47,48] described above, etc.

Conclusions. The interactions between sodium or magnesium ions and phosphate groups of the RNA backbone in water solution have been studied using ab initio Born–Oppenheimer molecular dynamics. Sodium ions have higher mobility (Figure 3e,f) than the magnesium ions (Figure 3g,h) and readily change their position with respect to the phosphate groups, from directly bonded to completely solvated state. Within the 104 ps simulation at 300 K the lifetime of bonded Na^+ was about 20 to 30 ps, during which the sodium ion binds to only one of the oxygen atoms from the phosphate group at about 235–255 pm (Figure 3e). One of the studied sodium ions remain completely solvated during the whole simulation and interacts with the phosphate groups through one or two water molecules.

Sodium ions coordinate 4–7 oxygen atoms from water molecules or phosphate group in their first coordination shell with the most frequently encountered coordination number being five (about 80% of the simulation time), followed by coordination number six (about 15% of the time). The coordination number of the sodium ions frequently changes in irregular intervals ranging from several femtoseconds to about 10 ps. The distance between the sodium ion and the oxygen atoms from the first coordination shell is about 235 pm and does not depend on the origin of the oxygen atom, from water molecule or phosphate group.

Two states of the systems containing magnesium ions, with Mg^{2+} directly bonded to the phosphate group and with completely solvated ion, were found stable for 140 ps simulations. The Mg^{2+} binds to one of the oxygen atoms of one of the phosphate group of the selected RNA fragment with optimal $Mg^{2+}\cdots O{=}P$ distance of about 205 pm. The completely solvated Mg^{2+} interacts with the phosphate groups through one or two water molecules. Both the directly bonded and completely solvated magnesium ions have exactly six oxygen atoms in their first coordination shell. Moreover, during the whole simulation at 300 and 320 K no exchange of ligand in the first coordination shells has been observed. The distance between the magnesium ion and the oxygen atoms from the first coordination shell is about 215 pm.

The terminal phosphate oxygen atoms are solvated by water molecules forming hydrogen bonds with typical distance $H\cdots O{=}P$ of about 175 pm. In the simulation involving solvated sodium or magnesium ions both phosphate groups are solvated by about 5 water molecules. The presence of a directly bonded ion reduces the number of the water molecules at the corresponding phosphate group by one for part of the simulation with sodium and by two for directly bonded Mg^{2+} ion.

The stability of the system containing sodium ions does not depend strongly on the position of the ions with respect to the phosphate groups, being directly bonded or interacting through a water molecule. The energy difference between the bonded and solvated states of one of the cations is only 6 kJ/mol (simulated at 300 K), negligible for the system, and could be attributed to minimal variations in the arrangement of the water molecules.

Classical MD simulations with AMBER or CHARMM force fields gave similar behavior as the ab initio MD simulations but the concrete distances, cationic positions and time scales differ and depend on the selected force field.

COMPUTATIONAL METHODS

Ab initio Born–Oppenheimer molecular dynamic simulations were performed using the CP2K/Quickstep package.[50,51] Density functional theory was applied within the generalized gradient approximation (GGA), using Perdew-Burke-Ernzerhof (PBE) functional.[52] Basis set DZVP-MOLOPT-SR-GTH,[53] which is optimized for calculating molecular properties in gas and condensed phase, was applied for all atoms in the studied systems. For reducing computational cost Gaussian and Plane-Wave (GPW) method was used.[51,54,55] This method uses an atom-centered Gaussian-type basis to describe the wave functions and an auxiliary plane wave basis to describe the electron density.[51] Only the valence electrons are explicitly treated. Their interaction with the remaining ions is described using the pseudopotentials of Goedecker–Teter–Hutter (GTH).[56,57] The charge density cutoff of the finest grid level is equal to 400 Ry. The number of used multigrids is 5.

All Born–Oppenheimer molecular dynamic simulations were carried out in NVT ensemble with a time step of 1 fs. The temperature was set to constant (at 300 or 320 K, as described below) using canonical sampling through velocity rescaling (CSVR) thermostat. Statistics were gained after thermal equilibration. The studied systems consist of nucleic acid dinucleotide fragment from RNA (with ribose) without the nucleobases, and the metal ions necessary to neutralize the negative charges of the phosphate groups, two Na^+ or one Mg^{2+} ion. The whole system is hydrated in a periodic box with dimensions: 1264.5 pm × 1700.0 pm × 1700.0 pm (see Figure 1a).

For simulations with sodium and magnesium ions the box contains 106 and 110 water molecules, respectively, that assures density of the water phase equal to 0.99 g/cm^3. The dinucleotide skeleton is oriented along the shortest axis x (1264.5 pm) and forms a monotonic infinite chain of a single-stranded nucleic acid backbone (e.g., RNA) with average distance between the phosphorus atoms equal to 635 pm. The initial state (atom coordinates) of the dinucleotide are taken from a section with single-stranded RNA from an atomistic classical MD simulation of the ribosome in water solution based on crystallographic structure by Harms et al.[58] In the present simulation the cations, necessary to neutralize the negative charges of the phosphate groups, are initially located as follows:

- Simulation with 2 sodium ions: one Na^+ ion directly coordinated at the phosphate group P1 and the second Na^+ ion separated from P1 and P2 by water molecules
- Simulation with one bonded Mg^{2+}: one Mg^{2+} ion directly located at the phosphate group P1 and interacting with the P2 phosphate group through a single water molecule
- Simulation with one solvated Mg^{2+}: one Mg^{2+} ion separated from the phosphate group P1 by a single water molecule and from the phosphate group P2 by two water molecules

Initial simulations were performed at 300 K and after 61 ps for the simulations with magnesium ions and 104 ps for the simulation with sodium ions the temperature was set to 320 K in order to speed up of the dynamics still preserving temperature of the system reasonably close to the biological one.

Harmonic vibrational frequencies were calculated in order to compare the results with trends in the experimental data from the literature. The procedure we used is as follows: selection of several local potential energy minima of the dynamics steps, corresponding to the most abundant coordination number of the phosphate oxygen atoms and the metal ions. Then the geometry of the selected structures was optimized without constraints and vibrational analysis was performed explicitly including all atoms in the systems. The same basis set and exchange-correlation functional, used for the dynamical simulations were used for the geometry optimization and vibrational analysis. None of the studied structures has imaginary frequencies following this procedure. Typically the calculated harmonic vibrational frequencies of isolated modes are corrected for the error of the computational method (which for the DFT calculations with PBE functional corresponds to scaling by a factor of 1.026) and for the anharmonicity. In case of interacting modes, as the symmetric and asymmetric modes of the phosphate groups, these errors affect the calculated frequencies in different directions and with different magnitude. Due to this problem the calculated frequencies cannot be corrected simultaneously in an unbiased way. By this reason we report uncorrected harmonic frequencies.

The classical MD simulation of dinucleotide with sodium or magnesium ions were performed with GROMACS package version 4.4.5 [59] with two different force fields, CHARMM27[60,61] and AMBER (ver. 2.0).[62] With both force fields the water molecules were described by TIP3P potential.[63] The time step was set to 1 fs, and the frame was recorded for every 10th fs of the simulation. NVT ensemble at T = 300 K was used. VMD package was used for visualization of the results.[64]

■ ASSOCIATED CONTENT

Supporting Information

Figures with radial distribution functions and integrals for the modeled systems and results from the classical MD simulations; tables with conformations of the phosphate groups and calculated frequencies of the phosphate groups vibrations and their intensities; and a movie for the ab initio MD simulation for the system with sodium ions. This material is available free of charge via the Internet at http://pubs.acs.org.

■ AUTHOR INFORMATION

Corresponding Author

*E-mail: gnv@chem.uni-sofia.bg.

Notes

The authors declare no competing financial interest.

■ ACKNOWLEDGMENTS

The authors thank the Bulgarian Research Fund of for financial support via grant no. DO 02−133/2008 and the Center of Excellence for supercomputer applications Super CA+. The authors are also grateful to the FP7 project BeyondEverest and the Bulgarian Supercomputer Center for provided computational resources and P. St. Petkov for the assistance.

■ REFERENCES

(1) Celander, D., and Cech, T. (1991) Visualizing the higher order folding of a catalytic RNA molecule. *Science 251*, 401−407.
(2) Sigel, A., Sigel, H., and Sigel, R. (2011) *Structural and Catalytic Roles of Metal Ions in RNA*, Vol. *9*, pp 101−124, RSC Publishing, Cambridge, U.K.
(3) Strick, R., Strissel, P. L., Gavrilov, K., and Levi-Setti, R. (2001) Cation-chromatin binding as shown by ion microscopy is essential for the structural integrity of chromosomes. *J. Cell Biol. 155*, 899−910.
(4) Levi-Setti, R., Gavrilov, K. L., and Rizzo, P. J. (2008) Divalent cation distribution in dinoflagellate chromosomes imaged by high-resolution ion probe mass spectrometry. *Eur. J. Cell Biol. 87*, 963−976.
(5) Hud, N. V., and Polak, M. (2001) DNA-cation interactions: the major and minor grooves are flexible ionophores. *Curr. Opin. Struct. Biol. 11*, 293−301.
(6) Egli, M. (2002) DNA-cation Interactions: Quo Vadis? *Chem. Biol. 9*, 277−286.
(7) Draper, D. E. (2004) A guide to ions and RNA structure. *RNA 10*, 335−343.
(8) Chen, S.-J. (2008) RNA folding: conformational statistics, folding kinetics, and ion electrostatics. *Annu. Rev. Biophys. 37*, 197−214.
(9) Klein, D. J., Moore, P. B., and Steitz, T. A. (2004) The contribution of metal ions to the structural stability of the large ribosomal subunit. *RNA 10*, 1366−1379.
(10) Bashan, A., and Yonath, A. (2008) The linkage between ribosomal crystallography, metal ions, heteropolytungstates and functional flexibility. *J. Mol. Struct. 890*, 289−294.
(11) Strobel, S. A., and Cochrane, J. C. (2007) RNA catalysis: ribozymes, ribosomes, and riboswitches. *Curr. Opin. Chem. Biol. 11*, 636−643.
(12) Shan, S., Kravchuk, A. V., Piccirilli, J. A., and Herschlag, D. (2001) Defining the catalytic metal ion interactions in the *Tetrahymena* ribozyme reaction. *Biochemistry 40*, 5161−5171.
(13) Guo, F., Gooding, A. R., and Cech, T. R. (2004) Structure of the *Tetrahymena* ribozyme: base triple sandwich and metal ion at the active site. *Mol. Cell 16*, 351−362.
(14) Leclerc, F. (2010) Hammerhead ribozymes: True metal or nucleobase catalysis? Where is the catalytic power from? *Molecules 15*, 5389−5407.
(15) Mizoguchi, K. (2010) Electronic states of M-DNA incorporated with divalent metal ions. *Proc. SPIE 7765*, No. 77650R-1.
(16) Johannsen, S., Megger, N., Böhme, D., Sigel, R. K. O., and Müller, J. (2010) Solution structure of a DNA double helix with consecutive metal-mediated base pairs. *Nat. Chem. 2*, 229−234.
(17) Zhao, Q., Nagaswamy, U., Lee, H., Xia, Y., Huang, H., Gao, X., and Fox, G. E. (2005) NMR structure and Mg^{2+} binding of an RNA segment that underlies L7/L12 stalk in the *E.coli* 50S ribosomal subunit. *Nucleic Acids Res. 33*, 3145−3153.
(18) Fürtig, B., Richter, Ch., Wöhnert, J., and Schwalbe, H. (2003) NMR spectroscopy of RNA. *ChemBioChem 4*, 936−962.
(19) Ahmad, R., Arakawa, H., and Tajmir-Riahi, H. A. (2003) A comparative study of DNA complexation with Mg(II) and Ca(II) in aqueous solution: major and minor grooves bindings. *Biophys. J. 84*, 2460−2466.
(20) Chiriboga, L., Xie, P., Yee, H., Vigorita, V., Zarou, D., Zakim, D., and Diem, M. (1998) Infrared spectroscopy of human tissue. I.

Differentiation and maturation of epithelial cells in the human cervix. *Biospectroscopy 4*, 47−53.
(21) Ponkumar, S., Duraisamy, P., and Iyandurai, N. (2011) Structural analysis of DNA interactions with magnesium ion studied by Raman spectroscopy. *Am. J. Biochem. Biotechnol. 7*, 135−140.
(22) Duguid, J., Bloomfield, V. A., Benevides, J., and Thomas, G. J., Jr. (1993) Raman spectroscopy of DNA-metal complexes. I. Interactions and conformational effects of the divalent cations: Mg, Ca, Sr, Ba, Mn, Co, Ni, Cu, Pb, and Cd. *Biophys. J. 65*, 1916−1928.
(23) Iyandurai, N., and Sarojini, R. (2009) Magnesium (II) ion induced changes on the structure of DNA: an FT−Raman study. *J. Appl. Sci. Res. 5*, 283−285.
(24) Gong, B., Chen, Y., Christian, E. L., Chen, J.-H., Chase, E., Chadalavada, D. M., Yajima, R., Golden, B. L., Bevilacqua, P. C., and Carey, P. R. (2008) Detection of innersphere interactions between magnesium hydrate and the phosphate backbone of the HDV ribozyme using Raman crystallography. *J. Am. Chem. Soc. 130*, 9670−9672.
(25) Chen, J.-H., Gong, B., Bevilacqua, P. C., Carey, P. R., and Golden, B. L. (2009) A catalytic metal ion interacts with the cleavage site G·U wobble in the HDV ribozyme. *Biochemisry 48*, 1498−1507.
(26) Gong, B., Chen, J.-H., Yajima, R., Chen, Y., Chase, E., Chadalavada, D. M., Golden, B. L., Carey, P. R., and Bevilacqua, P. C. (2009) Raman crystallography of RNA. *Methods 49*, 101−111.
(27) Stangret, J., and Savoie, R. (1992) Vibrational spectroscopic study of the interaction of metal ions with diethyl phosphate, a model for biological systems. *Can. J. Chem. 70*, 2875−2883.
(28) Guan, Y., Wurrey, C. J., and Thomas, G. J., Jr. (1994) Vibrational analysis of nucleic acids. I. The phosphodiester group in dimethyl phosphate model compounds: $(CH_3O)_2PO_2^-$, $(CD_3O)_2PO_2^-$, and $(^{13}CH_3O)_2PO_2^-$. *Biophys. J. 66*, 225−235.
(29) Anto, P. L., Anto, R. J., Varghese, H. T., Panicker, C. Y., and Philip, D. (2010) Vibrational spectroscopic studies and *ab initio* calculations of phenyl phosphate disodium salt. *J. Raman Spectrosc. 41*, 113−119.
(30) Perepelytsya, S. M., and Volkov, S. N. (2010) Intensities of DNA ion-phosphate modes in the low-frequency Raman spectra. *Eur. Phys. J. E 31*, 201−205.
(31) Ennifar, E., Walter, P., and Dumas, P. (2010) Cation-dependent cleavage of the duplex form of the subtype-B HIV-1 RNA dimerizaton initiation site. *Nucleic Acids Res. 38*, 5807−5816.
(32) Egli, M., Minasov, G., Su, L., and Rich, A. (2002) Metal ions and flexibility in a viral RNA pseudoknot at atomic resolution. *Proc. Natl. Acad. Sci. U.S.A. 99*, 4302−4307.
(33) Correll, C. C., Freeborn, B., Moore, P. B., and Steitz, T. A. (1997) Metals, motifs, and recognition in the crystal structure of a 5S rRNA domain. *Cell 91*, 705−712.
(34) Subirana, J. A., and Soler-López, M. (2003) Cations as hydrogen bond donors: a view of electrostatic interactions in DNA. *Annu. Rev. Biophys. Biomol. Struct. 32*, 27−45.
(35) Sines, C., McFail-Isom, L., Howerton, S., VanDerveer, D., and Williams, L. (2000) Cations mediate B-DNA conformational heterogeneity. *J. Am. Chem. Soc. 122*, 11048−11056.
(36) Auffinger, P., and Westhof, E. (2000) Water and ion binding around RNA and DNA (C, G) oligomers. *J. Mol. Biol. 300*, 1113−1131.
(37) Hamelberg, D., McFail-Isom, L., Williams, L., and Wilson, W. (2000) Flexible structure of DNA: ion dependence of minor-groove structure and dynamics. *J. Am. Chem. Soc. 122*, 10513−10520.
(38) Hamelberg, D., Williams, L., and Wilson, W. (2001) Influence of the dynamic positions of cations on the structure of the DNA minor groove: sequence-dependent effects. *J. Am. Chem. Soc. 123*, 7745−7755.
(39) Korolev, N., Lyubartsev, A. P., Rupprecht, A., and Nordenskiöld, L. (1999) Competitive binding of Mg^{2+}, Ca^{2+}, Na^+, and K^+ ion to DNA in oriented DNA fibers: experimental and monte carlo simulation results. *Biophys. J. 77*, 2736−2749.
(40) Yoo, J., and Aksimentiev, A. (2012) Improved parametrization of Li^+, Na^+, K^+, and Mg^{2+} ions for all-atom molecular dynamics simulations of nucleic acid systems. *J. Phys. Chem. Lett. 3*, 45−50.
(41) Ryjacek, F., Kubar, T., and Hobza, P. (2003) New parameterization of the Cornell et al. empirical force field covering amino group nonplanarity in nucleic acid bases. *J. Comput. Chem. 24*, 1891−1901.
(42) Ditzler, M., Otyepka, M., Sponer, J., and Walter, N. (2010) Molecular dynamics and quantum mechanics of RNA: conformational and chemical change we can believe in. *Acc. Chem. Res. 43*, 40−47.
(43) Petrov, A., Bowman, J., and Harvey, S. (2011) Bidentate RNA-magnesium clamps: on the origin of the special role of magnesium in RNA folding. *RNA 17*, 291−297.
(44) Banas, P., Jurecka, P., Walter, N. G., Sponer, J., and Otyepka, M. (2009) Theoretical studies of RNA catalysis: Hybrid QM/MM methods and their comparison with MD and QM. *Methods 49*, 202−216.
(45) Di Tommaso, D., and De Leeuw, N. H. (2010) Structure and dynamics of the hydrated magnesium ion and of the solvated magnesium carbonates: insights from first principles simulations. *Phys. Chem. Chem. Phys. 12*, 894−901.
(46) Schwegler, E. (2007) First-principles simulations of aqueous solutions. *J. Phys. Conf. Ser. 78*, 012065.
(47) Banavali, N., and MacKerell, A., Jr. (2001) Reevaluation of stereoelectronic contrubutions to the conformational properties of the phosphodiester and N3′ phospohoramidate moieties of nucleic acid. *J. Am. Chem. Soc. 123*, 6747−6755.
(48) Petrov, A., Funseth-Smotzer, J., and Pack, G. (2005) Computational study of dimethil phosphate anion and its complexes with water, magnesium, and calcium. *Int. J. Quantum Chem. 102*, 645−655.
(49) Andrushchenko, V., Wieser, H., and Bour, P. (2004) RNA structural forms studied by vibrational circular dichroism: Ab initio interpretation of the spectra. *J. Phys. Chem. B 108*, 3899−3911.
(50) The CP2K developers group, http://www.cp2k.org/, 2012.
(51) VandeVondele, J., Krack, M., Mohamed, F., Parrinello, M., Chassaing, T., and Hutter, J. (2005) QUICKSTEP: Fast and accurate density functional calculations using a mixed Gaussian and plane waves approach. *Comput. Phys. Commun. 167*, 103−128.
(52) Perdew, J. P., Burke, K., and Ernzerhof, M. (1996) Generalized gradient approximation made simple. *Phys. Rev. Lett. 77*, 3865−3868.
(53) VandeVondele, J., and Hutter, J. (2007) Gaussian basis sets for accurate calculations on molecular systems in gas and condensed phases. *J. Chem. Phys. 127*, 114105.
(54) Lippert, G., Hutter, J., and Parrinello, M. (1997) A hybrid Gaussian and plane wave density functional scheme. *Mol. Phys. 92*, 477−487.
(55) Lippert, G., Hutter, J., and Parrinello, M. (1999) The Gaussian and augmented-plane-wave density functional method for ab initio molecular dynamics simulations. *Theor. Chem. Acc. 103*, 124−140.
(56) Goedecker, S., Teter, M., and Hutter, J. (1996) Separable dual-space Gaussian pseudopotentials. *Phys. Rev. B54*, 1703−1710.
(57) Hartwigsen, C., Goedecker, S., and Hutter, J. (1998) Relativistic separable dual-space Gaussian pseudopotentials from H to Rn. *Phys. Rev. B58*, 3641−3662.
(58) Villa, E., Sengupta, J., Trabuco, L. G., LeBarron, J., Baxter, W. T., Shaikh, T. R., Grassucci, R. A., Nissen, P., Ehrenberg, M., Schulten, K., and Frank, J. (2009) Ribosome-induced changes in elongation factor Tu conformation control GTP hydrolysis. *Proc. Natl. Acad. Sci. U.S.A. 106*, 1063−1068.
(59) Hess, B., Kutzner, C., van der Spoel, D., and Lindahl, E. (2008) GROMACS 4: Algorithms for highly efficient, load-balanced, and scalable molecular simulation. *J. Chem. Theory Comput. 4*, 435−447.
(60) MacKerell, A. D., Jr., Bashford, D., Bellott, M., Dunbrack, R. L., Jr., Evanseck, J. D., Field, M. J., Fischer, S., Gao, J., Guo, H., Ha, S., Joseph-McCarthy, D., Kuchnir, L., Kuczera, K., Lau, F. T. K., Mattos, C., Michnick, S., Ngo, T., Nguyen, D. T., Prodhom, B., Reiher, W. E., III, Roux, B., Schlenkrich, M., Smith, J. C., Stote, R., Straub, J., Watanabe, M., Wiorkiewicz-Kuczera, J., Yin, D., and Karplus, M.

(1998) All-atom empirical potential for molecular modeling and dynamics Studies of proteins. *J. Phys. Chem. B 102*, 3586−3616.
(61) MacKerell, A. D., Jr., Banavali, N., and Foloppe, N. (2001) Development and current status of the CHARMM force field for nucleic acids. *Biopolymers 56*, 257−265.
(62) Wang, J., Wolf, R. M., Caldwell, J. W., Kollman, P. A., and Case, D. A. (2004) Development and testing of a general AMBER force field. *J. Comput. Chem. 25*, 1157−1174.
(63) Mahoney, M. W., and Jorgensen, W. L. (2000) A five-site model for liquid water and the reproduction of the density anomaly by rigid, nonpolarizable potential functions. *J. Chem. Phys. 112*, 8910−8922.
(64) Humphrey, W., Dalke, A., and Schulten, K. (1996) VMD - Visual Molecular Dynamics. *J. Mol. Graphics 14*, 33−38.

Food and Chemical Toxicology 55 (2013) 493–497

Contents lists available at SciVerse ScienceDirect

Food and Chemical Toxicology

journal homepage: www.elsevier.com/locate/foodchemtox

Brief communication

Two 6-(propan-2-yl)-4-methyl-morpholine-2,5-diones as new non-purine xanthine oxidase inhibitors and anti-inflammatory agents

Andrija Smelcerovic [a,*], Miroslav Rangelov [b], Zaklina Smelcerovic [c], Andrej Veljkovic [d], Emiliya Cherneva [e], Denitsa Yancheva [f], Goran M. Nikolic [a], Zivomir Petronijevic [g], Gordana Kocic [d]

[a] Department of Pharmacy, Faculty of Medicine, University of Nis, Bulevar Dr. Zorana Djindjica 81, 18000 Nis, Serbia
[b] Laboratory of BioCatalysis, Institute of Organic Chemistry with Centre of Phytochemistry, Bulgarian Academy of Sciences, Acad. G. Bonchev Str., Build. 9, 1113 Sofia, Bulgaria
[c] Center for Biomedicinal Science, Faculty of Medicine, University of Nis, Bulevar Dr. Zorana Djindjica 81, 18000 Nis, Serbia
[d] Institute of Biochemistry, Faculty of Medicine, University of Nis, Bulevar Dr. Zorana Djindjica 81, 18000 Nis, Serbia
[e] Department of Chemistry, Faculty of Pharmacy, Medical University of Sofia, 2 Dunav Str., 1000 Sofia, Bulgaria
[f] Laboratory of Structural Organic Analysis, Institute of Organic Chemistry with Centre of Phytochemistry, Bulgarian Academy of Sciences, Acad. G. Bonchev Str., Build. 9, 1113 Sofia, Bulgaria
[g] Faculty of Technology, University of Nis, Bulevar Oslobodjenja 124, 16000 Leskovac, Serbia

ARTICLE INFO

Article history:
Received 8 December 2012
Accepted 25 January 2013
Available online 11 February 2013

Keywords:
Cyclodidepsipeptides
Xanthine oxidase inhibition
Anti-inflamatory activity
NF-κB
Molecular modeling

ABSTRACT

Two cyclodidepsipeptides, 3-(2-methylpropyl)-6-(propan-2-yl)-4-methyl-morpholine-2,5-dione (**1**) and 3,6-di(propan-2-yl)-4-methyl-morpholine-2,5-dione (**2**), were evaluated for inhibitory activity against commercial enzyme xanthine oxidase (XO) *in vitro* and XO in rat liver homogenate as well as for anti-inflammatory response on human peripheral blood mononuclear cells (PBMCs). Both of cyclodidepsipeptides were excellent inhibitors of XO and significantly suppressed the nuclear factor of κB (NF-κB) activation. Allopurinol, a widely used XO inhibitor and drug to treat gout, relevated stronger inhibitory effect on rat liver XO activity than those of compounds **1** and **2**. Molecular docking studies were performed to gain an insight into their binding modes with XO. The studied morpholine-diones derivatives exerting XO inhibition and anti-inflammatory effect may give a promise to be used in the treatment of gout and other excessive uric acid production or inflammatory conditions.

© 2013 Elsevier Ltd. All rights reserved.

1. Introduction

Cyclodepsipeptides are known to exhibit a broad spectrum of biological activities, such as immunosuppressant, antibiotic, antifungal, anti-inflamatory or antitumoral activities (Sarabia et al., 2004). Two cyclodidepsipeptides, 3-(2-methylpropyl)-6-(propan-2-yl)-4-methyl-morpholine-2,5-dione (**1**) and 3,6-di(propan-2-yl)-4-methyl-morpholine-2,5-dione (**2**) (Fig. 1), were found for the first time in the natural products as potential precursors of enniatin B in the pathogenic fungi *Fusarium sporotrichioides*, isolated from the stem of fresh *Hypericum barbatum* Jacq. For identification and confirmation, those compounds were synthesized and studied by density functional theory calculations and infrared spectroscopy (Smelcerovic et al., 2011). Recently, we investigated the possible immunomodulatory effect and antimicrobial activity of **1** and **2**, due to well known biological activities of enniatin B (Pavlovic et al., 2012).

The prototypical xanthine oxidase (XO) inhibitor allopurinol, has been the cornerstone of the clinical management of gout and conditions associated with hyperuricemia for several decades. More recent data indicate that XO also plays an important role in various forms of ischemic and other types of tissue and vascular injuries, inflammatory diseases, and chronic heart failure. Allopurinol and its active metabolite oxypurinol showed considerable promise in the treatment of these conditions both in experimental animals and in small-scale human clinical trials (Pacher et al., 2006). Recently, Burns and Wortmann discussed febuxostat and several other drugs that target various steps in the pathogenesis of gout (Burns and Wortmann, 2011).

Nuclear factor of κB (NF-κB) is a sequence-specific transcription factor activated in response to inflammatory stimuli, known to be involved in the inflammatory and innate immune responses. NF-κB, which was discovered by Sen and Baltimore in 1986 as a factor in the nucleus of B cells that binds to the enhancer of the kappa light chain of immunoglobulin (Sen and Baltimore, 1986), has since been shown to be expressed ubiquitously in the cytoplasm of all cell types, conserved from Drosophila to man. It translocates to the nucleus only when activated, where it regulates the

* Corresponding author. Tel.: +381 18 4570029; fax: +381 18 4238770.
E-mail address: a.smelcerovic@yahoo.com (A. Smelcerovic).

0278-6915/$ - see front matter © 2013 Elsevier Ltd. All rights reserved.
http://dx.doi.org/10.1016/j.fct.2013.01.052

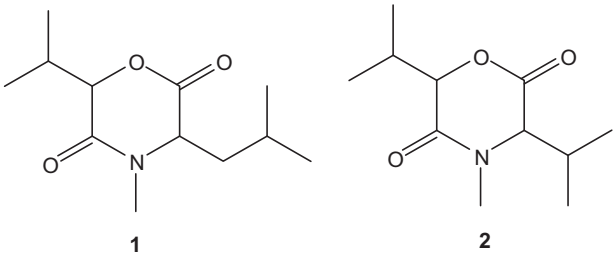


Fig. 1. Chemical structures of the compounds under study.

expression of over 200 genes that control the immune system, growth and inflammation (Pahl, 1999). NF-κB may function as the cellular checkpoint of metabolic stress conditions, such as hyperglycemia, oxidative, nitrosative stress and hyperuricemia, which may reflect disease processes associated with progression of autoimmune or autoinflammatory conditions (Kocic et al., 2011).

In the present study, two synthesized cyclodidepsipeptides **1** and **2** were evaluated for inhibitory activity against commercial enzyme XO *in vitro* and XO in rat liver homogenate as well as for anti-inflammatory response on human peripheral blood mononuclear cells (PBMCs). Molecular docking studies were performed in order to examine the binding mode of **1** and **2** with XO.

2. Materials and methods

2.1. Synthesis

The synthesis of the compounds **1** and **2** were performed via *N*-(α-bromoacyl)-α-amino acids as noncyclic intermediate products, as described in our previous study (Smelcerovic et al. 2011).

2.2. Evaluation of xanthine oxidase inhibition

2.2.1. Inhibition of commercial xanthine oxidase

Commercial bovine milk XO, purchased from Sigma–Aldrich, was employed for *in vitro* evaluation of enzyme inhibition, by measuring uric acid formation spectrophotometrically at 293 nm (Kizaki and Sakurada, 1977).

The inhibition was studied in a series of test-tubes with the reaction mixture (total volumen 350 μl), prepared in a following order: (i) *Test samples* contained 0.02 units of XO, 150 ng or 15 ng of test inhibitor **1** or test inhibitor **2** (both diluted in ethanol), 0.017 μmol of xanthine (Serva), and 20 μmol TRIS–HCl buffer (pH 7.8); (ii) *Solvent control samples* contained the same amount of XO, appropriate amount of ethanol, xanthine and TRIS–HCl buffer; (iii) *Control samples* contained the same amount of XO, xanthine and TRIS–HCl buffer adjusted to the same volume; and (iv) *Test substrate samples* were group of samples which contained in reaction mixture only XO, the compound **1** or **2** and TRIS–HCl buffer, in order to test if the compound **1** or **2** may be possible XO substrates. The tubes were allowed to incubate at 37 °C for 60 min, together with the corresponding duplicate blank aliquots, where the enzyme was omitted. After incubation, the reaction was stopped by adding perchloric acid, afterwards the XO was added in corresponding duplicate blank samples. The degree of enzyme inhibition was determined by measuring the difference in absorbance, associated with uric acid formation. It was calculated as a percent of change of the solvent control samples which involves only the effect of solvent ethanol. All experiments were conducted with six repetitions and averaged.

2.2.2. Inhibition of rat liver xanthine oxidase

The study was conducted in 6 weeks old female albino Wistar rats, weighing from 150 to 200 g. Rats were purchased from the farm of Military Medical Academy (Belgrade, Serbia) and bred in the vivarium of the Faculty of Medicine, University of Nis, under standard conditions. Animals used for the procedure were treated in accordance with the NIH Guide for Care and Use of Laboratory Animals (1985).

All experiments on animals were performed according to guidelines and had been approved by the Animal Ethics Board at the University of Nis Medical School beforehand.

Animals were anesthetized with ketamin (60 mg/kg) given intraperitoneally, and then sacrificed. Their livers were removed and cut in small pieces and homogenized in ice cold water, using homogenizer (IKA® Works de Brasil Ltda Taquara, RJ 22713-00). The homogenates (10% w/v) were centrifuged at 1500×*g* for 10 min at 4 °C. The resulting supernatant was separated and used for the biochemical analysis.

Inhibition of rat liver XO was monitored spectrophotometrically by a procedure similar to that described in Section 2.2.1. and procedure used in our recent report (Veljkovic et al., 2012).

The reaction mixture (total volume 2150 μl) was prepared in a following order: (i) *Test samples* contained 100 μl of 10% rat liver homogenate, 100 μg or 10 μg of **1** or **2** (diluted in ethanol), 1 μmol of xanthine (Serva), and 200 μmol TRIS–HCl buffer (pH 7.8); (ii) *Solvent control samples* contained the same amount of rat liver homogenate, appropriate amount of ethanol, xanthine and TRIS–HCl buffer; and (iii) *Control samples* contained the same amount of rat liver homogenate, xanthine and TRIS–HCl buffer adjusted to the same volume. Duplicate blank samples were prepared for each group of samples in the same way as the test solutions (i–iii). The obtained inhibition was calculated as a percent change of the control which involves the effect of appropriate amount of ethanol. Allopurinol was used as positive control. All experiments were performed in triplicate and averaged.

2.3. In vitro experiments on PBMC

Peripheral venous blood (350 ml) from 24 year old male healthy volunteer was drawn between 8 and 9 h into sterile heparinized tubes and was processed within 2 h. PBMC were isolated under sterile conditions by centrifugation in Ficoll Histopaque 1077 (Lymphoprep, Nycomed Pharma) according to the manufacturer instructions. Cell viability was above 90% using Trypan blue stain exclusion. After washing in PBS, obtained PBMC were resuspended in RPMI 1640 medium and 10% FCS.

2.4. Detection of NF-κB

All chemical were purchased from Sigma while the antibodies were purchased from Santa Cruz Biotechnology. Anti-inflamatory activity of **1** or **2**, diluted in appropriate amounts of ethanol (see Section 2.2.), was examined via determination of NF-κB, as described in our previous paper (Kocic et al., 2011). Washed PBMCs (each aliquot of 100 μl contained 10^5 cells) were distributed in 12-well plates and cultured for 4 h at 37 °C in 5% CO_2. The 50-μl aliquots of each sample were plated in 12 U-bottom 96-well culture plates. The cells were fixed by using 70% methanol and permeabilized with 0.1% Triton PBS. They were incubated with anti–NF-κB primary antibody (p65 C-20: sc-372 epitope mapping at the C-terminus of NF-κB p65), washed three times, and incubated with the FITC-conjugated secondary antibody. The mean fluorescence intensity (MFI; logarithmic scale) of cell populations was determined and analyzed on a Victor™ multiplate reader (Perkin Elmer-Wallace, Wellesley, MA). The results presented were obtained following subtraction of blank values treated with secondary antibodies only. The fluorescence intensity of cells indicated for both up or down regulating populations for each stimulus used, compared to intact PBMCs as well as to control samples with appropriate amounts of ethanol, and calculated as a percent change of the control PBMCs which involves the effect of appropriate amount of ethanol. All experiments were conducted with six repetitions and averaged.

2.5. Molecular docking

Molecular docking was carried out into the salicylic acid active site of XO (PDB entry code 1FIQ) using MOE software (Molecular Operating Environment, 2011). Water molecules from initial pdb were removed. Conformational search for preparation of the ligands was carried out by LowModelMD method which performs molecular dynamics perturbations along with low frequency vibrational modes with energy window 7 kCal/mol, and conformational limits of 1000. Placement of conformers was prepared according to alpha-triangle method on selected pharmacophores. Scoring of docking poses was performed by affinity dG, calculated with MMFF94x force field.

3. Results and discussion

3.1. Xanthine oxidase inhibition

1 or **2** were not substrates for XO when used instead of xanthine in reaction mixture. A significant inhibitory activity of two synthesized cyclodidepsipeptides on XO was observed to occur in a dose-dependent manner (Fig. 2).

2 exhibits more potent effects than **1**, and inhibits commercial bovine milk XO with an IC_{50} of about 0.2 μM (see dose of 42.9 ng/ml in Fig. 2), which is in the range of the allopurinol inhibitory activity towards XO (IC_{50} values of 0.2–50 μM) (Pacher et al., 2006).

The inhibitory activity of **1** and **2** on XO were further tested in rat liver homogenate and compared with allopurinol. **2** were found to be more active against rat liver XO than **1** (Fig. 3), which is in accordance with the inhibitory effect on activity of commercial bovine milk XO (Fig. 2). Allopurinol relevated stronger inhibitory effect than **1** and **2** in both tested concentrations (Fig. 3). However, allopurinol does have a number of serious side effects, and the cellular and molecular mechanisms of these side effects are incompletely understood. Some data indicate that the renal toxicity of allopurinol is related to impairment of pyrimidine metabolism (Horiuchi et al., 2000). There are no reliable or rapid screening tools that would predict the safety profile of novel XO inhibitors in terms of hypersensitivity reactions or organ toxicity; contact hypersensitivity mouse ear models and toxicity studies in rodents are being used to predict such side effects (Horiuchi et al., 1999). Intuitively, one would predict that novel XO inhibitors that would move away from the purine-based inhibitor structure may have fewer of the allopurinol-like side effects (of course, they may introduce new types of side effects or toxicities) (Pacher et al., 2006). Recently we have shown that **1** and **2** do not induce the toxicity and mitochondrial membrane potential decrease in rat thymocytes. The studied compounds do not trigger the significant intracellular reactive oxygen species production and exhibited antibacterial activity. The higher concentrations of **1** and **2** were able to stimulate proliferative activity of thymocytes, with mechanisms not yet known, indicating potential stimulatory effect on the cells of the immune system (Pavlovic et al., 2012). Therefore, **1** and **2** have potential to be used as novel XO inhibitors.

3.2. Rational design of xanthine oxidase inhibitors and molecular docking study

Recent studies on novel non-purine isosters of allopurinol (Okamoto et al., 2004; Nepali et al., 2011a,b) showed that consideration of certain structural features leads successfully to the development of new potent XO inhibitors. Those features should be designed to provide: (i) hydrophobic and hydrogen bonding interactions with enzyme; (ii) site for hydroxylation near the molybdenum metal; and (iii) non-purine skeleton to avoid unnatural nucleotide metabolites. It is also known that small molecules as salicylic acid could inhibit the enzyme without binding to the metal complex itself, only by blocking the approach of potential substrates toward the molybdenum (Enroth et al., 2000). For this reason it was thought worthwhile to test two synthesized cyclodidepsipeptides **1** and **2** for inhibitory activity against commercial enzyme XO *in vitro* as well as for anti-inflammatory response on PBMCs. Both compounds possess non-purine skeleton, alkyl and

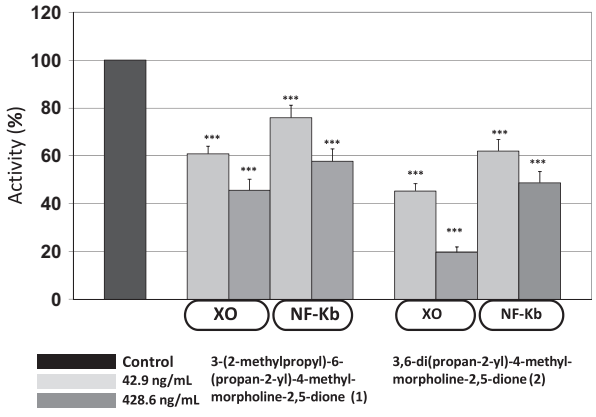


Fig. 2. Percentual dose-dependent effect of **1** and **2** on commercial bovine milk XO activity and PBMC NF-κB downregulation.

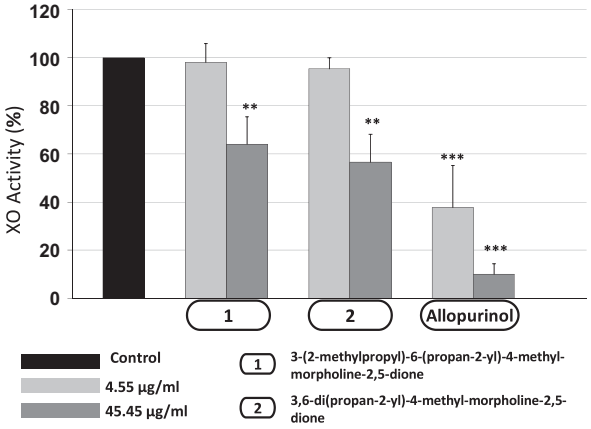


Fig. 3. Percentual dose-dependent effect of **1** and **2** on rat liver XO activity.

carbonyl groups that could provide favorable interactions with enzyme, and they could be potentially accommodated in the o/into the salicylic acid XO active site.

Considering the promising biological results, in order to examine the binding mode of **1** and **2** with XO, molecular docking was carried out into the salicylic acid active site of XO (PDB entry code 1FIQ) (Enroth et al., 2000). The docking conformations of **1** and **2** are shown in Figs. 4A and 5A.

Both ligands fit well in the active site pocket. Ligand **1** enters deeper in the cavity than **2** and has smaller exposure to the solvent. In case of **1** the ester carbonyl group has strong interaction with the dioxothiomolybdenum (MOS) moiety of molybdenum-pterin center (Fig. 4B). **2** is not directly interacting with MOS, but efficiently blocks the approach of potential substrates toward the metal. A number of lipophilic interactions with neighboring amino acid residues are stabilizing the ligand-pocket binding of both compounds (Figs. 4B and 5B).

The binding modes of **1** and **2** resemble those found by crystallographic studies on complexes of XO with inhibitors not forming a covalent bond with the molybdenum atom such as salicylic acid (Enroth et al., 2000) and febuxostat (Okamoto et al., 2003). It is known that the salicylic acid binds to the XO with the carboxylate atoms forming hydrogen bonds with Arg880 and Thr1010, the hydroxyl atom associated to Thr1010 also by hydrogen bonds, and the phenyl ring aligned parallel to the ring of Phe914 and perpendicular to the ring of Phe1009 (Fig. S1 in Supplementary materials). The binding of febuxostat in the enzyme involve interaction with similar amino acid residues.

As it could be seen from the 2D representations of the ligands in the pocket, introduction of protonodonor or acceptor groups in the side-chains of **1** and **2** could enhance further the interactions with the enzyme via hydrogen bonding and thus provide better inhibitor potency.

3.3. Anti-inflamatory activity

Compound **2** showed higher anti-inflammatory response on PBMCs, exerted through the NF-κB inhibition, than compound **1**. The activation of NF-κB is a double-edged sword. While needed for proper immune system function, inappropriate NF-κB activation can mediate inflammation and tumorigenesis. That duality is especially striking in relation to cancer, a proinflammatory disease (Balkwill and Mantovani, 2001). Extensive research over the last few years has shown that most inflammatory agents mediate their effects through the activation of NF-κB, with the expression of proinflammatory genes. Inhibition of NF-κB at the onset of inflammation leads to decreased inflammatory response (Lee et al., 2008).

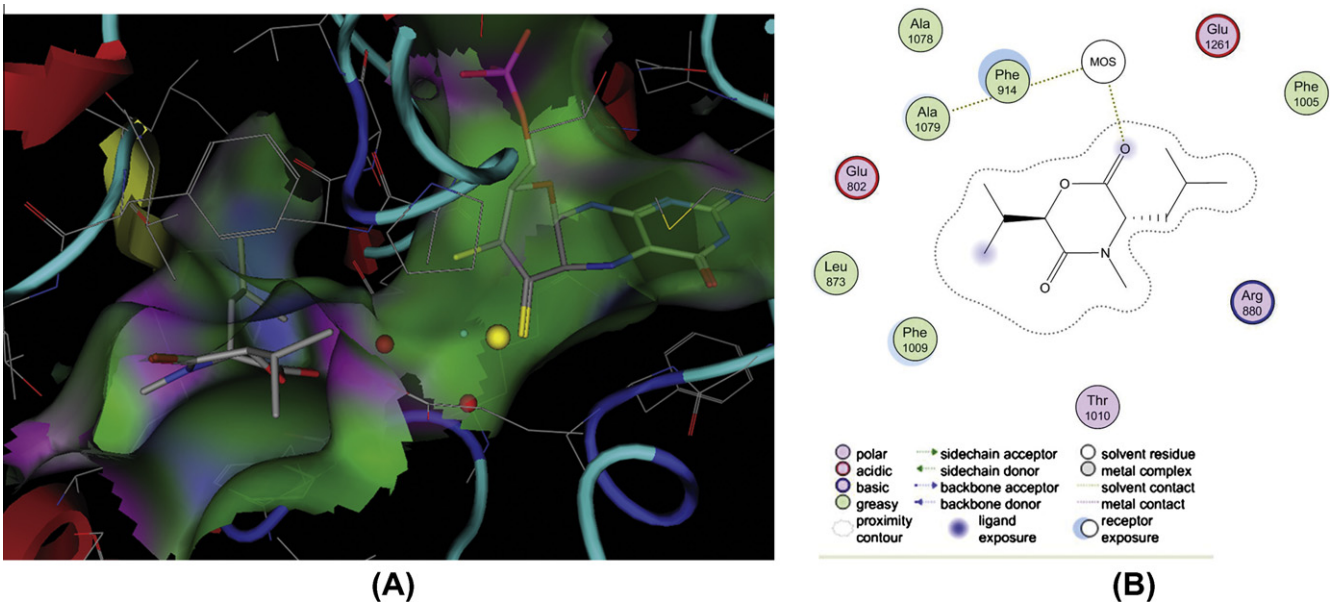


Fig. 4. Docking conformation of **1** (A) and 2D representation of the ligand interactions (B) in the pocket.

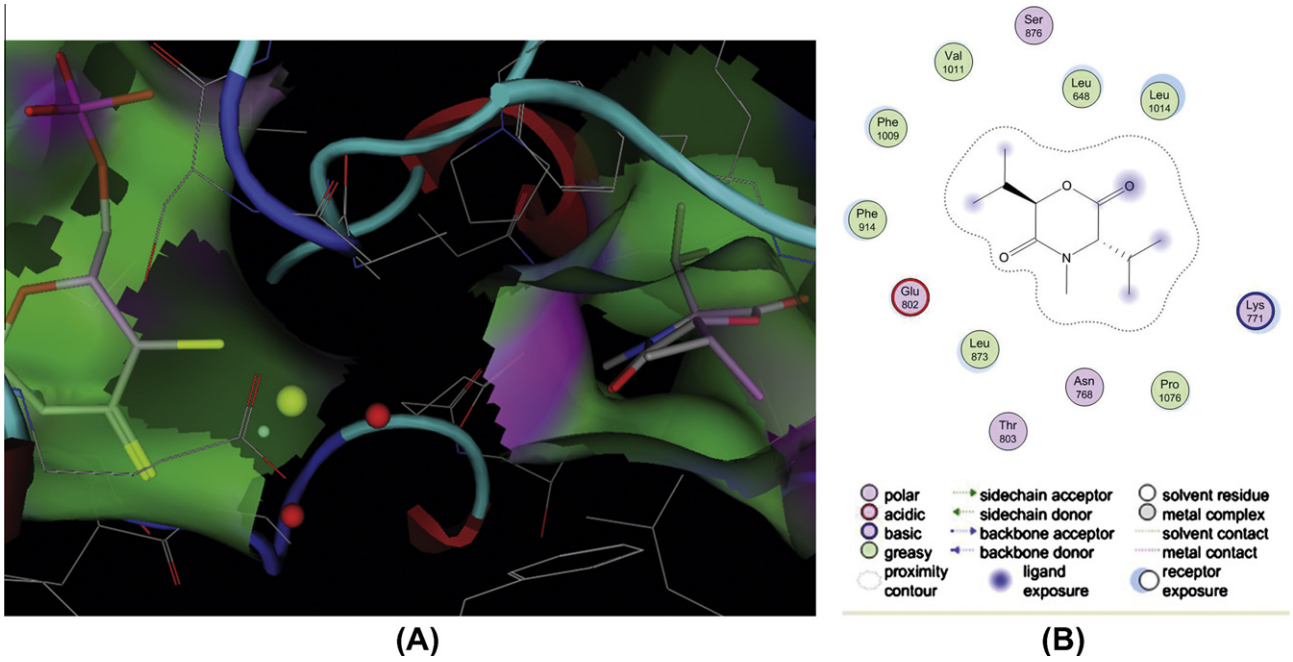


Fig. 5. Docking conformation of **2** (A) and 2D representation of the ligand interactions (B) in the pocket.

The urate crystals are capable of up-regulating effect and are capable of activating MyD88, the extracellular signal-regulated kinase 1 and 2 (ERK1/2), leading to NF-κB activation (Jaramillo et al., 2004a,b). These findings showed that two studied cyclodidepsipeptides suppress the NF-κB activation in a dose-dependent manner and suggest that **1** and **2** can show anti-inflammatory effects.

4. Conclusions

Two cyclodidepsipeptides, **1** and **2**, were documented to be the novel XO inhibitors. Based on molecular docking study, the binding modes of **1** and **2** with XO were clarified and recommendations for future structure-guided design of new morpholine-dione inhibitors of XO were drawn. Allopurinol were found to be more active against rat liver XO than **1** and **2**. The effect of **1** and **2** on antiinflammatory cascade was observed by testing the NF-κB response on PBMCs and a significant NF-κB downregulation was observed to occur in a dose-dependent manner. Both **1** and **2** were tested and confirmed as non-toxic in thymocytes (Pavlovic et al., 2012) so that studied morpholine-diones derivatives exerting XO inhibition and anti-inflammatory effect may give a promise to be used in the treatment of gout and other excessive uric acid production or inflammatory conditions. The *in vivo* study will be part of our further investigation, which will elucidate possibility of application of this novel class of non-purine XO inhibitors in therapy.

Conflict of Interest

The authors declare that there are no conflicts of interest.

Acknowledgements

The financial support of this work by Ministry of Science and Technological Development of Serbia (Projects OI 172044 and TR 31060) and National Science Fund of Bulgaria (young researchers project DMU-03/66) is gratefully acknowledged.

Appendix A. Supplementary material

Supplementary data associated with this article can be found, in the online version, at http://dx.doi.org/10.1016/j.fct.2013.01.052.

References

Balkwill, F., Mantovani, A., 2001. Inflammation and cancer: back to Virchow? Lancet 357, 539–545.

Burns, C.M., Wortmann, R.L., 2011. Gout therapeutics: new drugs for an old disease. Lancet 377, 165–177.

Enroth, C., Eger, B.T., Okamoto, K., Nishino, T., Nishino, T., Pai, E.F., 2000. Crystal structures of bovine milk xanthine dehydrogenase and xanthine oxidase: structure-based mechanism of conversion. Proc. Natl. Acad. Sci. USA 97, 10723–10728.

Horiuchi, H., Ota, M., Kitahara, S., Ohta, T., Kiyoki, M., Komoriya, K., 1999. Allopurinol increases ear swelling and mortality in a dinitrofluorobenzene-induced contact hypersensitivity mouse model. Biol. Pharm. Bull. 22, 810–815.

Horiuchi, H., Ota, M., Nishimura, S., Kaneko, H., Kasahara, Y., Ohta, T., Komoriya, K., 2000. Allopurinol induces renal toxicity by impairing pyrimidine metabolism in mice. Life Sci. 66, 2051–2070.

Jaramillo, M., Naccache, P.H., Olivier, M., 2004a. Monosodium urate crystals synergize with IFN-γ to generate macrophage nitric oxide: involvement of extracellular signal-regulated kinase 1/2 and NF-κB. J. Immunol. 172, 5734–5742.

Jaramillo, M., Godbout, M., Naccache, P.H., Olivier, M., 2004b. Signaling events involved in macrophage chemokine expression in response to monosodium urate crystals. J. Biol. Chem. 279, 52797–52805.

Kizaki, H., Sakurada, T., 1977. Simple micro assay methods for enzymes of purine metabolism. J. Lab. Clin. Med. 89, 1135–1144.

Kocic, G., Pavlovic, R., Najman, S., Nikolic, G., Sokolovic, D., Jevtovic-Stoimenov, T., Musovic, D., Veljkovic, A., Kocic, R., Djindjic, N., 2011. Circulating ribonucleic acids and metabolic stress parameters may reflect progression of autoimmune or inflammatory conditions in juvenile type 1 diabetes. ScientificWorldJournal 11, 1496–1508.

Lee, J.M., Hwang, K.T., Jun, W.J., Park, C.S., Lee, M.Y., 2008. Antiinflammatory effect of lactic acid bacteria: inhibition of cyclooxygenase-2 by suppressing nuclear factor-kappaB in Raw264.7 macrophage cells. J. Microbiol. Biotechnol. 18, 1683–1688.

Molecular Operating Environment (MOE), 2011. 10; Chemical Computing Group Inc., 1010 Sherbooke St. West, Suite #910, Montreal, QC, Canada, H3A 2R7, 2011.

Nepali, K., Singh, G., Turan, A., Agarwal, A., Sapra, S., Kumar, R., Banerjee, U.C., Verma, P.K., Satti, N.K., Gupta, M.K., Suri, O.P., Dhar, K.L., 2011a. A rational approach for the design and synthesis of 1-acetyl-3,5-diaryl-4,5-dihydro(1H)pyrazoles as a new class of potential non-purine xanthine oxidase inhibitors. Bioorg. Med. Chem. 19, 1950–1958.

Nepali, K., Agarwal, A., Sapra, S., Mittal, V., Kumar, R., Banerjee, U.C., Gupta, M.K., Satti, N.K., Suri, O.P., Dhar, K.L., 2011b. N-(1,3-Diaryl-3-oxopropyl)amides as a new template for xanthine oxidase inhibitors. Bioorg. Med. Chem. 19, 5569–5576.

Okamoto, K., Eger, B.T., Nishino, T., Kondo, S., Pai, E.F., Nishino, T., 2003. An extremely potent inhibitor of xanthine oxidoreductase. Crystal structure of the enzyme-inhibitor complex and mecanism of inhibition. J. Biol. Chem. 278, 1848–1855.

Okamoto, K., Matsumoto, K., Hille, R., Eger, B.T., Pai, E.F., Nishino, T., 2004. The crystal structure of xanthine oxidoreductase during catalysis: implications for reaction mechanism and enzyme inhibition. Proc. Natl. Acad. Sci. USA 101, 7931–7936.

Pacher, P., Nivorozhkin, A., Szabo, C., 2006. Therapeutic effects of xanthine oxidase inhibitors: renaissance half a century after the discovery of allopurinol. Pharmacol. Rev. 58, 87–114.

Pahl, H.L., 1999. Activators and target genes of Rel/NF-kappaB transcription factors. Oncogene 18, 6853–6866.

Pavlovic, V., Djordjevic, A., Cherneva, E., Yancheva, D., Smelcerovic, A., 2012. Stimulatory effect on rat thymocytes proliferation and antimicrobial activity of two 6-(propan-2-yl)-4-methyl-morpholine-2,5-diones. Food Chem. Toxicol. 50, 761–766.

Sarabia, F., Chammaa, S., Sanchez Ruiz, A., Martin Ortiz, L., Lopez Herrera, F.J., 2004. Chemistry and biology of cyclic depsipeptides of medicinal and biological interest. Curr. Med. Chem. 11, 1309–1332.

Sen, R., Baltimore, D., 1986. Inducibility of kappa immunoglobulin enhancer-binding protein Nf-kappa B by a posttranslational mechanism. Cell 47, 921–928.

Smelcerovic, A., Yancheva, D., Cherneva, E., Petronijevic, Z., Lamshoeft, M., Herebian, D., 2011. Identification and synthesis of three cyclodidepsipeptides as potential precursors of enniatin B in *Fusarium sporotrichioides*. J. Mol. Struct. 985, 397–402.

Veljkovic, A.R., Nikolic, R.S., Kocic, G.M., Pavlovic, D.D., Cvetkovic, T.P., Sokolovic, D.T., Jevtovic, T.M., Basic, J.T., Laketic, D.M., Marinkovic, M.R., Stojanovic, S.R., Djordjevic, B.S., Krsmanovic, M.M., 2012. Protective effects of glutathione and lipoic acid against cadmium-induced oxidative stress in rat's kidney. Renal Fail. 34, 1281–1287.

ResearchGate

See discussions, stats, and author profiles for this publication at: https://www.researchgate.net/publication/292391813

Inhibition mechanism and molecular modeling studies of the interactions of 6-(propan-2-yl)-3-methyl-morpholine-2,5-dione with xanthine oxidase

Article *in* Izvestiya po Khimiya Bulgarska Akademiya na Naukite · January 2015

CITATIONS
2

READS
65

8 authors, including:



Miroslav Rangelov
Bulgarian Academy of Sciences
26 PUBLICATIONS **177** CITATIONS
SEE PROFILE

Emiliya Cherneva
Medical University of Sofia
24 PUBLICATIONS **129** CITATIONS
SEE PROFILE



Sonja Kosta Stojanovic
University of Niš
59 PUBLICATIONS **93** CITATIONS
SEE PROFILE

Tatjana Jevtovic-Stoimenov
University of Niš
187 PUBLICATIONS **821** CITATIONS
SEE PROFILE

Some of the authors of this publication are also working on these related projects:

IR study on protein secondary structure View project

Evaluation of hypertensive left ventricular hypertrophy View project

All content following this page was uploaded by Denitsa Yancheva on 12 March 2016.

The user has requested enhancement of the downloaded file.

Bulgarian Chemical Communications, Volume 47, Number 3 (pp. 783 – 787) 2015

Inhibition mechanism and molecular modeling studies of the interactions of 6-(propan-2-yl)-3-methyl-morpholine-2,5-dione with xanthine oxidase

Ž. Šmelcerović[1]*, M. Rangelov[2], E. Cherneva[3], G. Kocić[4], S. Stojanović[4], T. Jevtović-Stoimenov[1,4], Ž. Petronijević[5], D. Yancheva[2]

[1]*Center for Biomedicinal Science, Faculty of Medicine, University of Niš, Bulevar Dr Zorana Djindjica 81, 18000 Niš, Serbia*

[2]*Institute of Organic Chemistry with Centre of Phytochemistry, Bulgarian Academy of Sciences, Acad. G. Bonchev Str., Build. 9, 1113 Sofia, Bulgaria*

[3]*Faculty of Pharmacy, Medical University of Sofia, 2 Dunav Str., 1000 Sofia, Bulgaria*

[4]*Institute of Biochemistry, Faculty of Medicine, University of Niš, Bulevar Dr Zorana Djindjica 81, 18000 Niš, Serbia*

[5]*Faculty of Technology, University of Niš, Bulevar Oslobodjenja 124, 16000 Leskovac, Serbia*

Received April 11, 2014, Revised April 27, 2015

Xanthine oxidase (XO) is an enzyme which catalyzes oxidation of hypoxanthine to xanthine and then to uric acid, and plays a key role in hyperuricemia. The inhibition of XO activity in rat liver homogenate by 6-(propan-2-yl)-3-methyl-morpholine-2,5-dione (**1**) was evaluated and compared with that of two previously studied cyclodidepsipeptides, 3,6-di(propan-2-yl)-4-methyl-morpholine-2,5-dione (**2**) and 3-(2-methylpropyl)-6-(propan-2-yl)-4-methyl-morpholine-2,5-dione (**3**), and allopurinol. Compound **1** showed significant inhibitory activity against rat liver XO (IC_{50} = 49.82 μg/mL), comparable with the activity of **2** and **3**. Allopurinol, a widely used XO inhibitor and drug to treat gout, exhibited a stronger inhibitory effect on rat liver XO than **1**-**3**. Compound **1** was synthesized as a mixture of two diastereoisomers, (*3S,6R*) and (*3S,6S*), and molecular docking studies were performed to gain an insight into their binding modes with XO. Lineweaver–Burk plot analysis of the inhibition kinetics data demonstrated that the studied compound (**1**) was a competitive inhibitor of XO. Both forms of **1** bind in the entrance of the narrow tunnel towards the dioxothiomolybdenum moiety of the active center of XO, blocking in this way the approach of the substrates toward the metal atom.

Keywords: inhibition kinetics; molecular modeling; 6-(propan-2-yl)-3-methyl-morpholine-2,5-dione; xanthine oxidase inhibition.

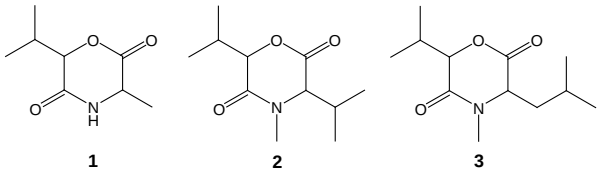
INTRODUCTION

Cyclodidepsipeptides are the simplest ones in the cyclodepsipeptide family containing one residue of amino acid and one residue of lactic, α-hydroxyisovaleric or other α-hydroxy acid. There are reports on their antioxidant [1], antimicrobial [2,3] and immunomodulatory [2,4,5] activities, as well as inhibitory activities towards acyl-CoA:cholesterol acyltransferase [6], α-glucosidase [7-9] and platelet aggregation [10]. Recently, we synthesized a novel cyclodidepsipeptide, 6-(propan-2-yl)-3-methyl-morpholine-2,5-dione (**1**; $C_8H_{13}NO_3$, M = 171.19) (Scheme 1), containing an alanine moiety [3]. Xanthine oxidase (XO) is a key enzyme which can catalyze oxidation of xanthine to uric acid causing hyperuricemia in humans [11] and recently, we evaluated two synthetic cyclodidepsipeptides 3,6-di-(propan-2-yl)-4-methyl-morpholine-2,5-dione (**2**; $C_{11}H_{19}NO_3$, M = 213.27) and 3-(2-methylpropyl)-6-(propan-2-yl)-4-methyl-morpholine-2,5-dione (**3**; $C_{12}H_{21}NO_3$, M = 227.30) [12] for inhibitory activity against commercial enzyme XO *in vitro* and XO in rat liver homogenate as well as anti-inflammatory response on human peripheral blood mononuclear cells (PBMCs) [13]. The two cyclodidepsipeptides were excellent inhibitors of XO and significantly suppressed the nuclear factor of κB (NF-κB) activation. Based on molecular docking study, the binding modes of **2** and **3** with XO were clarified and recommendations for future structure-guided design of new morpholine-dione inhibitors of XO were drawn [13].

In this paper, we investigated the inhibition of xanthine oxidase (XO) activity in rat liver homogenate by compound **1** and compared with that by cyclodidepsipeptides **2** and **3**, as well as allopurinol, a widely used XO inhibitor and drug to treat gout. Inhibition kinetics of compound **1** with XO was studied in order to determine the type of enzyme inhibition, while the molecular docking studies were performed in order to examine the binding mode of **1** with XO.

* To whom all correspondence should be sent:
E-mail: zsmelcerovic@yahoo.com

© 2015 Bulgarian Academy of Sciences, Union of Chemists in Bulgaria



Scheme 1. Chemical structure of cyclodidepsipeptides **1**-**3**

EXPERIMENTAL

Evaluation of xanthine oxidase inhibition

Inhibition of XO activity in rat liver homogenate was evaluated using a spectrophotometric method [14], by measuring uric acid formation at 293 nm. The reaction mixture (volume 2200 μL) was prepared by allocating the following test sample groups: i) Test sample group contained 100 μL of 10 % rat liver homogenate, one of the studied compounds (**1**-**3**) diluted in DMSO (the final concentration of DMSO in the assay was 4.55 % v/v), 454.5 μM of xanthine (Serva), and 45.5 mM TRIS-HCl buffer (pH 7.8); ii) Solvent control group contained the same amount of rat liver homogenate, appropriate amount of DMSO, xanthine and TRIS-HCl buffer; iii) Control group contained the same amount of rat liver homogenate, xanthine and TRIS-HCl buffer adjusted to the same volume. Corresponding blank samples were prepared for each group in the same way as the test solutions (i-iii). The obtained inhibition was calculated as a percent change of the control which involves the effect of appropriate amount of DMSO. All samples were assayed for XO inhibitory activity at concentration of 50 μg/mL. Those showing greater than 50 % inhibition at this concentration were tested further to ascertain the corresponding IC_{50} values. IC_{50} curves were generated using three concentrations of studied compounds (50, 40 and 25 μg/mL). Allopurinol was used as positive control. All experiments were performed in triplicate and averaged.

Lineweaver–Burk plots

To determine the mode of inhibition by compound **1**, Lineweaver–Burk plot analysis was performed. This kinetics study was carried out in the absence and presence of the inhibitor with varying concentrations of xanthine as the substrate. Commercial bovine milk XO, purchased from Sigma-Aldrich, was employed for *in vitro* evaluation of enzyme inhibition. The inhibition was studied in a series of test-tubes with the reaction mixture (total volumen 2150 μL) containing 0.01 units of XO and 46.5 mM TRIS-HCl buffer (pH 7.8). Xanthine concentration was varied (0, 18.6, 46.5, 93, 232.5 or 930 μM) at three series of fixed concentrations of compound **1** (0, 13.6 and 54.4 μM). Amount of generated uric acid formation was measured at 293 nm.

Molecular docking

Molecular docking was carried out into the salicylic acid active site of XO (PDB entry code 1FIQ) using MOE software [15]. Water molecules from initial pdb were removed. Conformational search for preparation of the ligands was carried out by LowModelMD method which performs molecular dynamics perturbations along with low frequency vibrational modes with energy window 7 kCal/mol, and conformational limits of 1000. Placement of conformers was prepared according to alpha-triangle method on selected pharmacophores. Docking was done using the induced-fit docking protocol allowing the side-chain and backbone movement in the receptor to accommodate the ligand. Scoring of docking poses was performed by affinity dG, calculated with MMFF94x force field.

RESULTS AND DISCUSSION

Compound **1** showed a significant inhibitory activity against rat liver XO (IC_{50} = 49.82 μg/mL (291 μM)), comparable with activity of **2** (IC_{50} = 41.88 μg/mL (196 μM)) and **3** (IC_{50} = 46.66 μg/mL (205 μM)). As cyclodidepsipeptides **1**-**3** have a common part of the structure (6-(propan-2-yl)-morpholine-2,5-dione core), it can be concluded that the presence of isopropyl groups at position 3 and a methyl group at position 4 of morpholine ring (structural characteristics of compound **2**) are more favorable for XO inhibition then the presence of isobutyl group at position 3 and a methyl group at position 4 of morpholine ring (structural characteristics of compound **3**) or the presence of a methyl group at position 3 and the absence of substituents at position 4 of morpholine ring (structural characteristics of compound **1**).

Allopurinol (IC_{50} = 0.79 μg/mL (5.8 μM)), a widely used XO inhibitor and drug to treat gout, exhibited stronger inhibitory effect on rat liver XO than **1**-**3**. However, allopurinol does have a number of serious side effects, and the cellular and molecular mechanisms of these side effects are incompletely understood. Some data indicate that the renal toxicity of allopurinol is related to impairment of pyrimidine metabolism [16]. There are no reliable or rapid screening tools that would predict the safety profile of novel XO inhibitors in terms of hypersensitivity reactions or organ toxicity; contact hypersensitivity mouse ear models and toxicity studies in rodents are being used to predict such side effects [17]. Intuitively, one

would predict that novel XO inhibitors that would move away from the purine-based inhibitor structure may have fewer of the allopurinol-like side effects (of course, they may introduce new types of side effects or toxicities) [18]. In the recent literature there are data on non-purine XO inhibitors [19-22].

We also determined the type of enzyme inhibition. The related inhibition type of the title compound on XO was identified from Lineweaver–Burk plots (Fig. 1). The compound **1** was a competitive inhibitor of XO.

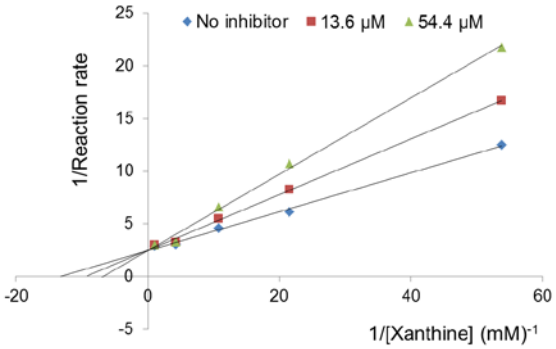


Fig. 1. Lineweaver–Burk plots for the inhibition of xanthine oxidase by compound **1** with xanthine as substrate (see the Methods and Materials section for details)

The interaction of the inhibitor with the XO was studied also by molecular docking into the salicylic acid active site of the bovine milk enzyme (PDB entry code 1FIQ) [23]. Based on recent spectral and computational studies, it is known that the keto form of the title compound is much more energetically favored than the corresponding enol form. The reported NMR and IR data show no evidences for enol formation neither in polar nor in nonpolar medium (3). For this reason only the keto forms of the two diastereoisomers of **1**, (*3S,6R*) and (*3S,6S*), were taken into consideration in the molecular docking studies. The docking poses of the ligands **1**(*3S,6R*) and **1**(*3S,6S*), are presented in Fig. 2.

Both forms of **1** bind in the entrance of the narrow tunnel towards the dioxothiomolybdenum moiety of the active center of XO, blocking in this way the approach of the substrates toward the metal atom (Fig. 2). As can be seen from the 2D 2D representation of the ligand interactions in the pocket (Fig. 3), the ligand-pocket binding of both diastereoisomers is stabilized via hydrogen bonds with Thr1010 and Arg880 and a number of lipophilic interactions with neighboring amino acid residues. In the case of **1**(*3S,6R*) the hydrogen bond is formed between the amide O-atom and Thr1010, while **1**(*3S,6S*) interacts with Thr1010 and Arg880 through its ester carbonyl group (Fig. 3). **1**(*3S,6S*) enters deeper in the cavity. The molecular interactions of title compound to XO resemble those found by crystallographic studies on complexes of XO with other inhibitors not forming a covalent bond with the molybdenum atom such as salicylic acid [23] and febuxostat [24]. These results demonstrate that both diastereoisomers have good binding capacity toward the XO.

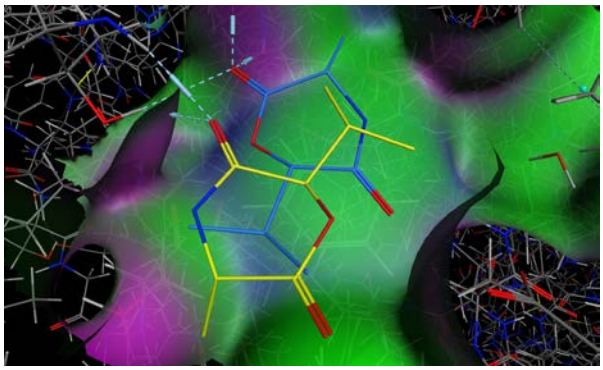


Fig. 2. Docking poses of: **1**(*3S,6R*) - yellow carbons; **1**(*3S,6S*) - blue carbons

1(*3S,6R*) **1**(*3S,6S*)

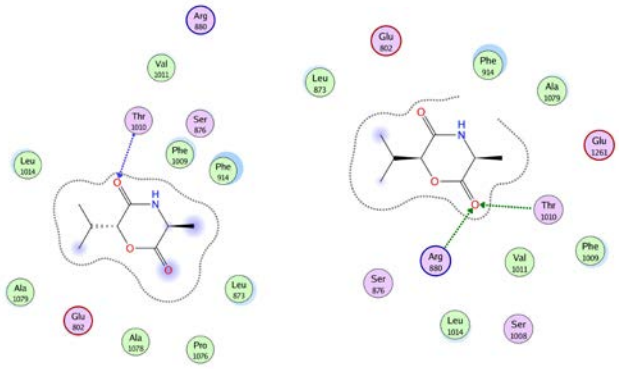


Fig. 3. 2D representation of the ligand interactions in the pocket.

CONCLUSIONS

Cyclodidepsipeptide **1** showed a potent inhibitory effect on XO in a competitive mode. Both diastereoisomers, **1**(*3S,6R*) and **1**(*3S,6S*), bind in the entrance of the narrow tunnel towards the dioxothiomolybdenum moiety of the active center of XO, blocking in this way the approach of the substrates toward the metal atom. Allopurinol was found to be more active against rat liver XO than **1-3.** Chronic allopurinol administration for the inhibition of XO is clinically effective against the hyperuricemia associated with gout, but undesirable side effects have prompted efforts to isolate or synthesise other types of XO inhibitors [25]. Therefore, the results of this study as well as results of our previous study [13] may suggest that 6-(propan-2-yl)-morpholine-2,5-diones are likely to be adopted as candidates to treat gout and may be

taken for further evaluation by using *in vivo* studies. The synthesis of new morpholine-diones derivatives as well as evaluation of their potential for inhibition of XO activity will be part of our further investigation.

Acknowledgements: *The financial support of this work by National Science Fund of Bulgaria (Contract DMU-03/66) and Ministry of Science and Technological Development of Serbia (Projects OI 172044 and TR 31060) is gratefully acknowledged.*

REFERENCES

1. V. Stankov-Jovanovic, J.C. Tabet, P. Dzodic, L. Daskalova, E. Cherneva, D. Yancheva, A. Smelcerovic, *Acta Chim. Slov.*, **59**, 939 (2012).
2. V. Pavlovic, A. Djordjevic, E. Cherneva, D. Yancheva, A. Smelcerovic, *Food Chem. Toxicol.*, **50**, 761 (2012).
3. D. Yancheva, L. Daskalova, E. Cherneva, B. Mikhova, A. Djordjevic, Z. Smelcerovic, A. Smelcerovic, *J. Mol. Struct.*, **1016**, 147 (2012).
4. M. Iijima, T. Masuda, H. Nakamura, H. Naganawa, S. Kurasawa, Y. Okami, M. Ishizuka, T. Takeuchi, Y. Iitaka, *J. Antibiot.*, **45**, 1553 (1992).
5. V. Pavlovic, E. Cherneva, D. Yancheva, A. Smelcerovic, *Food Chem. Toxicol.*, **50**, 3014 (2012).
6. K. Hasumi, C. Shinohara, T. Iwanaga, A. Endo, *J. Antibiot.*, **46**, 1782 (1993).
7. A. Arcelli, D. Balducci, A. Grandi, G. Porzi, M. Sandri, S. Sandri, *Monatsh. Chem.*, **135**, 951 (2004).
8. A. Arcelli, D. Balducci, A. Grandi, G. Porzi, M. Sandri, S. Sandri, *Tetrahedron: Asymmetry*, **16**, 1495 (2005).
9. A. Arcelli, D. Balducci, S.F.E. Neto, G. Porzi, M. Sandri, *Tetrahedron: Asymmetry*, **18**, 562 (2007).
10. T. Kagamizono, E. Nishino, K. Matsumoto, A. Kawashima, M. Kishimoto, N. Sakai, B.-M. He, Z.-X. Chen, T. Adachi, S. Morimoto, K. Hanada, *J. Antibiot.*, **48**, 1407 (1995).
11. J.-F. Hsieh, S.-H. Wu, Y.-L. Yang, K.-F. Choong, S.-T. Chen, *Bioorg. Med. Chem.*, **15**, 3450 (2007).
12. A. Smelcerovic, D. Yancheva, E. Cherneva, Z. Petronijevic, M. Lamshoeft, D. Herebian, *J. Mol. Struct.*, **985**, 397 (2011).
13. A. Smelcerovic, M. Rangelov, Z. Smelcerovic, A. Veljkovic, E. Cherneva, D. Yancheva, G.M. Nikolic, Z. Petronijevic, G. Kocic, *Food Chem. Toxicol.*, **55**, 493 (2013).
14. Z. Smelcerovic, A. Veljkovic, G. Kocic, D. Yancheva, Z. Petronijevic, M. Anderluh, A. Smelcerovic, *Chem.-Biol. Interact.*, **229**, 73 (2015).
15. Molecular Operating Environment (MOE), 2011.10; Chemical Computing Group Inc., 1010 Sherbooke St. West, Suite #910, Montreal, QC, Canada, H3A 2R7, 2011.
16. H. Horiuchi, M. Ota, S. Nishimura, H. Kaneko, Y. Kasahara, T. Ohta, K. Komoriya *Life Sci.*, **66**, 2051 (2000).
17. H. Horiuchi, M. Ota, S. Kitahara, T. Ohta, M. Kiyoki, K. Komoriya, *Biol. Pharm. Bull.*, **22**, 810 (1999).
18. P. Pacher, A. Nivorozhkin, C. Szabo, *Pharmacol. Rev.*, **58**, 87 (2006).
19. K. Nepali, G. Singh, A. Turan, A. Agarwal, S. Sapra, R. Kumar, U.C. Banerjee, P.K. Verma, N.K. Satti, M.K. Gupta, O.P. Suri, K.L. Dhar, *Bioorg. Med. Chem.*, **19**, 1950 (2011).
20. K. Nepali, A. Agarwal, S. Sapra, V. Mittal, R. Kumar, U.C. Banerjee, M.K. Gupta, N.K. Satti, O.P. Suri, K.L. Dhar, *Bioorg. Med. Chem.*, **19**, 5569 (2011).
21. S. Sharma, K. Sharma, R. Ojha, D. Kumar, G. Singh, K. Nepali, P.M.S. Bedi, *Bioorg. Med. Chem. Lett.*, **24**, 495 (2014).
22. H. Singh, S. Sharma, R. Ojha, M.K. Gupta, K. Nepali, P.M.S. Bedi, *Bioorg. Med. Chem. Lett.*, **24**, 4192 (2014).
23. C. Enroth, B.T. Eger, K. Okamoto, T. Nishino, T. Nishino, E.F. Pai, *Proc. Natl. Acad. Sci. USA*, **97**, 10723 (2000).
24. K. Okamoto, B.T. Eger, T. Nishino, S. Kondo, E.F. Pai, T. Nishino, *J. Biol. Chem.*, **278**, 1848 (2003).
25. F. Borges, E. Fernandes, F. Roleira, *Curr. Med. Chem.*, **9**, 195 (2002).

МЕХАНИЗМИ НА ИНХИБИРАНЕ И МОЛЕКУЛНО МОДЕЛИРАНЕ НА НА ВЗАИМОДЕЙСТВИЯТА НА 6-(ПРОПАН-2-ИЛ)-3-МЕТИЛ-МОРФОЛИН-2,5-ДИОН С КСАНТИН ОКСИДАЗА

Ж. Шмелцерович[1]*, М. Рангелов[2], Е. Чернева[3], Г. Коцич[4], С. Стоянович[4], Т. Йевтович-Стоименов[1,4], Ж. Петрониевич[5], Д. Янчева[2]

[1]*Център за биомедицински науки, Медицински факултет, Университет в Ниш, Сърбия*
[2]*Институт по органична химия с Център по фитохимия, Българска академия на науките, 1113 София, България*
[3]*Факултет по фармация, Медицински университет в София, 1000 София, България*
[4]*Институт по биохимия, Медицински факултет, Университет в Ниш, Сърбия*
[5]*Технологичен факултет, Университет в Ниш, Сърбия*

Постъпила на 11 април2014 г.; коригирана на 27 април, 2015 г.

(Резюме)

Ксантин оксидазата (XO) е ензим, катализиращ окислението на хипоксантина до ксантин, а след това до пикочна киселина. С това той има ключова роля при хиперурицемията. Оценено е инхибирането на активността на XO в препарат от черен дроб на плъхове чрез 6-(пропан-2-ил)-3-метил-морфолин-2,5-дион (**1**) и е сравнено с това на две по-рано изследвани цикло-дипепсипептиди: 3,6-ди(пропан-2-ил)-4-метил-морфолин-2,5-дион (**2**) и 3-(2-метилпропил)-6-(пропан-2-ил)-4-метил-морфолин-2,5-дион (**3**) и алопуринол. Съединението **1** показва значителна инхибираща активност спрямо XO от плъхове (IC_{50} = 49.82 μg/mL), сравнима с активността на **2** и **3**. Алопуринолът, като широко използван инхибитор на XO и лекарство за лечение на подагра проявява по-силен инхибиращ ефект върху XO от съединенията **1**-**3**. Съединенията **1** са синтезирани като смес от два диастереоизомера (*3S,6R*) и (*3S,6S*). Молекулно моделиране е приложено за да даде поглед върху връзките им с ензимните активни центрове. Обработката на данните с помощта на координатите на Lineweaver–Burk показват, че съединение (**1**) е конкурентен инхибитор на XO. Двете форми на **1** се свързват с входа на тесен „тунел“ към диоксо-тиомолибденовата половина на активния център на XO, блокирайки по този начин достъпа на субстратите до металния атом.

View publication stats

ResearchGate

See discussions, stats, and author profiles for this publication at: https://www.researchgate.net/publication/274008725

CHEMICAL ANALYSIS OF ORGANIC RESIDUES FOUND IN HELLENISTIC TIME AMPHORAE FROM SE BULGARIA ХИМИЧЕСКИЙ АНАЛИЗ ОРГАНИЧЕСКИХ ОСТАТКОВ ИЗ АМФОР ЭЛЛИНИСТИЧЕСКОЙ ЭПОХИ, НАЙДЕННЫХ ….

Article *in* Journal of Applied Spectroscopy · May 2015

DOI: 10.1007/s10812-015-0089-9

CITATIONS
6

READS
83

2 authors:



Boika Zlateva
Sofia University "St. Kliment Ohridski"
22 PUBLICATIONS **71** CITATIONS
SEE PROFILE



Miroslav Rangelov
Bulgarian Academy of Sciences
26 PUBLICATIONS **177** CITATIONS
SEE PROFILE

Some of the authors of this publication are also working on these related projects:

CHEMICAL CONTENT OF THE BUCKLES FROM THE TIME OF THE GREAT MIGRATION OF PEOPLES View project

All content following this page was uploaded by Boika Zlateva on 25 March 2015.

The user has requested enhancement of the downloaded file.

CHEMICAL ANALYSIS OF ORGANIC RESIDUES FOUND IN HELLENISTIC TIME AMPHORAE FROM SE BULGARIA

B. Zlateva [1*], M. Rangelov [2]

[1] University of Sofia, J. Bauchier 1 blvd, Sofia 1164, Bulgaria;e-mail: ahbz@chem.uni-sofia.bg
[2] Institute of Organic Chemistry with Centre of Phytochemistry, Bulgarian Academy of Science, Sofia, Bulgaria

We have used IR spectroscopy, ^{1}H NMR spectroscopy, high-performance liquid chromatography and thin-layer chromatography to study the composition of resin residues found in 22 amphorae from Apollonia Pontika (SE Bulgaria). In particular this analysis of the resin residues was aimed at discovering the content of the amphorae and to verify the hypothesis on the transport of wine, named "Retsina". Additionally this hypothesis has been confirmed by a similar analysis of the modern resin sample from Aleppo pine (Pinus Halepensis) growing in the Attica region (Greece).

Keywords: *ancient resin residue, IR and NMR spectra, high-performance liquid chromatography, thin-layer chromatography, Hellenistic time amphorae, wine.*

ХИМИЧЕСКИЙ АНАЛИЗ ОРГАНИЧЕСКИХ ОСТАТКОВ ИЗ АМФОР ЭЛЛИНИСТИЧЕСКОЙ ЭПОХИ, НАЙДЕННЫХ НА ЮГО-ВОСТОКЕ БОЛГАРИИ

B. Zlateva [1*], M. Rangelov [2]

УДК 543.544

[1] Софийский университет,
1164, София, бульв. Дж. Баучиера, 1, Болгария; e-mail: ahbz@chem.uni-sofia.bg
[2] Институт органической химии с центром фитохимии Болгарской академии наук, София, Болгария

(Поступила 22 мая 2014)

Методами ИК спектроскопии, ядерного магнитного резонанса, а также высокоэффективной жидкостной и тонкослойной хроматографии исследован состав остатков смолы из 22 амфор, найденных в Аполлония Понтика на юго-востоке Болгарии, с целью получения сведений о содержимом амфор и проверки гипотезы о транспортировке вина марки "Рецина". Гипотеза дополнительно подтверждена результатами аналогичного анализа образцов современной смолы сосны Алеппо (Pinus Halepensis), растущей в регионе Аттика (Греция).

Ключевые слова: *остаток древней смолы, ИК- и ЯМР-спектры, высокоэффективная жидкостная хроматография, тонкослойная хроматография, амфоры эллинистической эпохи, вино.*

Introduction. Pottery played an important role in ancient societies in the transporation and conservation of food, as well as in everyday cooking. A good opportunity to discover the designation of pottery vessels is offered by examination of the organic residues from the material that had been stored in the vessels. Over the past 20–25 years the interest in this research has constantly increased thanks to the growing capabilities of the organic instrumental analysis, which is the basis of such investigations. One of the probable uses of Greek amphorae was transportation of wine.

Chemical evidence supporting the assumed presence of wine includes the detection of compounds that can be indicative of wine in the preserved contents of the ancient ceramic vessels or in the residues attached to the ceramic matrix of unglazed pottery sherds. Such compounds include L-tartaric acid, a molecule abundant in wine [1–4], and resins deliberately added to wine for its preservation or flavor enhancement [3, 4]. Elemental analysis, infrared (IR), ultraviolet (UV) spectroscopy, gas chromatography (GC), gas chromatography-mass spectromet-

ry (GC-MS), pyrolysis GC, thin-layer chromatography (TLC), high-performance liquid chromatography (HPLC), and amino acid analysis are the most common techniques that had been used, either singly or in combination, to characterize organic archaeological materials [5–13]. NMR spectroscopy is complementary to these techniques and in the past years there was a wide range of applications of NMR for archaeometric investigations [1, 2, 14].

Of special interest is the typical Greek wine "Retsina" well known even nowadays. "Retsina" is a wine with a three-thousand year tradition, which is specific and has been prepared with the addition of a pine resin from Aleppo pine (Pinus Halepensis). The unique taste of "Retsina" comes from the resin of pine trees that grow in the heart of mainland Greece, Attica, near Athens [15]. The "Pine" wine is mentioned often in ancient literature and even Dionysus, the God of wine, is portrayed sometimes with pine cones at the end of his wand.

Adding resin to wine is a process that dates back to ancient times when a pine resin or a combination of a pitch and a resin were used for making impermeable clay vessels (amphorae), in which the wine was stored and transported via sea [16, 17]. The ancient Greeks noticed that the pine resin had not only helped to seal amphorae and isolate it from moisture, but also had played the role of a curing agent and helped to keep the wine during transporting it by sea [18]. The Pine resin was also used to suppress the smell of goat skin, which was used as vessel for a short distance transport of wine. In this way the technology of producing "Retsina" was developed and is still used today. Before the invention of impermeable glass bottles, oxygen in the air had caused many changes both in the taste, the aroma, and the color of the wine, so that the wine was rendered unsuitable for drinking within a year. The Pine resin helped to eliminate the effect of oxygen in the air while imparting a specific wine aroma of resin. Over the course of time, the practice of adding resins during the fermentation process remained the same; only the amount of resin had increased, and as a result of this even stronger "resinated" wine was obtained. (This made the beverage obviously more lasting.) The Romans began to use barrels to transport wine until the Third Century AD, leading to the elimination of all enological needs for addition of the resin, but the actual taste was so popular that the manner of production remains to this day. This is probably the most consumed wine in Greece.

The aim of the present study is to determine the origin of organic contents of the amphorae, excavated in the Apollonia Pontika complex in Southeastern Bulgaria, based on resin residues found inside them. The working hypothesis was the use of the amphorae for transport of wine, in particular the well-known (even today) Greek wine "Retsina".

This investigation is a continuation of the analysis of the organic residue from inner walls of amphorae which was analyzed in the laboratories of the Faculty of Chemistry and Pharmacy of the Sofia University "St. Kl. Ohridski". It was also carried out and compared to samples of a gum separated from the evergreen pine tree – *Pinus Halepensis*. As a result, it was found that the capital of the Thracian tribe Getae, Hellis, had been supplied with resinated wine, today's Greek Retsina [19, 20].

Materials and methods. All samples of resins and resin similar substances as well as soil samples from the inner walls of the amphorae were taken from the Apollonia Pontika archaeological complex in Sozopol. Samples with consecutive numbers from 1 to 17 were taken during archeological excavations carried out in the locality Kolokita [21], while the other resins were sampled from amphorae belonging to the repository of the Archaeological Museum Sozopol.

Tumulus 8 was excavated in 2006 and the amphora structure had been broken by treasure hunters. Except for some fragments of cups, the only findings from the mound were storage amphorae. In the locality Kolokita the position of the amphorae with the mouth downwards suggests that they were deposited empty. Probably the wine was used in the ritual but in what way is beyond recovery [21].

The amphorae from the Archaeological Museum had been found occasionally during building works and there was no archaeological context. Modern resin of Aleppo pine was taken from the pines growing near Nea Fokia, in the Attica region, Greece and analyzed for comparison.

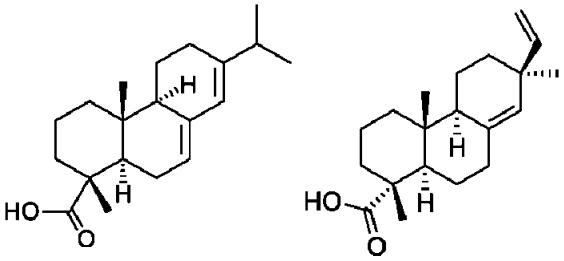
The following methods were used in the present investigation. The FTIR analysis was performed using a reflection attachment (MIRacle-ZnSe, ATR) in the region (4000–500 cm^{-1}) of the FTIR Tenzor 27-Bruker spectrometer with a resolution of 2 cm^{-1} and 128 scans. The ^{1}H spectra of the samples were recorded in $CDCl_3$ solvent using a Bruker Avance II + 600 MHz spectrometer and a 5 mm inverse triple-resonance (TBI) $^{1}H/^{31}P - ^{109}Ag/^{13}C$ with actively shielded Z-gradient. ^{1}H NMR chemical shifts have been calibrated relative to the signal of TMS. Only part of the archaeological resin samples and sample of contemporary resin were the object of the NMR analysis.

HPLC analysis of the samples and standards was carried out on a liquid chromatograph (Waters 2795) separation module and a dual lambda absorbance detector (Waters 2487). Separation was performed on a Licrokart C18 column (5 μm particle size, 4 mm column diameter, 25 cm column length) with an eluent flow rate of 1 ml/min. The column was kept in air an conditioned room with constant temperature of 18°C, while the autosampler was at 35°C. The volume of sample injected was 80 (20) μl. The following gradient was used: 0–10 min – 100% H_2O and 0.01% H_2SO_4 and then to 100% AcCN in the range of 10–40 min, constant up to 20 min, 50–60 min H_2O, and for the last 75 min – H_2O and 0.01% H_2SO_4. Peaks were detected at 210 and 245 nm.

Two approaches were used to achieve the best results. The first one used methanol for dissolution of the samples and subsequent separation with HPLC grade eluent methanol at different flow gradients with detection at 210 and 245 nm. The second approach was more appropriate: all samples of resin were dissolved in 1.5 ml AcCN for 8 h in an ultrasonic bath.

Thin layer chromatography (TLC). Only the soil samples selected from inner walls of the amphorae from Kolokita regions, Sozopol were the subject of TLC. The soil weighing, approximately 200–300 g, was air-dried. A subsample of approximately 10 g weight was further dried in an oven at 105°C; then all roots and parts of organic origin and pebbles were carefully removed using tweezers. The soil subsample was carefully mixed in an agate mortar to avoid contamination. From this homogenized soil 0,1 g samples was taken and extracted with 0.1 N HCl in a shaker for 8 h. The extract was filtered through "Blue Ribbon" paper filter and subjected to TLC with mobile phase $CHCl_3$, and tartaric acid was used as standard.

Results and discussion. The plant resins are composed of numerous components; the chief among these are terpenoid and alkene polycyclic compounds such as derivatives of abietic, oleanolic, and pimaric and/or isopimaric acids [22]:



Abietic acid Pimaric acid

Along with a carboxyl group, most of them contain conjugated or unconjugated double bonds and methyl groups as well. Therefore, their identification can be performed precisely by the characteristic frequencies of these functional groups (IR determination), specific environment (^{1}H NMR spectrometry), or by the time for elution of the individual compounds from the resin (for the HPLC analysis).

Since the ancient resin has undergone oxidation with time, which affected mostly double bonds, organic peroxides were formed, which in the presence of moisture were subsequently converted to alcohols and ketones. Oxidation of the methyl group is possible, followed by its transformation into the hydroxyl group [23]. Considering these degradation processes accompanying pine resin with time, it is logical to observe spectral changes in some frequencies (new onset and disappearance of old ones), the appearance of new peaks, and/or change in the intensity of old peaks. It is worth mentioning that the investigated resins were mixed with particles of sand, shells, and soil, which further complicates the interpretation of results due to contamination of the samples.

The appearance of strong absorption bands in the region between 4000–2500 cm^{-1} usually comes from stretching vibrations between hydrogen and some other atoms with mass 19 or less. Absorptions in the region of 1300 to 600 cm^{-1} include the contribution from complex interacting vibrations, giving rise to the unique fingerprint for each compound. A good match between the IR spectra of the two compounds in all frequency ranges strongly indicates that they have the same molecular structure. From the vibrational spectroscopic point of view, the most characteristic spectroscopic regions are those joined with the CH-stretching vibrations (2936–2654 cm^{-1}), ν_{C-O} stretching odes (1750–1690 cm^{-1}), bands within 1650–1400 cm^{-1} ($\nu_{C=C}$), as well as the so-called "finger print region" within 1350–400 cm^{-1}.

The temporal changes in the archaeological resins investigated by the ratio of the intensity of the alkene (C=C) stretching band at about 1640 cm^{-1} to that of the methylene ($C=CH_2$) deformation band at about 1440 cm^{-1} provide an analytical variable that relates to the age of the samples.

The results obtained by IR spectroscopy for all samples, where the identification of the old and new resins is performed in the characteristic frequencies at 1724, 1697, 1608, 1376, 885 cm^{-1}, are given in Table 1. An additional comparison is made to the spectrum of the natural resin (colophony), which contains a mixture of abietic and pimaric acids (Fig. 1).

IR spectrometry allowed identification of aromatic structures (~3100 cm^{-1}), aldehydes (~2750 cm^{-1}), ketones (~1694 cm^{-1}), esters (~1720 cm^{-1}), and the vibrations of the CH_3–CH_2-chain. A comparison of the spectra of archaeological resins with the modern one shows that they are very similar (Fig. 2a). Unfortunately, positive identification was possible only for six cases (R-001.SOZ R-002.SOZ, R-003.SOZ, R-004.SOZ, R-005.SOZ and R-034.SOZ). All of these samples were collected from the Archaeological Museum of Sozopol. For samples R-021.SOZ and R-026.SOZ (from Kolokita region), there is also a high probability that they contained resinated wine but maybe from other conifer plant [22]. Additionally a comparison is made between IR spectra of tartaric

TABLE 1. Results from IR Analysis

Case	Frequency, cm^{-1}
$\nu_{C=O(ester)}$	1724
$\nu_{C=O\ (COOH)}$	1697
$\nu_{C=C}$	1608
δ_{CH_3}	1376
δ_{C-H}	1387
$\tau_{C-H\ (CH_2)}$	885
$\tau_{C-H\ (=)}$	823
$\nu_{C-H\ (>=<)}$	3066
$\nu_{C-H\ (CH_3,\ CH_2)}$	2956, 2931

acid and calcium tartarate, which are used as indicators of wine. Absorption bands with maximum at 1725 cm^{-1} due to the carboxylic acid group of tartaric acid and at maximum 1612 cm^{-1} resulting from the carboxylate group of calcium tartarate [4] were established, which can be introduced by the chromic luvisol typical of the Black sea coast.

Although the ^1H NMR spectra of the resin samples are rather complicated, the nonoverlapping lines belonging to aromatic, olefinic, and methyl protons can be used for their analysis. The chemical shifts of these protons are given in Table 2. Other signals are due to multiplets having insignificant intensity, so identifying them in a mixture of resin acids is rather complicated. A complete analysis of the ^1H NMR spectra of resin acids requires the use of two-dimensional spectroscopy and was not done in this case. A comparison of the spectra from ^1H NMR analysis confirms the conclusions already made by IR spectrometry for the same samples. The largest differences occurred in the area of 7–9 ppm (aromatic and olefin proton region), which could be due to changes induced in the resin during the stay into the ground.

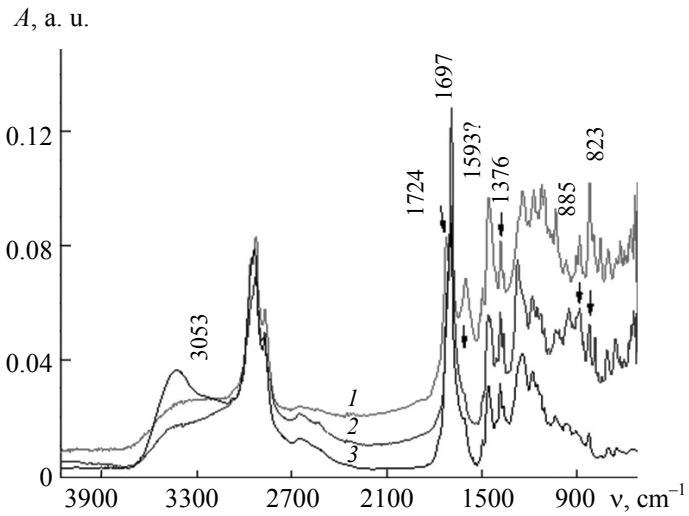


Fig. 1. IR spectra of sample R-002 (1), modern pine resin (2), and natural colophony (3).

The presence of peaks with δ (chemical shift) in the region of 0.5–3 proton NMR spectrum of the samples is clear evidence of the presence of terpenoid components in the resins [1, 2]. Considering the origin of the vegetable gums, in particular pine (Pinus Halepennsis), the presence of the bicyclic and tricyclic diterpenes [22] can be expected in addition to the above mentioned acids, as well as aromatic quaternary carbons, phenyl components, and to a lesser extent aromatic hydrocarbons [14]. A comparison with data from other authors [14] permits us to clarify the presence of pimaric acid (5.293 ppm), dehydroabietic (7.255, 7.166, 6.989 ppm), and abietic acid (5.78 ppm).

All samples were subject to HPLC analysis. The results at 210 and 245 nm are given in Fig. 2 and they show complete identity of the ancient resins, while noticeable difference in the intensity of the detected peaks and a slight shift of the retention times were established by comparison of these results with the chromatograms of the modern resin.

TABLE 2. Results from ^{1}H NMR Spectroscopy

Alkanes (R-CH_3)	1–0.5
Diterpenoid acids	3–0.5
Alcohols	4.5–3.5
Aliphatic carbohydrates to aromatic structure	4.9–6
Aromatic	8.3–6

The chromatograms are rich in peaks, and several of them have the same retention times in old and new resin samples. The presence of six identical peaks in the spectra at 210 nm with retention times 2.9, 25.8, 27.8, 29.09, 29.4, and 30.5 min enabled the confirmation that the same compound is present in six of the studied archaeological samples and also in the modern one (Fig. 2a). Additional information is obtained from the HPLC spectra at 245 nm where identical compounds have retention times 2.9, 16.4, 27.4, and 30.6 min (Fig. 2b).

A comparison of the spectra of archaeological resins with the modern one shows that they are very similar. Positive identification was possible again for the same samples that have a similar pattern by IR and ^{1}H NMR spectroscopy.

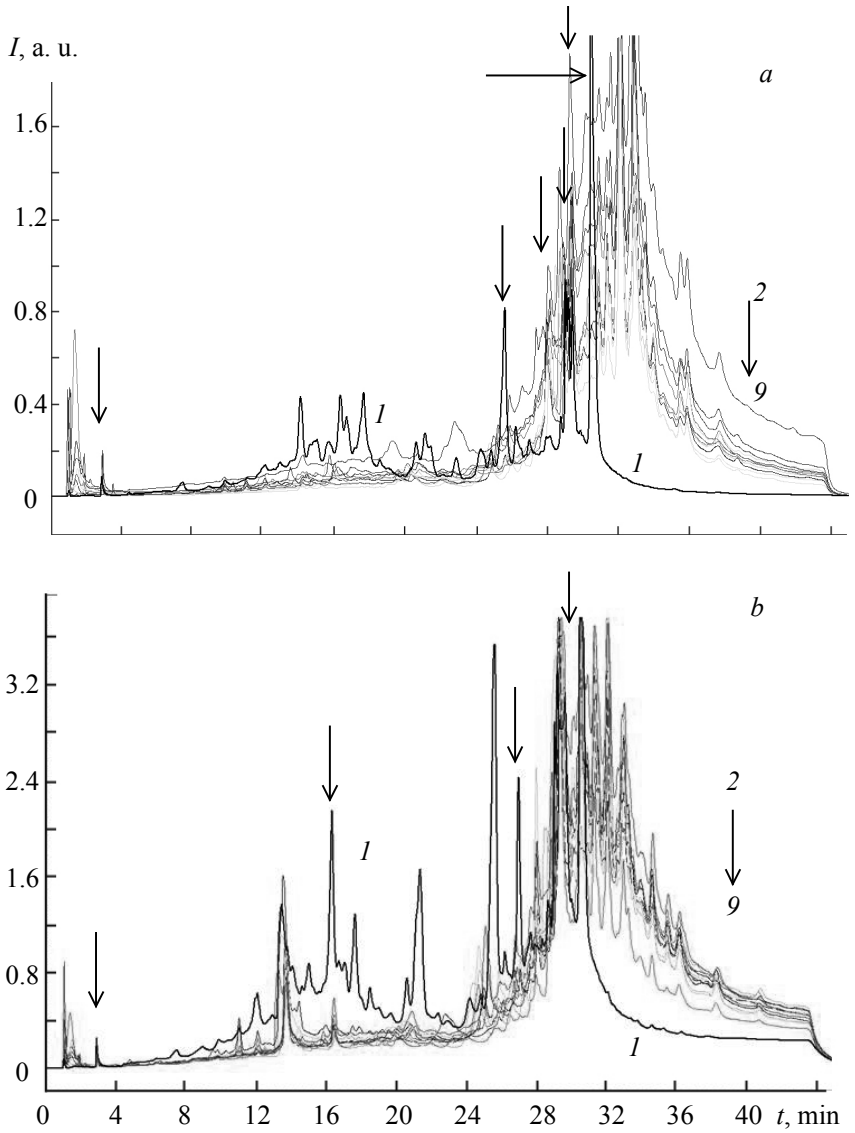


Fig. 2. Chromatograms of ancient (R-001.SOZ R-002.SOZ, R-003.SOZ, R-004.SOZ, R-005.SOZ, R-034.SOZ, R-021.SOZ and R-026.SOZ) (2–9) and modern resin samples (1) at 210 (a) and 245 nm (b).

It is worth mentioning that the extracts from the old resins and the soil extract from two of the samples from Kolokita region (R-021.SOZ and R-0026.SOZ) have comparable chromatographic patterns with peaks in the soil extract showing much lower absorbance. Since the amounts of original samples taken for extraction were the same and some of the peaks were found also in the extract from the contemporary resin, it is highly possible that the soil taken from the archeological place contained some amounts of the resin.

In order to clarify the hypothesis of wine supplying for the remaining 15 amphorae from Kolokita region, the TLC analysis of soil extract from the inner walls of the amphorae was performed. The results show that all of them have some amount of L-tartaric acid, a compound that exists in grape and is very often used as an indicator of wine content. Unfortunately, all the ceramic vessels from these amphorae had been washed during archaeological excavation and despite this result, no other analytical evidence of wine content in the amphorae is obtained.

The use of analytical techniques allowed the qualitative identification of the origin of ancient resin samples with numbers R-001.SOZ, R-002.SOZ, R-003.SOZ, R-004.SOZ, R-005.SOZ and R-034.SOZ, for which a high degree of probability exists that they contained "Retsina" wine. Possibly R-021.SOZ and R-0026.SOZ samples contained wine, but probably another type of resin had been used. Unfortunately, as already mentioned, these two samples and the remaining 15 ones were washed during the excavations, which precludes positive identification.

The type of investigated amphorae is very different. The amphorae from locality "Kolokita" are from Heraclea Pontika production center and dates back to the late 5^{th} to the first quarter of the 4^{th} century BC [21]. The other amphorae are form the Greek islands Chios, Mende, and Thasos, and they date back also to the 5^{th} to 4^{th} century BC. There are many archaeological evidences for trade connections between the Greek colony on the Black sea coast, but on the basis of the present results we can conclude that the investigated amphorae, in spite of their origin difference, had been used for transportation of the Greek wine "Retsina". In this way we confirm our previous results for the trade contacts between Thracians and ancient Greek in Hellenistic time especially for supplying wine [19, 20].

Conclusion. Twenty-two samples of resin residues and soil samples found in the inner parts of Hellenistic time amphorae from Apollonia Pontika were analyzed using different analytical methods (HPLC, NMR, IR, and TLC). Comparison with modern resin samples, collected from pine trees (Pinus Halepsensis) grown in the Attica region (Greece, near Athens), shows a similarity between the ancient and modern resin samples. On this basis it may be assumed that the content of the amphorae has been wine, probably Retsina, the object of trade connections between the Greek colony in Apollonia Pontika and Greece.

Modern diets include many foods and beverage used in ancient times. Wine was the main desirable grape product, because of its unique taste, dietary and medical benefits, and psychotropic effects. The identification of resinated wine of Hellenistic time is particularly significant because of this beverage's impact on social customs and religious, ethnic, and economical relations.

REFERENCES

1. E. L. Ghisalberti and I. M. Godfrey, *Stud. Conserv.*, **43**, No. 4, 215–230 (1998).
2. E. L. Ghisalberti and I. M. Godfrey, *Bull. Austral. Inst. Mar. Arch*., **14**, 1–8 (1990).
3. P. E. McGovern, D. L. Glusker, L. J. Exner, and M. M. Voigt, *Nature*, **381**, 480–481 (1996).
4. V. R. Badler, P. E. McGovern, and D. L. Glusker, *Deutch. Arch. Inst. Orient-Abteilung Baghdader Mitteilungen*, Verlag Philipp von Zabern, Mainz, **27**, 39–44 (1996).
5. J. S. Mills, R. White, and L. J. Gough, *Chem. Geol*., **47**, 15–39 (1984-85).
6. M. Saltzman, *Am. Chem. Soc.*, 172–185 (1978).
7. H. E. Hill and J. Evans, In "*Archaeometry: Further Australasian Studies*", Eds. W. R. Ambrose and J. M. J. Mummery, The Australian National University, Canberra, 90–96 (1987).
8. D. W. von Endt, *J. Arch. Sci*., **4**, 367–376 (1977).
9. J. Rullkotter and A. Nissenbaum, *Naturwissenschaften*, **75**, 618–621 (1988).
10. I.M. Godfrey and G.W. Richardson, *Bull. Aust. Inst. Conserv. Cult. Mater*., **16**, 73–84 (1990).
11. H. Barnard, S. H. Ambrouse, D. E. Beehr, M. D. Forster, R. E. Lanehart, M. E. Malanineу, R. E. Paar, M. Rider, S. Collazzo, and R. M. Yohem, *J. Arch. Sci*., **34**, 28–37 (2007).
12. M. R. Guasch-Jene, C. Andres-Lacueva, O. Jauregui, and R. M. Lamuela-Raventos, *J. Arch. Sci*., **33a**, 1075–1080 (2006).
13. M. R. Guasch-Jene, C. Andres-Lacueva, O. Jauregui, and R. M. Lamuela-Raventos, *J. Arch. Sci*., **33b**, 98–101 (2006).
14. E. D. Skakovskii, L. Yu. Tychinskaya, O. A. Gaidukevich, N. G. Kozlov, A. Yu. Klyuev, S. A. Lamotkin, S. I. Shpak, and S. V. Rykovd, *J. Appl. Spectrosc*., **75**, No. 3, 439–443 (2008).
15. N. Manesis, *The Greek Wine Guide*, Olive Press, Corfu, Greece (1996).

16. N. Boulton and C. Heron, In "*Ancient Egyptian Materials and Technology*", Eds. P. T. Nicholson, I. Shaw, Cambridge University Press, Cambridge, 599–603 (2000).
17. B. Stern, C. Heron, T. Tellefsen, and M. Serpico, *J. Arch. Sci.*, **35**, 2188–2203 (2008).
18. M. Serpico and R. White, In "*Ancient Egyptian Materials and Technology*", Eds. P. T. Nicholson, I. Shaw, Cambridge University Press, Cambridge, 430–474 (2000).
19. I. Surovic, B. Zlateva, and A. Ilieva, *Proc. 5th Int. Archaeological Conf. of Amber*, 1–7.06.2005, Belgrad (Serbia), 30–39 (2008).
20. B. Zlateva, I. Kuleff, and R. Djingova, *Proc. Int. Archaeological Conf., The Lower Danube in Antiquity*, 6–7.10.2005, Tutrakan (Bulgaria), 55–58 (2007).
21. A. Petrova, In *PITBAS II, Production and Trade of Amphorae in the Black Sea*, Eds. Ch. Tzochev, T. Stoyanov, A. Bozkova, Sofia, 101–109 (2011).
22. H. Panda, *Handbook on Oleoresin and Pine Chemicals (Rosin, Terpene Derivatives, Tall Oil, Resin, & Dimer Acids)*, Asia Pacific Business Press Inc. (2008).
23. K. J. Van Den Berg, J. J. Boon, I. Pastorova, and L. F. M. Spetter, *J. Mass Spectrosc.*, **35**, 512–533 (2000).

View publication stats

European Journal of Medicinal Chemistry 123 (2016) 69–79

Contents lists available at ScienceDirect

European Journal of Medicinal Chemistry

journal homepage: http://www.elsevier.com/locate/ejmech

Research paper

Synthesis, anticancer activity and photostability of novel 3-ethyl-2-mercapto-thieno[2,3-*d*]pyrimidin-4(3*H*)-ones

Anelia Ts Mavrova [a, *], Stefan Dimov [a], Denitsa Yancheva [b], Miroslav Rangelov [b], Diana Wesselinova [c], Jordan A. Tsenov [b]

[a] University of Chemical Technology and Metallurgy, Department of Organic Synthesis, 8 Kliment Ohridski Blvd., 1756, Sofia, Bulgaria
[b] Institute of Organic Chemistry with Centre of Phytochemistry, Bulgarian Academy of Sciences, Acad. G. Bonchev Str., Build. 9, 1113, Sofia, Bulgaria
[c] Institute of Experimental Morphology, Pathology and Anthropology with Museum, Bulgarian Academy of Science, 1113, Sofia, Bulgaria

ARTICLE INFO

Article history:
Received 20 February 2016
Received in revised form
10 July 2016
Accepted 12 July 2016
Available online 14 July 2016

Keywords:
Thieno[2,3-*d*]pyrimidin-4(3*H*)-ones
DFT
Cytotoxicity
Photo stability
Anticancer activity
B-Raf

ABSTRACT

Some derivatives of 3-ethyl-2-mercapto-thieno[2,3-*d*]pyrimidin-4(3*H*)-ones were synthesized using ethyl 2-aminothiophene-3-carboxylates as precursors in order to estimate their cytotoxicity, respectively proliferative activity.

Thienopyrimidinones containing thiosemicarbazide as well as 1,3,4-thiadiazole moieties were evaluated for their cytotoxical effect on four cancer cell lines: HT-29, breast cancer cells MDA-MB-231, HeLa, HepG2 as well as human diploid cell line Lep-3. Compounds **5b**, **6a** and **6b** revealed cytotoxicity to the four studied cancer cell lines. The highst cytotoxicity against MDA-MB-31 exhibited the thiosemicarbazide **5b** with IC_{50} $2.31.10^{-4}$ μM, but most active towards HT-29 cell lines was thienopyrimidine **6c** with IC_{50} 0.001 μM. Compound **6a** showed the highest inhibitory activity with IC_{50} - 0.99 μM to human liver carcinoma *HepG2* cells and low cytotoxicity towards *Lep3* (IC_{50} = 191 μM). The thienopyrimidine derivative linked to thiadiazole **6b** was toxic to the four studied cancer cell lines, especially to HeLa (IC50–0.83 μM), and besides that the compound demonstrated toxicity to Lep 3 cells at very high concentration 89 × 10^3 μM.

The solid-state photostability of the derivatives **5a-c** and **6a-c** was tested by irradiation with UV light. All of the studied compounds show solid-state photostability in 240 min of irradiation.

Using MOE software molecular docking of the three ligands **5b**, **6b** and **7** was accomplished into an internal pocket formed by the activation segment and the P-loop of ^{V599E}B-Raf. It was established that the binding of the ligands to ^{V599E}B-Raf promotes an inactive conformation of the enzyme.

© 2016 Elsevier Masson SAS. All rights reserved.

1. Introduction

It is well known that the pyrimidine structure is closely related to three of the four nucleobases uracil, thymine and cytosine, which fact makes pyrimidines essential building blocks of all living cells [1]. Thieno[*d*]pyrimidines are found to have broad spectrum of biological activity as anticancer [2], antibacterial [3], antiviral [4], antioxidant [5], antihistaminic [6], anti-inflammatory [7], analgesic [8,9].

It was found that some thieno[3,2-*d*]pyrimidines are bioisosters of *lapatimib* (IC_{50} 120nM) [10] and some of them have shown better inhibitory activity (IC_{50} 11nM) towards epidermal growth factor receptor tyrosine kinase (EGFR/ErbB-2), compared to the 4-aminoquinazoline derivative – *lapatimib*.

Many thieno[2,3-*d*]pyrimidines have showed significant *in vitro* cytotoxic activity against hepatocellular carcinoma (*Hep G-2*) compared to the reference drug *Doxorubicin* [11,12]. *Wang* et al. have found that some 5,6,7,8-tetrahydrothieno[2,3-*d*]pyrimidine-4-ones preferentially affect *p21*-deficient cancer cells (IC_{50} 2.3μM) [13]. The further SAR analysis indicated that one of the important structural-activity recommendations is the presence of oxygen in C-4 position of the pyrimidine ring.

The 1,3,4-thiadiazole (TDA) derivatives are known because of their pharmacological activity as anti-inflammatory [14], antibacterial [15], antitumor [16]. The anticancer effect of 1,3,4-thiadiazoles is mainly related to the high electron-donating ability of the two nitrogen atoms to form *H*-bonds. 2-Amino-1,3,4-

* Corresponding author. Department of Organic Synthesis, University of Chemical Technology and Metallurgy, 8 Kliment Ohridski Blvd., 1756, Sofia, Bulgaria.
E-mail address: anmav@abv.bg (A.T. Mavrova).

http://dx.doi.org/10.1016/j.ejmech.2016.07.022
0223-5234/© 2016 Elsevier Masson SAS. All rights reserved.

thiadiazoles have a variety of anticancer activity against melanoma, glioblastoma, lymphosarcoma [17]. Some thiadiazole derivatives have shown anticancer activity against *HepG-2* [18,19] and *HeLa* cell lines compairable with *staurosporine*, resulting from *H*-bond between the nitrogen atom from the 1,3,4-thiadiazole and the amino hydrogen of *GLY505* amino acid – part of the ATP binding site of focal adhesion kinase [20]. There was reported a series of 2-amino-1,3,4-thiadiazoles that display growth inhibition in *A549* lung carcinoma cells by inhibiting ERK1/2 pathway and cell cycle progression through G_1 into S phase [21]. In addition, same TDA-based compounds are shown to possess significant anticancer activity against prostate cancer (*LnCaP*, *DU145* and *PC3*) and breast cancer cell lines (*MCF-7* and *MDA-MB-231*) [22,23].

The mesoionic nature of thiadiazoles makes these compounds to be more able to cross cellular membranes [24]. Therefore, combining TDA with an effective anticancer adenine and guanine based pyrimidine bioisoster as thieno[2,3-*d*]pyrimidine-4-ones could lead to potential inhibiting effect on purine synthesis and less toxic anticancer agents. In the literature it has been described that the 1,3,4-thiadiazole containing 5,6,7,8-tetrahydrothieno[2,3-*d*]pyirimidine-4-ones possess anticancer activity [25,26]. This fact has drawn our attention for further investigation of that biphar-macophoric compounds as potential anticancer drugs on four human cancer cells and one non-tumorogenic cell line.

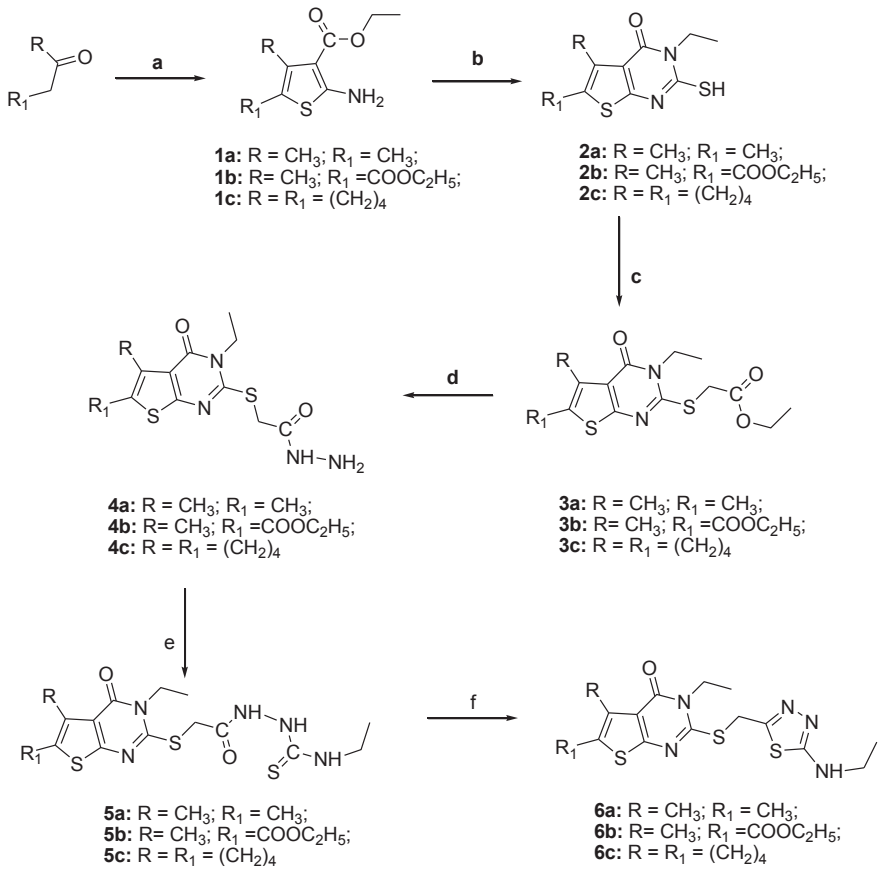
2. Chemistry

The synthesis of *N*-ethyl-thieno[2,3-*d*]pyrimidine-4-one derivatives, containing 1,3,4-thiadiazole moiety is illustrated on Scheme 1.

The 2-aminothiophene esters **1a-c** used as starting materials were synthesized by *Gewald* reaction which is a one-pot reaction method for 2-aminothiophene synthesis [27–30]. The synthesis of *N*-ethyl-2-mercapto-thieno[2,3-*d*]pyrimidine-4-ones **2a-c** was accomplished by alkaline catalized cyclocondensation of the 2-aminoesters **1a-c** with ethyl isothiocyanate. The *S*-nucleophilic substitution between the 2-mercapto-thienopyrimidine-2-ones and ethyl chloroacetate, using triethylamine as an organic base gave thioacetate derivatives **3a-c**. The interaction of the esters **3a-c** with hydrazine hydrate in absolute alcohol led to the obtaining of the hydrazides **4a-c**. The latter, by treatment with the corresponding ethyl isothiocyanate under reflux gave the semicarbazides **5a-c** with high yields. The cyclocondensation to the corresponding semicarbazides **5a-c** was carried out in water solution of sodium hydroxide under reflux, followed by acidification with hydrochloric acid. The thiadiazole containing thieno[2,3-*d*]pyrimidin-4(*3H*)-ones **6a-c** were obtained from compounds **5a-c** in cooled concentrated sulfuric acid.

3. Pharmacology

The semicarbazides **5a-c** and thiadiazole containing thieno[2,3-*d*]pyrimidin-4(*3H*)-ones **6a-c** were evaluated for their cytotoxicity to human colorectal cancer cell line *HT-29*, breast cancer cells *MDA-MB-231*, cervical cancer cells *HeLa*, human liver carcinoma cell line *HepG2* and human normal diploid cell line *Lep3* by using the MTS (3-(4,5-dimethylthiazol-2-yl)-5-(3-carboxymethoxyphenyl)-2-(4-sulfophenyl)-*2H*-tetrasolium inner salt) test [31].



Scheme 1. Synthesis of semicarbazide and 1,3,4-thiadiazole derivatives of thieno[2,3-*d*]pyrimidine-4-ones: a) ethyl cyanacetate, $HNEt_2$, S_8, ethanol; b) ethyl isothiocyanate, NaOH, DMF; c) ethyl 2-chloroacetate, NEt_3, benzene, reflux; d) hydrazine hydrate, ethanol, reflux; e) ethyl isothiocyanate, ethanol, reflux; f) 98% sulfuric acid, 0 °C, NH_4OH.

4. Results and discussion

A series of 2-aminothiophenes has been prepared for the aim of our research via a multicomponent condensation between appropriate ketone, ethyl cyanoacetate, sulfur and diethyl amine under conditions, described by Gewald [27]. The pyrimidine ring formation of 3-ethyl-2-mercapto-thieno[2,3-*d*]pyrimidin-4(*3H*)-ones **2a-c** was performed by basic catalyzed heterocyclic cyclocondensation of the 2-aminothiophenes **1a-c** and ethyl isothiocyanate. It is known that equilibrium between the thiol and thione form exists, but in an alkaline medium the presence of the thiol form is advantageous, therefore the acidic 2-SH group of the thienopyrimidin-2-thiols was alkylated with ethyl chloroacetate in presence of triethyl amine. The reaction of esters **3a-c** with excess amount of hydrazine hydrate in absolute ethanol led to acetohydrazides **4a-c**. Within that group, the synthesis of **4c** occured with the highest yield – reaching 94%. The aforementioned compounds were treated with 12-fold access of ethyl isothiocyanate giving thiosemicarbazides **5a-c** with excellent yields from 88% to 96%. 1,3,4-Thiadiazoles **6a-c** were obtained from thiosemicarbazides **5a-c** by dehydrative cyclization in acidic medium. The yields of the final thiadiazole **6b** and **6c** were in the range from 90 to 95%.

The chemical structures of the new compounds were established by elemental analyses, IR-, ^{1}H NMR and the results are presented in the Experimental part. The elemental analyses indicated by the symbols of the elements were within ±0.4% of theoretical values. In the ^{1}H NMR spectra, particularly meaningful are characteristic SCH_2CO signals (singlets) of the substituted in 2 place compounds as well as the as the signals of S-CH_2 between the both heterocycles, shifted downfield due to deshielding effect of both S-atom and the CO group respectively the pyrimidine and thiadiazole rings. The chemical shift values varied in the range from 3.99 to 7.43 ppm for the esters, 4.08–4.11 ppm for the thiosemicarbazides and from 4.45 to 4.84 ppm depending of the solvents and substituents. The labile NH protons are not characteristic and their chemical shifts depend on the water quantity in the solvent. Some ^{1}H NMR spectra are given in the Supplementary material.

The thiosemicarbazide (**5a-c**) and 1,3,4-thiadiazole (**6a-c**) thieno[2,3-*d*]pyrimidine-4-one derivatives were subjected to *in vitro* screening in order to estimate their effects towards human cancer *HT-29*, *MDA-MB-231*, *HeLa*, *HepG2* and normal human *Lep3* cell lines.

The cell proliferation was established using the MTS assay, based on the reduction of the tetrazolium salt into a coloured, aqueous soluble formazan product by mitochondrial activity of viable cells at 37 °C. The released amount of formazan produced by dehydrogenase enzymes is proportional to the number of living cells in the culture and can be measured spectrophotometrically at λ_{max} = 492 nm [32]. The higher levels of formazan indicate to a higher vitality of the cells, whereas the low amount of formazan is an indicator for the cytotoxicity of the tested compounds [33,34]. In addition, the relative cell viability, expressed as a percentage of the untreated control (100% viability) was calculated for each concentration. All data points represent an average of three independent assays. The obtained results were plotted and EC_{50} (Table 1) and IC_{50} (Table 2) were calculated. Statistical significant differences in the level of cells in both control and experimental groups were determined ($p \leq 0.05$).

It can be seen that the most of the examined compounds exhibited wide inhibitory concentration range for all tested human cell lines. Among the thieno[2,3-*d*]pyrimidine-4-ones, containing thiosemicarbazide moiety, compound **5b** was toxic against all cancer cell lines, used in that study, especially against breast cancer cells *MDA-MB-231* ($IC_{50} = 2{,}31.10^{-4}$ μM), while in the same time it revealed cytotoxicity to *Lep3* in a much higher concentration with IC_{50} = 0,8 μM.

In the group of the thienopyrimidine derivatives linked to thiadiazole ring, compound **6b** was toxic to the four studied cancer cell lines, especially to HeLa cells (IC_{50} - 0.83 μM), besides the compound demonstrated toxicity to Lep 3 cells at very high concentrations, the determined IC_{50} value was 89.10^3 μM. The low cytotoxic profile to *Lep3* can provide high selectivity towards all four cancer cell lines at small concentrations.

Apparently, the most active against human colorectal cancer cell line *HT-29* was compound **6c** with IC_{50} 0.001 μM, followed by **6a** with IC_{50} 3.58 μM, respectively, but derivative **6c** exibits about 100-*fold* lower cytotoxicity against normal diploid cell line *Lep3*.

With respect to human liver carcinoma *HepG2* cells compound **6a** showed the highest inhibitory activity with IC_{50} - 0.99 μM and the second lowest cytotoxicity towards *Lep3* (IC_{50} = 191 μM).

In summary, it can be noted that thieno[2,3-*d*]pyirimidine-4-ones containing thiosemicarbazide (**5a-c**) and thiadiazole moiety (**6a-c**) exhibit high effect on cell proliferation towards all tested human cancer and normal cell lines, whereat compound **6b** showed comparatively much lower toxicity against normal *Lep3* cells (Fig. 1). This makes the thiadiazole derivative **6b** efficient anticancer agent against all tested tumor cells at low concentration, and at the same time the compound will not demonstrate any cytotoxicity upon normal human cells. It was observed that the variation of substituents at *5*-C and *6*-C position of the thiophene ring leads to a major decrease of *Lep3* cell line vitality, whereas the only significant increase (1000-*fold*) of the apoptotic effect was indicated for the more lipophilic tetrahydro-substituted compound **6c** against *MDA-MB-231* and *HT-29* cancer cells.

The term 'photostability' includes not only the degradation caused by exposure to light, but also processes as radical formation, energy transfer and luminescence [35]. A large number of drug substances absorb radiation in the ultraviolet and/or visible area and are thus sensitive to light. They undergo photodegradation in liquid media or in solid state on exposure to light [36]. To the photodegradation factors of drug dosage forms in the solid state belong the particle sizes, the surface area, the colour and crystal structure, the photodimerization or isomerization. There is correlation between the transparency of the products and the radiation being used. The radiation to which a sample is exposed may be reflected, scattered, transmitted or absorbed. Only the absorbed radiation participates in photodegradation. There are many results for the photodegradation of substances in aqueous solution, but relatively few studies are done on photostability in solid state. Correlations between photochemical behaviour in solution and in

Table 1
The proliferative activity (EC_{50}) of the studied compounds.

Compounds	EC_{50} ± SE (μM)				
	HT-29	MDA-MB-231	HeLa	Hep G2	Lep3
5a	0.085 ± 0.20	8.86 ± 0.10	0.43 ± 0.03	–	–
5c	1.13 ± 0.16	9.33 ± 0.12	7.97 ± 0.72	2.72 ± 0.31	8.25 ± 0.24
6c	–	0.001 ± 0.14	9.28 ± 0.03	–	–

Table 2
In vitro cytotoxicity against HeLa, Hep G2, HT-29, MDA-MB-231 and Lep 3 cells.

Compounds	IC_{50} ± SE (μM)				
	HT-29	MDA-MB-231	HeLa	Hep G2	Lep3
5a	–	–	–	–	0.01 ± 0.22
5b	7.38 ± 0.71	$2.31.10^{-4}$ ± 0.04	8.71 ± 0.09	8.71 ± 0.58	0.8 ± 0.18
6a	3.58 ± 0.25	9.4 ± 0.15	7.42 ± 0.22	0.99 ± 0.52	191 ± 0.03
6b	9.12 ± 0.37	2.13. ± 0.13	0.83 ± 0.18	9.51 ± 0.03	89.10^{3} ± 0.27
6c	0.001 ± 0.11	–	–	9.8 ± 0.18	9.77 ± 0.09

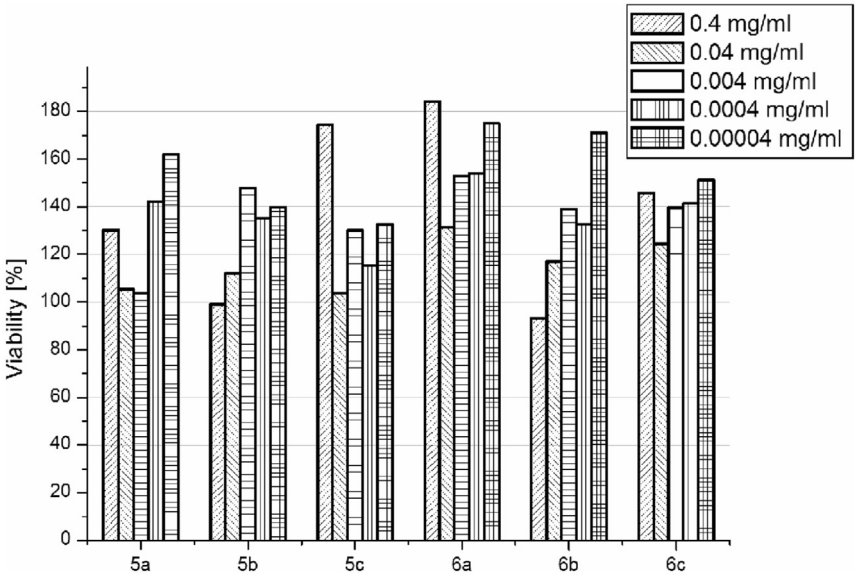


Fig. 1. Viability of Lep 3 cells (%) after treatment.

solid state are not clearly established.

The solid-state photostability of the novel thieno[2,3-*d*]pyrimidine-4-one derivatives **5a-c** and **6a-c**, was tested by irradiation with UV light in a SUNTEST equipment. The kinetics of the compound photodegradation was monitored colorimetrically. As no changes were established in the absorption maxima (λ_A) of compound **5b-c** and **6a-c** during the irradiation, the correlation between the drug concentration and the time of irradiation was constant value (Fig. 2a). The 240 min irradiation of thiosemicarbazide **5a** resulted with nearly 30% photodegradation (Fig. 2b).

For promising pharmacological potential, the studied thieno[2,3-*d*]pyrimidine-4-ones should possess favourable pharmacokinetic properties *in vivo* i.e. sufficient bioavailability and

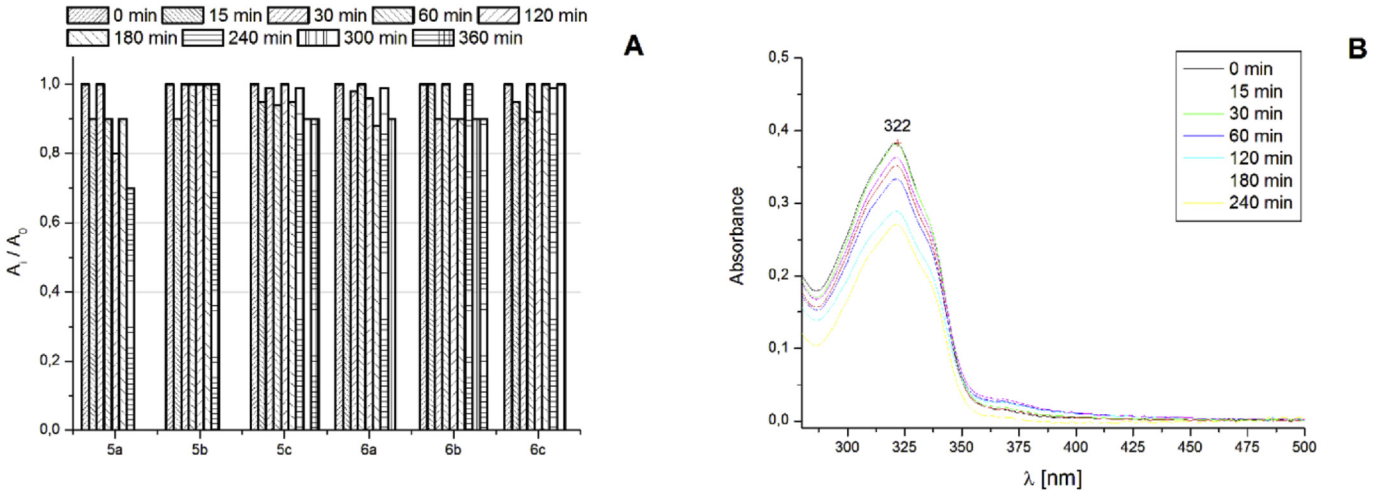


Fig. 2. (a) Solid-state photostability ratiometric analysis of **5a** (C = 3128.10^{-5} ± 0.125 mol/L), **5b** (C = 2185.10^{-5} ± 0.087 mol/L), **5c** (C = 3916.10^{-5} ± 0.158 mol/L), **6a** (C = 5242.10^{-5} ± 0.209 mol/L), **6b** (C = 2275.10^{-5} ± 0.091 mol/L), **6c** (C = 4089.10^{-5} ± 0.164 mol/L) in DMF solution; **(b)** Absorbtion spectrum of compound **5a**.

transportation through the different membranes to the desired receptor binding site, as well as an optimal metabolization and elimination profile. Calculated molecular properties such as lipophilicity, molecular size, flexibility and presence of hydrogendonor and acceptors could provide useful information in this relation.

It can be seen from the SAR analysis (Table 3), made by using Molinspiration tool [37], that all of the examined compounds **5a-c** and **6a-c** respond to Lipinski's *"Rule of Five"* [38]. It appeared that compounds **6a** and **6c** possessing the one and the same low topologic polar surface area (TPSA) of 72.71 Å^2 and an equal number of hydrogen donors (N_{HD}) and acceptors (N_{HA}), were the most active against *HT-29* cell line. The low TPSA provides a sufficient intestinal absorbtion on the drug in humans [39] and the higher number of N_{HA} provides higher solubility, which explains their citotoxicity against *HT-29* and makes **6a** and **6c** promising candidates for *in vivo* analysis. The least toxic compounds against human normal diploid cell line *Lep3* **6a** and **6b** have the TPSA = 72.71 Å^2 and 99.01 Å^2 respectively.

The most active to *MDA-MB-231* cells compound (**5b**) has the highest sum of H-bond donor (N_{HD}) and acceptor (N_{HA}) groups of all examined compounds as well as the highest TPSA, 114.35 Å respectively. It is well known that to show an acceptable bioavailability one compound should have TPSA lower than 140–150 Å^2. These molecular properties coincide well with those characterizing the structurally related thieno[2,3-*d*]pyrimidine-4-one **A** (*ethyl 2-(2-{2-[(ethylamino)carbonothioyl] hydrazino}-2-oxoethyl)-5-methyl-4-oxo-3,4-dihydrothieno[2,3d]pyrimidine-6-carboxylate* Fig. 3), that shows *MDA-MB-231* selectivity and was recently reported under number **8** in Ref. [23]. It can be assumed that the high TPSA, molecular weight (M.W.) and volume (Vol.) of **5b** contribute to a better fitting with the active center, inhibiting cancer *MDA-MB-231* cell line growth. The high cytotoxicity of **5b** should be attributed to the alkylation of the amide group in the pyrimidine ring and to the replacement of the aliphatic spacer with thiomethylene group (Fig. 3).

Based on the structures of **5b** and **7** (Fig. S14), optimized at DFT B3LYP/6-311++G** level of theory [40,41], it can be presumed, that the replacement of the methylene group at *2*-nd position of the pyrimidine with sulfur spacer leads to a much flatter molecular conformation of **5b**. That fact, combined with the N-alkylation at 3-rd position, results in larger molecular volume of **5b** than **A**.

Protein tyrosine kinases are key regulators of cell function, which represent one of the largest and most functionally different gene families with particular relevance to many human diseases, including cancer. The kinases are particularly eminent in signal transduction and coordination of complex functions at the cell cycle. Beside that fact in the literature it has been reported that the highly selective carbamide derivative (*sorafenib*, **S**. Fig. S15) shows evidence for tumor regressions after 9 days of oral dosing against breast cancer *MDA-MB-231* cells [42,43]. In addition a series of thieno[2,3-*d*]pyrimidines was synthesized and identified as inhibitors to the most critical isoform of the Raf family – B-Raf [44–46]. It is assumed that such cell line selectivity of the carbamide and respectively thiosemicarbazides (**5b, 6b** and **A**) share the same bioisosteric mechanism of action by affecting tumor growth through blocking two cellular processes essential for tumor development: inhibition of the MAPK pathway and inhibition of tumor angiogenesis.

In order to clarify the possible binding modes of **5b**, **6b** and **A** with B-Raf, the compounds were docked into the crystal structures of human oncogenic ^{V599E}B-Raf in complex with sorafenib (PDB code: 1UWJ [43]) using MOE software [47].

The kinase domain of ^{V599E}B-Raf has a bilobal structure typical also for other members of the protein kinase family group [43]. Similarly to sorafenib (Fig. S15) the three ligands are bound to the interfacial cleft, buried between the N and C lobes of the kinase domain. The docking conformations of **5b**, A and **6b** are shown in Figs. 4(a), 5(a) and 6(a).

In all cases, the *N*-ethyl-thieno[2,3-*d*]pyrimidine-4-one fragment occupies a pocket formed by residues Val503, Leu504, Ile571, Phe594, Lys482 and Gly592, with only the ethoxy group exposed to the solvent (Figs. 4(b), 5(b) and 6(b)). The van der Waals interactions dominate the contacts of **5b** and **7** with ^{V599E}B-Raf as it could be seen from the 2D representations of the ligands in the pocket (Figs. 4(b) and 5(b)).

Polar interactions to the catalytic Glu500, Gly592 from the activation segment of the DFG motif and Lys482 or Thr528 also contribute to the stabilization of the ligand-pocket binding. The thiosemicarbazides moiety of **5b** is connected via two hydrogen bonds to Thr528 and Asp593. The other MDA-MB-231 selective thieno[2,3-*d*]pyrimidine-4-one **7** forms hydrogen bonds to Lys482 and Asp593.

In the case of **6b**, one of the N-atoms of the thiadiazole moiety acts as hydrogen bond acceptor to Thr528, while the N-ethyl substituent is oriented towards the polar Glu500 and Asp593.

These polar interactions along with the hydrophobic interaction to Phe594 connect the three ligands to the activation segment of the DFG motif. On the other side, as it was mentioned above a number of contacts to the catalytic residues Lys482, Glu500 is formed. In that way the binding of the ligands to ^{V599E}B-Raf promotes an inactive conformation of the enzyme by holding the activation segment of the DFG motif and hindering its phosphorylation.

Table 3
Calculated molecular properties of the tested compounds: partition coefficients (logP), molecular weight (MW) [g/mol], topologic polar surface area (TPSA) [Å^2], molecular volume (Vol.) [Å^3], sum of OH and NH H-bond donors (N_{HD}) and sum of O and N H-bond acceptors (N_{HA}).

Compounds	*logP*	*M.W.*	*TPSA*	*Vol*	N_{HA}	N_{HD}
5a	2.14	399.57	88.05	337.77	7	3
5b	2.36	457.60	114.35	382.54	9	3
5c	2.71	425.61	88.05	361.01	7	3
6a	2.98	381.55	72.71	319.93	6	1
6b	3.21	439.59	99.01	364.70	8	1
6c	3.56	407.59	72.71	343.17	6	1
A[a]	1.28	397.48	125.21	330.67	9	4

[a] The compound is previously reported in Ref. [23]; for molecular structure see Fig. 3.

5. Conclusion

A serie of eight new thieno[2,3-*d*]pyrimidin-4(*3H*)-ones containing different substituted thiosemicarbazide, 1,2,4-triazoles and 1,3,4-thiadiazoles heterocycles were synthesized using the corresponding 2-(thieno[2,3-*d*]pyrimidin-2-yl)thioacetohydrazides as precursors under optimized reaction conditions with good yields.

The initial biological screening *in vitro*, using MTS tetrazolium assay has showed that the studied thiosemicarbazide containing thieno[2,3-*d*]pyirimidine-4-one **5b**, connected through sulfur linker possess high cytotoxicity against *MDA-MB-231* cells. The cytotoxic effect of **5b** towards *Lep3* cells was comparatively much lower. Among the thienopyrimidinones containing 1,3,4-thiadiazole ring compounds **6b** revealed cytotoxicity to all screening cancer cells with IC_{50} from 9,51.10^{-5} μM against *Hep G2* to 0.83 μM against *HeLa* cell line, while at the same time indicated relatively high vitality levels of *Lep3* with IC_{50} - 89.10^3 μM. Compound **6c** demonstrated selective cytotoxicity to *HT-29* and *Hep G2* cancer cell lines, and also the 5,6-dimethyl substituted

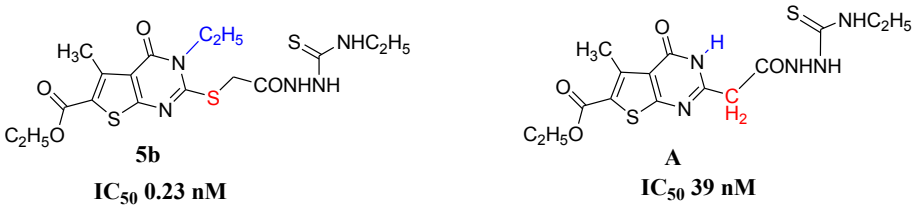


Fig. 3. Structures of MDA-MB-231 cell line growth inhibitors **5b** and **A**.

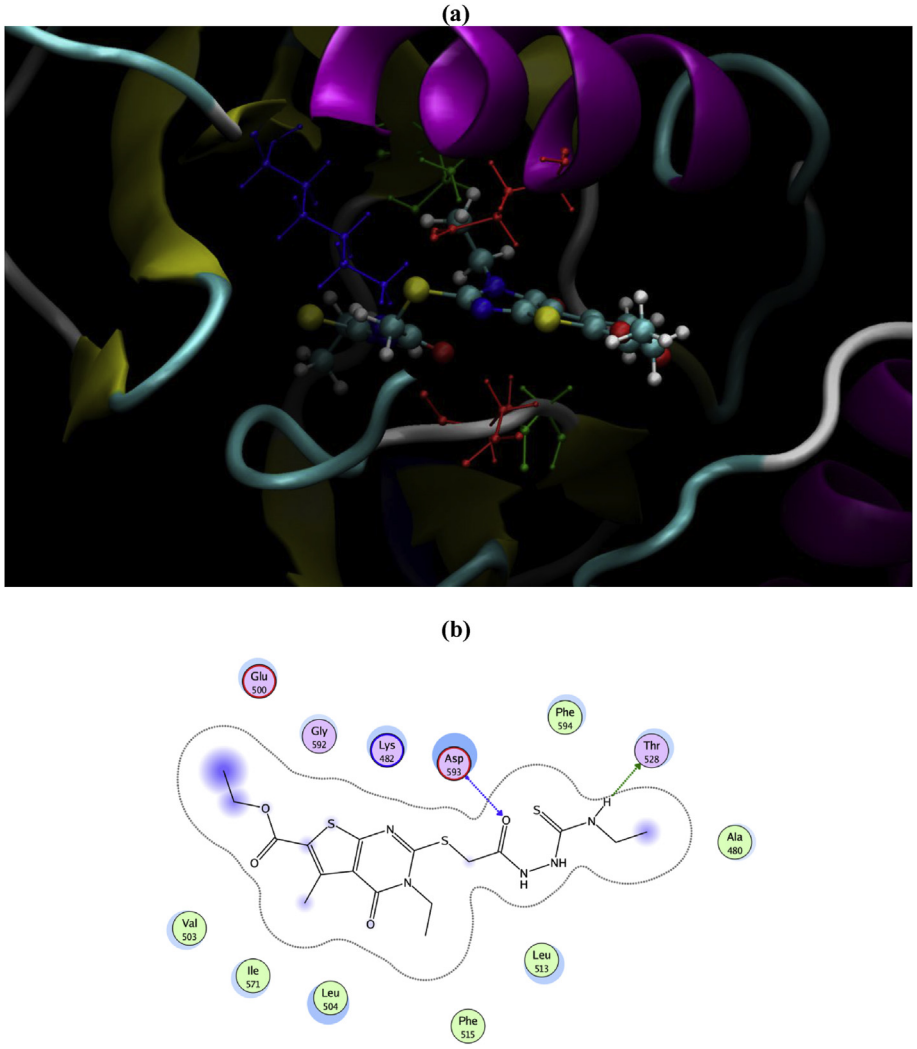


Fig. 4. **(a)** Docking conformation of **5b** with shown amino acid residues Thr528, Asp593, Lys482, Glu500, Gly592; **(b)** 2D representation of the interactions of **5b** with ^{V599E}B-Raf.

thienopyrimidone **6a** showed cytotopxicity to all four cancer cells, however both thiadiazole derivatives showed proliferative effects on human diploid cells. In contrast to **5a**, all of the examined compounds show solid-state photostability in 240 min period of irradiation.

Based on molecular docking study, the binding modes of **5b**, **6b** and a structurally related compound **A** were clarified. By association to catalytic amino acid residues Lys482, Glu500 and Gly592, Asp593 and Phe594 from the activation segment of ^{V599E}B-Raf, the ligands promote an inactive conformation of the enzyme and hinder its phosphorylation.

The obtained activity results towards *MDA-MB-231* cells indicate that the thiosemicarbazide moiety (**5b**), connected through a sulfur atom in the pyrimidinone skeleton as well as the results exhibited by **6b** to *HeLa* and *Lep3* prove the necessity for further investigation *in vivo* to estimate the exact inhibition pathway in the cellular processes, essential for tumor development related to the antitumor potential of the tested compounds.

6. Experimental part

Melting points (mp) were determined on an Electrothermal AZ 9000 3MK4 apparatus and were uncorrected. The thin layer chromatography (TLC, Rf values) was performed on F254 or silica gel plates F254 (Merck, 0.2 mm thick) and visualization was effected with ultraviolet light. IR spectrawere recorded on a Bruker Equinox

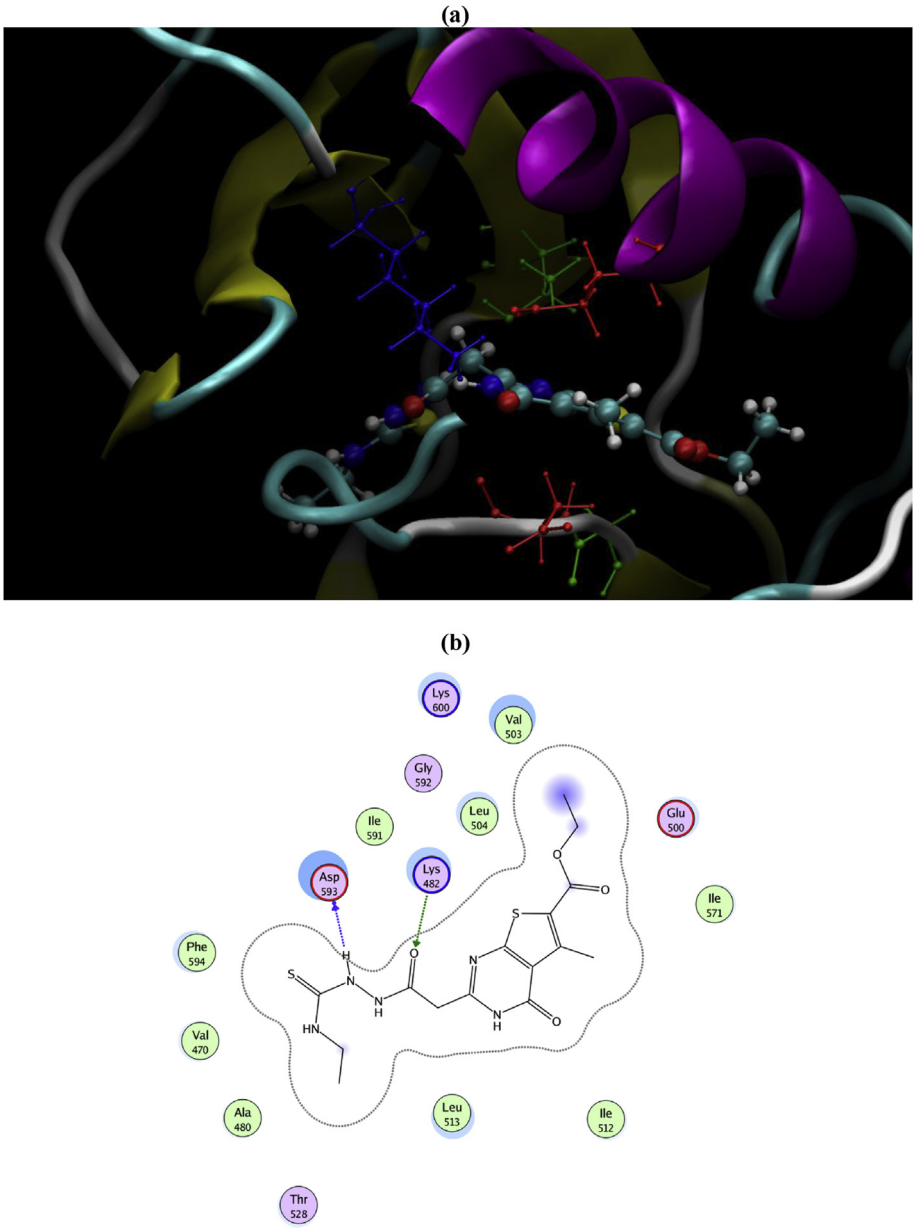


Fig. 5. **(a)** Docking conformation of **A** with shown amino acid residues Thr528, Asp593, Lys482, Glu500, Gly592; **(b)** 2D representation of the interactions of **A** with ^{V599E}B-Raf.

55 spectrophotometer as potassium bromide discs. All ^{1}H-NMR spectra were recorded on a Bruker Avance DRX 250 spectrometer (Bruker, Faelanden, Switzerland) operating at 250.13 MHz and a Bruker Avance DRX 600 spectrometer (Bruker, Faelanden, Switzerland) operating at 600 MHz. Chemical shifts were expressed relative to tetramethylsilane (TMS) and were reported as δ (*ppm*). The measurements were carried out at ambient temperature (300 K). The microanalyses for C, H, N and S were performed on PerkineElmer elemental analyzer.

6.1. General procedure of the synthesis of ethyl 2-aminothiophene-3-carboxylates ***1a-c***

Diethylamine (0.1 mol) was added dropwise for 30 min to a suspension of the appropriate ketone (0.1 mol), ethyl cyanacetate 0.1 mol (11 ml) and 3.2 g sulfur in 30 ml ethanol and the reaction mixture was stirred at room temperature for about 75 min. When the synthesis was completed the mixture was cooled. The obtained 2-aminothiophene crystalized in the form of yellow powder. The precipitate was filtrated, washed with water and recrystallized from ethanol to give the 2-aminothiophene derivatives [27].

6.1.1. Ethyl 2-amino-4,5-dimethylthiophene-3-carboxylate (***1a***)

Yield: 61%; Mp. 97–100 °C [1]; IR (KBr): 3300 cm^{-1} (NH), 2920 cm^{-1} (CH_3), 2860 cm^{-1} (CH_3), 1640 cm^{-1} (C=O), 1160 cm^{-1} (C–O); Analysis: Calc. for $C_9H_{13}NO_2S$: C, 54.25; H, 6.58; N, 7.03; O, 16.06; S, 16.09; Found: C, 54.30; H, 6.55; N, 7.08; O, 16.10; S, 16.10.

6.1.2. Diethyl 5-amino-3-methylthiophene-2,4-dicarboxylate (***1b***)

Yield: 65%; Mp. 104–106 °C [1]; IR (KBr): 3300 cm^{-1} (NH), 2960 cm^{-1} (CH_3), 2860 cm^{-1} (CH_2), 1640 cm^{-1} (C=O), 1230 cm^{-1} (C–O); Analysis: Calc. for $C_{11}H_{15}NO_4S$: C, 51.35; H, 5.88; N, 5.44; O, 24.87; S, 12.46; Found: C, 51.33; H, 5.85; N, 5.52; O,

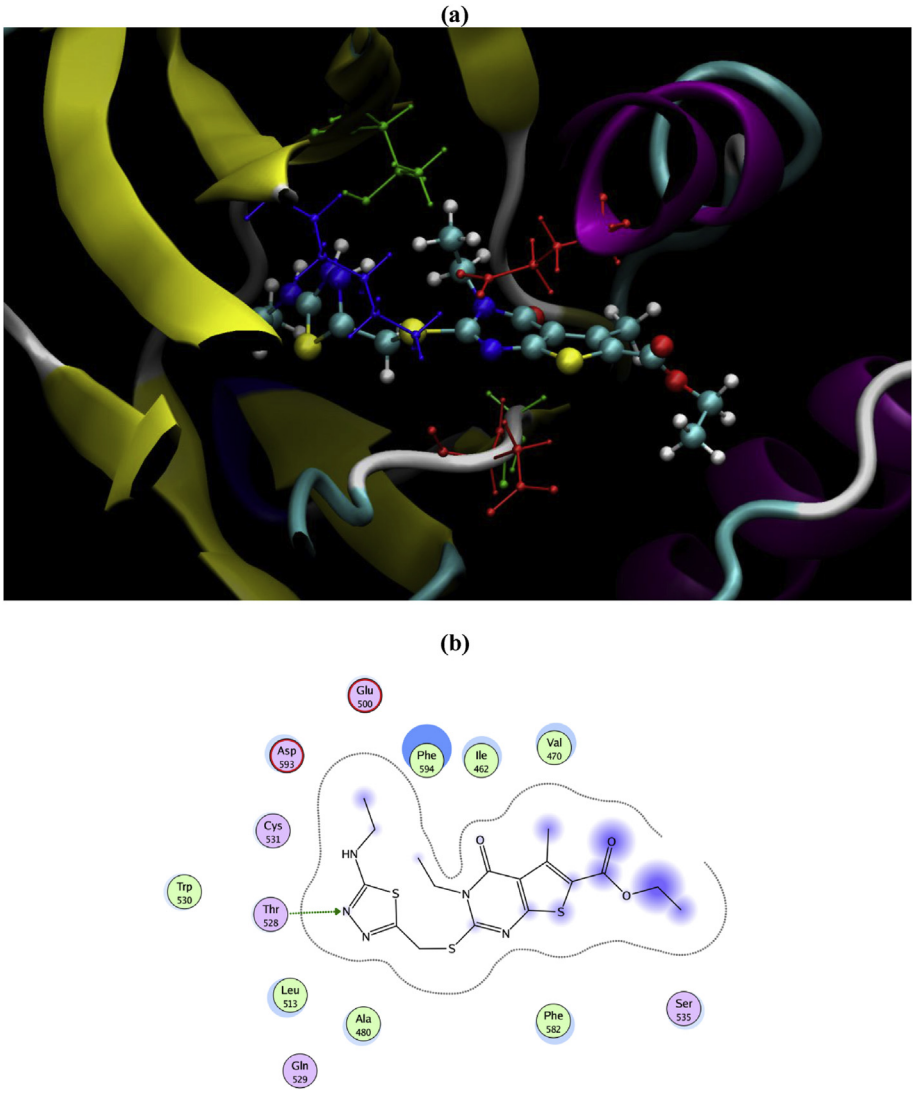


Fig. 6. **(a)** Docking conformation of **6b** with shown amino acid residues Thr528, Asp593, Lys482, Glu500, Gly592; **(b)** 2D representation of the interactions of **6b** with ^{V599E}B-Raf.

24.86; S, 12.46.

*6.1.3. Ethyl 2-amino-4,5,6,7-tetrahydrothiophene-3-carboxylate (**1c**)*

Yield: 82%; Mp. 114–115 °C [1]; IR (KBr): 3300 cm^{-1} (NH), 2920 cm^{-1} (CH_3), 2800 cm^{-1} (CH_2), 1640 cm^{-1} (C=O), 1260 cm^{-1} (C–O); Analysis: Calc. for $C_{11}H_{15}NO_2S$: C, 58.64; H, 6.71; N, 6.22; O, 14.20; S, 14.23; Found: C, 58.74; H, 6.73; N, 6.26; O, 14.19; S, 14.29.

*6.2. Synthesis of 3-ethyl-2-mercaptothieno[2,3-d]pyrimidin-4(3H)-ones **2a-c***

To a solution of 0.025 mol of 2-aminothiophene ***1a-c*** and 0.025 mol of NaOH in DMF (30 ml) 0.025 mol ml ethyl isothiocyanate (2.18 ml) was added dropwise. The mixture was stirred for 3 h and after that poured in 750 ml water. The solution was acidified to pH~5 by use of 50% (*v/v*) acetic acid. The formed precipitate was filtered, washed with water and recrystallized from ethanol.

*6.2.1. 3-Ethyl-2-mercapto-5,6-dimethylthieno[2,3-d]pyrimidin-4(3H)-one (**2a**)*

Yield: 95%; Mp. 253–255 °C; IR (KBr): 3250 cm^{-1} (NH), 2900 cm^{-1} (CH_3), 1660 cm^{-1} (CONH); Analysis: Calc. for $C_{10}H_{12}N_2OS_2$: C, 49.97; H, 5.03; N, 11.66; O, 6.66; S, 26.68; Found: C, 50.02; H, 5.05; N, 11.65; O, 6.71; S, 26.69.

*6.2.2. Ethyl 3-ethyl-2-mercapto-5-methyl-4-oxo-3,4-dihydrothieno [2,3-d]pyrimidine-6-carboxylate (**2b**)*

Yield: 96%; Mp. 252–254 °C; IR (KBr): 3195 cm^{-1} (NH), 2950 cm^{-1} (CH_3), 1740 cm^{-1} (COOEt), 1680 cm^{-1} (CONH), 1100 cm^{-1} (C–O); Analysis: Calc. for $C_{12}H_{14}N_2O_3S_2$: C, 48.30; H, 4.73; N, 9.39; O, 16.09; S, 21.49; Found: C, 48.33; H, 4.78; N, 9.41; O, 16.09; S, 21.45.

*6.2.3. 3-Ethyl-2-mercapto-5,6,7,8-tetrahydrobenzo [4,5]thieno[2,3-d]pyrimidin-4(3H)-one (**2c**)*

Yield: 86%; Mp. 263–266 °C [9]; IR (KBr): 3190 cm^{-1} (NH), 2915 cm^{-1} (CH_3), 2810 cm^{-1} (CH_2), 1640 cm^{-1} (CONH); ^{1}H NMR ($CDCl_3$): 1.35 (t, 3H, CH_3), 1.70 (m, 4H, $(CH_2)_2$), 2.48 (s, 2H, CH_2), 2.70 (s, 2H, CH_2), 3.84 (q, 2H, CH_2), 6.30 (s, 1H, NH, exchangeable with D_2O); Analysis: Calc. for $C_{12}H_{14}N_2OS_2$: C, 54.11; H, 5.30; N, 10.52; O,

6.01; S, 24.07; Found: C, 54.14; H, 5.40; N, 10.59; O, 6.01; S, 23.99.

6.3. General procedure for the synthesis of thieno[2,3-d]pyrimidin-2-yl-thioacetates **3a-c**

A solution of 2-mercapto-thieno[2,3-*d*]pyrimidin-4-one ***2a-c*** (0.01 mol), ethyl 2-chloroacetate (0.01 mol) and NEt_3 (0.01 mol) in 30 ml benzene was refluxed for 4 h. After the reaction was completed, the solid triethylamine hydrochloride was removed through hot filtration. The solvent was removed under reduced pressure and the obtained solid was recrystallized with methanol.

6.3.1. Ethyl 2-((3-ethyl-5,6-dimethyl-4-oxo-3,4-dihydrothieno[2,3-d]pyrimidin-2-yl)thio) acetate (**3a**)

Yield: 81%; Mp. 91–95 °C; IR (KBr): 2920 cm^{-1} (CH_3), 2880 cm^{-1} (CH_3), 2820 cm^{-1} (CH_2), 1740 cm^{-1} (COOEt), 1670 cm^{-1} (CONH), 1120 cm^{-1} (C–O); ^{1}H NMR ($CDCl_3$): 1.24 (t, 9H, $3CH_3$), 2.24 (s, 3H, CH_3), 2.30 (s, 3H, CH_3), 3.84 (s, 2H, CH_2), 4.00 (q, 4H, $2CH_2$); Analysis: Calc. for $C_{14}H_{18}N_2O_3S_2$: C, 51.51; H, 5.56; N, 8.58; O, 14.70; S, 19.65; Found: C, 51.54; H, 5.61; N, 8.56; O, 14.73; S, 19.66.

6.3.2. Ethyl 2-((2-ethoxy-2-oxoethyl)thio)-3-ethyl-5-methyl-4-oxo-3,4-dihydrothieno[2,3-d]pyrimidine-6-carboxylate (**3b**)

Yield: 78%; Mp. 119–122 °C; IR (KBr): 2990 cm^{-1} (CH_3), 2820 cm^{-1} (CH_2), 1750 cm^{-1} (COOEt), 1720 cm^{-1} (COOEt), 1690 cm^{-1} (CONH), 1120 cm^{-1} (C–O); ^{1}H NMR ($CDCl_3$): 1.35 (t, 9H, $3CH_3$), 2.91 (s, 3H, CH_3), 3.99–4.31 (dq, 6H, $3CH_2$), 4.73 (s, 2H, CH_2); Analysis: Calc. for $C_{16}H_{20}N_2O_5S_2$: C, 49.98; H, 5.24; N, 7.29; O, 20.81; S, 16.68; Found: C, 49.88; H, 5.33; N, 7.31; O, 20.71; S, 16.70.

6.3.3. Ethyl 2-((3-ethyl-4-oxo-3,4,5,6,7,8-tetrahydrobenzo [4,5]thieno[2,3-d]pyrimidin-2-yl)thio) acetate (**3c**)

Yield: 82%; Mp. 130–133 °C; IR (KBr): 2950 cm^{-1} (CH_3), 2900 cm^{-1} (CH_3), 2820 cm^{-1} (CH_2), 1740 cm^{-1} (COOEt), 1670 cm^{-1} (CONH), 1100 cm^{-1} (C–O); ^{1}H NMR (DMSO-d_6): 1.19 (t, 3H, CH_3), 1.25 (t, 3H, CH_3), 1.75 (m, 4H, $(CH_2)_2$), 2.69 (t, 2H, CH_2), 2.70 (t, 2H, CH_2), 4.05 (s, 2H, CH_2), 4.12 (t, 2H, CH_2); Analysis: Calc. for $C_{16}H_{20}N_2O_3S_2$: C, 54.52; H, 5.72; N, 7.95; O, 13.62; S, 18.19; Found: C, 54.56; H, 5.75; N, 7.97; O, 13.70; S, 18.22.

6.4. Synthesis of thieno[2,3-d]pyrimidin-2-yl-thioacetohydrazides **4a-c**

A mixture of 0.01 mol thieno[2,3-*d*]pyrimidin-2-yl-thioacetate ***3a-c*** and 0.04 mol hydrazine hydrate in 40 ml absolute ethanol was refluxed for 8 h. The reaction mixture was cooled and the formed crystalline product was filtered and recrystallized with ethanol.

6.4.1. 2-((3-Ethyl-5,6-dimethyl-4-oxo-3,4-dihydrothieno[2,3-d]pyrimidin-2-yl)thio)acetohydrazide (**4a**)

Yield: 69%; Mp. 175–178 °C; IR (KBr): 3200 cm^{-1} (NH_2), 2920 cm^{-1} (CH_3), 2880 cm^{-1} (CH_2), 1660 cm^{-1} (CONH); Analysis: Calc. for $C_{12}H_{16}N_4O_2S_2$: C, 46.13; H, 5.16; N, 17.93; O, 10.24; S, 20.53; Found: C, 46.16; H, 5.26; N, 17.92; O, 10.28; S, 20.51.

6.4.2. Ethyl 3-ethyl-2-((2-hydrazinyl-2-oxoethyl)thio)-5-methyl-4-oxo-3,4-dihydrothieno[2,3-d]pyrimidine-6-carboxylate (**4b**)

Yeild: 63%; Mp. 180–185 °C; IR (KBr): 3240 cm^{-1} (NH_2), 2950 cm^{-1} (CH_3), 2920 cm^{-1} (CH_2), 1720 cm^{-1} (COOEt), 1670 cm^{-1} (CONH), 1250 cm^{-1} (C–O); ^{1}H NMR ($CDCl_3$): 1.36 (dt, 6H, $2CH_3$), 2.89 (s, 3H, CH_3), 4.01 (s, 2H, CH_2), 4.15 (q, 2H, N-CH_2CH_3), 4.38 (q, 2H, O-CH_2CH_3) 7.73 (s, 1H, NH, exchangeable with D_2O); Analysis: Calc. for $C_{14}H_{18}N_4O_4S_2$: C, 45.39; H, 4.90; N, 15.12; O, 17.28; S, 17.31; Found: C, 45.44; H, 4.91; N, 15.15; O, 17.31; S, 17.39.

6.4.3. 2-((3-Ethyl-4-oxo-3,4,5,6,7,8-tetrahydrohydrobenzo [4,5]thieno[2,3-d]pyrimidin-2-yl)thio)aceto hydrazide (**4c**)

Yield: 94%; Mp. 210–214 °C; IR (KBr): 3250 cm^{-1} (NH_2), 2950 cm^{-1} (CH_3), 2880 cm^{-1} (CH_2), 2820 cm^{-1} (CH_2), 1660 cm^{-1} (CONH); Analysis: Calc. for $C_{14}H_{18}N_4O_2S_2$: C, 49.68; H, 5.36; N, 16.55; O, 9.45; S, 18.95; Found: C, 49.71; H, 5.46; N, 16.61; O, 9.38; S, 19.00.

6.5. Synthesis of thieno[2,3-d]pyrimidin-2-yl-thiosemicarbazides **5a-c**

To a suspension of the appropriate hydrazide ***4a-c*** (0.003 mol) in 20 ml absolute ethanol ethyl isothiocyanate (0.036 mol) was added. The mixture was refluxed for 5 h. After cooling the formed precipitate was filtered and recrystallized with ethanol.

6.5.1. N-ethyl-2-(2-(((3-ethyl-5,6-dimethyl-4-oxo-3,4-dihydrothieno[2,3-d]pyrimidin-2-yl)thio)methyl) hydrazinyl)-2-oxoethanethioamide (**5a**)

Yield: 88%; Mp. 197–200 °C; UV (DMF) $\lambda_{max} = 322$ nm; IR (KBr): 3300 cm^{-1} (NH), 2920 cm^{-1} (CH_3), 2880 cm^{-1} (CH_3), 2800 cm^{-1} (CH_2), 1680 cm^{-1} (CONH); ^{1}H NMR (DMSO-d_6): 1.02 (t, 3H, CH_3), 1.26 (t, 3H, CH_3), 2.33 (s, 3H, CH_3), 2.36 (s, 3H, CH_3), 4.08 (m, 6H, $3CH_2$), 7.88 (s, 1H, NH, exchangeable with D_2O), 9.30 (s, 1H, NH, exchangeable with D_2O), 10.14 (s, 1H, NH, exchangeable with D_2O); Analysis: Calc. for $C_{15}H_{21}N_5O_2S_3$: C, 45.09; H, 5.30; N, 17.53; O, 8.01; S, 24.08; Found: C, 45.11; H, 5.40; N, 17.56; O, 8.11; S, 24.13.

6.5.2. Ethyl 3-ethyl-2-(((2-(2-(ethylamino)-2-thioxoacetyl) hydrazinyl)methyl)thio)-5-methyl-4-oxo-3,4-dihydrothieno[2,3-d] pyrimidine-6-carboxylate (**5b**)

Yield: 91%; Mp. 182–184 °C; UV (DMF) $\lambda_{max} = 394$ nm; IR (KBr): 3180 cm^{-1} (NH), 2940 cm^{-1} (CH_3), 2900 cm^{-1} (CH_3), 2880 cm^{-1} (CH_2), 1690 cm^{-1} (CONH), 1270 cm^{-1} (C–O); ^{1}H NMR (DMSO-d_6): 1.04 (t, 3H, CH_3), 1.26 (m, 6H, $2CH_3$), 2.79 (d, 3H, CH_3), 4.00 (m, 2H, CH_2), 4.09 (s, 2H, CH_2), 4.27 (dq, 4H, $2CH_2$), 8.04 (s, 1H, NH, exchangeable with D_2O), 9.35 (d, 1H, NH, exchangeable with D_2O), 9.89 (d, 1H, NH, exchangeable with D_2O); Analysis: Calc. for $C_{17}H_{23}N_5O_4S_3$: C, 44.62; H, 5.07; N, 15.30; O, 13.99; S, 21.02; Found: C, 44.63; H, 5.11; N, 15.40; O, 13.95; S, 21.03.

6.5.3. N-ethyl-2-(2-(((3-ethyl-4-oxo-3,4,5,6,7,8-tetrahydrobenzo [4,5]thieno[2,3-d]pyrimidin-2-yl) thio)methyl)hydrazinyl)-2-oxoethanethioamide (**5c**)

Yield: 96%; Mp. 188–192 °C; UV (DMF) $\lambda_{max} = 322$ nm; IR (KBr): 3200 cm^{-1} (NH), 2920 cm^{-1} (CH_3), 1670 cm^{-1} (CONH); ^{1}H NMR (DMSO-d_6): 1.02 (t, 3H, CH_3), 1.25 (m, 3H, CH_3), 1.77 (m, 4H, $(CH_2)_2$), 2.70 (d, 2H, CH_2), 2.85 (d, 2H, CH_2), 4.08 (m, 6H, $3CH_2$), 7.90 (s, 1H, NH, exchangeable with D_2O), 9.29 (s, 1H, NH, exchangeable with D_2O), 10.15 (s, 1H, NH, exchangeable with D_2O). Analysis: Calc. for $C_{17}H_{23}N_5O_2S_3$: C, 47.98; H, 5.45; N, 16.46; O, 7.52; S, 22.60; Found: C, 48.02; H, 5.39; N, 16.49; O, 7.51; S, 22.62.

6.6. Cyclocondensation of thieno[2,3-d]pyrimidin-2-yl-thiosemicarbazides to 1,3,4-thiadiazoles **6a-c**

The thiosemicarbazide ***5a-c*** (0.001 mol) was added portionwise to 3 ml 98% sulfuric acid at 5 °C by stirring. The reaction mixture was cooled and poured into ice-water and neutralized with NH_4OH. The formed precipitate was filtered and recrystalized wit methanol.

6.6.1. 3-Ethyl-2-(((5-(ethylamino)-1,3,4-thiadiazol-2-yl)methyl) thio)-5,6-dimethylthieno[2,3-d] pyrimidin-4(3H)-one (**6a**)

Yield: 63%; Mp. 208–212 °C; UV (DMF) $\lambda_{max} = 322$ nm; IR (KBr): 3300 cm^{-1} (NH), 2920 cm^{-1} (CH_3), 2880 cm^{-1} (CH_3), 2800 cm^{-1}

(CH_2), 1670 cm^{-1} (CONH); ^1H NMR (DMSO-d_6 + $CDCl_3$): 1.38 (t, 6H, $2CH_3$), 2.24 (s, 6H, $2CH_3$), 3.10 (q, 2H, CH_2), 3.86 (q, 2H, CH_2), 4.41 (s, 2H, CH_2), 6.85 (s, 1H, NH, exchangeable with D_2O); Analysis: Calc. for $C_{15}H_{19}N_5OS_3$: C, 47.22; H, 5.02; N, 18.36; O, 4.19; S, 25.21; Found: C, 47.26; H, 5.03; N, 18.44; O, 4.17; S, 25.23.

*6.6.2. Ethyl 3-ethyl-2-(((5-(ethylamino)-1,3,4-thiadiazol-2-yl) methyl)thio)-5-methyl-4-oxo −3,4-dihydro thieno[2,3-d] pyrimidine-6-carboxylate (**6b**)*

Yield: 95%; Mp. 188–193 °C; UV (DMF) $\lambda_{max} = 394$ nm; IR (KBr): 3420 cm^{-1} (NH), 3350 cm^{-1} (NH), 2920 cm^{-1} (CH_3), 2880 cm^{-1} (CH_3), 2820 cm^{-1} (CH_2), 1720 cm^{-1} (COOEt), 1680 cm^{-1} (CONH); ^1H NMR (DMSO-d_6): 1.27 (dt, 9H, $3CH_3$), 3.02 (s, 3H, CH_3), 4.01–4.29 (dq, 6H, $3CH_2$), 4.71 (s, 2H, CH_2), 8.13 (s, 1H, NH, exchangeable with D_2O); Analysis: Calc. for $C_{17}H_{21}N_5O_3S_3$: C, 46.45; H, 4.82; N, 15.93; O, 10.92; S, 21.88; Found: C, 46.45; H, 4.88; N, 15.95; O, 10.93; S, 21.91.

*6.6.3. 3-Ethyl-2-(((5-(ethylamino)-1,3,4-thiadiazol-2-yl)methyl) thio)-5,6,7,8-tetrahydrobenzo [4,5] thieno[2,3-d]pyrimidin-4(3H)-one (**6c**)*

Yield: 90%; Mp. 202–204 °C; UV (DMF) $\lambda_{max} = 324$ nm; IR (KBr): 3180 cm^{-1} (NH), 2920 cm^{-1} (CH_3), 2880 cm^{-1} (CH_3), 2820 cm^{-1} (CH_2), 1670 cm^{-1} (CONH); ^1H NMR (Pyridine-d_6): 1.27 (t, 6H, $2CH_3$), 1.66 (t, 4H, $(CH_2)_2$), 2.61 (t, 2H, CH_2), 3.05 (s, 2H, CH_2), 3.56 (q, 2H, HN-CH_2CH_3), 4.01 (q, 4H, N-CH_2CH_3), 4.84 (s, 2H, CH_2), 7.20 + 7.57 (ds, 1H, NH, exchangeable with D_2O); Analysis: Calc. for $C_{17}H_{21}N_5OS_3$: C, 50.10; H, 5.19; N, 17.18; O, 3.93; S, 23.60; Found: C, 50.08; H, 5.21; N, 17.23; O, 3.83; S, 23.60.

6.7. Biological assay

The compounds were dissolved in DMSO at the concentration of 4 mg/ml. The investigation was carried out by dilution of the stock solution in ratio 1:10, 1:100, 1:1000 and 1:10,000. Samples of cells, grown in non-modified medium served as a control. After 24 h of incubation of the samples MTS colorimetric assay of cell survival was performed. The wells were treated with MTS solution and incubated for 2 h at 37 °C under 5% carbon dioxide and 95% air atmosphere. The absorbance of each well at 490 nm was read by an automatic microplate reader ("Tecan", Austria).

6.8. Photostability

The study on the photodegradation of the compounds was conducted in a solar simulator SUNTEST CPS equipment (Heraeus, Germany), supplied with an arc aircooled Xenon lamp (Hanau, 1.1 kW, 765 Wm^{-2}), at ambient temperature. The irradiation was performed in solid state of the compounds. The UV–vis absorption spectra were recorded on a spectrophotometer Hewlett Packard 8452A in DMF solution at concentration 10^{-5} mol/L.

6.9. Computational details

The most probable conformers of the studied molecules (including thione-thiol and lactam-lactime tautomerism) were constructed and energy minimized using *Avogadro*'s software [48]. Based on the energy analysis the most stable conformers were selected and optimized by density functional theory (DFT). The theoretical calculations were performed using the Gaussian 09 package [40] of programs. Geometry and vibrational frequencies of the studied species were performed by analytical gradient technique without any symmetry constraint. The results were obtained, employing the B3LYP (Becke's three-parameter non-local exchange [40] and Lee et al. correlation [41] potentials) in conjunction with the 6-311++G** basis set. The optimized structures were further characterized by analytical computations of harmonic vibrational frequencies at the same level.

6.10. Molecular docking

Initial molecular modeling coordinates of the enzyme were taken from the crystal structure of oncogenic mutant ^{V599E}B-Raf kinase domain in complex with *sorafenib* (PDB code: 1UWJ [43]). The inhibitors were doked into an internal pocket formed by the activation segment and the P-loop of ^{V599E}B-Raf (PDB entry code 1UWJ) using MOE software [47]. Conformational search for preparation of the ligands was carried out by LowModelMD method which performs molecular dynamics perturbations along with low frequency vibrational modes with energy window 7 kCal/mol, and conformational limits of 1000. Placement of conformers was prepared according to alpha-triangle method on selected pharmacophores. Scoring of docking poses was performed by affinity dG, calculated with MMFF94x force field. VMD [49] was used to produce 3-D figures of binding modes.

Acknowledgements

The financial support of this work by the National Science Fund of Bulgaria (Contracts RNF01/0110) and Science Fund/Chemical Technology and Metallurgy University grant 11429.

Appendix A. Supplementary data

Supplementary data related to this article can be found at http://dx.doi.org/10.1016/j.ejmech.2016.07.022.

References

[1] R. Dudhea, P.K. Sharma, P. Verma, A. Chaudhary, Pyrimidine As anticancer agent: a review, J. Adv. Sci. Res. 2 (3) (2011) 10–17.
[2] S. Pedeboscq, D. Gravier, F. Casadebaig, G. Hou, A. Gissot, C. Rey, F. Ichas, F. DeGiorgi, L. Lartigue, J.-P. Pometan, Synthesis and evaluation of apoptosis induction of thienopyrimidine compounds on KRAS and BRAF mutated colorectal cancer cell lines, Bioorg. Med. Chem. 20 (2012) 6724–6731.
[3] W.A. El-Sayed, O.M. Ali, R.A.F. Zyada, A.A. Mohamed, A.A.-H. Abdel-Rahman, Synthesis and antimicrobial activity of new substituted thienopyrimidines, their tetrazolyl and sugar derivatives, Acta Poloniae Pharm. Drug Res. 69 (3) (2012) 439–447.
[4] M.A. El-Sherbeny, M.B. El-Ashmawy, H.I. El-Subbagh, A.A. El-Emam, F.A. Badria, Synthesis, antimicrobial and antiviral evaluation of certain thienopyrimidine derivatives, Eur. J. Med. Chem. 30 (5) (1995) 445–449.
[5] Y. Kotaiah, N. Harikrishna, K. Nagaraju, C. Venkata Rao, Synthesis and antioxidant activity of 1,3,4-oxadiazole tagged thieno[2,3-d]pyrimidine derivatives, Eur. J. Med. Chem. 58 (2012) 340–345.
[6] N.L. Shirole, K.D. Shirole, R.D. Deore, R.A. Fursule, G.S. Talele, Synthesis, characterization and pharmacological evaluation of 2-Substituted thieno[2,3-d]pyrimidine-4 (3H)-ones, Asian J. Chem. 19 (7) (2007) 4985–4992.
[7] A. Cannito, M. Perrissin, C. Luu Duc, F. Huguet, C. Gaultier, G. Narcisse, Synthesis and pharmacological activities of some 3-substituted thienopyrimidin-4-one-2-thiones, Eur. J. Med. Chem. 25 (8) (1990) 635–639.
[8] E. Bousquet, G. Romeo, F. Guerrera, A. Caruso, M.A. Roxas, Synthesis and analgesic activity of 3-substituted derivatives of pyrido [3′,2′:4,5]thieno[3,2-d] pyrimidin-4 (3H)-ones, Ed. Schientifica 40 (11) (1985) 869–874.
[9] H.M. Ashour, O.G. Shaaban, O.H. Rizk, I.M. El-Ashmawy, Synthesis and biological evaluation of thieno [2′,3′:4,5]pyrimido[1,2-b] [1,2,4]triazines and thieno[2,3-d][1,2,4]triazolo[1,5-a]pyrimidines as anti-inflammatory and analgesic agents, Eur. J. Med. Chem. 62 (2013) 341–351.
[10] R.D. Hubbard, S.H. Dickerson, H.K. Emerson, R.J. Griffin, M.J. Reno, K.R. Hornberger, D.W. Rusnak, E.R. Wood, D.E. Uehling, A.G. Waterson, Dual EGFR/ErbB-2 inhibitors from novel pyrrolidinyl-acetylenic thieno[3,2-d]pyrimidines, Bioorg, Med. Chem. Lett. 18 (21) (2008) 5738–5740.
[11] M.A. Shaaban, M.M. Ghorab, H.I. Heiba, M.M. Kamel, N.H. Zaher, M.I. Mostafa, Novel thiophenes, thienopyrimidines, and triazolothienopyrimidines for the evaluation of anticancer and augmentation effects of gamma-radiation, Arch. Pharm. 343 (7) (2010) 404–410.
[12] A.A. Abu-Hashem, M.F. El-Shehry, F.A. Badria, Design and synthesis of novel thiophenecarbohydrazide, thienopyrazole and thienopyrimidine derivatives as antioxidant and antitumor agents, Acta Pharm. 60 (3) (2010) 311–323.

[13] Y.D. Wang, S. Johnson, D. Powell, J. McGinnis, M. Miranda, S.K. Rabindran, Inhibition of tumor cell proliferation by thieno[2,3-d]pyrimidin-4(1H)-one-based analogs, Bioorg. Med. Chem. Lett. 15 (16) (2005) 3763–3766.
[14] E. Palaska, G. Sahin, P. Kelicen, N.T. Durlu, G. Altinok, Synthesis and anti-inflammatory activity of 1-acylthiosemicarbazides, 1,3,4-oxadiazoles, 1,3,4-thiadiazoles and 1,2,4-triazole-3-thiones, II Farm. 57 (2) (2002) 101–107.
[15] H.N. Dogan, A. Duran, S. Rollas, G. Sener, M.K. Uysal, D. Gulen, Synthesis of new 2,5-Disubstituted-1,3,4-thiadiazoles and preliminary evaluation of anti-convulsant and antimicrobial activities, Bioorg. Med. Chem. Lett. 10 (9) (2002) 2893–2898.
[16] A. Mavrova, D. Wesselinova, Examination on the citotoxicity of some 2,5-disubstitutes-1,2,4-triazoles and 1,3,4-thiadiazoles and their precursors towards guinea hen cells, J. Univ. Chem. Technol. Metall. 47 (3) (2012) 251–256.
[17] D. Kumar, N.M. Kumar, K.-H. Chang, K. Shah, Synthesis and anticancer activity of 5-(3-indolyl)-1,3,4-thiadiazoles, Eur. J. Med. Chem. 45 (10) (2010) 4664–4668.
[18] X.-W. Kong, Y.-H. Zhang, T. Wang, Y.-S. Lai, S.-X. Peng, Synthesis and cytotoxic evaluation of novel dimethyl [1,1′-Biphenyl]-2,2′-dicarboxylates bearing 1,3,4-Thiadiazole moieties, Chem. Biodiver. 5 (9) (2008) 1743–1752.
[19] J. Sun, Y.-S. Yang, W. Li, Y.-B. Zhang, X.-L. Wang, J.-F. Tang, H.-L. Zhu, Synthesis, biological evaluation and molecular docking studies of 1,3,4-hiadiazole derivatives containing 1,4-benzodioxan as potential antitumor agents, Bioorg. Med. Chem. Lett. 21 (20) (2011) 6116–6121.
[20] M. Juszczak, J. Matysiak, M. Szeliga, P. Pozarowski, A. Niewiadomy, J. Albrecht, W. Rzeski, 2-Amino-1,3,4-thiadiazole derivative (FABT) inhibits the extracellular signal-regulated kinase pathway and induces cell cycle arrest in human non-small lung carcinoma cells, Bioorg. Med. Chem. Lett. 22 (17) (2012) 5466–5469.
[21] D. Kumar, B.R. Vaddula, K.H. Chang, K. Shah, One-pot synthesis and anticancer studies of 2-arylamino-5-aryl-1,3,4-thiadiazoles, Bioorg. Med. Chem. Lett. 21 (8) (2011) 2320–2323.
[22] Y. Li, J. Geng, Y. Liu, S. Yu, G. Zhao, Thiadiazole - a promising structure in medicinal chemistry, Chem. Med. Chem. 8 (1) (2013) 27–41.
[23] A.T. Mavrova, D. Wesselinova, J.A. Tsenov, L.A. Lubenov, Synthesis and anti-proliferative activity of some new thieno[2,3-d]pyrimidin-4(3H)-ones containing 1,2,4-triazole and 1,3,4-thiadiazole moiety, Eur. J. Med. Chem. 86 (2014) 676–683.
[24] N. Sivasubramanian, M.V. Reddy, M. Aravinda, R. Sravanthi, S. Sirisha, Synthesis, characterization, anti-microbial and Anti-Cancer activity of novel heterocyclic system containing bridgehead nitrogen atom, Chem. Sci. Trans. 1 (2) (2012) 401–409.
[25] O.K. Al-Duaij, H.N. Hafez, A.-R.B.A. El-Gazzar, Synthesis of novel series of benzothieno[2,3-d]pyrimidine derivatives, promising anticancer agents, J. Chem. Chem. Eng. 7 (2013) 725–742.
[26] K. Nagaraju, Y. Kotaiah, C. Sampath, N. Harikrishna, C.V. Rao, A facile synthesis of some novel fused [1,2,4]triazolo[3,4-b][1,3,4]thiadiazol derivatives, J. Sulfur Chem. 34 (3) (2013) 264–275.
[27] K. Gewald, E. Schinke, H. Bottcher, Heterocyclen aus CH-aciden Nitrilen, VIII. 2-Amino-thiophene aus methylenaktiven Nitrilen, Carbonylverbindungen und Schwefel, Chem. Ber. 99 (1966) 94–100.
[28] Z. Puterova, A. Krutosikova, D. Vegh, Gewald reaction: synthesis, properties and applications of substituted 2-aminothiophenes, ARKIVOC i (2010) 209–246.
[29] R.W. Sabnis, D.W. Rangnekar, N.D. Sonawane, 2-aminothiophenes by the gewald reaction, J. Heterocycl. Chem. 36 (2) (1999) 333–345.
[30] R.W. Sabins, The Gewald synthesis, Sulfur Rep. 16 (1994) 1–17.
[31] CellTiter 96 Non-Radioactive Cell proliferation assay, Technical Bulletin #TB112, Promega Corporation USA. Revised 12/99.
[32] G. Malich, B. Markovic, C. Winder, The sensitivity and specificity of the MTS tetrazolium assay for detecting the in vitro cytotoxicity of 20 chemicals using human cell lines, Toxicology 124 (3) (1997) 179–192.
[33] M.V. Berridge, A.S. Tan, Characterization of the cellular reduction of 3-(4,5-dimethylthiazol-2-yl)-2,5-diphenyltetrazolium bromide (MTT): subcellular localization, substrate dependence, and involvement of mitochondrial electron transport in MTT reduction, Arch. Biochem. Biophys. 303 (2) (1993) 474–482.
[34] R. Jover, X. Ponsoda, J.V. Castell, M.J. Gomez-Lechon, Acute cytotoxicity of ten chemicals in human and rat cultured hepatocytes and in cell lines: correlation between in vitro data and human lethal concentrations, Toxicol. Vitro 8 (1) (1994) 47–54.
[35] H.H. Tonnesen (Ed.), The Photostability of Drugs and Drug Formulations, second ed., Culinary and Hospitality Industry Publications Services, Weimer, Texas, 2004.
[36] B.D. Glass, C. Novak, M.E. Brown, The thermal and photostability of solid pharmaceuticals, J. Therm. Anal. Cal. 77 (2004) 1013–1036.
[37] Molinspiration Cheminformatics, Molinspiration Property Engine v2015.01, 2015. www.molinspiration.com.
[38] C.A. Lipinski, F. Lombardo, B.W. Dominy, P.J. Feeney, Experimental and computational approaches to estimate solubility and permeability in drug discovery and development settings, Adv. Drug. Del. Rev. 23 (1997) 3–25.
[39] K. Palm, P. Stenberg, K. Luthman, P. Artursson, Polar molecular surface properties predict the intestinal absorption of drugs in humans, Pharm. Res. 14 (5) (1997) 568–571.
[40] M.J. Frisch, G.W. Trucks, H.B. Schlegel, G.E. Scuseria, et al., Gaussian 09, Revision A.1, Gaussian Inc., Wallingford CT, 2009.
[41] P.J. Stephens, F.J. Devlin, C.F. Chabalowski, M.J. Frisch, Ab initio calculation of vibrational absorption and circular dichroism spectra using density functional force fields, J. Phys. Chem. 98 (1994) 11623–11627.
[42] S.M. Wilhelm, C. Carter, L. Tang, D. Wilkie, A. McNabola, H. Rong, C. Chen, X. Zhang, P. Vincent, M. McHugh, Y. Cao, J. Shujath, S. Gawlak, D. Eveleigh, B. Rowley, L. Liu, L. Adnane, M. Lynch, D. Auclair, I. Taylor, R. Gedrich, A. Voznesensky, B. Riedl, L.E. Post, G. Bollag, P.A. Trail, BAY 43-9006 exhibits broad spectrum oral antitumor activity and targets the RAF/MEK/ERK pathway and receptor tyrosine kinases involved in tumor progression and angiogenesis, Cancer Res. 64 (2004) 7099–7109.
[43] P.T.C. Wan, M.J. Garnett, S.M. Roe, S. Lee, D. Niculescu-Duvaz, V.M. Good, Cancer Genome Project, C.M. Jones, C.J. Marshall, C.J. Springer, D. Barford, R. Marais, Mechanism of activation of the RAF-ERK signaling pathway by oncogenic mutations of B-RAF, Cell 116 (6) (2004) 855–867.
[44] E.Z. Elrazaz, R.A.T. Serya, N.S.M. Ismail, D.A. Abou El Ella, K.A.M. Abouzid, Thieno[2,3-*d*]pyrimidine based derivatives as kinase inhibitors and anticancer agents, Int. J. Pharm. Sci. 1 (2) (2015) 33–41.
[45] H. Park, C. Lee, J.S. Yang, B.-Y. Joe, K. Chun, H. Kim, H.Y. Kim, J.S. Kang, J.I. Lee, M.-H. Kim, G. Han, Discovery of thienopyrimidine-based FLT3 inhibitors from the structural modification of known IKKb inhibitors, Bioorg. Med. Chem. Lett. 24 (2014) 2655–2660.
[46] G.K. Packard, P. Papa, J.R. Riggs, P. Erdman, L. Tehrani, D. Robinson, R. Harris, G. Shevlin, S. Perrin-Ninkovic, R. Hilgraf, M.A. McCarrick, T. Tran, Y. Fleming, A. Bai, S. Richardson, J. Katz, Y. Tang, J. Leisten, M. Moghaddam, B. Cathers, D. Zhu, S. Sakata, Discovery and optimization of thieno[2,3-d]pyrimidines as B-Raf inhibitors, Bioorg. Med. Chem. Lett. 22 (2012) 747–752.
[47] Molecular Operating Environment (MOE), 2011.10; Chemical Computing Group Inc., 1010 Sherbooke St. West, Suite #910, Montreal, QC, Canada, H3A 2R7, 2011.
[48] M.D. Hanwell, D.E. Curtis, D.C. Lonie, T. Vandermeersch, E. Zurek, G.R. Hutchison, J. Cheminform 4 (2012) 1–17. Avogadro: an open-source molecular builder and visualization tool. Version 1.0.1, http://www.avogadro.openmolecules.net.
[49] W. Humphrey, A. Dalke, K. Schulten, VMD–visual molecular dynamics, J. Molec. Graph. 14 (1996) 33–38.

Bulgarian Chemical Communications, Special Issue E, (pp. 50 – 53) 2017

In silico investigation of single-chain variable fragment (scFv) antibody, structurally similar to native C1q globular heads

M.A. Rangelov[1*], N.H. Todorova[2], I.G. Tsacheva[3*]

[1] *Institute of Organic Chemistry with Centre of Phytochemistry (IOCCP), Bulgarian Academy of Sciences, Acad. G. Bontchev str. bl. 9, 1113 Sofia, Bulgaria*

[2] *Institute of Biodiversity and Ecosystem Research (IBER), Bulgarian Academy of Sciences, Yurii Gagrin Str.2, 1113 Sofia, Bulgaria*

[3] *Biology Faculty, Sofia University "St. Kliment Ohridski", 8 Dragan Tsankov Blv., 1164 Sofia, Bulgaria*

Received September 29, 2016; Revised February 04, 2017

Homology model of a selected single-chain variable fragment (scFv) inhibitory antibody A1 is generated using Generalized Born/Volume Integral (GB/VI) methodology and MMFF94 force field. Comparative analysis of scFvA1 homology model and ghC1q chains is further used to find conformational and electrostatic similar regions, crucial for the biological binding regions in C1q globular heads.

Key words: homology modeling, anti-C1q scFv

INTRODUCTION

Phage-displayed single-chain variable fragment (scFv) antibodies obtain serious advantages that make them preferable tool for application in research, laboratory diagnostics and medicine. Recent progress in antibody engineering together with the microbial expression systems are milestones for design and production of antibodies for numerous applications [1]. Variety of selection and screening strategies could be used to simultaneously derive many high-affinity scFv with different relevance [2]. Importance of their diverse collection relies on high specificity and selectivity of antibodies, while offering distinct biological profiles in tissue distributions of unique molecules [3].

C1q is the recognizing first subcomponent of the classical complement pathway, which undergo a conformation transition by its activation, exposing neo-epitopes. Naive phage library is used to create a single-chain variable fragment (scFv) antibody, that mimics the globular head regions of native C1q (ghC1q). It is further used in in-silico modelling to characterise crucial for biological binding regions in C1q globular heads.

EXPERIMENTAL

scFv A1 construction and sequencing

'Griffin' library, provided by Greg Winter, MRC, Cambridge, UK, is used to create large, nonimmunized fully human scFv repertoires [4], with high specificity of binding to human self-antigens [5]. This kind of library construction of naturally rearranged V genes in a phagemid vector ensures natural diversity in length of the VH CDR3 and a higher number of functional scFv [2]. ScFv A1, showing functional mimicry with only to the globular head region of C1q, is obtained after several panning rounds. pHEN2 region, containing genes for scFv A1 is amplifyed by using in-situ polymerase chain reaction (PCR) of the Escherichia coli clone and primers LMB3 (5`-CAGGAAACAGCTATGAC-3`) and fd-SEQ1 (5`-GAATTTTCTGTATGAGG-3`), using amplification programm of Liners *et al.* 2005 [6]. The product is purfied and further send for iboth sides sequencing (Macrogen Europe). Derived sequence is deposited in GenBank under accession number KX981596 .

Homology Search

Searches for protein structures that are homologous to a query sequence are performed on a database of protein structures and sequences that have been clustered into families. A scan is performed to create an initial list of candidates using a generalized version of the FASTA methodology [7]. Expectation value (E-Value) is determined for each sequence and low E-Values, that correspond to good scores were used as evaluation criteria.

Homology Model of scFv A1

We performed alignment of the target sequence to the selected parts of best scored selected proteins according to the modified version of Needleman

* To whom all correspondence should be sent:
E-mail: marangelov@gmail.com

© 2017 Bulgarian Academy of Sciences, Union of Chemists in Bulgaria

and Wunsch algorithm [8] with sequence alignment imposed on amino acid BLOSUM 62 substitution matrix. Homology Model is carried out by Boltzmann-weighted randomized modeling procedure using coulomb and generalized Born implicit solvent [9] interaction energies. Best models were further refined by Merck Molecular Forcefield MMFF94 [10] for all energy minimization.

Comparative analysis of scFvA1 homology model and ghC1q chains

Sequence comparison of crystallized globular heads domains of human C1q, according to the 1PK6 PDB and H-chain of generated homology model of scFv A1 is performed, using secondary structure information of those sequences having associated atomic coordinates. The target sequence is sequence-to-group aligned to each one of ghC1q chains. Manual alignment is used for refining CDR frames of scFv A1 H-chain and loops in A-, B- and C- ghC1q.

RESULTS AND DISCUSSION

Sequence and structure similarity analysis

Analysis of the CDR3 regions of scFv clones from the library, both VH and VL, shows considerable variability in their length, which is similar to the distribution of the length of CDR3 in unselected library.

ScFv A1 nucleotide sequence is translated to amino acids (Fig. 1), compared to deposited germ-line V genes and most likely CDR regions in both VL and VH were predicted in VBASE2 [11]. Heavy chain V segment is of the IGHV4 family, while the one of the light chain used IGKV1 subgroup. No J-segment is discovered in the VL, but the junction in VH participated as expected in the CDR3 formation

The scFv A1 model

Sequence alignment is performed using MOE [12] software with database deposited scFv antibodies by BLOSUM 62 algorithm as substitution scoring matrix, with algorithm penalty for gap opening -12 and gap extension -2 and evaluated with E-value accepted $1.e^{-12}$. The first five hits (PDB ID: 1YNL, 1A5F, 1ETZ, 1DEE, 1AD9) showing statistically significant similarity, the most similar one having $E \sim 2.e^{-42}$, were chosen for further analysis (Fig. 2).

Further multiple sequence alignment determines the correspondences between residues of selected related protein chains employing *sequence-derived* and *structure-based* information. BLOSUM 62 substitution matrix is chosen as based on observed alignments and immunoglobulin superfamily having many specific members.

>Amino acid sequence of H-chain scFv A1

RCSSRSRGAGLLKPSETLSLTCAVYGGSFSGYYWSWIRQPPGKGLEWIGEINHSGSTNYNPSLKSRVTISVDTSKNQFSLKLSSVTAADTAVYYCARSHSAAWGQGTLVTVS

>Amino acid sequence of L-chain scFv A1

DIQLTQSPSFLSASVGDRVTITCRASQGISSYLAWYQQKPGKAPKLLIYAASTLQSGVPSRFSGSGSGTEFTLTISSLQPEDFATYHCQQLNSY

CDR analysis of H-chain scFv A1

GGSFSGYY....___INHSGST...___ARSHSAA

----CDR1---> <--CDR2--> <---CDR3----

CDR analysis of L-chain scFv A1

QGISSY.....___AAS.....___QQLNSY

----CDR1---> <--CDR2--> <---CDR3----

Fig. 1. ScFv A1 H- and L-chain amino acid sequence, derived from nucleotide sequence, using standard genetic code in VBASE2, with predicted CDR 1, 2 and 3 in H- and L-chains.

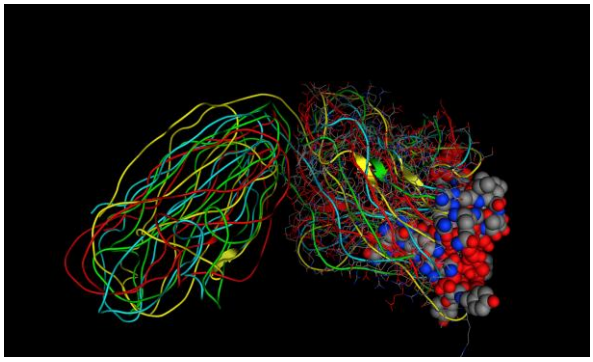


Fig. 2. Comparison of scFv VL and VH structure to high scored similar PDBs of crystallized antibodies, shown in different colors. CDR1, 2 and 3 of VH is visualized as CPK.

Homology model of scFv A1 is generated using Generalized Born/Volume Integral (GB/VI) methodology and MMFF94 force field (Fig. 3).

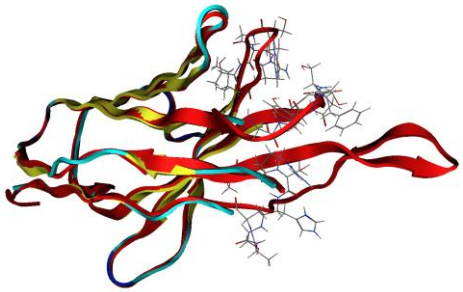


Fig. 3. Representation of the known 3D structure of crystallized antibodies in red and the generated model backbone of scFv A1 in color coding (yellow beta-structure, blue for loops).

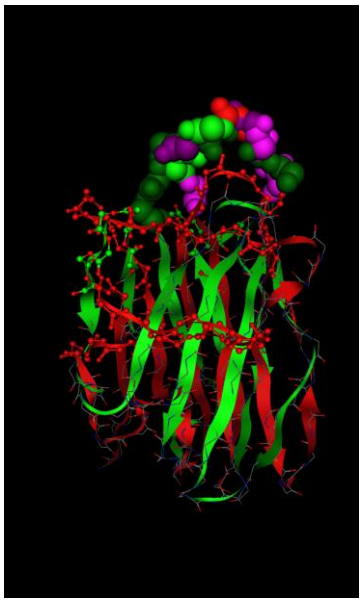


Fig. 4. CDR1 H-chain scFv A1 according to the model: GGSFSGYY dark color and A-chain of C1q: TTNKGLF; light color.

ScFv A1 H-chain and ghC1q comparison and loop similarity analysis

ScFv A1 CDR1, 2 and 3 were compared loop by loop with C1q separate chains loop. Similarity in using AA coding is: polar + and – separately; polar uncharged and nonpolar. Backbone is analyzed only as amino acid side chain (R) polarity due to the mobility of R in solution, and not as a chain position in the loop. The following color coding is formed according to amino acid R-chain properties analysis (Table 1):

Table 1. Good correlation of R polarity between C1q globular head chains and CDR loops of H-chain scFv A1 is achieved for B-chain and CDR2, A-chain and CDR1 and C-chain and CDR3.

CDR1	H		G	G	S	F	S	G	Y	Y	
Ac1q		55-60	L	S	Q	W	E	I	C	L	
Bc1q		82-91	D	Y	A	Y	N	T	F	Q	V
Cc1q		79	H	T	S	K	T	N	Q	V	
CDR2	H		I	N	H	S	G	S	T		
Ac1q		121-128	D	A	E	S	G	Q	Y	I	
Bc1q		116-123	G	N	E	G	A	N	S	I	
Cc1q		55-63	A	S	H	T	A	N	L	C	
CDR3	H		A	R	S	H	S	A	A		
Ac1q		81-88	T	T	N	K	G	L	F	Q	
Bc1q		36-43	A	S	S	R	G	N	L	C	
Cc1q		112-119	V	G	I	Q	G	S	D	S	

R,H,K -> positively charged in darker gray; D,E -> negatively charged in dark gray; S,T,N,Q,P,C -> polar uncharged (H-bonds) in gray; G,A,V,I,L,M,F,Y,W -> hydrophobic in light gray.

CONCLUSIONS

Based on the nucleotide sequence of an inhibitory scFv A1, a structural 3D model of resulting polypeptide chain is generated, as homology model according to alignment on the deposited crystallized scFv PDBs. The resulting structure is used to find conformational (Fig. 4) and electrostatic similar regions between homology structure and native human C1q globular heads. This similarity helps to clarify crucial recognising regions from C1q molecule. The presented model will be further helpful giving insights into new scFv binding properties that represent a step toward understanding the recognition mechanisms of C1q and their biological targets.

REFERENCES

1. Z.A. Ahmad, S.K. Yeap, A.M. Ali, W.Y. Ho, N.B.M. Alitheen, M. Hamid, *Clin Dev Immunol.*, **2012**, 1 (2012).
2. S. Lennard, Standard Protocols for the Construction of scFv Libraries, Vol. 178 Methods in Molecular Biology Series, Humana Press, Inc., Tutowa NJ, 2002.
3. A.L. Nelson, *Mabs*, **2**, 77 (2010).
4. A.S. Zlatarova, I. Tsacheva, M.S. Kojouharova, *Biotechnol. & Biotechnol. Eq.*, **19**, 2 (2005).

5. A.D. Griffiths, M. Malmqvist, J.D. Marks, J.M. Bye, M.J. Embleton, J. McCafferty, M. Baier, K.P. Holliger, B.D. Gorick, N.C. Hughes-Jones, H.R. Hoogenboom, G. Winter, *The EMBO Journal*, **12**, 725 (1993).
6. F. Liners, W. Helbert, P. Van Cutsem, *Glycobiology*, **15**, 849 (2005).
7. W. R. Pearson, *Meth. Enz.*, R. F. Doolittle, ed. (San Diego: Academic Press) **266,** 227 (1996).
8. S.B. Needleman, C.D. Wunsch, *Journal of Molecular Biology*, **48**, 443 (1970).
9. P. Labute, *J. Comp. Chem.*, **29**, 1693 (2008).
10. T.A. Halgren, *J. Comput. Chem.*, **17**, 490 (1996).
11. I. Retter, H.H. Althaus, R. Münch, W. Müller, *Nucleic Acids Res.*, **33** (Database issue), D671 (2005).
12. Molecular Operating Environment (MOE), 2011.10; Chemical Computing Group Inc., 1010 Sherbooke St. West, Suite #910, Montreal, QC, Canada, H3A 2R7, 2011.

In silico ИЗСЛЕДВАНЕ НА ЕДНОВЕРИЖНИ АНТИТЕЛА (scFv), СТРУКТУРНО ПОДОБНИ НА НАТИВНИТЕ ГЛОБУЛАРНИ ФРАГМЕНТИ НА C1q

М.А. Рангелов[1*], Н.Х. Тодорова[2], И.Г. Цачева[3*]

[1] Институт по органична химия с Център по фитохимия (ИОХЦФ), Българска академия на науките, ул. "Акад. Г. Бончев" бл. 9, 1113 София, България
[2] Институт по биоразнообразие и екосистемни изследвания (ИБЕИ), Българска Академия на Науките, ул. "Юрий Гагарин" 2, 1113 София, България
[3] Биологически факултет, Софийски университет "Св. Климент Охридски", бул. "Драган Цанков" 8, 1164 София, България

Постъпила на 29 септември 2016 г.; Коригирана на 4 февруари, 2017 г.

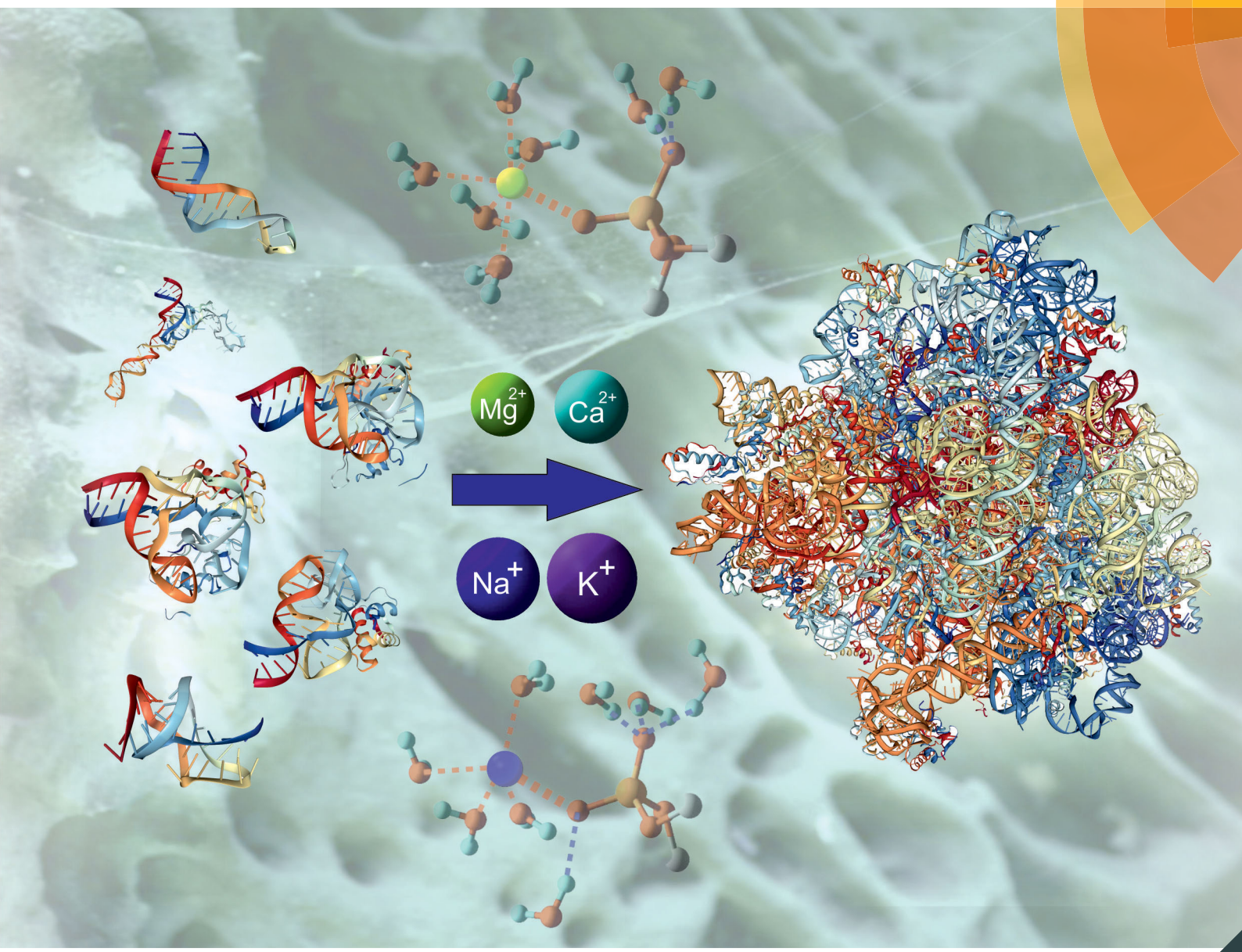
(Резюме)

Генериран е хомоложен модел на избрано едноверижно инхибиращо антитяло (single-chain variable fragment (scFv) A1 посредством алгоритъма Generalized Born/Volume Integral (GB/VI) и MMFF94 силово поле. Анализиран е хомоложния модел на scFvA1 спрямо глобуларните фрагменти на C1q (ghC1q) резултатите от анализа са използвани за откриване на конформационни и електростатични региони на подобие, критични за биологичните функции на свързване в глобуларните региони на C1q.

Volume 10 | Number 5 | May 2018 | Pages 653–770

Metallomics

rsc.li/metallomics



ISSN 1756-591X

ROYAL SOCIETY OF CHEMISTRY

CRITICAL REVIEW
Georgi N. Vayssilov *et al.*
Interaction of Na^+, K^+, Mg^{2+} and Ca^{2+} counter cations with RNA

Indexed in Medline!

Metallomics

CRITICAL REVIEW

View Article Online
View Journal | View Issue

Published on 11 April 2018. Downloaded by University of California - Santa Barbara on 8/5/2018 1:51:21 PM.

Check for updates

Cite this: *Metallomics*, 2018, **10**, 659

Interaction of Na^+, K^+, Mg^{2+} and Ca^{2+} counter cations with RNA

Stefan K. Kolev,[a] Petko St. Petkov,[b] Miroslav A. Rangelov,[c] Dimitar V. Trifonov,[d] Teodor I. Milenov[a] and Georgi N. Vayssilov*[b]

Received 25th February 2018,
Accepted 10th April 2018

DOI: 10.1039/c8mt00043c

rsc.li/metallomics

Alkaline and alkaline earth ions, namely Na^+, K^+, Mg^{2+} and Ca^{2+}, are critical for the stability, proper folding and functioning of RNA. Moreover, those metal ions help to facilitate macromolecular interactions as well as the formation of supramolecular structures (*e.g.* the ribosome and the ribozymes). Therefore, identifying the interactions between ions and nucleic acids is a key to the better comprehension of the physical nature and biological functions of those biomolecules. The scope of this review is to highlight the preferential location and binding sites of alkaline and alkaline earth metal ions compensating the negatively charged backbone of nucleic acids and interacting with other electronegative centers, focusing on RNA. We summarize experimental studies from X-ray crystallography and spectroscopic analysis (infrared, Raman and NMR spectroscopies). Computational results obtained with classical and *ab initio* methods are presented afterwards.

1. Introduction

The scope of this review is to highlight the preferential location and binding sites of Na^+, K^+, Mg^{2+} and Ca^{2+} metal ions compensating the negatively charged backbone of nucleic acids (NA) and interacting with other electronegative centers in those molecules, focusing on RNA. Metal ions are necessary to neutralize the negatively charged phosphate groups in the NA backbone. Na^+, K^+, Mg^{2+} and Ca^{2+} are exactly the counter cations that play a key role in maintaining the stability, proper folding and functioning of nucleic acids.[1–3] Thus, Na^+, K^+, Mg^{2+} and Ca^{2+} were chosen for the review because of their biological importance. The ions carrying single positive charge, Na^+, K^+, form the ionic atmosphere around nucleic acids.[4] On the other hand, divalent ions, Mg^{2+}, Ca^{2+}, can bind to specific parts of the

[a] *Acad. E. Djakov Institute of Electronics, Bulgarian Academy of Sciences, 72 Tzarigradsko Chaussee Blvd., 1784 Sofia, Bulgaria*
[b] *Faculty of Chemistry and Pharmacy, University of Sofia, Boulevard James Bouchier 1, 1126 Sofia, Bulgaria. E-mail: gnv@chem.uni-sofia.bg*
[c] *Laboratory of BioCatalysis, Institute of Organic Chemistry, Bulgarian Academy of Sciences, Str. Acad. G. Bontchev, Bl. 9, 1113 Sofia, Bulgaria*
[d] *BioDiscovery, Pensoft, Prof. Georgi Zlatarski Street 12, 1700 Sofia, Bulgaria*



Stefan K. Kolev

Stefan K. Kolev earned his MS from the University of Sofia "St. Kliment Ohridski", Bulgaria, graduating summa cum laude in 2007, and his PhD in Chemistry from the University of Sofia in 2014 for his research in the area of computational chemistry. From 2013 to 2016, he worked as a chemical technologist at Bioinnovative Ltd, Varna, Bulgaria. Dr Kolev is currently an Assistant professor at the Institute of Electronics, Bulgarian Academy of Sciences. His current research is focused on the physical properties of carbon-based materials and computational chemistry of biologically inspired structures.



Petko St. Petkov

Petko Stoev Petkov studied Chemistry and completed his PhD at the University of Sofia "St. Kliment Ohridski", Bulgaria. He did his post-doctoral research in computational modeling of materials at the school of engineering and science, Jacobs University Bremen, and in Wilhelm-Ostwald-Institute at Leipzig University in Germany. He habilitated for Theoretical chemistry in 2018 at the Faculty of Chemistry and Pharmacy, University of Sofia. His research is focused on computational modeling of structure and properties of different class of materials (bio-polymers, MOFs, COFs, zeolites).

Published on 11 April 2018. Downloaded by University of California - Santa Barbara on 8/5/2018 1:51:21 PM.

NA backbone, thus stabilizing the secondary and tertiary structure.[5] The presence of metal ions is required so that the structural integrity of chromosomes in various living cells (including mammalian cells) is preserved.[6,7] These ions ensure proper folding of the chromosomal DNA. In addition to neutralizing the negative charge of the backbone and maintaining the spatial form of DNA and RNA, metal ions act as mediators of the interaction between different macromolecules and formation of supramolecular structures.[5,8–10] A typical example is the stabilization of the whole ribosome, containing both RNA and proteins.[11–16] Another example is the participation of Mg^{2+} for inducing conformational changes at the internal ribosome entry site of the hepatitis C virus.[17] Some metal ions can as well be used as dopants capable of changing the electro-chemical and physical properties of NA in order to produce new materials with applications in electronics and photonics.[18]

Interactions between metal ions and various DNA or RNA sequences have been investigated by various experimental techniques. The centers, where mono- and divalent ions bind to macromolecules, have been characterized in solution as well as in crystal phase by NMR spectroscopy.[8,9,19–21] Vibrational techniques have been used as well, including infrared (IR) spectroscopy[22,23] and Raman spectroscopy.[24–29] The interactions between the ions and phosphate group have been analyzed *via* the symmetric and asymmetric vibrations of the later. Model esters of the phosphoric acid with alcohols were used to help assign the phosphate vibrations.[30–32] Also, low frequency vibrations were found to be indicative for the presence of alkali metal ions near the phosphate groups of DNA.[33]

The locations of the metal ions in crystal phase can be determined by X-ray crystallography.[8,9,11,12,34–38] However, it is often difficult to determine exact positions due to irregular distribution of the ions. A specific problem is distinguishing Na^+ ion from the water molecules.[8] Another complication in the interpretation of the results is the different structure of biomolecules in the crystal form and in solution. Experimental data derived from solution based systems at physiological conditions are more relevant for biological systems, but the techniques used in these studies (NMR, EPR, vibration spectroscopies) give only indirect information about the metal



Miroslav A. Rangelov

Miroslav A. Rangelov studied organic and analytical chemistry at University of Sofia "St. Kliment Ohridski", Faculty of Chemistry and completed his PhD at the Institute of Organic Chemistry with Centre of Phytochemistry, Bulgarian Academy of Sciences, where it works thereafter. His research focuses on the computational modeling of biomolecular systems.



Dimitar V. Trifonov

Dimitar Trifonov studied Medical and Pharmaceutical Biotechnology at the University of Applied Sciences Krems (Krems an der Donau, Austria). He is an author of research articles and reviews on drug discovery and development and works as an assistant editor for BioDiscovery. His research interests include areas such as molecular biology, pharmacology and toxicology.



Teodor I. Milenov

Dr Teodor I. Milenov studied chemical engineering in 1980–1985. Later on he completed his PhD in Solid State Physics at the Institute of Solid State Physics-Bulgarian Academy of Sciences (ISSP-BAS). He was promoted to an Associate Professor position in the ISSP-BAS in 2000. He was appointed Laboratory Head of the newly founded Laboratory of Multifunctional materials in the Institute of Electronics – Bulgarian Academy of Sciences in 2017. His research interests are focused on the simulations/synthesis/characterization by XRD; TEM; SEM; XP, IR and Raman spectroscopies of carbon phases, complex oxides and semiconductors.



Georgi N. Vayssilov

Georgi N. Vayssilov is Professor in the University of Sofia "St. Kliment Ohridski", Bulgaria. He holds PhD in Organic Chemistry and DSc in Theoretical Chemistry, and was Humboldt fellow in the Technical University of Munich. He is co-author of more than 100 scientific publications in the field of computational modelling of different types of inorganic, organic and biochemical systems and processes. Prof. Vayssilov served as President of the Federation of European Zeolite Associations, of the Humboldt Union in Bulgaria, and of the Executive board of the Bulgarian Science Fund.

This journal is © The Royal Society of Chemistry 2018

Published on 11 April 2018. Downloaded by University of California - Santa Barbara on 8/5/2018 1:51:21 PM.

ion–nucleic acid interactions. In most cases these techniques can yield only qualitative results.

The structure and processes taking place in the studied systems, derived from the experimental techniques, may be complemented by simulations, based on different theoretical methods. Commonly used theoretical approaches for simulation of the dynamics of biomolecules such as proteins, DNA or RNA are classical molecule dynamics (MD)[39–41] and Monte Carlo (MC) methods.[42] As the classic methods for MD simulations are parameterized for strictly defined systems, they can yield precise results if the parameterization is appropriate for the studied system.[43] In particular, the description of the local interactions of the metal ions with nucleic acid backbone within these methods strongly depends on the force field parameters. On the other hand, those interactions can be described adequately by simulations based on quantum chemical methods as most often density functional theory approach is used. Properly selected methods of first-principles quantum chemistry can precisely describe all types of interactions between atoms, ions, molecules or functional groups in the system, including electrostatic interactions, electron transfer and transitions, mutual polarization, Pauli repulsion. In addition to direct simulations of relevant systems, quantum chemical methods are used to parameterize potentials for the specific interactions employed in the classic MD or MC simulations.[44] A more detailed evaluation of the advantages, disadvantages and applications of classical and quantum mechanics as well as hybrid quantum mechanics-molecular mechanics methods for simulating the structure and properties of RNA can be found in the work of Ditzler *et al.*[45]

The application of quantum chemical methods can be done by structural optimization or *ab initio* dynamical simulations of biomolecule's fragments of interest. Examples of the optimization approach are studies of RNA fragments, containing Na^+ or Mg^{2+} ions. The water phase is usually modeled as a continuum solvent.[46] Quantum mechanical/molecular mechanical (QM/MM) methods can also be applied.[45,47] By performing cluster model, non-periodic simulations with implicit solvation, it has been determined that Na^+ and Mg^{2+} ions have binding affinity to the phosphate groups of RNA. The affinity of Mg^{2+} is higher than that of Na^+.[46] The other approach, *ab initio* molecular dynamic simulations, has been successfully used to determine the behavior of metal ions in various systems. Such systems include carbonates, or Na^+ and Mg^{2+} cations with RNA, studied in aqueous solutions.[48,49]

In the present review, we summarize results for RNA, based on experimental studies from X-ray crystallography and spectroscopic analysis (infrared, Raman and NMR spectroscopies). Computational results obtained with classical and *ab initio* methods are presented afterwards. In some parts of the review structures of DNA are also discussed.

2. Investigation of metal ions in nucleic acids by X-ray crystallography

2.1. Studies of short RNA sequences

The location of alkaline (Na^+ and K^+) and alkaline earth (Mg^{2+} and Ca^{2+}) ions in RNA or DNA molecules can be determined by X-ray crystallographic analysis with a relatively good spatial resolution, around 200 pm. High resolution has been achieved with small RNA/DNA sequences (less than 100 nucleotides).[50–52] RNA fragments from viral[35,53–55] or bacterial origin[36,56,57] have been used in the X-ray crystallographic studies. However, human RNA has also been utilized.[58] One should note that the structures of biomolecules in the living cells differ from those obtained from crystallographic images. The XRD results represent a single picture in time, without dynamical changes, while in the living cells biomolecules and ions interact dynamically in order to carry out their functions. Moreover, solid state RNA and DNA molecules have restricted conformational freedom compared to aqueous solution. The results are also affected by the low temperature, 100–120 K, at which the XRD measurements are performed.[37]

Tables 1–4 contain X-ray crystallographic data of the corresponding metal ions, interacting with RNA molecules (less than 100 nucleotides). Only structures with a resolution better than 200 pm are selected. Those examples consist of short sequences, because their aim is to present the first coordination shell of the ions, with maximal resolution and precision. High resolution is

Table 1 Examples of atoms, which are in direct contact with selected Mg^{2+} ions and form their first coordination shell. All listed results are obtained from X-ray crystallographic data for RNA molecules, the corresponding reference is shown in parentheses. The distances are given in pm

PDB code		*R*(Mg–O) or *R*(Mg–N)		
Resolution	Ion #	H_2O	PO_4^-	Others
2OE5/150[58]	Mg 103	212, 225, 202, 217, 200, 200		
Human ribosomal decoding site	Mg 104	216, 221, 192, 218, 216, 193		
1F27/130[51]	Mg 34	221, 209, 199, 204, 246, 204, 219		Mg 39–288
Synthetic biotin-binding pseudoknot	Mg 35	204, 209, 208		O4U-231
	Mg 36	203, 216, 212, 206, 216	201	
	Mg 37	230, 224, 207, 197, 197	192	
	Mg 39	202, 225, 196, 196, 211, 213, 307		Mg 34–288
2A43/134[54]	Mg 201	209, 213, 227, 230, 224		O6G-237
Luteoviral RNA pseudoknot	Mg 207	216, 218, 210, 209, 210, 219, 312		
354D/150[36]	Mg 200	219, 212, 229, 197, 226, 190		
Loop E from *Escherichia coli* 5S ribosomal RNA	Mg 201	227, 247, 221, 181, 214	205	Mg 202–270
	Mg 202	241, 220, 188, 211, 268	214	Mg 201–270
	Mg 203	208, 216, 194, 232, 239, 221		
	Mg 204	227, 227, 222, 235, 201		O6G-260

Published on 11 April 2018. Downloaded by University of California - Santa Barbara on 8/5/2018 1:51:21 PM.

Table 2 Examples of atoms, which are in direct contact with selected Ca^{2+} ions and form their first coordination shell. All listed results are obtained from X-ray crystallographic data for RNA molecules, the corresponding reference is shown in parentheses. The distances are given in pm. O2′ and O3′ denote corresponding oxygen atoms in the ribose moiety

PDB code		*R*(Ca–O)		
Resolution	Ion #	H_2O	PO_4^-	Others
397D/130[53]	Ca 48	242, 236, 237	232, 228, 232	
HIV-1 trans-activation region RNA fragment	Ca 49	241, 246, 242, 233, 236, 248	236	
	Ca 50	238, 249, 234, 244, 237, 244	232	
	Ca 51	251, 266, 247, 217, 247, 242, 241, 242		
1J8G/61[52]	Ca 509	245, 255, 255, 257, 261, 252		O2′-271, O3′-257
RNA tetraplex (UGGGGU)(4)	Ca 510	260, 271, 268, 256, 253, 258	253	O4U-255
	Ca 511	260, 269, 280, 218		O2′-276, O3′-276
2ZY6/175[50]	Ca 102	238, 243, 235, 237, 235	231	
Modified transfer RNA fragment TPHE39A	Ca 103	239, 247, 230, 242	221	O6G-256
	Ca 104	242, 252, 240, 250, 242, 243, 253		
	Ca 105	225, 230, 267, 220, 248, 252		O4U-258
	Ca 106	241, 228, 255	228, 232	O2C-231
	Ca 107	239, 230, 236, 249, 270		
	Ca 108	236, 223, 246		O6G-237

Table 3 Examples of atoms, which are in direct contact with selected Na^+ ions and form their first coordination shell. All listed results are obtained from X-ray crystallographic data for RNA molecules, the corresponding reference is shown in parentheses. The distances are given in pm. O2′ and O4′ denote corresponding oxygen atoms in the ribose moiety

PDB code		*R*(Na–O) or *R*(Na–N)		
Resolution	Ion #	H_2O	PO_4^-	Others
434D/116[57]	Na 8	255, 222, 223, 296, 294		
435D/140[57]	Na 1	241, 210, 241, 224		
	Na 8	222, 211		
466D/116[56]	Na 102	231, 231, 220, 220, 276, 276		
3ND3/137[59]	Na 19	225, 228, 228, 233		O2′-255, O4′-257
1J8G/61[52]	Na 512			O4U-235, 235, 235, 235
	Na 513	240		O4U-237, 237, 237, 237
1L2X/125[35]	Na 61	267	269	O2′-288, N3G-284, N7A-309
	Na 62	277	274	O2′-271, O2C-274
	Na 63	293	265	O2′-259, O4′-305
3ND4/152[59]	Na 19	224, 239, 256, 262, 216		N7A-264

Table 4 Examples of atoms, which are in direct contact with selected K^+ ions and form their first coordination shell. All listed results are obtained from X-ray crystallographic data for RNA molecules, the corresponding reference is shown in parentheses. The distances are given in pm. O2′, O3′ and O4′ denote corresponding oxygen atoms in the ribose moiety

PDB code		*R*(K–O)		
Resolution	Ion #	H_2O	PO_4^-	Others
2QEK/180[60]	K 9001	275, 274		O4U-275, O6G-273
	K 9002	288		O4U-283, O6G-275
	K 9003	282, 268, 307		O4U-267, O6G-261
3C44/200[60]	K A 25	285		O4′-295
	K B 25	274		O4U-268, O6G-266
	K B 28	291		O2′-298, O3′-303
2OIY/160[34]	K A 24	302, 288, 321, 305		O2C-277, 286
	K B 24	296, 251, 277		O2′-278, 320, O2C-273, O4′-296
	K A 25	292, 305, 308, 321		O6G-305, 291, O4U-278
1ZCI/165[55]	K A 24	260, 274, 272, 271		O6G-270, O4U-262
	K B 24	286, 268, 290, 261		O6G-265, O4U-258
	K C 24	261, 276, 312, 272		O6G-274, O4U-264
	K D 24	263, 270, 265, 270		O6G-271, O4U-261

difficult to be achieved in larger amorphous systems, like the whole ribosomal subunits.[11] Thus, the chosen structures are either parts of larger biomolecules, or short synthetic sequences.[34–36,50–60] Molecules classified as small RNAs have not been included.[61] The files with the corresponding PDB codes can be found in the Protein Data Bank (http://www.rcsb.org).

Table 1 shows data from PDB files of various structures containing Mg^{2+} ions forming complexes with RNA molecules.

 This journal is © The Royal Society of Chemistry 2018

Published on 11 April 2018. Downloaded by University of California - Santa Barbara on 8/5/2018 1:51:21 PM.

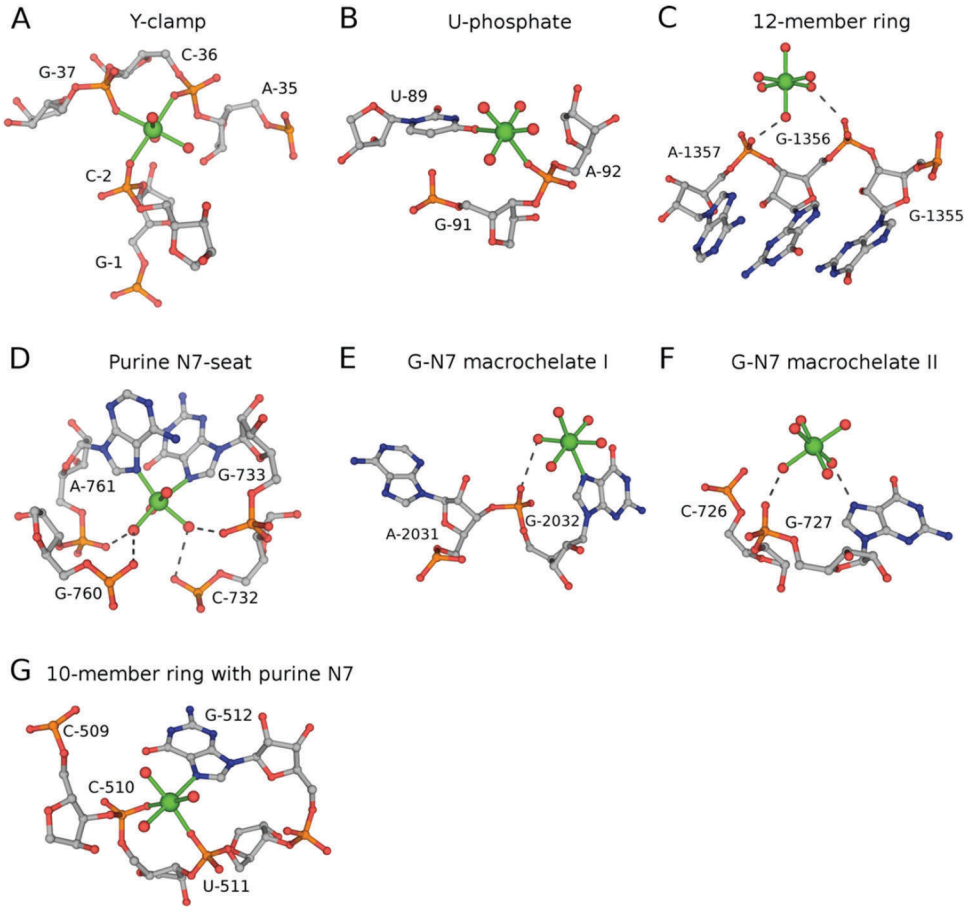


Fig. 1 Magnesium-binding architectures (motifs) in RNA crystal structures as reported by Zheng *et al.*[58] Mg^{2+} ions are shown in green. Hydrogen bonds are shown as gray dashed lines. The motif-forming nucleotides are labeled. (Reprinted from ref. 58 under Creative Commons CC BY License, Copyright 2015 Oxford University Press.)

The chosen structures include the loop E from *Escherichia coli* 5S ribosomal RNA;[36] synthetic biotin-binding pseudoknot;[51] luteoviral RNA pseudoknot,[54] and human ribosomal decoding site fragment.[58] Zheng *et al.* identified seven Mg^{2+}-binding motifs in RNA crystal structures: a Y-clamp motif (Fig. 1A); a U-phosphate motif (Fig. 1B); a 12-member ring motif (Fig. 1C); a purine N7-seat motif (Fig. 1D); G-N7 macrochelates I and II motifs (Fig. 1E and F).[62] A 10-member ring with purine N7 motif has also been observed, Fig. 1G.

Due to its strong electrostatic field, the divalent magnesium cation has high affinity toward electronegative atoms and groups. The most frequent coordination number of Mg^{2+} is 6 (Table 1 and Fig. 1), which corresponds to 6 electronegative centers, arranged octahedrally. Such centers include the oxygen atoms of water molecules, denoted below as $O(H_2O)$, and O atoms of phosphate groups, belonging to nucleic acid backbone. Nitrogen or oxygen atoms of the nucleobases are included in the coordination shells of Mg^{2+} ions in rare cases. The Mg^{2+}–$O(H_2O)$ distances vary between 181 and 268 pm for double-stranded RNA complexes (Table 1). The average Mg^{2+}–$O(H_2O)$ distance, observed in Mg^{2+} complexes with DNA is 207.5 pm. This value is determined for structures composed of double-stranded DNA, consisting of less than 100 nucleotides.[37] When Mg^{2+} ions are directly bonded to an oxygen atom of the phosphate groups in the Mg^{2+}–RNA complex, the corresponding Mg^{2+}–O is in the range of 200–215 pm. The average distance between the Mg^{2+} ion and PO_4^- group in DNA complexes is about 203 pm.[37]

A typical example of magnesium ion, directly bonded to a phosphate group is Mg^{2+} 201 from PDB 354D, with Mg^{2+}–$O(PO_4^-)$ distance of 205 pm (Fig. 2A). Magnesium ions can also make contacts with the PO_4^- groups through water molecules, like Mg^{2+} 200 from PDB 354D (Fig. 2B). An example of the rare case, where the Mg^{2+} ion is coordinated to the electronegative centers of nucleobases, is Mg^{2+} 201 ion from PDB 2A43 (Fig. 2C). The Mg^{2+} 201 ion is directly bonded to the O6 oxygen atom of guanine with Mg^{2+}–O6G distance of 237 pm.[54] Another example is Mg^{2+} 204 from PDB 354D, where the Mg^{2+}–O6G distance is 260 pm.[36] The oxygen atom O4 of uracil can also act as a ligand for the coordination of Mg^{2+} ions, as the Mg^{2+} 35 from PDB 1F27 with Mg^{2+}–O4U distance of 231 pm.[51] The Mg^{2+} ions can also be coordinated to the N7 nitrogen atoms of guanine with Mg^{2+}–N7G distances of 233 pm as reported for Mg^{2+}–DNA complexes.[37]

Crystallographic data for the complexes of Ca^{2+} is presented in Table 2. The chosen RNA structures, interacting with the ions, include: modified transfer RNA fragment TPHE39A;[50]

Published on 11 April 2018. Downloaded by University of California - Santa Barbara on 8/5/2018 1:51:21 PM.

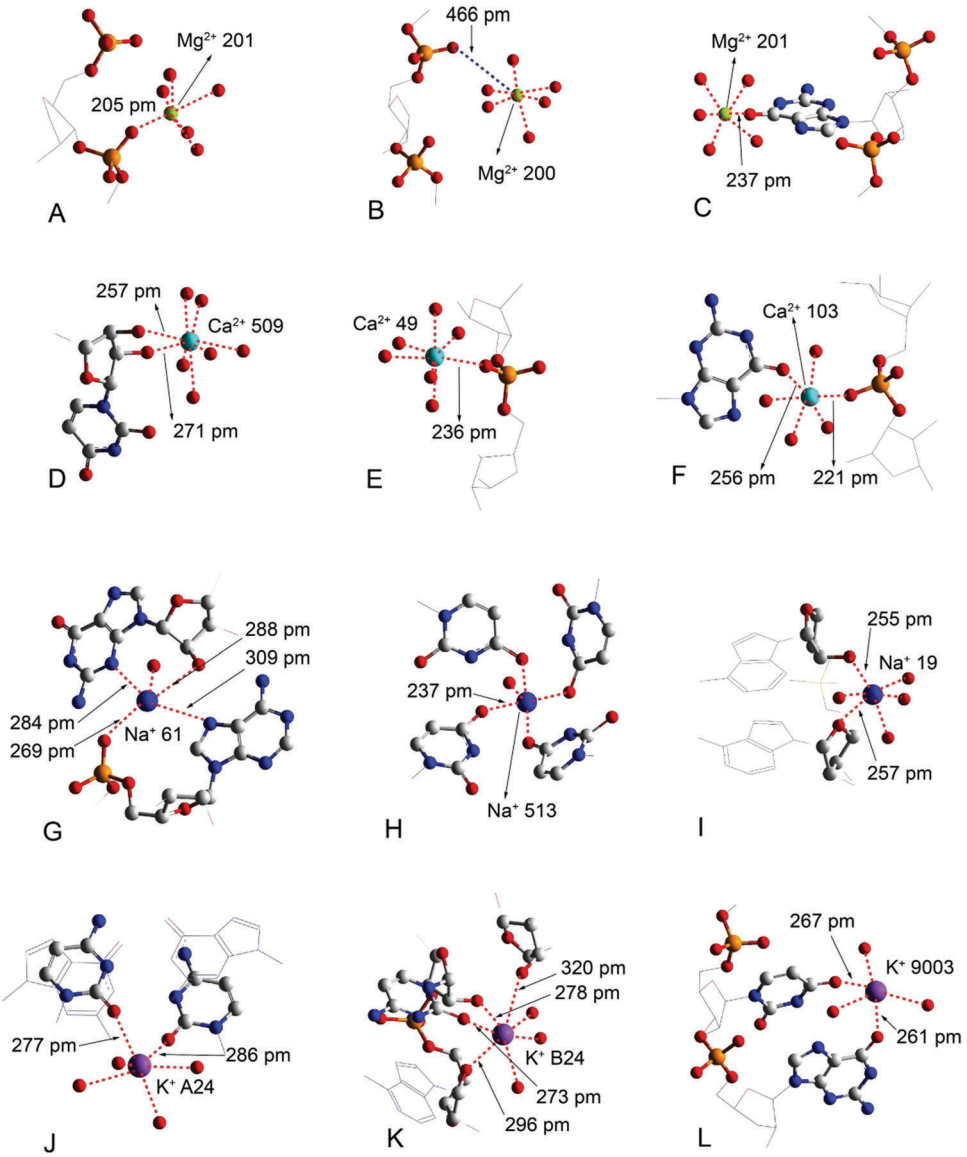


Fig. 2 Sketches of specific ways of interaction of metal ions with RNA molecules based on data from PDB structures: (A–C) – with Mg^{2+} ions. Respective structure sources: PDB 354D (A and B)[36] and 2A43;[54] (D–F) – with Ca^{2+} ions. Respective structure sources: PDB 1J8G,[52] 397D[53] and 2ZY6;[50] (G–I) – with Na^{+} ions. Respective structure sources: PDB 1L2X,[35] 1J8G[52] and 3ND3;[59] (J–L) – with K^{+} ions. Respective structure sources: PDB 2OIY (J and K)[34] and 2QEK.[60]

RNA tetraplex (UGGGGU)(4)[52] and *HIV-1* trans-activation region RNA fragment.[53] The first coordination shell of Ca^{2+} ions is composed of 6 to 8 electronegative centers (Table 2 and Fig. 2D–F), most often oxygen atoms from water molecules. The Ca^{2+}–O(H_2O) distance is in the range of 217–280 pm (Table 2). Ca^{2+} ions also have an affinity to the oxygen atoms of the phosphate groups with Ca^{2+}–O(PO_4^-) with distances being in the rage of 221–253 pm (Table 2). They can bind to more than one phosphate group as well. Thus, a Ca^{2+} ion can stabilize the loop formation in a single strand of RNA by directly interaction with three phosphate groups (Fig. 3), resulting in folding of the molecule.[53]

Apart from neutralizing the negatively charged phosphate groups of the RNA backbone, the Ca^{2+} ions also show an affinity to the oxygen atoms O2′ and O3′ of the ribose moiety. Measured distances between the ions and those centers are in the range of 257–276 pm.[52] In some crystals of Ca^{2+}–RNA complexes, direct contacts between the calcium cation and nucleobases have been observed: Ca^{2+}–O6G (with oxygen atoms of guanine) with lengths of 256 pm and 237 pm, or with O4 oxygen atoms of uracil with lengths of 255 pm and 258 pm.[50,52]

Crystallographic data for the complexes of Na^{+} is presented in Table 3. The chosen RNA structures, interacting with the ions, include RNA pseudoknot from beet western yellow virus;[35] RNA heptamer double helix (*Escherichia coli* transfer RNA fragment);[56] modified transfer RNA fragments from *Escherichia coli*[57] and 16-mer double-stranded RNA fragments (precursor messenger RNA from *Trypanosoma brucei*).[59] The monovalent

 This journal is © The Royal Society of Chemistry 2018

Published on 11 April 2018. Downloaded by University of California - Santa Barbara on 8/5/2018 1:51:21 PM.

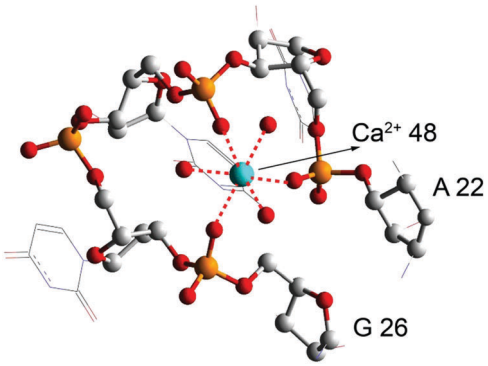


Fig. 3 Folding of the RNA strand stabilized by the direct interaction of the Ca^{2+} ion with oxygen centers of three phosphate groups. Respective structure source: PBD 397D.[53]

ions have affinity mainly to water molecules and RNA nucleobases, as presented in Tables 3 and 4. Na^+ ions have between four and six ligands. The Na^+–O(H_2O) distances are in the range of 210–270 pm, as exceptional cases some longer distances are reported (Table 3 and Fig. 2G–I).

In some complexes of Na^+ ions with RNA molecules sodium ion is coordinated to the phosphate group of the backbone with Na^+–O(PO_4^-) distance is in the range of 265–275 pm.[35] The same Na^+ ions are coordinated to O2′ and O4′ oxygen atoms of ribose and/or a center from a nucleobases. In the reported structures the measured Na^+–O2′ distances range between 255 pm and 288 pm.[35,59] Na^+–O4′ distances of 257 pm and 305 pm are reported.[35,59] Sodium can stabilize quadruple-stranded structures (Fig. 2H), where the Na^+ ion is directly bonded to four carbonyl oxygen atoms, O4U, from four uracil nucleobases (PDB 1J8G with resolution of 61 pm). Na^+–O4U distances of 235 and 237 pm are measured in such structures.[52] Sodium ions have affinity to the other nucleobases as well, and bind directly to their electronegative centers. For example, Na^+ 19 from PDB 3ND4 binds directly to the N7 nitrogen atom of adenine (Na^+–N7A distance is 264 pm).[59]

Dimerization initiation site *HIV-1* RNA fragments are chosen as examples of K^+–RNA crystalline complexes, Table 4.[34,55,60] K^+ ions usually coordinate 5–7 electronegative centers, Fig. 2J–L. In some potassium positions, however, some of the coordinated water molecules were not detected with X-ray crystallography (see RDB 2QEK and 34CC, Table 4). The K^+–O(H_2O) distance is in the range of 251–321 pm (Table 4). The K^+–O2′ distance to the oxygen atom O2′ of ribose is in the range of 280–320 pm, see PDB 3C44 and 2OIY.[34,60] Furthermore, K^+ ions can be in direct contact with the O4 oxygen atoms of uracil or O6 oxygen atoms of guanine, with K^+–O distances of 261–283 pm and 261–305 pm, respectively.

2.2. Transfer RNA

The transfer RNA (tRNA) function is to deliver specific amino acids to the peptidyl transferase region in the ribosome according to the messenger RNA (mRNA) sequence.[63] Moreover, tRNA takes part in the catalysis during the peptide biosynthesis. The tRNA molecule is flexible and capable of forming double-stranded regions as well

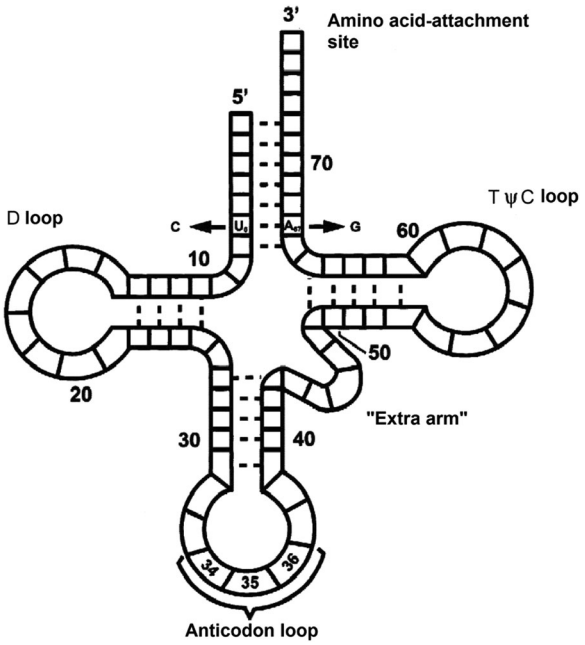


Fig. 4 Secondary structure of phenylalanine tRNA derived from yeast according to ref. 70. The double-stranded regions as well as the D-loop (nucleotides 13–22), TψC loop (nucleotides 53–61), anticodon (nucleotides 34–36), and the 3′ end, which binds to the amino acid, are shown here. (Reprinted from ref. 70 under Creative Commons License Attribution NonCommercial 4.0 International License, 2000, Publisher: Cold Spring Harbor Lab Press.)

as loops (Fig. 4). The anticodon loop contains 7 nucleotides, including 34, 35 and 36. The anticodon binds to the specific trinucleotide code of the mRNA, which assures the proper sequence of amino acids during the synthesis of the polypeptide chain. The amino acid binds to the amino acid-attachment site of tRNA *via* the process of aminoacylation, which is aided by the enzyme aminoacyl tRNA synthetase. It is the 2′-OH group of the 3′ end of the aminoacylated tRNA that takes part in the catalysis during the peptide biosynthesis.[64,65]

The divalent cations are found critical for preservation the structural stability of tRNA. The X-ray crystallographic studies have shown that Mg^{2+} ions bind directly to the phosphate groups or nucleobases of the nucleotides of tRNA as well as *via* water molecules, see PDB files 4TNA, 1TRA, 2TRA, 4TRA, 6TNA and 1EHZ.[66–70] Table 5 shows data from PDB files (PDB 1EHZ; 2TRA) of the various structures containing Mg^{2+} ions forming complexes with tRNA molecules. The crystallographic study of Shi *et al.* on phenylalanine tRNA (PDB 1EHZ), which has good resolution – 193 pm, is chosen for analyzing the interaction Mg^{2+}–tRNA (see PDB 1EHZ Table 5). Fig. 5 illustrates the most complex region of phenylalanine tRNA regarding the interactions with magnesium cations. Mg^{2+} 560 is fully hydrated with 6 molecules of water and is located in the center of a cycle formed of nucleotides 7–13. The ions Mg^{2+} 580 and Mn^{2+} 550 form a two center complex which interacts with the tRNA between the amino acid-attachment site and the D-loop. The ion Mn^{2+} 550 is directly bonded to the N7G nitrogen atom of guanine from nucleotide G15, while Mg^{2+} 580 is bonded to

Published on 11 April 2018. Downloaded by University of California - Santa Barbara on 8/5/2018 1:51:21 PM.

Table 5 Examples of atoms which are in direct contact with selected Mg^{2+} ions and form their first coordination shell. All listed results are obtained from X-ray crystallographic data for RNA molecules, the corresponding reference is shown in parentheses. The distances are given in pm

PDB code		*R*(Mg–O) or *R*(Mg–N)		
Resolution	Ion #	H_2O	PO_4^-	Other
1EHZ/193[70]	Mg 510	200, 200, 200, 200, 201		
	Mg 540	200, 200, 200	207, 211	
	Mg 560	200, 200, 200, 200, 200, 201		
	Mg 570	200, 200, 200, 200, 200, 201		
	Mg 580	200, 278, 323	193, 261	
	Mg 590		253	N6A-300, N7A-309
	Mn 520	200, 200, 200, 200, 200		N7G-230
	Mn 530	200, 200, 201, 201	219	O2'-234
	Mn 550	200, 200, 200, 200, 201		N7G-248
2TRA/300[67]	Mg 77	199, 199, 199, 198, 198, 197		

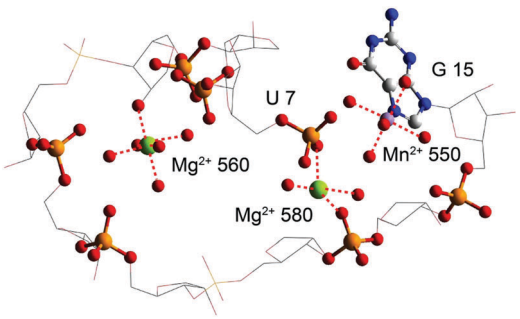


Fig. 5 An outline of tRNA from uracil 7 to guanine 15 stabilized by the metal ions Mg^{2+} 560, Mg^{2+} 580 and Mn^{2+} 550. Respective structure source: PDB 1EHZ.

the phosphate groups of nucleotides U7 and A14. In Fig. 5, only four of all six ligands of Mg^{2+} 580 are shown – two oxygen centers from the phosphate groups and two oxygen atoms from water molecules. The oxygen atoms from the other two water molecules are omitted for clarity. The location of the metal ions between two phosphate groups stabilize the folding of the tRNA by bridging the negatively charged phosphate groups, thus transforming electrostatic repulsion between them into electrostatic attraction to the magnesium ions.

2.3. Ribosomal RNA

Metal ions are necessary also for the proper structure and the protein biosynthesis function of ribosomes in the living cells. Typical concentration of alkaline and alkaline-earth cations in the cytosol (for mammalian cells) are 139 mM L^{-1} for K^+; 12 mM L^{-1} for Na^+; 0.8 mM L^{-1} for Mg^{2+}; and <0.0002 mM L^{-1} for Ca^{2+}.[63] This relatively high concentration of K^+ ions in the cytosol is connected with their role in the proper functioning of the ribosomal RNA (rRNA). K^+ ions are needed, in order to provide nonspecific charge neutralization of the rRNA phosphate backbone. Potassium ions can also bind to specific sites of the rRNA, thus stabilizing the tertiary structure.[71,72]

The structure and functioning of the ribosomes also depend on the presence of Mg^{2+} ions. For example, Mg^{2+} ions contribute to the coupling of the small and large ribosomal subunits in the living cells.[73–75] Pioneering studies of McCarthy had shown that cultivation of *Escherichia coli* in the absence of Mg^{2+} ions leads to a decrease in the number of ribosomes in the bacterial cells.[76] This effect may be related to the participation of Mg^{2+} ions in the formation and preservation of the structural integrity of the ribosomes. Moreover, if the negative charges of the RNA phosphate groups are compensated by protonated polyamines, instead of metal ions, the large ribosomal subunit of *E. coli* irreversibly loses its quaternary structure. The peptidyl transferase activity is lost too.[77,78] The processes of polynucleotides coupling in the ribosome, as well as the attachment of the ribosome to the endoplasmic reticulum, are found to be dependent on the presence of Mg^{2+} ions.[79,80]

Magnesium ions are part of the peptidyl transferase domain, where they coordinate to phosphate groups or ribose, without taking part in the protein biosynthesis.[13–16]

The importance of K^+ ions to the functionality of mammalian ribosomes is deducible by the loss of peptidyl transferase activity and spatial structure, when they are placed in an environment without K^+ ions.[81] On the other hand, the ribosomes of *E. coli* decompose into the individual subunits when they are exposed to high concentrations of K^+ ions.[82] Apparently, this is due to the competitive binding of K^+ ions to the centers, which accommodate Mg^{2+} in order to accomplish subunits coupling.

In order to analyze the interaction of ribosomal RNA with metal ions, an X-ray crystallographic study on the large subunit of *Haloarcula marismortui* has been performed. Resolution of 240 pm has been achieved (PDB 1S72).[11] The investigated subunit contains 3045 nucleotides. Additionally, 31 proteins and 116 Mg^{2+} ions have been identified in it.[83] Part of the ions is completely solvated by water, while another part interacts directly with fragments of the ribosomal subunit.

Magnesium ions are classified into six types, from type 0 to type V, according to the number of the ligands from RNA or proteins, coordinated to them. Type 0 have zero ligands (Fig. 6A), type I – one (Fig. 6B), type II – two (Fig. 6C and D), type III – three (Fig. 6E and F), type IV – four, and type V – five. Six ligands have not been observed. Type I–III, presented in Fig. 6, are the ion configurations most often observed.[11] Type II structures have been divided in two groups, according to the location of the bonded ligands. In group "a" – the ligands are located only on one side of the ion, Fig. 6C. In group "b" – the ligands are located on the both sides, Fig. 6D. In Mg^{2+} ions type IIIa, the inner-sphere ligands lie in a single plane that includes

 This journal is © The Royal Society of Chemistry 2018

Published on 11 April 2018. Downloaded by University of California - Santa Barbara on 8/5/2018 1:51:21 PM.

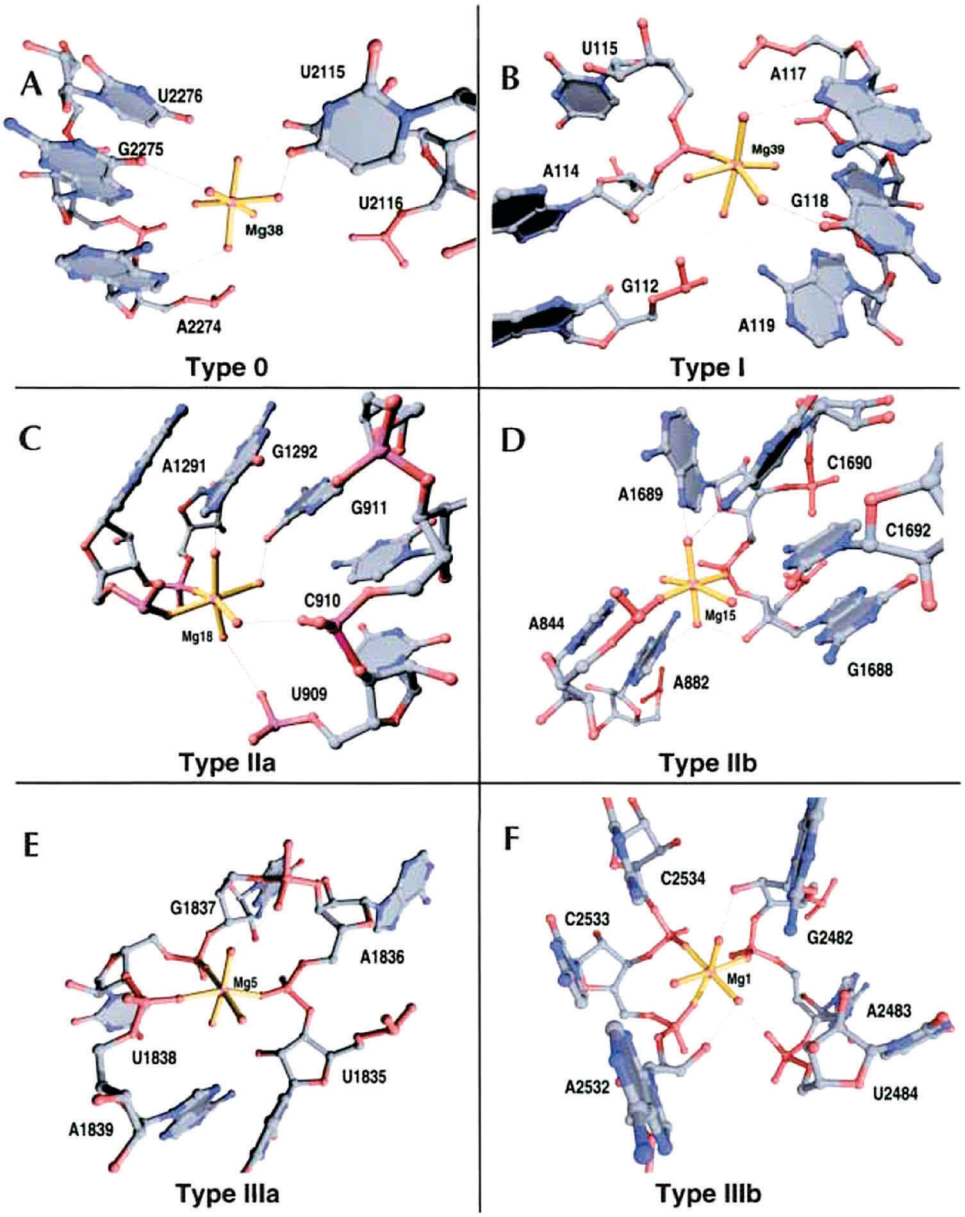


Fig. 6 Examples of different types of coordination of Mg^{2+} ions, as observed in the large subunit of the *H. marismortui* ribosome.[11] The six bonds from the coordination shell of the Mg^{2+} ions are shown in yellow. (Reprinted from ref. 11 under Creative Commons License Attribution NonCommercial 4.0 International License, 2004, Publisher: Cold Spring Harbor Lab Press.)

the metal ion, whereas in type IIIb, the inner-sphere ligands are mutually orthogonal, Fig. 6E and F.

The role of Mg^{2+} ions, presented in the large ribosomal subunit is to stabilize the structure of the 23S RNA. The Mg^{2+} from type IIa (40 ions, 34.5%) are most frequently observed, followed by the type I (37 ions, 31.9%). The Mg^{2+} ions of both types usually neutralize regions of the secondary RNA structures with closely packed PO_4^- groups. Only nine type 0 ions are observed. The Mg^{2+} ions of types III, IV and V contribute to the remaining 17.2% of the total number of Mg^{2+} ions in the system, as only single Mg^{2+} ions belong to types IV and V. These ions, types III to V, are usually bonded to specific single-stranded structures such as loops *etc.* For the whole structure 200 direct contacts of the Mg^{2+} ions with ligands originating from RNA are counted. Direct Mg^{2+}–$O(H_2O)$ contacts are 378. From all direct contacts of Mg^{2+} ions with RNA-originating ligands, those with oxygen atoms of phosphate groups are the most frequently observed: 73% of all direct contacts. The indirect interactions of the magnesium ion and phosphate group mediated *via* water molecules (Mg^{2+}–H_2O–PO_4^-) account for 50% of all indirect interactions.

The indirect interactions, *via* water molecule, of Mg^{2+} ions with N7 atoms of adenine and guanine are substantially more frequent than the direct contacts, 63 and 11, respectively.[11] Mg^{2+} ions are also found in the groove regions of double-stranded RNA.[84]

Published on 11 April 2018. Downloaded by University of California - Santa Barbara on 8/5/2018 1:51:21 PM.

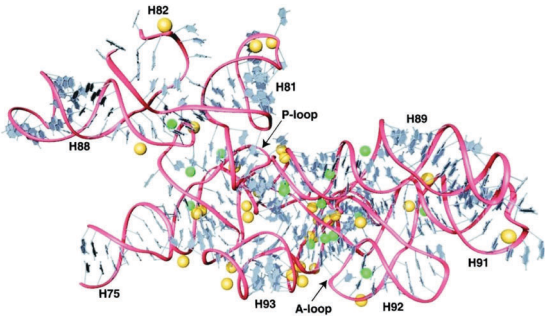


Fig. 7 3D representation of metal ion binding centers in the peptidyl transferase region. The RNA backbone is shown in red, the nucleobases are shown in grey, the Mg^{2+} ions and the monovalent cations are colored in yellow and in green, respectively. The nucleotides with numbers 2084–2127, 2266–2321 and 2419–2660 are shown in the figure (the numbering is according to the rRNA of *H. marismortui*).[11] (Reprinted from ref. 11 under Creative Commons License Attribution NonCommercial 4.0 International License, 2004, Publisher: Cold Spring Harbor Lab Press.)

About half of the Mg^{2+} ions and one third of the Na^+ ions, found in the large ribosomal subunit, are located within the peptidyl transferase region of domain V and the evolutionary preserved regions of domains II and IV.[11] The later regions are in direct contact with the peptidyl transferase center (Fig. 7). Around 40% of all nucleotides in the central loop of domain V interact directly with Na^+, K^+ or Mg^{2+} ions.[11] The double-helix region 90 (helix 90) and the location, where it couples with the central loop, contain a large amount of metal ions stabilizing the structure. For example, the nucleotide G2618 is in direct contact with 3 Mg^{2+} ions, two of which are of type I, and the third one is of type II. The first two ions are bonded directly to the phosphate group of G2618. The third Mg^{2+} ion bridges the phosphate groups of nucleotides G2618 and G2617. Thus, metal ions, especially the Mg^{2+}, play a crucial role ensuring the stability of the peptidyl transferase region. However, metal ions do not take part in the peptide biosynthesis.

The monovalent cations Na^+ and K^+ do not have preferred coordination geometry. More specifically, 88 monovalent cations have been detected in the large ribosomal subunit of *H. Marismortui*.[11] They are classified in four groups according to their location and the electronegative centers to which they bind: (1) ions within the major groove in double-stranded RNA; (2) ions bonded to ribosomal proteins; (3) ions located in the space between the ribosomal proteins and RNA; and (4) ions bonded to specific electronegative centers. The most frequently observed contacts of the monovalent ions with 23S RNA are with the guanine nucleobases or stacked guanine and cytosine bases in the area of the major groove of the RNA. The cation usually interacts directly with O6 atoms of guanine or O4 atoms of uracil. The typical distance between the Na^+ ions and the atoms from the RNA nucleaobases is between 280 and 320 pm.

Comparing the binding of the monovalent ions within the ribosome with that of the Mg^{2+} ions, one may conclude that the Mg^{2+} ions coordinate predominantly to the oxygen centers of the phosphate groups of the RNA backbone. The monovalent cations coordinate in most cases to the electronegative centers of nucleobases and ribosomal proteins. In the example discussed above, Na^+ and K^+ ions have in total 138 direct contacts to nucleobases and only 55 to phosphate groups.[11]

3. Investigation of metal ions in nucleic acids *via* spectroscopic methods

In this part we will summarize the studies of the interaction of metal ions with nucleic acids using spectroscopic methods – vibrational spectroscopies, infrared and Raman, and NMR spectroscopy.

3.1. Vibrational spectroscopies

Most of the studies on the interaction of metal ions with RNA or DNA using vibrational spectroscopies, infrared (IR) and Raman, consider the shifts of the symmetric and antisymmetric vibrations of the phosphate groups in nucleic acids as an indication for their interactions with metal ions. Simplified model compounds (like sodium diethyl phosphate and sodium dimethyl phosphate) are used for clarifying the trend in the frequency shifts of symmetric (ν_s) and antisymmetric (ν_{as}) vibrations of the esterified phosphate group.[30,31] The vibrational spectra of the compounds have been studied in solution at neutral pH = 7 for $Na^+Et_2PO_4^-$ and at pH = 7.2 for $Na^+Me_2PO_4^-$.[30,31] For dimethyl phosphate, studied by Raman spectroscopy in solution (Fig. 8, upper spectrum) the symmetric vibrations appear at 1083 cm^{-1}. The antisymmetric vibrations are observed at higher frequencies, 1217 cm^{-1}.[31] In the crystal phase (Fig. 8, middle spectrum) both the symmetric and antisymmetric vibrations shift to higher frequencies, at 1125 cm^{-1} and 1245 cm^{-1}, respectively.[31] The intensity of the symmetric vibrations observed in Raman spectra is high, whereas that of antisymmetric vibrations is low.

In the IR spectrum of sodium diethyl phosphate (water solution), the symmetric vibrations have a medium intensity and appear at

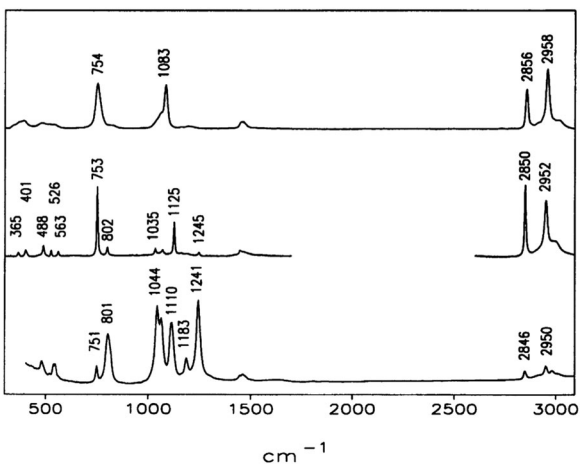


Fig. 8 Vibration spectra of $Na^+(CH_3)_2PO_4^-$: upper spectrum – Raman spectrum in 0.8 M solution at pH = 7.2, middle spectrum – Raman spectrum in polycrystalline solid phase, lower spectrum – infrared spectrum of the compound in KBr pellets.[31] (Reprinted from ref. 31, Copyright 1994 with permission from Elsevier.)

This journal is © The Royal Society of Chemistry 2018

Published on 11 April 2018. Downloaded by University of California - Santa Barbara on 8/5/2018 1:51:21 PM.

1080 cm^{-1}, whereas the antisymmetric ones have high intensity and are observed at 1200 cm^{-1}.[30]

The spatial arrangements of DNA and RNA molecules differ because of the different tasks they perform. The RNA molecules form more complex tertiary and quaternary structures in order to accomplish their diverse functions: translation of genetic code into proteins, acting as a messenger molecule, selective delivery of amino acids, catalyzing synthesis of the peptide bonds. DNA molecules, on the other hand, remain mostly in double-stranded form, in order to store genetic information.[63] Thus, the way of interaction between magnesium ions and DNA or RNA is expected to be different. Spatial effects make direct binding of Mg^{2+} ions to RNA more probable, than binding to DNA. Vibrational spectroscopy studies illustrate this different behavior of Mg^{2+} ions, towards the nucleic acids.[24,27]

By using Raman spectroscopy, the influence of Mg^{2+} ions on the vibration frequencies of the phosphate groups of DNA in solution has been studied.[24,26] The measured frequency of symmetric vibrations of the phosphate groups in absence of metal ions is 1093 cm^{-1} (ref. 26) or 1079 cm^{-1}.[24] The frequency is slightly downshifted by adding Mg^{2+} ions to the solution.[24,26] While in pure DNA solution the frequency is detected at 1079 cm^{-1}, in 0.98 mM L^{-1} Mg^{2+} ions solution the frequency downshifts to 1075 cm^{-1}, and by increasing of the Mg^{2+} concentration up to 8.33 mM L^{-1} Mg^{2+} the frequency shifts further to 1063 cm^{-1}.[24] The observed moderate frequency downshift has been interpreted as an indication of the formation of Mg^{2+}–$O(H_2O)$–PO_4^- aggregates, in which the water molecules solvating Mg^{2+} ion have increased acidity. This increase results in a stronger hydrogen bond between them and the phosphate groups of the DNA leading to slight decrease of the vibrational frequency of the phosphate groups. Therefore, the authors concluded that the predominant part of Mg^{2+} ions in solution do not bind directly to the phosphate groups of the nucleic acid, but rather the magnesium–phosphate interaction is mediated by a water molecule.[24] Another reason for that is the double helix structure of DNA, which does not allow the formation of tertiary loops, suitable for fixing the Mg^{2+} ions.

Magnesium and calcium ions are especially important for the functioning of chromosomal DNA.[6,7] This is another reason to study and compare the behavior of both metals. The interaction of Ca^{2+} with the phosphate groups of DNA has been investigated *via* IR spectroscopy.[22] It has been shown that the peak for antisymmetric vibrations, which in absence of calcium ions is observed at 1222 cm^{-1}, splits into three peaks at 1216, 1231 and 1250 cm^{-1} after addition of Ca^{2+} ions in the solution. Increase of the peak intensity by about 30% is also observed. The results are interpreted as indication for direct interaction between the Ca^{2+} cations and the phosphate groups of DNA.[22] The different behavior of Mg^{2+} ions (solvated) and Ca^{2+} ions (bonded) can be explained by the higher ionic radius of Ca^{2+}. It allows Ca^{2+} to make more contacts at longer distances, both direct and through water molecules, with the electronegative centers of DNA. Mg^{2+}–$O(PO_4^-)$, Ca^{2+}–$O(PO_4^-)$ and the corresponding distances to other electronegative centers are discussed in Section 2.1. Calcium has higher electropositivity as well, thus higher affinity for the phosphate groups. XRD studies also confirm calcium ions in direct contact with the phosphate groups of double-stranded DNA. Such examples are Ca^{2+} 103 and Ca^{2+} 104 from PDB 463D.[85]

In contrast to the double-stranded DNA, where magnesium ions interact with phosphates *via* water molecules, Raman spectroscopy studies suggest that in RNA, Mg^{2+} ions are likely directly bound to the phosphate groups.[27–29] The measurements have been carried out in crystal phase. It has been shown that the symmetric vibrations of the PO_4^- groups, detected at 1100 cm^{-1} (negative band in Fig. 9A), increase frequency by 17 cm^{-1} to 1117 cm^{-1} (positive band at Fig. 9A). For this measurement, the RNA crystals of *Hepatitis D virus* (HDV) ribozyme have been placed in 20 mM L^{-1} solution of Mg^{2+} ions.

Another change detected in the difference spectra in Fig. 9B is the positive peak at 322 cm^{-1}, assigned to metal–oxygen Mg^{2+}–$O(PO_4^-)$ vibration in the cases when the Mg^{2+} ion is coordinated to less than six water molecules. The peak shifts from 360 cm^{-1} for magnesium hexahydrate to 322 cm^{-1} for the inner coordinated species. The isotopic change of H_2O by D_2O or $H_2{}^{18}O$ resulted in the shift of the peak at 322 cm^{-1} to 305 cm^{-1} (Fig. 9B), which suggest that the peak does not involve contribution of O–H vibration since in the latter case much higher shift is expected. Thus, based on the spectra shown in Fig. 9A and B, the authors concluded that there is direct interaction between the Mg^{2+} ions and the phosphate groups of RNA in the case of the HDV ribozyme.[27–29]

A reference study of dimethyl phosphate solution in the presence and absence of magnesium ions in higher concentration, 1 M solution of $MgCl_2$ (Fig. 10) has shown shift of three peaks related to vibration of the PO_4^-.[27] The bands at 1084, 753 and 360 cm^{-1} shift to 1107, 775 and 321 cm^{-1}. These results are interpreted as indications for direct binding of the magnesium ion to the phosphate groups, confirming the conclusions for such type of binding for RNA in HDV ribozyme. Crystallographic XRD

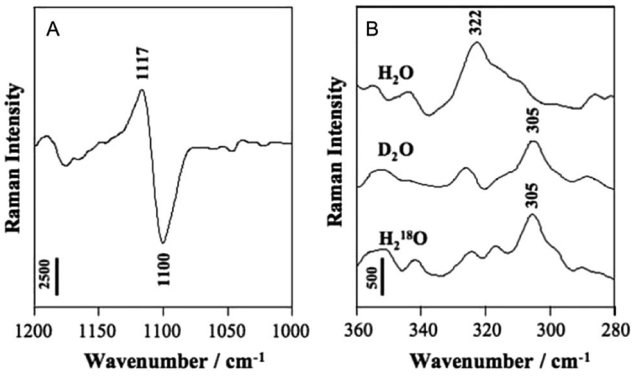


Fig. 9 Raman spectra showing the difference between the Raman spectra of HDV ribozyme crystal in contact with Mg^{2+} ions (A) symmetric vibrations of the phosphate groups directly linked to Mg^{2+} ions at 1117 cm^{-1}, the negative band at 1100 cm^{-1} is due to decrease of the intensity of free phosphate groups; (B) Raman spectra indicating the presence of Mg hydrates (tetra- or pentahydrates) bound directly to phosphate groups in solution of H_2O and isotopically exchanged D_2O and $H_2{}^{18}O$.[27] (Reprinted with permission from ref. 27, Copyright 2008 American Chemical Society.)

Published on 11 April 2018. Downloaded by University of California - Santa Barbara on 8/5/2018 1:51:21 PM.

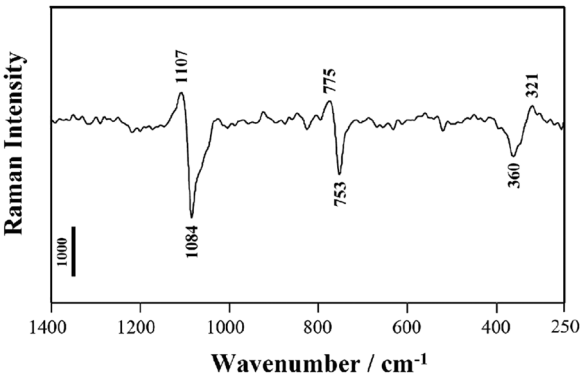


Fig. 10 Raman difference spectroscopy showing the spectrum difference between 200 mM dimethyl phosphate + 1 M $MgCl_2$ and 200 mM dimethyl phosphate. The background spectrum of 1 M $MgCl_2$ is also subtracted in order to account for the spectrum interference of $Mg^{2+}(H_2O)_6$.[27] (Reprinted with permission from ref. 27, Copyright 2008 American Chemical Society.)

evaluation of the HDV ribozyme structure also detects five direct bonds of the phosphate groups with Mg^{2+}. The measured distances Mg^{2+}–O(PO_4^-) are less than 280 pm.[86] In addition, magnesium cations interact with the N7G and O6G atoms of the nucleobase guanine.

3.2. NMR spectroscopy

NMR spectroscopy is not among the main methods for investigation of the interaction between nucleic acids and metal ions since it can provide only indirect information about the location and dynamics of the ions. NMR studies have shown that the main part of the monovalent ions, Na^+ and K^+, remain completely solvated by water molecules in the presence of single or double-stranded DNA.[5] These ions form the so called ''ion atmosphere'' around the double-stranded NA. Furthermore, the NMR studies have shown that the Mg^{2+} ions prefer to bind to the major groove of NA, as well as at the stacked pair guanine–adenine bases.[20] In addition, the contacts of Mg^{2+} ions with O6 atoms of guanine have been suggested.

4. Investigation of metal ions in nucleic acids by computational methods

As described in the Introduction, the location of metal ions obtained by the X-ray crystallography cannot be applied directly to understanding their properties in the biological systems since the structure and solvation of the studied macromolecules and ions in crystal phase can differ from that in solution. The vibrational spectroscopic studies can be performed in appropriate solution but the obtained information about the location of the ions is only qualitative. Geometrical parameters like distances and angles cannot be obtained. In addition, X-ray crystallographic methods provide information about the location of the ions in a constant periodical crystal structure, whereas the results from vibrational spectroscopy approaches are characteristic for local interactions averaged for the duration of the measurement. It is essentially not possible by those approaches to follow the ion dynamic in real time in a system under conditions close to biological ones. Therefore, computational methods including both molecular dynamics approaches and isolated models have been applied to study the interaction between metal ions and nucleic acids including both local interactions and dynamics of the systems.[40,41,87,101]

4.1. Classical molecular dynamics simulations

The most widely used force fields for molecular dynamics of RNA systems are CHARMM and AMBER.[88] CHARMM is parameterized upon the assumption that interactions between biomolecules can be described using the MP2 *ab initio* method. The parameters, especially suitable for RNA were released in 2011 as CHARMM-36.[89] Also, it has been suggested that a degree of polarizability can be used to simulate the response of atoms to their local environment. This way a general purpose CHARMM force field is combined with a Drude harmonic oscillator. A Drude-DNA model has been found to describe better the ion–DNA interactions.[90]

AMBER is amongst the most popular force fields in the area of molecule dynamics. AMBER ff99/94 are generally used, but they are not specifically designed to treats RNA. Series of improvements, specific for RNA systems have been developed, including ff99-χ_{YIL},[91] ff99-χ_{OL}[92] and the Chen and Garcia force field.[93] High-level quantum mechanical reference data and comparison with experimental results are used for their parameterization.

In the MD simulations, water models are important for the accurate estimation of solvent interaction with ions and biomolecules. Three, four and five point water models have been developed. The 3-point models include SPC/E[94] and TIP3P.[95] The more recent 4-point models include TIP4P and TIP4P-Ew.[96] Five point models were also developed, TIP5P.[97] Four point and five point models generally achieve better accuracy, at additional computational cost.

The interaction of Mg^{2+} ions with double-stranded DNA has been modeled by classical molecular dynamics (MD) simulations using AMBER ff98 force field.[98] Part of the Mg^{2+} ions was found to interact with electronegative centers of the nucleobases such as N7G and N7A nitrogen atoms of guanine and adenine as well as O6G oxygen atom of guanine. Another part of the Mg^{2+} ions compensates the negatively charged phosphate groups of DNA.[98] The average distances to the different electronegative centers are Mg^{2+}–O6G about 400 pm; Mg^{2+}–N7G about 500 pm; Mg^{2+}–N7A about 500 pm and Mg^{2+}–PO_4^- about 800 pm. The distances of 300 to 600 pm correspond to an interaction *via* one or two water molecules, whereas the greater distances indicate an interaction *via* more than two water molecules. The data derived from the MD simulations are consistent with the conclusions from the experimental studied of DNA by vibrational spectroscopy, discussed above, that the interaction between Mg^{2+} ions and the phosphate groups is accomplished *via* water molecules.[24,26]

 This journal is © The Royal Society of Chemistry 2018

Published on 11 April 2018. Downloaded by University of California - Santa Barbara on 8/5/2018 1:51:21 PM.

Na^+ ions are also used as counter ions in MD simulations of nucleic acids.[40,41,87] The interaction of double-stranded DNA with Na^+ ions has been studied, using the AMBER software package and the force field of Cornell *et al.*[99] It has been found, that Na^+ ions have high affinity to the electronegative centers of the nucleobases, especially thymine and guanine.[40,41] A direct coordination of the Na^+ ions to the carbonyl oxygen atom of thymine was observed. Part of the Na^+ ions is coordinated to the O4′ oxygen atoms of deoxyribose, too. The coordination position, located in the minor groove of double-stranded DNA, was found occupied for more than 6000 ps of the simulation. Sodium ions interact with the phosphate groups of the DNA backbone either directly, or indirectly *via* water molecules.[40,41] When Na^+ is coordinated to each phosphate group in the minor groove, the width of the minor groove is around 400 pm, while in absence of sodium ions, the width of the minor groove increases to around 550 pm.

Using the AMBER suite of programs with parmbsc0 modifications to the parm99 force field, Lavery *et al.* simulated the distribution of K^+ ions in DNA.[100] The study shows that highest K^+ concentration occurs within the DNA grooves, close to electronegative base sites, rather than close to the charged phosphate groups.

The interaction of metal ions with RNA is more complex than the interaction with DNA. The reason for this is the more complex tertiary and quaternary structure of RNA. The ribozyme of the *Hepatitis D virus* (HDV) is a commonly used model for studying the interaction of RNA with Na^+ and Mg^{2+} ions. MD simulations using this rybozyme have been performed with the AMBER software package and the force field Parm 99.[101] In these simulations, both fully solvated as well as directly bound Mg^{2+} ions were observed. The Mg^{2+} ions in fully hydrated state have octahedral coordination shell made up of six water molecules. During the direct interaction with electronegative centers of nucleobases, ribose or phosphate groups, the octahedral surrounding of the ion is preserved. Oxygen or nitrogen atom from the different RNA fragment takes place of a water molecule. A direct bond between Mg^{2+} and O4U oxygen atom of uracil has a length of about 198 pm, while the bond between Mg^{2+} and an oxygen atom from a phosphate group is found to be shorter, about 187 pm. It was also reported that during the simulations with total duration of 15 ns, Mg^{2+} ions do not exchange water molecules from their first coordination shells. The average life time of a water molecule from the second solvation shell of Mg^{2+} is about 15 ps. Mg^{2+} ions were also found within the catalytic center of the HDV ribozyme.[101] There, a Mg^{2+} ion is directly bound to an oxygen atom of the phosphate group of the nucleotide U23, with a Mg^{2+}–O(PO_4^-) distance of about 185 pm and remains coordinated to 5 water molecules. One of these water molecules forms a hydrogen bond with the O2U atom of uracil (nucleotide U20). The equatorially coordinated water molecules in the surrounding of Mg^{2+} form hydrogen bonds with the phosphate groups of neighboring nucleotides G1, C22 and U23.

The water molecules from the solvation shells of Na^+ ions are much more mobile than those of Mg^{2+} shells.[101] The average lifetime of a water molecule from the first solvation shell of a fully hydrated Na^+ is 17 ps. The longest recorded duration of a water molecule in from the first solvation shell of Na^+ is 200 ps. When solvated Na^+ ions are located in the active center of the HDV ribozyme, their average resident time is 180 ps, and the maximal one is 4.3 ns. The general conclusion from the simulations is that the Na^+ ions are much more mobile than the Mg^{2+}. Sodium ions can freely migrate from the electronegative centers of RNA to the solution or from one center to another with the longest recorded duration of bound state being in the order of 6–13 ns.[101]

The reason for the experimentally observed magnesium affinity for the phosphate group of RNA, see Tables 1 and 5, is revealed by the use of molecular dynamics.[102,103] Systems with directly bonded Mg^{2+} ions are fond to be much more thermodynamically stable, with much lower Gibbs free energy, compared to the cases, where the Mg^{2+} ions interact with the nitrogen bases and sugar moieties.

4.2. Quantum chemical studies using isolated models

The essential advantage of classical MD methods is that they provide the opportunity to study large scale systems and to achieve long simulation times. However, these methods also have several disadvantages. The type and strength of interactions in classical MD methods are predetermined by the used force field. Classical MD might yield incorrect results for the system/interactions if the parameterizations are inappropriate. In order to obtain results independent on the predefined parameters, the modeling should be performed with quantum chemical methods. Those methods, however, require significantly more computational resources than classical methods. Thus, the methods based on quantum chemistry are commonly applied to models or fragments with a limited number of atoms, usually in the range 50–100 atoms, which represent the most important feature of the studied system.

Model complexes of dimethyl phosphate with hydrated Mg^{2+} and Ca^{2+} ions have been studied using density functional theory approach with the hybrid exchange–correlation functional B3LYP and basis set 6-31G(d,p).[104] The solvent (water), in which the processes presumably take place, is accounted for by the conductor-like polarizable continuum model (CPCM). The metal ion is modeled to be fully solvated as well as directly bonded to the phosphate groups. The interaction energy has been calculated for a replacement reaction involving 1 or 2 ligands by using the following equation:

$$M^{2+}(H_2O)_6 + DMP^- \rightarrow M^{2+}(H_2O)_{6-n}DMP^- + nH_2O$$

where n = 0, 1 and 2 represents the ion (Mg^{2+} or Ca^{2+}) solvated by 6, 5 or 4 water molecules. The most stable complexes are those in which the Mg^{2+} ions are fully solvated. Complexes, in which the Mg^{2+} ion interacts directly with one of the O atoms of the PO_4^- group, are less stable by 48 kJ mol^{-1}. The complexes with the lowest stability (by about 100 kJ mol^{-1} lower than that of complexes containing fully solvated ions) are those in which the Mg^{2+} is in contact with two O atoms of the phosphate group and is solvated by 4 water molecules. The geometry optimization of a system with Ca^{2+}, in which the ion is fully solvated,

Published on 11 April 2018. Downloaded by University of California - Santa Barbara on 8/5/2018 1:51:21 PM.

Table 6 Binding energies of hydrated cations to dinucleotides (in kJ mol^{-1}).[104] Notations RNA and DNA denote that the cluster model include ribose and deoxyribose, respectively

Complex	Water (CPCM)
$RNA^{2-}Mg^{2+}(H_2O)_4$	−133.5
$DNA^{2-}Mg^{2+}(H_2O)_4$	−85.4
$RNA^{2-}Ca^{2+}(H_2O)_4$	−89.9
$DNA^{2-}Ca^{2+}(H_2O)_4$	−69.0
$RNA^{2-}Na^{+}(H_2O)_4$	−17.1
$DNA^{2-}Na^{+}(H_2O)_4$	25.5

results a Ca^{2+} directly bonded to oxygen center from PO_4^- group.[104] The complex of Ca^{2+}, in which the ion is coordinated to one O atom of PO_4^-, is found more stable by 55 kJ mol^{-1} than the case, where Ca^{2+} is coordinated to two oxygen centers of the same phosphate group.[104]

Systems with Na^+, Mg^{2+} and Ca^{2+} ions directly bonded to two phosphate groups of nucleic acids have been modeled with the same simulation method and a larger basis set, 6-311++G(d,p).[46] The cluster models used in the simulations are composed of two phosphate groups linked to the 3′ and 5′ hydroxyl groups of ribose or deoxyribose. The binding energy of the hydrated ions to the dinucleotide cluster models, presented in Table 6, is calculated for the following formula:

$$M^{2+}(H_2O)_6 + RNA^{2-} \rightarrow RNA^{2-}M^{2+}(H_2O)_4 + 2H_2O$$
$$(\text{for } Na^+ = M^+).$$

The affinity of the metal ions for binding to the phosphate groups decreases in the order $Mg^{2+} > Ca^{2+} > Na^+$, *i.e.* it is the highest for Mg^{2+} with binding energy of −134 kJ mol^{-1} and −85 kJ mol^{-1} for RNA and DNA models. The binding of the metal ions in the models containing ribose is stronger than those containing deoxyribose. The difference in the binding energy is about 50 kJ mol^{-1} for the complexes of Mg^{2+}, 20 kJ mol^{-1} for the complexes of Ca^{2+} and 40 kJ mol^{-1} for the complexes of Na^+, as in the latter case the positive value is calculated.

The symmetric vibrational frequency ν_s of the phosphate group is characteristic of the presence of directly bonded metal ions, as discussed above. For this reason, such frequencies have been calculated for the interaction of Mg^{2+} and Ca^{2+} ions with dimethylphosphate as a model compound.[104] The calculations are carried out with a hybrid exchange–correlation functional B3LYP and basis set 6-31G(d,p). The complexes are studied in the gas phase and by explicitly taking into account part of the solvent molecules (4 to 6 molecules of water) using the CPCM solvent model. Three cases are modeled: the metal ion is fully solvated with six water molecules and interacts with the phosphate group *via* water molecule (case I); the metal ion is directly bonded to one O atom of PO_4^- group and is solvated by five water molecules (case II); the metal ion is bonded to two oxygen centers from the PO_4^- fragment and is solvated by 4 water molecules (case III).

Since the vibrational frequencies of PO_4^- group are affected by the conformation of fragment O═P–O–C, two conformations

Table 7 Calculated vibrational frequencies (in cm^{-1}) of the complexes of Mg^{2+} and Ca^{2+} with dimethyl phosphate.[104] The frequencies for the complexes with Mg^{2+} and Ca^{2+} are given in the first columns. In the following columns, numerical values of the displacement for the respective complex types and conformation of PO_4^- are given. I–III corresponds to the case whether the metal ion is fully solvated, or bonded to one or two oxygen centers from a PO_4^- fragment. The letter "a" means – calculated in gas phase and "b" – calculated using polarized continuum (CPCM)

Complex	Mg^{2+}	Complex	Mg^{2+}	Ca^{2+}	Complex	Mg^{2+}	Ca^{2+}
I (*gg*)a	1027	II (*gg*)a	+68	1065	III (*gg*)a	+71	+25
I (*gg*)b	1057	II (*gg*)b	+9	1063	III (*gg*)b	+27	+17
I (*tg*)a	1071	II (*tg*)a	−14	1065	III (*tg*)a	+1	+8
I (*tg*)b	1058	II (*tg*)b	+9	1061	III (*tg*)b	+11	+10

denoted *gg* and *tg* have been considered.[104] The terms *t* and *g* denote two possible positions of the methyl group with respect to the oxygen atoms of the phosphate group: *t* – *trans*, *g* – *gauche*. Accordingly, in *gg* both methyl groups are in the *gauche* conformation, and in *tg* conformation one group is *trans* and the other is *gauche*. The calculated values for the symmetric vibrations ν_s are presented in Table 7. The band shifts to higher frequencies when Mg^{2+} is directly bonded to one O atom of the phosphate group. Further shift to higher frequencies is observed when the metal ion is directly bonded to two of the O atoms. This effect is stronger in the *gg* conformation of the phosphate groups (Table 7). Analogous effect is also observed in the complexes of the calcium ions. Complexes of Ca^{2+}, in which the ions interact with phosphate groups through water molecules, are not modeled.[104]

Sushko *et al.* reported the use of classical density functional theory (cDFT) to simulate the equilibrium ion–DNA, ion–water, and ion–ion interactions in different ionic atmospheres.[105] The simulations presented in their paper have the following model set-up: a B-form DNA molecule surrounded by an ionic atmosphere of either RbCl, $SrCl_2$, or $CoHexCl_3$ (cobalt hexammine chloride). The accuracy of the cDFT calculations was verified by comparison between experimental and simulated anomalous small-angle X-ray scattering curves. The calculations showed that there are significant differences between monovalent, divalent, and trivalent cation distributions around the B-form DNA molecule. In terms of DNA-bound Rb^+ ions: approx. 50% of them penetrate into the minor DNA groove and the other half adsorb on the backbone of the DNA molecule. As for the larger Sr^{2+} ions, their fraction in the minor groove is lower than that of Rb^+ ions, whereas all $CoHex^{3+}$ ions are adsorbed on the DNA backbone.

In addition to simulating ion–DNA interactions, quantum mechanical/molecular mechanical (QM/MM) calculations have also been used to model reaction paths in the active site of enzymes. A prominent example is the modeling of pyrophosphorolysis (*i.e.* reverse reaction of DNA synthesis) done by Perera *et al.*[106] Based on their calculations, Perera *et al.* described a time-specific order of metal binding during the pyrophosphorolysis reaction. There are 3 distinct metal ion sites (the catalytic metal ion site, the nucleotide metal ion site and the product-associated metal ion site), which modulate the equilibrium of the above-cited biochemical process. However, a

 This journal is © The Royal Society of Chemistry 2018

Published on 11 April 2018. Downloaded by University of California - Santa Barbara on 8/5/2018 1:51:21 PM.

specific set of sodium and magnesium ions must occupy the 3 distinct metal ion sites so that the reaction can occur. According to the reported QM/MM calculation results, pyrophosphorolysis is initiated when the catalytic metal site is occupied by a magnesium ion. The nucleotide metal ion site is occupied by a magnesium ion throughout the whole reaction. In contrast, the product metal site is occupied by a magnesium ion only in the early stages of the reaction. In the later stages of the reaction, a magnesium ion in the product metal site acts as a reaction inhibitor, and hence is replaced by a sodium ion.

Replica-exchange molecular dynamics (REMD) is another method, used to study metal ions affecting the function of biomolecules. Swadling *et al.* investigated how structure and dynamics influence the function of a ribozyme in different inorganic settings. The full hammerhead ribozyme is used as a model.[107] It was discovered, by sampling major conformational states, that its structure can manifest a free-energy landscape similar to that of proteins which have a "funnel" topology. The analysis of the ribozyme's conformations explains the experimentally observed differences between the catalytic activity in bulk water and when it interacts with clay materials.

4.3. *Ab initio* molecular dynamic simulations

A study of the interactions between sodium and magnesium ions and the RNA phosphate groups, in water solution, is performed using *ab initio* Born–Oppenheimer molecular dynamics. Duration of the simulations is about 140 ps. Results analysis has shown that sodium ions are notably more mobile than the Mg^{2+} (Fig. 11).[49] Each type of the modeled ions can be either directly bonded to the phosphate group or completely solvated by water molecules.

Sodium ion changes its position between coordinated to the phosphate group at about 235 pm, and completely solvated by water. During the simulation, the ion remains directly bonded to the phosphate for approximately 20–30 ps, *e.g.* 20% of the time. The sodium ions can coordinate from 4 to 7 oxygen atoms from water molecules or phosphate groups in their first coordination shell with the most frequent coordination number

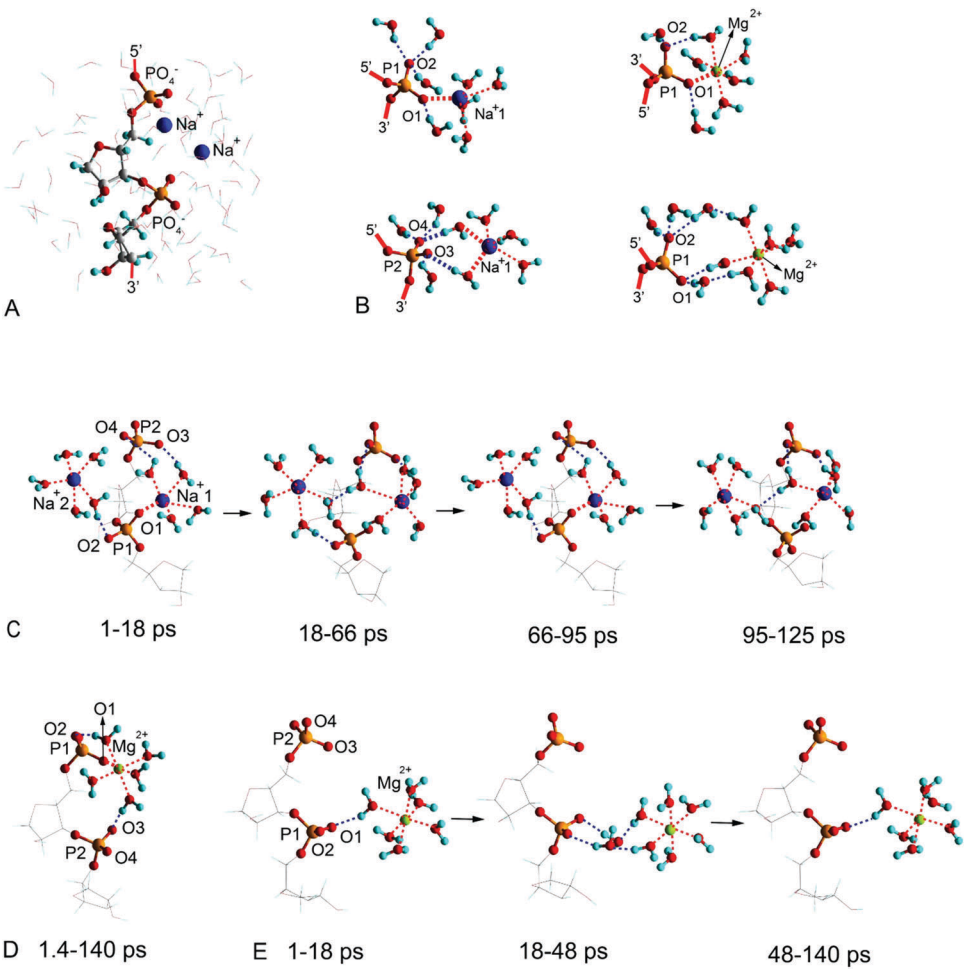


Fig. 11 Selected moments from the simulation: (A) the periodic box in which the simulation was carried out containing a phosphate backbone of RNA and two sodium ions (water molecules are simply depicted as lines); (B) the water molecules solvating the phosphate groups P1 and P2 as well as the cations in directly bonded or completely solvated state; (C) the sodium ions in different moments of the simulation; (D) the directly bonded magnesium ion and (E) the completely solvated magnesium ion in different moments of the simulation. (Reprinted with permission from ref. 49, Copyright 2013 American Chemical Society.)

Published on 11 April 2018. Downloaded by University of California - Santa Barbara on 8/5/2018 1:51:21 PM.

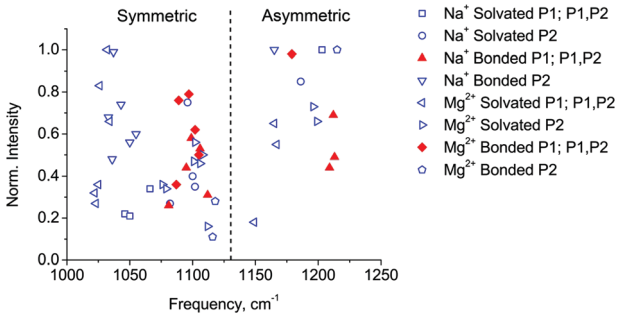


Fig. 12 Calculated frequencies of the symmetric and asymmetric vibrations of the phosphate groups and their normalized intensities. The filled red symbols indicate vibrations of a phosphate group which has a bonded metal ion. The empty blue symbols indicate vibrations of a phosphate group which is solvated only by water molecules with no metal ion bonded. (Reprinted with permission from ref. 49, Copyright 2013 American Chemical Society.)

being 5 (approx. 80% of simulation time), followed by 6 (approx. 15% of simulation time).

In the system with two sodium ions, the potential energy local minima and maxima do not correlate to some specific positions of the metal ions in respect to the phosphate groups. Potential energy fluctuations indicate variations in the arrangement of water molecules in the system. The average value of the potential energy, when the ion Na^+ is directly bonded, is lower than the case, when the ion is completely solvated, by 6 kJ mol^{-1}. This value is negligibly small for the system. Similarly, the local minima and maxima of the systems with Mg^{2+} do not correlate to some specific positions of the ions in relation to the phosphate groups.

During the entire simulations, the magnesium ions do not change their initial position – they remain directly bonded to the phosphate group or completely solvated. The magnesium ion binds to one of the oxygen atoms of the phosphate group with an optimal distance of 205 pm.

A complete vibration analysis, explicitly including water molecules, shows that the symmetrical vibrations of the phosphate groups can be used to determine the position of the sodium or magnesium ion with respect to the phosphate groups. In the absence of a directly bonded cation, both a low frequency as well as a high frequency zones are observed. If a directly bonded cation is presented, the intensity of the low frequency vibrations decreases and that of the high frequency vibrations increases, Fig. 12. Note that P1 and P2 indicate the different phosphate groups in the model. When the metal ion is directly bonded, it is attached to the P1 group. Experimental Raman spectroscopy results confirm the shifting to higher frequencies, when directly bonded cation is presented.[27]

5. Summary and outlook

Alkaline and alkaline earth metal ions play an important role for the stability and formation of tertiary and quaternary structures of different types of nucleic acids, in particular RNA and the ribosome. Magnesium ions are critical for preserving the tertiary structure of RNA. Their presence, especially between phosphate groups, stabilizes the folding of the molecule. Negatively charged groups are bridged, thus transforming electrostatic repulsion between them into attraction. Quaternary structure of the ribosome also depends on the presence of Mg^{2+} ions, as they contribute to the coupling of the small and large subunits. Tertiary ribosomal structure and in particular the structure of the peptidyl transferase center are stabilized by Na^+, K^+ and Mg^{2+} ions. This stabilization is achieved by non-specific compensation of the phosphate groups' negative charges (especially by K^+ ions) and by coordination of the cation to specific centers (the most typical for Mg^{2+} ions). Thus, those cations are needed for the ribosome to perform its function (peptide synthesis) without participating directly in the catalytic process.

All cations, considered in the present review, Na^+, K^+, Mg^{2+} and Ca^{2+}, are required for the maintaining of chromosomal DNA structural integrity. They perform this function mainly by neutralization of the phosphate groups' negative charges. Mg^{2+} and Ca^{2+} are especially important, because they can bridge distant phosphate groups, and additionally contribute for the packing of DNA. Ca^{2+} ions are more probable to bridge the groups by direct contacts. Mg^{2+} ions can perform this task either by binding to the phosphate groups directly or *via* water molecules.

As described above, the crystallographic methods and various spectroscopies, IR, Raman, and NMR, are used to study the static interactions between ions and nucleic acids, mainly in crystal phase. Those methods suggest that divalent ions can be bonded directly or indirectly to more than one phosphate group or other electronegative centers, thus forming a bridge between different parts of the macromolecules or between different macromolecules. The monovalent cations with their specific ionic radii and affinity for water molecules and the nitrogen centers from the electronegative bases can stabilize quadruplex structures. The monovalent cations bonded to the nitrogen bases interact with the phosphate groups usually through one or two water molecules forming ionic atmosphere around the nucleic acids.

Computational methods provide the means to study the affinity and dynamics of monovalent and divalent ions around DNA and RNA at an atomic scale. Classical methods suggest that divalent cations bind to specific centers of RNA, containing phosphate groups, and in this bonded state they can remain for a time in the order of nanoseconds or more. In particular, magnesium ions do not exchange water molecules of their first coordination shells for a time of about 15 ns. Both classical and *ab initio* simulations suggest that the monovalent cations generally have picosecond dynamics and often change their position towards the RNA nucleotides and that the water molecules of their first solvation shell are much more mobile.

The combination of experimental and theoretical methods suggests that divalent cations, Mg^{2+} and Ca^{2+}, have high affinity to the phosphate groups of the nucleic acids. On the other hand, Na^+ and K^+ have higher affinity to the nitrogen bases and are often found in the groves of RNA or DNA. Also, the

 This journal is © The Royal Society of Chemistry 2018

Published on 11 April 2018. Downloaded by University of California - Santa Barbara on 8/5/2018 1:51:21 PM.

monovalent ions are much more mobile than the divalent ones. Thus, the combination of experimental and theoretical methods is the most productive strategy for the study of metal ions–nucleic acids interactions. This is essential if an atomic scale resolution is needed in a dynamic environment.

Conflicts of interest

There are no conflicts of interest to declare.

Acknowledgements

PStP and GNV are grateful for the support by the Horizon2020 program of the European Commission (project Materials Networking – grant agreement 692146).

References

1 D. Celander and T. Cech, Visualizing the higher order folding of a catalytic RNA molecule, *Science*, 1991, **251**, 401–407.
2 A. Sigel, H. Sigel and R. Sigel, *Structural and catalytic roles of metal ions in RNA*, RSC Publishing, Cambridge, UK, 2011.
3 M. Serra, J. Baird, T. Dale, B. Fey, K. Retatagos and E. Westhof, Effects of magnesium ions on the stabilization of RNA oligomers of defined structures, *RNA*, 2002, **8**, 307–323.
4 P. Auffinger, L. D'Ascenzo and E. Ennifar, Sodium and potassium interactions with nucleic acids, in *The Alkali Metal Ions: Their Role for Life*, ed. A. Sigel, H. Sigel and R. K. O. Sigel, Springer, 2016, pp. 167–203.
5 D. E. Draper, A guide to ions and RNA structure, *RNA*, 2004, **10**, 335–343.
6 R. Strick, P. L. Strissel, K. Gavrilov and R. Levi-Setti, Cation–chromatin binding as shown by ion microscopy is essential for the structural integrity of chromosomes, *J. Cell Biol.*, 2001, **55**, 899–910.
7 R. Levi-Setti, K. L. Gavrilov and P. J. Rizzo, Divalent cation distribution in dinoflagellate chromosomes imaged by high-resolution ion probe mass spectrometry, *Eur. J. Cell Biol.*, 2008, **87**, 963–976.
8 N. V. Hud and M. Polak, DNA–cation interactions: the major and minor grooves are flexible ionophores, *Curr. Opin. Struct. Biol.*, 2001, **11**, 293–301.
9 M. Egli, DNA-cation interactions: Quo vadis?, *Chem. Biol.*, 2002, **9**, 277–286.
10 S. J. Chen, RNA folding: conformational statistics, folding kinetics, and ion electrostatics, *Annu. Rev. Biophys.*, 2008, **37**, 197–214.
11 D. J. Klein, P. B. Moore and T. A. Steitz, The contribution of metal ions to the structural stability of the large ribosomal subunit, *RNA*, 2004, **10**, 1366–1379.
12 A. Bashan and A. J. Yonath, The linkage between ribosomal crystallography, metal ions, heteropolytungstates and functional flexibility, *J. Mol. Struct.*, 2008, **890**, 289–294.
13 S. A. Strobel and J. C. Cochrane, RNA catalysis: ribozymes, ribosomes, and riboswitches, *Curr. Opin. Chem. Biol.*, 2007, **11**, 636–643.
14 S. Shan, A. V. Kravchuk, J. A. Piccirilli and D. Herschlag, Defining the catalytic metal ion interactions in the Tetrahymena ribosome reaction, *Biochemistry*, 2001, **40**, 5161–5171.
15 F. Guo, A. R. Gooding and T. R. Cech, Structure of the Tetrahymena ribozyme: base triple sandwich and metal ion at the active site, *Mol. Cell*, 2004, **16**, 351–362.
16 F. Leclerc, Hammerhead ribozymes: true metal or nucleobase catalysis? Where is the catalytic power from?, *Molecules*, 2010, **15**, 5389–5407.
17 A. Garcia-Sacristán, M. Moreno, A. Ariza-Mateous, E. López-Camacho, R. M. Jáudenes, L. Vázquez, J. Gómez, J. Á. Martín-Gago and C. Briones, A magnesium-induced RNA conformational switch at the internal ribosome entry site of hepatitis C virus genome visualized by atomic force microscopy, *Nucleic Acids Res.*, 2015, **43**, 565–580.
18 K. Mizoguchi, Electronic states of M-DNA incorporated with divalent metal ions, Nanobiosystems: Processing, Characterization, and Applications III, *Proc. SPIE*, 2010, **7765**, 77650R.
19 S. Johannsen, N. Megger, D. Böhme, R. K. O. Sigel and J. Müller, Solution structure of a DNA double helix with consecutive metal-mediated base pairs, *Nat. Chem.*, 2010, **2**, 229–234.
20 Q. Zhao, U. Nagaswamy, H. Lee, Y. Xia, H. Huang, X. Gao and G. E. Fox, NMR structure and Mg^{2+} binding of an RNA segment that underlies the L7/L12 stalk in the *E. coli* 50S ribosomal subunit, *Nucleic Acids Res.*, 2005, **33**, 3145–3153.
21 B. Fürtig, C. Richter, J. Wöhnert and H. Schwalbe, NMR Spectroscopy of RNA, *ChemBioChem*, 2003, **4**, 936–962.
22 R. Ahmad, H. Arakawa and H. A. Tajmir-Riahi, A comparative study of DNA complexation with Mg(II) and Ca(II) in aqueous solution: major and minor grooves bindings, *Biophys. J.*, 2003, **84**, 2460–2466.
23 L. Chiriboga, P. Xie, H. Yee, V. Vigorita, D. Zarou, D. Zakim and M. Diem, Infrared spectroscopy of human tissue. I. Differentiation and maturation of epithelial cells in the human cervix, *Biospectroscopy*, 1998, **4**, 47–53.
24 S. Ponkumar, P. Duraisamy and N. Iyandurai, Structural analysis of DNA interactions with magnesium ion studied by Raman spectroscopy, *Am. J. Biochem. Biotechnol.*, 2011, **7**, 135–140.
25 J. Duguid, V. A. Bloomfield, J. Benevides and G. J. Thomas Jr., Raman spectroscopy of DNA-metal complexes. I. Interactions and conformational effects of the divalent cations: Mg, Ca, Sr, Ba, Mn, Co, Ni, Cu, Pd, and Cd, *Biophys. J.*, 1993, **65**, 1916–1928.
26 N. Iyandurai and R. Sarojini, Magnesium (II) ion induced changes on the structure of DNA: an FT-Raman study, *J. Appl. Sci. Res.*, 2009, **5**, 283–285.
27 B. Gong, Y. Chen, E. L. Christian, J. H. Chen, E. Chase, D. M. Chadalavada, R. Yajima, B. L. Golden, P. C. Bevilacqua and P. R. J. Carey, Detection of innersphere

Published on 11 April 2018. Downloaded by University of California - Santa Barbara on 8/5/2018 1:51:21 PM.

interactions between magnesium hydrate and the phosphate backbone of the HDV ribozyme using Raman crystallography, *J. Am. Chem. Soc.*, 2008, **130**, 9670–9672.

28 J. H. Chen, B. Gong, P. C. Bevilacqua, P. R. Carey and B. L. Golden, A catalytic metal ion interacts with the cleavage site G·U wobble in the HDV ribozyme, *Biochemistry*, 2009, **48**, 1498–1507.

29 B. Gong, J. H. Chen, R. Yajima, Y. Chen, E. Chase, D. M. Chadalavada, B. L. Golden, P. R. Carey and P. C. Bevilacqua, Raman crystallography of RNA, *Methods*, 2009, **49**, 101–111.

30 J. Stangret and R. Savoie, Vibrational spectroscopic study of the interaction of metal ions with diethyl phosphate, a model for biological systems, *Can. J. Chem.*, 1992, **70**, 2875–2883.

31 Y. Guan, C. J. Wurrey and G. J. Thomas Jr., Vibrational analysis of nucleic acids. I. The phosphodiester group in dimethyl phosphate model compounds: $(CH_3O)_2PO_2^-$, $(CD_3O)_2PO_2^-$, and $(^{13}CH_3O)_2PO_2^-$, *Biophys. J.*, 1994, **66**, 225–235.

32 P. L. Anto, R. J. Anto, H. T. Varghese, C. Y. Panicker and D. Philip, Vibrational spectroscopic studies and ab initio calculations of phenyl phosphate disodium salt, *J. Raman Spectrosc.*, 2010, **41**, 113–119.

33 S. M. Perepelytsya and S. N. Volkov, Intensities of DNA ion-phosphate modes in the low-frequency Raman spectra, *Eur. Phys. J. E: Soft Matter Biol. Phys.*, 2010, **31**, 201–205.

34 E. Ennifar, P. Walter and P. Dumas, Cation-dependent cleavage of the duplex form of the subtype-B HIV-1 RNA dimerization initiation site, *Nucleic Acids Res.*, 2010, **38**, 5807–5816.

35 M. Egli, G. Minasov, L. Su and A. Rich, Metal ions and flexibility in a viral RNA pseudoknot at atomic resolution, *Proc. Natl. Acad. Sci. U. S. A.*, 2002, **99**, 4302–4307.

36 C. C. Correll, B. Freeborn, P. B. Moore and T. A. Steitz, Metals, motifs, and recognition in the crystal structure of a 5S rRNA domain, *Cell*, 1997, **91**, 705–712.

37 J. A. Subirana and M. Soler-López, Cations as hydrogen bond donors: a view of electrostatic interactions in DNA, *Annu. Rev. Biophys. Biomol. Struct.*, 2003, **32**, 27–45.

38 C. Sines, L. McFail-Isom, S. Howerton, D. VanDerveer and L. Williams, Cations mediate B-DNA conformational heterogeneity, *J. Am. Chem. Soc.*, 2000, **122**, 11048–11056.

39 P. Auffinger and E. Westhof, Water and ion binding around RNA and DNA (C, G) oligomers, *J. Mol. Biol.*, 2000, **300**, 1113–1131.

40 D. Hamelberg, L. McFail-Isom, L. Williams and W. Wilson, Flexible structure of DNA: ion dependence of minor-groove structure and dynamics, *J. Am. Chem. Soc.*, 2000, **122**, 10513–10520.

41 D. Hamelberg, L. Williams and W. Wilson, Influence of the dynamic positions of cations on the structure of the DNA minor groove: sequence-dependent effects, *J. Am. Chem. Soc.*, 2001, **123**, 7745–7755.

42 N. Korolev, A. P. Lyubartsev, A. Rupprecht and L. Nordenskiöld, Competitive binding of Mg^{2+}, Ca^{2+}, Na^+, and K^+ ions to DNA in oriented DNA fibers: experimental and Monte Carlo simulation results, *Biophys. J.*, 1999, **77**, 2736–2749.

43 J. Yoo and A. Aksimentiev, Improved parametrization of Li^+, Na^+, K^+, and Mg^{2+} ions for all-atom molecular dynamics simulations of nucleic acid systems, *J. Phys. Chem. Lett.*, 2012, **3**, 45–50.

44 F. Ryjacek, T. Kubar and P. J. Hobza, New parameterization of the Cornell *et al.* empirical force field covering amino group nonplanarity in nucleic acid bases, *Comput. Chem.*, 2003, **24**, 1891–1901.

45 M. Ditzler, M. Otyepka, J. Sponer and N. Walter, Molecular dynamics and quantum mechanics of RNA: conformational and chemical change we can believe in, *Acc. Chem. Res.*, 2010, **43**, 40–47.

46 A. Petrov, J. Bowman, S. Harvey and L. Williams, Bidentate RNA–magnesium clamps: on the origin of the special role of magnesium in RNA folding, *RNA*, 2011, **17**, 291–297.

47 P. Banas, P. Jurecka, N. G. Walter, J. Sponer and M. Otyepka, Theoretical studies of RNA catalysis: hybrid QM/MM methods and their comparison with MD and QM, *Methods*, 2009, **49**, 202–216.

48 D. Di Tommaso and N. H. De Leeuw, Structure and dynamics of the hydrated magnesium ion and of the solvated magnesium carbonates: insights from first principles simulations, *Phys. Chem. Chem. Phys.*, 2010, **12**, 894–901.

49 S. Kolev, P. Petkov, M. Rangelov and G. Vayssilov, *Ab initio* molecular dynamics of Na^+ and Mg^{2+} countercations at the backbone of RNA in water solution, *ACS Chem. Biol.*, 2013, **8**, 1576–1589.

50 Y. Tanaka, S. Yamagata, Y. Kitago, Y. Yamada, S. Chimnaronk, M. Yao and I. Tanaka, Deduced RNA binding mechanism of ThiI based on structural and binding analyses of a minimal RNA ligand, *RNA*, 2009, **15**, 1498–1506.

51 J. Nix, D. Sussman and C. Wilson, The 1.3 Å crystal structure of a biotin-binding pseudoknot and the basis for RNA molecular recognition, *J. Mol. Biol.*, 2000, **296**, 1235–1244.

52 J. Deng, Y. Xiong and M. Sundaralingam, X-ray analysis of an RNA tetraplex (UGGGGU) 4 with divalent Sr^{2+} ions at subatomic resolution (0.61 Å), *Proc. Natl. Acad. Sci. U. S. A.*, 2001, **98**, 13665–13670.

53 J. A. Ippolito and T. A. Steitz, A 1.3 Å resolution crystal structure of the HIV-1 trans-activation response region RNA stem reveals a metal ion-dependent bulge conformation, *Proc. Natl. Acad. Sci. U. S. A.*, 1998, **95**, 9819–9824.

54 P. S. Pallan, W. S. Marshall, J. Harp, F. C. Jewett III, Z. Wawrzak, B. A. Brown II, A. Rich and M. Egli, Crystal structure of a luteoviral RNA pseudoknot and model for a minimal ribosomal frameshifting motif, *Biochemistry*, 2005, **44**, 11315–11322.

55 E. Ennifar and P. Dumas, Polymorphism of bulged-out residues in HIV-1 RNA DIS kissing complex and structure comparison with solution studies, *J. Mol. Biol.*, 2006, **256**, 771–782.

56 U. Mueller, Y. A. Muller, R. Herbst-Irmer, M. Sprinzl and U. Heinemann, Disorder and twin refinement of RNA

 This journal is © The Royal Society of Chemistry 2018

Published on 11 April 2018. Downloaded by University of California - Santa Barbara on 8/5/2018 1:51:21 PM.

heptamer double helices, *Acta Crystallogr., Sect. D: Biol. Crystallogr.*, 1999, **55**, 1405–1413.
57 U. Mueller, H. Schubel, M. Sprinzl and U. Heinemann, Crystal structure of acceptor stem of tRNA Ala from *Escherichia coli* shows unique G·U wobble base pair at 1.16 Å resolution, *RNA*, 1999, **5**, 670–677.
58 T. Hermann, V. Tereshko, E. Skripkin and D. Patel, Apramycin recognition by the human ribosomal decoding site, *J. Blood Cells Mol. Dis*, 2007, **38**, 193–198.
59 B. H. Mooers and A. Singh, The crystal structure of an oligo (U): pre-mRNA duplex from a trypanosome RNA editing substrate, *RNA*, 2011, **17**, 1870–1883.
60 S. Freisz, K. Lang, R. Micura, P. Dumas and E. Ennifar, Binding of aminoglycoside antibiotics to the duplex form of the HIV-1 genomic RNA dimerization initiation site, *Angew. Chem., Int. Ed.*, 2008, **47**, 4110–4113.
61 G. Storz, An expanding universe of noncoding RNAs, *Science*, 2002, **296**(5571), 1260.
62 H. Zheng, I. G. Shabalin, K. B. Handing, J. M. Bujnicki and W. Minor, Magnesium-binding architectures in RNA crystal structures: validation, binding preferences, classification and motif detection, *Nucleic Acids Res.*, 2015, **43**, 3789–3801.
63 H. Lodish, A. Berk, L. Zipursky, P. Matsudaira, D. Baltimore and J. Darnell, *Molecular cell biology*, W. H. Freeman, New York, NY, 4th edn, 2000.
64 M. A. Rangelov, G. N. Vayssilov, V. M. Yomtova and D. D. Petkov, The syn-oriented 2-OH provides a favorable proton transfer geometry in 1,2-diol monoester aminolysis: implications for the ribosome mechanism, *J. Am. Chem. Soc.*, 2006, **128**, 4964–4965.
65 M. A. Rangelov, G. P. Petrova, V. M. Yomtova and G. N. Vayssilov, Catalytic role of vicinal OH in ester aminolysis: proton shuttle versus hydrogen bond stabilization, *J. Org. Chem.*, 2010, **75**, 6782–6792.
66 B. Hingerty, R. S. Brown and A. Jack, Further refinement of the structure of yeast tRNAPhe, *J. Mol. Biol.*, 1978, **124**, 523–534.
67 E. Westhof, P. Dumas and D. Moras, Restrained refinement of two crystalline forms of yeast aspartic acid and phenylalanine transfer RNA crystals, *Acta Crystallogr., Sect. A: Found. Crystallogr.*, 1988, **44**, 112–123.
68 E. Westhof and M. Sundaralingam, Restrained refinement of the monoclinic form of yeast phenylalanine transfer RNA. Temperature factors and dynamics, coordinated waters, and base-pair propeller twist angles, *Biochemistry*, 1986, **25**, 4868–4878.
69 J. L. Sussman, S. R. Holbrook, R. W. Warrant, G. M. Church and S. H. Kim, Crystal structure of yeast phenylalanine transfer RNA: I. Crystallographic refinement, *J. Mol. Biol.*, 1978, **123**, 607–630.
70 H. Shi and P. B. Moore, The crystal structure of yeast phenylalanine tRNA at 1.93 Å resolution: a classic structure revisited, *RNA*, 2000, **6**, 1091–1105.
71 S. Basu, R. P. Rambo, J. Strauss-Soukup, J. H. Cate, A. R. Ferre-D'Amare, S. A. Strobel and J. A. Doudna, A specific monovalent metal ion integral to the AA platform of the RNA tetraloop receptor, *Nat. Struct. Biol.*, 1998, **5**, 986–992.
72 R. Shiman and D. E. Draper, Stabilization of RNA tertiary structure by monovalent cations, *J. Mol. Biol.*, 2000, **302**, 79–91.
73 F. C. Chao and H. K. Schachman, The isolation and characterization of a macro-molecular ribonucleoprotein from yeast, *Arch. Biochem. Biophys.*, 1956, **61**, 220–230.
74 F. C. Chao, Dissociation of macromolecular ribonucleoprotein of yeast, *Arch. Biochem. Biophys.*, 1957, **70**, 426–431.
75 A. Tissieres, J. D. Watson, D. Schlessinger and B. R. Hollingworth, Ribonucleoprotein particles from *Escherichia coli*, *J. Mol. Biol.*, 1959, **1**, 221–233.
76 B. McCarthy, The effects of magnesium starvation on the ribosome content of *Escherichia coli*, *Biochim. Biophys. Acta*, 1962, **55**, 880–888.
77 B. W. Kimes and D. R. Morris, Cations and ribosome structure. II. Effect of the 50S subunit of substituting polyamines for magnesium ion, *Biochemistry*, 1973, **12**, 442–449.
78 J. Gordon and F. Lipmann, Role of divalent ions in poly U-directed phenylalanine polymerization, *J. Mol. Biol.*, 1967, **23**, 23–33.
79 P. B. Moore, Polynucleotide attachment to ribosomes, *J. Mol. Biol.*, 1966, **18**, 8–20.
80 J. A. Khawaja and A. Raina, Effect of spermine and magnesium on the attachment of free ribosomes to endoplasmic reticulum membranes *in vitro*, *Biochem. Biophys. Res. Commun.*, 1970, **41**, 512–518.
81 P. H. Naslund and T. Hultin, Effects of potassium deficiency on mammalian ribosomes, *Biochim. Biophys. Acta*, 1970, **204**, 237–247.
82 R. S. Zitomer and J. G. Flaks, Magnesium dependence and equilibrium of the *Escherichia coli* ribosomal subunit association, *J. Mol. Biol.*, 1972, **71**, 263–279.
83 N. Ban, P. Nissen, J. Hansen, B. Moore and A. Steitz, The complete atomic structure of the large ribosomal subunit at 2.4 A resolution, *Science*, 2000, **289**, 905–920.
84 J. H. Cate and J. A. Doudna, Metal-binding sites in the major groove of a large ribozyme domain, *Structure*, 1996, **4**, 1221–1229.
85 J. Liu and A. Subirana, Structure of d(CGCGAATTCGCG) in the presence of Ca(2+) ions, *J. Biol. Chem.*, 1999, **274**, 24749–24752.
86 A. R. Ferre-D'Amare, K. Zhou and J. A. Doudna, Crystal structure of a hepatitis delta virus ribozyme, *Nature*, 1998, **395**, 567.
87 J. Schwarz, C. Contescu and K. Putyera, *Dekker Encyclopedia of Nanoscience and Nanotechnology*, Marcel Dekker, Inc., New York, NY, 2004.
88 S. Vangaveti, S. Ranganathan and A. Chen, Advances in RNA molecular dynamics: a simulator's guide to RNA force fields, *Wiley Interdiscip. Rev.: RNA*, 2017, **8**, 2.
89 E. J. Denning, U. D. Priyakumar and L. Nilsson, Impact of 20-hydroxyl sampling on the conformational properties of

Published on 11 April 2018. Downloaded by University of California - Santa Barbara on 8/5/2018 1:51:21 PM.

RNA: update of the CHARMM all-atom additive force field for RNA, *J. Comput. Chem.*, 2011, **32**, 1929–1943.

90 A. Savelyev and A. D. MacKerell, All-atom polarizable force field for DNA based on the classical Drude oscillator model, *J. Comput. Chem.*, 2014, **35**, 1219–1239.

91 I. Yildirim, S. D. Kennedy, H. A. Stern, J. M. Hart, R. Kierzek and D. H. Turner, Revision of AMBER torsional parameters for RNA improves free energy predictions for tetramer duplexes with GC and iGiC base pairs, *J. Chem. Theory Comput.*, 2012, **8**, 172–181.

92 M. Zgarbova, M. Otyepka, J. Sponer, A. Mladek, P. Banas and P. Jurecka, Refinement of the Cornell *et al.* nucleic acids force field based on reference quantum chemical calculations of glycosidic torsion profiles, *J. Chem. Theory Comput.*, 2011, **7**, 2886–2902.

93 A. A. Chen and A. E. Garcia, High-resolution reversible folding of hyperstable RNA tetraloops using molecular dynamics simulations, *Proc. Natl. Acad. Sci. U. S. A.*, 2013, **110**, 16820–16825.

94 H. J. C. Berendsen, J. R. Grigera and T. P. Straatsma, The missing term in effective pair potentials, *J. Phys. Chem.*, 1987, **91**, 6269.

95 W. L. Jorgensen, J. Chandrasekhar, J. D. Madura, R. W. Impey and M. L. Klein, Comparison of simple potential functions for simulating liquid water, *J. Chem. Phys.*, 1983, **79**, 926.

96 H. W. Horn, W. C. Swope, J. W. Pitera, J. D. Madura, T. J. Dick, G. L. Hura and T. Head-Gordon, Development of an improved four-site water model for biomolecular simulations: TIP4P-Ew, *J. Chem. Phys.*, 2004, **120**, 9665–9678.

97 M. W. Mahoney and W. L. Jorgensen, A five-site model for liquid water and the reproduction of the density anomaly by rigid, nonpolarizable potential functions, *J. Chem. Phys.*, 2000, **112**, 8910.

98 M. Gueroult, O. Boittin, O. Mauffret, C. Etchebest and B. Hartmann, Mg^{2+} in the major groove modulates B-DNA structure and dynamics, *PLoS One*, 2012, **7**, e41704.

99 W. D. Comell, P. Cieplak, C. I. Bayly, I. R. Gould, K. M. Merz, D. M. Ferguson, D. C. Spellmeyer, T. Fox, J. W. Caldwell and P. A. Kollman, A second generation force field for the simulation of proteins, nucleic acids, and organic molecules, *J. Am. Chem. Soc.*, 1995, **117**, 5179–5196.

100 M. Pasi, J. Maddocks and R. Lavery, Analyzing ion distributions around DNA: sequence-dependence of potassium ion distributions from microsecond molecular dynamics, *Nucleic Acids Res.*, 2015, **43**, 2412–2423.

101 M. Krasovska, J. Sefcikova, K. Reblova, B. Schneider, N. G. Walter and J. Sponer, Cations and hydration in catalytic RNA: molecular dynamics of the hepatitis delta virus ribozyme, *Biophys. J.*, 2006, **91**, 626–638.

102 H. Zheng, I. G. Shabalin, K. B. Handing, J. M. Bujnicki and W. Minor, Magnesium-binding architectures in RNA crystal structures: validation, binding preferences, classification and motif detection, *Nucleic Acids Res.*, 2015, **43**, 3789–3801.

103 R. Cunha and G. Bussi, Unraveling Mg^{2+}-RNA binding with atomistic molecular dynamics, *RNA*, 2017, **23**, 628–638.

104 A. Petrov, J. Funseth-Smotzer and G. Pack, Computational study of dimethyl phosphate anion and its complexes with water, magnesium, and calcium, *Int. J. Quantum Chem.*, 2005, **102**, 645–655.

105 M. L. Sushko, D. G. Thomas, S. A. Pabit, L. Pollack, A. V. Onufriev and N. A. Baker, The role of correlation and solvation in ion interactions with B-DNA, *Biophys. J.*, 2016, **110**, 315–326.

106 L. Perera, B. D. Freudenthal, W. A. Beard, D. D. Shock, L. G. Pedersen and S. H. Wilson, Requirement for transient metal ions revealed through computational analysis for DNA polymerase going in reverse, *Proc. Natl. Acad. Sci. U. S. A.*, 2015, **112**, E5228–E5236.

107 J. B. Swadling, D. W. Wright, J. L. Suter and P. V. Coveney, Structure, dynamics, and function of the hammerhead ribozyme in bulk water and at a clay mineral surface from replica exchange molecular dynamics, *Langmuir*, 2015, **31**, 2493–2501.

 This journal is © The Royal Society of Chemistry 2018

WORLD SEAS

AN ENVIRONMENTAL EVALUATION

EDITED BY CHARLES SHEPPARD

SECOND EDITION



VOLUME I

EUROPE, THE AMERICAS AND WEST AFRICA

World Seas: An Environmental Evaluation

This page intentionally left blank

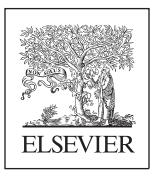
World Seas: An Environmental Evaluation

Volume I: Europe, The Americas and West Africa

Second Edition

Edited by

Charles Sheppard
Emeritus Professor, School of Life Sciences
University of Warwick, United Kingdom





ACADEMIC PRESS
An imprint of Elsevier

Academic Press is an imprint of Elsevier
125 London Wall, London EC2Y 5AS, United Kingdom
525 B Street, Suite 1650, San Diego, CA 92101, United States
50 Hampshire Street, 5th Floor, Cambridge, MA 02139, United States
The Boulevard, Langford Lane, Kidlington, Oxford OX5 1GB, United Kingdom

© 2019 Elsevier Ltd. All rights reserved.

No part of this publication may be reproduced or transmitted in any form or by any means, electronic or mechanical, including photocopying, recording, or any information storage and retrieval system, without permission in writing from the publisher. Details on how to seek permission, further information about the Publisher's permissions policies and our arrangements with organizations such as the Copyright Clearance Center and the Copyright Licensing Agency, can be found at our website: www.elsevier.com/permissions.

This book and the individual contributions contained in it are protected under copyright by the Publisher (other than as may be noted herein).

Notices
Knowledge and best practice in this field are constantly changing. As new research and experience broaden our understanding, changes in research methods, professional practices, or medical treatment may become necessary.

Practitioners and researchers must always rely on their own experience and knowledge in evaluating and using any information, methods, compounds, or experiments described herein. In using such information or methods they should be mindful of their own safety and the safety of others, including parties for whom they have a professional responsibility.

To the fullest extent of the law, neither the Publisher nor the authors, contributors, or editors, assume any liability for any injury and/or damage to persons or property as a matter of products liability, negligence or otherwise, or from any use or operation of any methods, products, instructions, or ideas contained in the material herein.

Library of Congress Cataloging-in-Publication Data
A catalog record for this book is available from the Library of Congress

British Library Cataloguing-in-Publication Data
A catalogue record for this book is available from the British Library

ISBN 978-0-12-805068-2

For information on all Academic Press publications
visit our website at https://www.elsevier.com/books-and-journals



Publisher: Candice Janco
Acquisition Editor: Louisa Hutchins
Editorial Project Manager: Hilary Carr
Production Project Manager: Prem Kumar Kaliamoorthi
Cover Designer: Matthew Limbert

Typeset by SPi Global, India

Contents

Contributors xiii
Introduction to World Seas: An Environmental Evaluation xix

1. Antarctic Seas

Jonathan S. Stark, Tania Raymond, Stacy L. Deppeler, Adele K. Morrison

1.1 The Defined Region 1
1.2 Natural Environmental Variables and Seasonality 5
1.3 Pelagic Ecosystems 11
1.4 Benthic Ecosystems 14
1.5 Climate Change Impacts 19
1.6 Human Populations Affecting the Area 21
1.7 Resources 26
1.8 Management Regimes 32
1.9 Summary, Prognoses, or Needs 35
Acknowledgment 38
References 38

2. The Seas Around Greenland: An Environmental Status and Future Perspective

Frank Rigét, Anders Mosbech, David Boertmann, Susse Wegeberg, Flemming Merkel, Peter Aastrup, Tom Christensen, Fernando Ugarte, Rasmus Hedeholm, Janne Fritt-Rasmussen

2.1 Introduction 45
2.2 The Region 45
2.3 Anthropogenic Impacts 51
2.4 Resources 55
2.5 Management Regimes 60
References 63
Further Reading 68

3. The Environmental Status of Norwegian Coastal Waters

Christopher Harman, Trine Bekkby, Sara Calabrese, Hilde Trannum, Eivind Oug, Anders G. Hagen, Norman Green, Øyvind Kaste, Helene Frigstad

3.1 Introduction 69
3.2 The Region, Environmental Variables, and Important Habitats 69
3.3 Overall Trends in Pollutant Inputs and Concentrations 74
3.4 Resources 78
3.5 Management and Conservation Regimes 81
References 82
Further Reading 84

4. The Baltic Sea

Beata Szymczycha, Agata Zaborska, Jacek Bełdowski, Karol Kuliński, Agnieszka Beszczyńska-Möller, Monika Kędra, Janusz Pempkowiak

4.1 Introduction 85
4.2 Physical Setting 85
4.3 Major Habitats in the Baltic Sea 94
4.4 Biogeochemical Cycles 96
4.5 Submarine Groundwater Discharge 98
4.6 Chemical Pollution of the Baltic Sea 99
4.7 Resources 104
References 107
Further Reading 111

5. The Bay of Biscay

Angel Borja, David Amouroux, Pierre Anschutz, Moncho Gómez-Gesteira, María C. Uyarra, Luis Valdés

5.1 Description of the Area 113
5.2 Seasonality and Natural Environmental Variables 113
5.3 Major Habitats and Ecosystem Components 119
5.4 Populations Affecting the Area 130
5.5 Effects of Human Activities 134
5.6 Conservation and Status Assessment 138
5.7 Perspectives 142
References 145
Further Reading 152

6. The English Channel: La Manche

Jean-Claude Dauvin

6.1 Main Characteristics of the English Channel 153
6.2 Major Coastal and Shallow Habitats 157
6.3 Offshore Systems 160
6.4 Climate Change Impacts 164
6.5 Human Populations Affecting the Area 166
6.6 Resources 171
6.7 Management Regimes, Protection, and Conservation Measures 178
6.8 Needs and Prognoses 182
References 183

7. The Portuguese Coast

Patricia G. Cardoso, Marina Dolbeth, Ronaldo Sousa, Paulo Relvas, Rui Santos, Alexandra Silva, Victor Quintino

7.1 Historical Context 189
7.2 The Defined Region 189
7.3 Major Oceanographic Settings 191
7.4 Major Coastal Habitats 192
7.5 Antropogenic impacts 197
7.6 Water Management in the Portuguese Continental Coast 200
7.7 Final Remarks 204
Acknowledgments 204
References 204

8. Black Sea

Nadezhda Todorova, Sergey V. Alyomov, Brindusa Cristina Chiotoroiu, Bettina Fach, Tatyana S. Osadchaya, Miroslav Rangelov, Baris Salihoglu, Vasil Vasilev

8.1 Geography, Topography, and Geological Description 209
8.2 Physical Oceanography and Climate 211
8.3 Major Coastal and Shallow Habitats 212
8.4 Offshore Systems 213
8.5 Climate Change Impacts 214
8.6 Human Populations Affecting the Area 216
8.7 Resources 220
8.8 Threats and Management 221
8.9 Summary, Prognoses, or Needs 223
References 223
Further Reading 226

9. Greece

Nomiki Simboura, Panagiota Maragou, Giorgos Paximadis, Kostas Kapiris, Vassilis P. Papadopoulos, Dimitris Sakellariou, Alexandra Pavlidou, Ioannis Hatzianestis, Maria Salomidi, Christos Arvanitidis, Panayotis Panayotidis

9.1 Geography, Topography, Geological Description 227
9.2 Physical Oceanography 227
9.3 Natural Environmental Variables, Seasonality 230
9.4 Biodiversity 230
9.5 Major Habitats 231
9.6 Resources 236
9.7 Human Activities Affecting the Hellenic Seas 240
9.8 Climate Change Impacts 242
9.9 Impacts of Human Activities on the Marine Environment 244
9.10 Threats to Sustainable Use of Resources 250
9.11 Management Regimes 250
9.12 Prognoses, Deficiencies and Missing Measures 254
Acknowledgments 256
References 256

10. Tunisia

Lotfi Aleya, Béchir Béjaoui, Amel Dhib, Boutheina Ziadi, Mouna Fertouna-Bellekhal, Mohamed-Amine Helali, Inès Khedhri, Walid Oueslati, Rym Ennouri, Cintia Yamashita, Noureddine Zaaboub, Achref Othmani, Monia El Bour, Lamia Trabelsi, Mohamed M. Abdel-Daim, François Galgani, Maria Virgínia Alves Martins, Souad Turki

10.1 Introduction 261
10.2 Gulfs 261
10.3 Coastal Wetlands 264
10.4 Conclusion 278
Acknowledgment 278
References 278
Further Reading 282

11. Italian Seas

Roberto Danovaro, Ferdinando Boero

11.1 The Italian Seas 283
11.2 Physical Oceanography of the Mediterranean Sea 283

Chapter 8

Black Sea

Nadezhda Todorova*,[1], Sergey V. Alyomov[†], Brindusa Cristina Chiotoroiu[‡], Bettina Fach[§], Tatyana S. Osadchaya[†], Miroslav Rangelov[¶], Baris Salihoglu[§], Vasil Vasilev*

*Institute of Biodiversity and Ecosystem Research, Bulgarian Academy of Sciences (IBER-BAS), Sofia, Bulgaria, [†]The A.O. Kovalevsky Institute of Marine Biological Researches (IMBR), Sevastopol, Russia, [‡]Constanta Maritime University, Constanta, Romania, [§]Institute of Marine Sciences, Middle East Technical University, Erdemli, Turkey, [¶]Institute of Organic Chemistry with Center of Phytochemistry, Bulgarian Academy of Sciences (IOCCP-BAS), Sofia, Bulgaria

8.1 GEOGRAPHY, TOPOGRAPHY, AND GEOLOGICAL DESCRIPTION

The Black Sea, is situated in south-eastern Europe, partly bordering Asia. Its south coast is the Pontic Mountains with the Caucasus Mountains to the northeast, while the topography of the north-western (NW) coast (except for Crimea) is relatively low and flat. Its coastline is about 4400 km long. The Black Sea is classified geomorphologically into a shelf, the continental slope and a deep-sea depression (Fig. 8.1). The shelf edge slope is steep and the shelf is basically narrow except for the NW.

Its connection to the World Ocean is through the Aegean and Mediterranean Sea, where 300 $km^3\,year^{-1}$ of mesohaline water passes out through the Bosphorus Strait (Ludwig, Dumont, Meybeck, & Heussner, 2009). As part of a two-way hydrological exchange, the Black Sea's cooler and less saline outflow floats over the warm, more saline Mediterranean inflow. Part of this passage include the Sea of Azov and the Strait of Kerch.

Although total basin precipitation is less than evaporation (Jaoshvili, 2002), the water supply from several big rivers, such as Danube, Dnieper, Rioni, etc. with a total river catchment area of about $2.4 \times 10^6\,km^2$, give a positive freshwater balance, resulting in a low salinity in the upper layer of between 18 psu in the open sea to 16 psu close to the shore. The river input in the NW causes a drop of salinity of up to 5 psu close to river mouth regions. The amount of freshwater and nutrient input into the southern parts of the Black Sea is relatively small.

Beach sediment texture is variable, and coarse and medium sediments form about 35% of the beaches (Fig. 8.2) (Allenbach et al., 2015), providing sedimentation rates in the NW part of 2.3 $mm\,year^{-1}$ (Gulin, Aarkrog, Polikarpov, Nielsen, & Egorov, 1997).

Terrigenous fine sand supplied by the big rivers forms the main new accumulations of sediments, actively transported by wave-induced longshore currents. Deep sediment depositions contain three layers, with the uppermost containing organic carbonates and pyrite, followed by one of low-carbonate high organic content and a bottom layer with very low organic content (Yucel, Moore, Butler, Boyce, & Luther III, 2012).

The Black Sea margin is well studied, but as it is sediment-starved, its subsidence record is difficult to reconstruct (Shillington et al., 2008). The region has experienced several episodes of extension and shortening since the Permian (Robertson et al., 2014) and can be subdivided into eastern and western basins according to its basement structures. For extended periods during the Quaternary, it formed a lacustrine environment. The Holocene flooding over the shallow sill of the Bosphorus Strait (Esin, Yanko-Hombach, & Kukleva, 2010), was followed by a more gradual marine transgression. The modern sedimentary environments of the basin comprise continental shelves, canyon-scarred continental slopes and deep-sea fans (Allenbach et al., 2015).

1. Except the corresponding author (NT), all other co-authors are listed alphabetically and have equivalent contributions.

World Seas: An Environmental Evaluation. https://doi.org/10.1016/B978-0-12-805068-2.00011-5
© 2019 Elsevier Ltd. All rights reserved.



FIG. 8.1 The Black Sea.

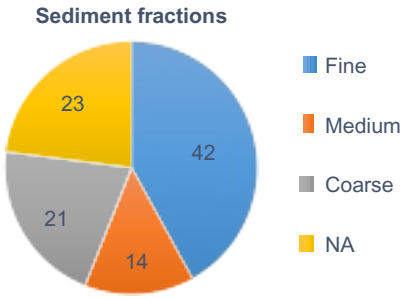


FIG. 8.2 Characteristics of the Black Sea beach sediment texture (according to Allenbach et al., 2015).

8.2 PHYSICAL OCEANOGRAPHY AND CLIMATE

8.2.1 Circulation Characteristics

The horizontal flow is strongly influenced by the cyclonic Rim Current, a permanent feature of the upper layer circulation (Kubryakov & Stanichny, 2015). This current is meandering and encircles the entire basin, forming a large cyclonic gyre and two cyclonic cells in the central basin (see Fig. 8.1). The general circulation is driven by buoyancy difference caused by the large freshwater input on the NW shelf, and by water from the Bosphorus Strait (Ivanov & Belokopytov, 2013), in addition to the wind stress curl, and it follows the steep continental slope. Current speed varies with the amount of discharge from rivers and variations in the wind. Current speeds of 50–150 cm s^{-1} have been measured in the upper layer of the Rim Current (Oguz & Besiktepe, 1999) and its meanders typically have a timescale of 50–150 days (Korotaev, Oguz, Nikiforov, & Koblinsky, 2003).

The Rim Current is most intense in winter–spring. Strong mesoscale variability is observed causing the formation of a number of quasi-permanent anticyclonic eddies on the coastal side of this current. The dynamic events of meandering, eddy formation, and detachment take place on weekly timescales and may lead to considerable exchange between coastal regions and offshore areas (Oguz, Deshpande, & Malanotte-Rizzoli, 2002).

Intermediate and deep layers have strong currents and a well-organized flow structure (Korotaev, Oguz, & Riser, 2006). A well-defined cyclonic circulation extends from the surface to the bottom, without reversal in its direction. Deep currents are steered by the steep topographic slope, and are well correlated with surface currents.

8.2.2 Main Physical Features and Freshwater Discharges

The Black Sea exhibits strong and permanent vertical stratification, with well-mixed low-salinity surface waters of river origin and precipitation, overlying high-salinity deep waters of Mediterranean origin (Ozsoy & Unluata, 1997). An important thermal feature is the cold intermediate layer (CIL), a structure conventionally identified by temperatures <8°C and a vertical extent that is limited to the upper 100 m layer, corresponding typically to ~15.4 kg m^{-3} isopycnal. The CIL forms as a result of intense cooling of surface waters during winter and it prevails in the form of a distinct subsurface water mass during the rest of the year when the surface-mixed layer is stratified by warming, and/or increased river runoff (Akpinar, Fach, & Oguz, 2017). Decoupling of vertical mixing leads to a deep-water salinity increase to 22.3 psu and temperatures rise to around 8.9°C (Fig. 8.3) (Ostrovskii & Zatsepin, 2016). The main source of oxygen for deeper waters is the permanent CIL at depths of 50–130 m.

The hydrochemical environment also shifts from oxygenated to anoxic, as bacterial decomposition of sunken biomass utilizes all of the free oxygen. Weak geothermal heating and a long residence time create a very thick convective bottom layer (Korotaev et al., 2003).

The biologically productive, oxic layer extends to nearly 50 m, after which there is undetectable dissolved oxygen (<5 mmol O_2/m^3) (Gregg & Yakushev, 2005). This deoxygenation process is different to that in the deep sea and is induced by intrinsic hydrodynamic reasons, and on human-induced NW shelf hypoxic events. Model-based simulations and observations show distinct evidence of both phenomena (Vandenbulcke, Capet, & Grégoire, 2017). Seasonal hypoxic events occur annually in the northern part of the shelf, and the oxygen-rich top layer of the Black Sea shallowed from 140 to 90 m deep between 1955 and 2015 (Capet, Stanev, Beckers, Murray, & Grégoire, 2016).

The buoyancy flux affects Black Sea circulation dynamics (Korotaev et al., 2006). Net buoyancy flux, that is, buoyancy due to net heat flux and freshwater flux at the sea surface (thermal/haline buoyancy flux), shows a gain (i.e., the upper ocean stabilizes from March through September, and shows a loss (i.e., destabilizes) in other months. River runoff, in particular the Danube, has a large influence on the dynamics of the continental shelf by changing the heat and freshwater

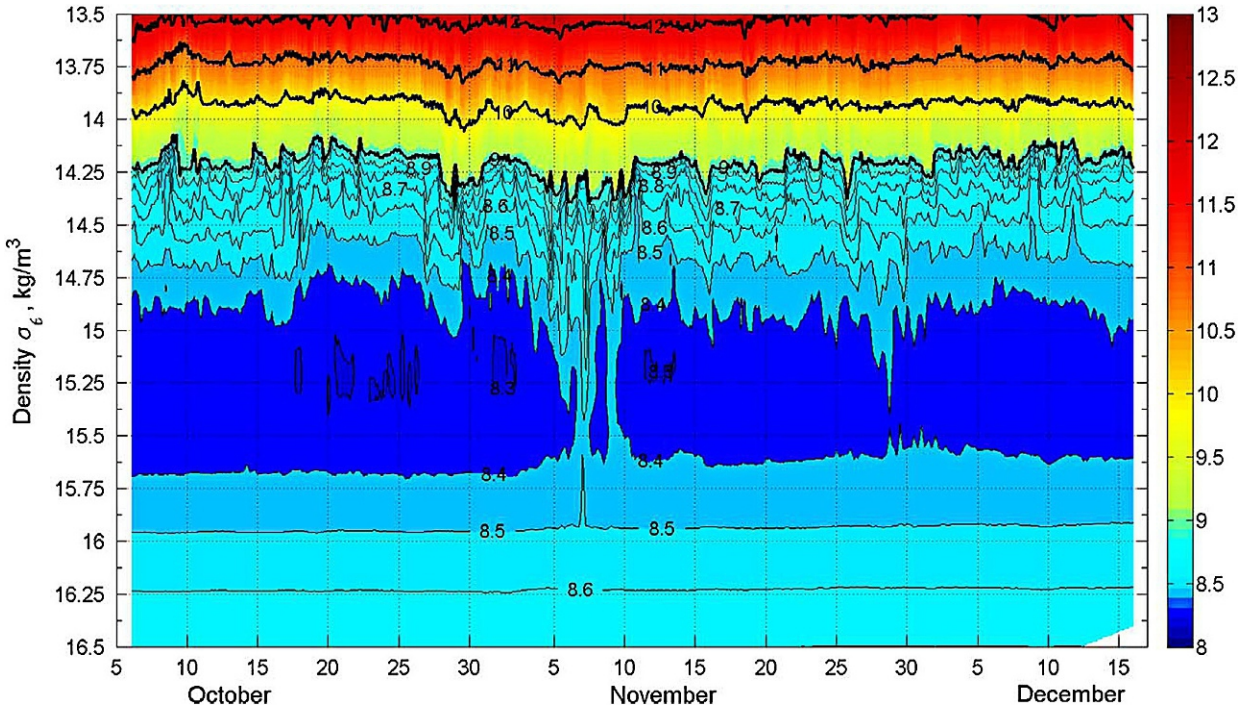


FIG. 8.3 Time-potential density diagram of sea temperatures in Gelendzhik Bay, Rim Current area, derived in December 2014 (according to Ostrovskii & Zatsepin, 2016).

fluxes, especially in the NW shelf. The Danube monthly mean discharge ranges from 4000 to 9000 $m^3 s^{-1}$ on climatological timescales (Vorosmarty et al., 1997), which contributes to the dilution of surface waters (Stanev, Bowman, Peneva, & Staneva, 2003).

Interruptions in the permanent pycnocline current velocity and related increases of vertical turbulent mixing may occur sporadically throughout the entire year in the core area of the Rim Current, being more frequent in the autumn or winter. The deep ventilation mechanism in the aerobic zone may be important for maintaining the thickness of the aerobic layer and for keeping the upper boundary of the H_2S zone within the permanent pycnocline area (Ostrovskii & Zatsepin, 2016). In the Black Sea, the most important phenomena sustaining the ecosystem is the retention of the H_2S boundary in the permanent pycnocline layer.

8.2.3 Atmospheric Circulation

The Black Sea is influenced by North Atlantic climate through cross-Europe atmospheric connections. High- and low-pressure centers over the Caspian and North Seas, alongside the North Atlantic Oscillation, provide coherent synchronous fluctuations with Black Sea hydrometeorological properties (Oguz, Dippner, & Kaymaz, 2006).

In summer, clear and dry weather is mainly due to the extension of the Azores anticyclone ridge across Europe and Mediterranean to the Black Sea. In winter, a vast anticyclone over Siberia has a ridge extending to NW coasts of the Black Sea, where pressure is generally lower. If a separate high-pressure center develops over the Baltic and Scandinavia, very cold Arctic air is brought to the Black Sea. It was found, however, that extreme daily minimum temperatures have increased in south-east Romania during recent decades (Croitoru & Piticar, 2013). Snow storms and regional strong winds in the NW Black Sea are due to the coupling between this cold advection and the warmer air brought by mobile depressions coming mostly from the Mediterranean Sea (Georgescu, Tascu, Caian, & Banciu, 2009).

8.3 MAJOR COASTAL AND SHALLOW HABITATS

The Black Sea is a basic European watershed, with higher productivity than the neighboring Mediterranean (Oral, 2013), with dynamic wetland ecosystems in coastal areas and in the mouths of rivers. According to the Habitat Directive (92/43/EEC) and the Interpretation Manual of European Union Habitats—EUR28, 2013 (Milchakova, Aleksandrov, Bondareva,



FIG. 8.4 *Left*: Coast near *Zostera* sp. field after a storm, photo by Miroslav Rangelov IOCCP-BAS. *Right*: *Zostera*_fields, photo by Sonya Tsoneva & Valeri Georgiev IBER-BAS, Roman Tashev INB-BAS.

Pankeeva, & Chernysheva, 2015; Zaharia, Micu, Todorva, Maximov, & Nita, 2008), coastal and halophytic habitat classes of prior importance are as follows:

1110–1 *Zostera* meadows on clear or slightly muddy fine sands, with very high conservation value. These are highly productive zones and provide a number of ecosystem services, such as provision of habitat and enhanced biodiversity. As an important bioindicator of system health, they stabilize sediments and are natural hotspots for carbon sequestration. The seagrass beds are being reduced as a result of human activities such as turbidity increase, eutrophication, dredging and fishing, direct clearance due to coastal or harbor constructions, and negative effects of climate change (Duarte, 2002) (Fig. 8.4).
1110–4 Well-sorted sands. These are inhabited by indicator species as *Tellina tenuis*, *Diogenes pugilator*, *Donax trunculus*, *Chamelea gallina*, etc., with very high conservation value.
1130 Estuaries. The Danube's mouths, with its former estuary filled with sediments, form a Delta, that, with the Black Sea water, form a characteristic mixing zone shaping specific biocenoses, down to 20 m depth.
1140–3 Midlittoral sands. These are of particular importance as feeding grounds of water birds, and contain diverse invertebrate and algal communities.
1150 Coastal lagoons. These support both marine and brackish species, with characteristic fish species and rich and diverse vegetation.
1170–4 Boulders and blocks. Occurring in the midlittoral and infralittoral of rocky shores, this habitat has high structural complexity, forming mosaics of microhabitats, allowing species of deeper areas to inhabit nearshore zones.
1170–8 Infralittoral rock with *Cystoseira* sp., *Phylliphora* sp., etc. This habitat is the richest in species and has highest diversity in the Black Sea. Its dynamics are influenced by their seasonally diverse vegetation. *Phyllophora* fields are nursery areas for many species of aquatic organisms.
1170–9 Infralittoral rock with *Mytilus galloprovincialis.* Overlapping with 1170–8, but continuing to deeper waters, this habitat contains highly diverse fauna of endangered invertebrates and fishes, and has a crucial ecological role in benthic-pelagic coupling.

The countries of the Black Sea have attempted to synchronize their legislation (Milchakova & Phillips, 2003) of Protected Areas based on the EU NATURA 2000 list, the European Red List of Habitats (http://ec.europa.eu/environment/nature/knowledge/redlist_en.htm), EUNIS (http://eunis.eea.europa.eu/) classification, and other interacting directives. These instruments review the current status of all natural and seminatural marine habitats, highlight the pressures they face, and provide guidelines for environmental protection and restoration within the EU2020 Biodiversity Strategy.

8.4 OFFSHORE SYSTEMS

Coastal biogeochemical processes are connected dynamically to the deep sea (Zatsepin et al., 2003). Productivity of the shelf system appears to be primarily phosphorus-limited, whereas the open sea system would appear to be nitrogen-limited and much more dependent on mixing processes for nutrient supply (Garnier et al., 2002).

The physiochemical conditions dictate seasonal dynamics that support food webs that are well adapted to the brackish, nutrient-rich conditions (Oguz et al., 2002). Predation at upper- and mid-trophic levels drives system-wide trophic cascades (Daskalov, 2002). The annual cycle of phytoplankton in the Black Sea has been well studied, but only limited studies have focused on deep waters. The main groups of phytoplankton are dinoflagellates, diatoms, coccolithophores, and cyanobacteria near river estuaries (Agirbas, Koca, & Aytan, 2017). Generally, there is a usually high phytoplankton biomass in winter, represented mainly by diatom and dinoflagellate-dominated species, with maxima in open waters in January to March (Berseneva, Churilova, & Georgieva, 2004), often containing the same species as during the spring and this is recognized as the winter–spring bloom (Mikaelyan, Chasovnikov, Kubryakov, & Stanichny, 2017). This is often followed by a weaker mixed assemblage below the seasonal thermocline during summer months, forming marked vertical stratification and a warm, shallow mixed layer (Oguz & Merico, 2006), and a surface-intensified autumn production. The benthic zone also plays an important role in Black Sea nutrient cycling, as chemosynthetic organisms and anoxic geochemical pathways recycle nutrients that can be upwelled to the photic zone, enhancing productivity (Friedrich et al., 2002).

In recent decades, the spring bloom has become smaller than the autumn proliferation of algae and often is not observed at all. This is atypical for temperate seas, where the prominent spring phytoplankton increases occur. A new Pulsing-Bloom hypothesis was proposed by Mikaelyan et al. (2017), for the highly stratified waters of the Black Sea. It relates the biological response to physical forcing and chemical fluxes and predicts the pulsing episodes of phytoplankton in the upper layer in winter–spring during cold and regular years. This is supported by chlorophyll dynamics, and the pattern of depleted inorganic nitrogen during the winter–spring period, when the phosphate concentration remains relatively high.

The Pulsing-Bloom hypothesis predicts that in the absence of cold winters, spring blooms will disappear, with unpredictable consequences for higher trophic levels. Decoupling the periods of food abundance and reproduction of zooplankton and pelagic fish can lead to decreases in their populations (Arashkevich et al., 2014). These changes induced by climate shifts should receive more attention (Mikaelyan et al., 2017).

The Black Sea's pelagic ecosystem has experienced substantial changes since the 1960s. Nutrient enrichment was followed by food web changes, such as additional phytoplankton summer blooms (Dorofeyev et al., 2012) and large increases of gelatinous and opportunistic species. This lasted till the early 1990s, and resulted in regime shifts in zoo- and phytoplankton populations (Daskalov, Grishin, Rodionov, & Mihneva, 2007).

Since then, less eutrophication and a decline of the invasive ctenophore *Mnemiopsis leidyi* (Shiganova, 1998) has occurred. This has been followed by oscillations of blooms of the comb jelly and the collapse and recovery of the anchovy fishery (Miladinova, Stips, Garcia-Gorriz, & Macias Moy, 2016). Changes in the planktonic food web are also reported for ciliate protists, which are especially sensitive to the changes in the Black Sea food chain (Gavrilova & Dolan, 2007).

Although some potential for partial recovery have been observed in the Black Sea, whether the Black Sea will continue its current way to recovery or will return to its highly eutrophic state will depend, to a large degree, on socioeconomic choices (Langmead et al., 2009). Even in the most optimistic scenario, the Black Sea will never revert to the pre-1960s state after the introduction of *Mnemiopsis* (Llope et al., 2010).

8.5 CLIMATE CHANGE IMPACTS

8.5.1 Shrinking of the Habitable Area

Capet et al. (2016) discovered that the oxygen-rich top layer of the Black Sea decreased in its vertical extent from 140 to 90 m deep, which amounts to a >40% decrease in habitable waters.

The report stated two causes: an abundance of nutrients leading to algal blooms and increased oxygen consumption, and global warming. Warmer winters lower the volume of dense water, and this lowers the oxygen content as well. Further atmospheric warming will directly affect the vertical stability of the Black Sea oxygenated layer, thus causing ecological and economic damage in the region.

8.5.2 Air Temperature Rise and Precipitations

The Black Sea experiences alternating warm and cold regional climatic periods with a mean duration of about 10–12 years (Oguz et al., 2006). The last cold period was replaced by a warm period in the mid-1990s, but the expected return to a cold period in the 2000s did not occur (Agirbas, Feyzioglu, Aytan, Valente, & Yildiz, 2015), with winters of 2014 and 2015 being two of the warmest in last 30 years.

Future projections for air temperatures and precipitation (IPCC AR4, 2007) show that the most significant projected changes by 2080 relate to the increase in air temperature (warmer summers, more frequent/intense heat-wave periods) and to a reduction in precipitation for the Black Sea region, with more intense rainstorms, drought, and heat-waves.

8.5.3 Sea Surface Temperatures

Seasonal sea surface temperatures (SST) characteristics, based on AVHRR data from 1982 to 2012, show average summer temperatures of 23.24°C for the Black Sea, with winter temperatures being 7.49°C (Shaltout & Omstedt, 2014). Sea ice is more frequent in the NW but it can form along the west coast during the coldest winters. Ice disappears completely by the end of March.

As with air temperature, long-term anomaly data since 1885 shows a linear warming trend with an overall temperature rise of 0.9°C (Oguz & Merico, 2006).

During recent decades, the upper water column layer has shown distinct physical changes. There is a clear warming trend (von Schuckmann et al., 2017), as high as 0.08°C year^{-1} between 1982 and 2012 and 1993–2015, and an average increase of 1.9°C over the 23-year period. This increase was low between 1982 and 1994, and was followed by a pronounced warming phase during 1993–2014. Similar variations were observed in the summer–autumn (May–November) mean subsurface CIL temperature fields. This indicates climatic changes within the upper 100 m water column above the permanent pycnocline. Oguz et al. (2006) found that strengthening of the NAO coincided with the general warming trend and its positive phase resulted in colder, drier winters in the Black Sea. Decadal scale temperature changes in the Black Sea are much more pronounced with respect to the global warming signal (oceanic average increase since the 1980s is 0.5°C in the upper 100 m). This has likely impacted the flow, stratification, and mixing characteristics of the Black Sea as well as its ecosystem (Shaltout & Omstedt, 2014).

8.5.4 Sea Level Rise (SLR) and Erosion

Sea level change along the Black Sea coast is monitored from long-term station information and new applicable satellite data (Avsar, Jin, Kutoglu, & Gurbuz, 2016). Tsimplis, Josey, Rixen, and Stanev (2004) observed a trend of 2.2 mm year^{-1} sea level change rate over the period 1960–2000, attributed largely to the surface fresh water flux. The reported tide gauge data collected from 1930 to 2000 for cities around the Black Sea are as follows: 3.7 mm year^{-1} for Pito (Georgia), 6.8 mm year^{-1} for Batumi (Georgia), and 1 to 2 mm year^{-1} for the other cities (Varna in Bulgaria, Constantza in Romania, Sevastopol in Ukraine, Tuapse in Russia), which is consistent with global trends (Karaca & Nicholls, 2008). The Copernicus Marine Environment Monitoring Service (CMEMS) Black Sea Monitoring and Forecasting Center (BS-MFC) operates daily analysis and forecasts for the Black Sea, covering the period 2005–2015. Argo floats have been the main observing network for measuring sub-surface temperature and salinity in the Black Sea over the last decade (Balan et al., 2017).

Significant sea level (SLR) rise could cause flooding over large areas in the Danube Delta and NW part of the Black Sea coast. This risk is limited as SLR is expected to be modest, tides are nonexistent and currents very weak along the Black Sea shoreline. However, most of the coastline is potentially vulnerable to erosion processes. Since sea level will continue to rise, changes in water level and increased storminess could lead to beach erosion, cliff retreat, and to the degradation of protective structures such as breakwaters.

The Black Sea catchment is facing important climatic and land use changes that may increase pollution, vulnerability of water resources, and beach erosion through SLR, while appropriate decision-making is hindered by the lack of reliable environmental monitoring data (Lehmann et al., 2017).

8.5.5 pH Change

The surface layer shows a pH change as a result of increased uptake of carbon dioxide in the troposphere. This phenomenon is potentially dangerous for marine biota (Polonsky, 2012), but acidification can also be a result of seawater pollution.

Significant century-scale acidification of the upper Black Sea layer cannot be determined from available data for the last century because of its incompleteness, high level of noise, and strong interannual to decadal variability. Decadal-scale acidification for the periods 1960, 1980, and 2000, was 0.4 pH units decade^{-1} at the surface, and 0.2 pH units decade^{-1} at 10 m. This high rate of upper layer acidification is mostly due not to the concentration of CO_2 in the atmosphere, but to intensification of the upward motion in the subsurface layer transporting low-pH water to the surface (Polonsky, 2012).

8.5.6 Storms

The western and north-eastern parts of the Black Sea have the most intense storms, with waves estimated as 7.8 m in height and period of 11.0 s with a return period of 100 years, maximal possible height being >14 m (Gippius, Arkhipkin, & Surkova, 2012).

>50% of storm events identified for 32 years are the consequence of "coupling" of a continental anticyclone with a Mediterranean cyclone arriving over the Black Sea (Chiotoroiu & Ciuchea, 2009).

Storm distribution along the Romanian and Bulgarian coast shows a contrast between a very active interval (1961 until the 1980s), which caused high-intensity coastal erosional and accretion processes with high sediment transport rates, and a relatively quiet period with low variability (1979–2000) (Valchev, Trifonova, & Andreeva, 2012; Vespremeanu-Stroe & Tatui, 2005). The same study, based on a 63-year period (1948–2010), found a shortening of storm duration due to a shift to the north of the prevailing direction of storm forcing winds.

Extreme storms in the NW region have a mean recurrence rate of 7 years and are considered to be responsible for the sediment transport south from the Danube delta coast (Zainescu, Tatui, Valchev, & Vespremeanu-Stroe, 2017). Critical thresholds for storm impacts on Bulgarian coastal morphology (Trifonova, Valchev, Andreeva, & Eftimova, 2012) showed that storms with integral wave energy varying within threshold values $0.4–0.7 \times 10^6\,J\,m^{-2}$ are regarded as capable of causing significant morphological changes.

Estimations of wave height with return periods between 1 and 100 years, based on SWAN models showed that waves of >8 m height are common during autumn storms, occurring about once in 10–20 years (Lopatoukhin, Boukhanovsky, & Chernysheva, 2009).

8.6 HUMAN POPULATIONS AFFECTING THE AREA

8.6.1 Cities and People

About 140 million people live along the Black Sea coast (Allenbach et al., 2015), the highest population densities being in big port cities (see Fig. 8.1).

The Black Sea region and its surrounding territories have served as a crossroad between Europe, Asia, and Africa. The ports around it owed their prosperity to commercial connections, as they developed secure trade routes to a network of overseas locations (Lyratzopouoou & Zarotiadis, 2014). One major change to the region is the Danube–Black Sea Canal, completed in 1984, which made a link to the North Sea (through the Rhine–Main–Danube Canal) and the traffic through the river and the industry along it has increased substantially since then. Aquaculture, fishing, and agriculture alongside transport, accommodation, and food services are some of the basic elements of the economy in the coastal area (EUNETMAR, 2014, Black Sea).

In many coastal areas, high population density is seasonal due to the large number of tourist resorts that increase populations 10-fold, causing serious anthropogenic pressure. This, based on intense urbanization of some valuable land and protected areas including dunes and sea beaches, has damaged many of the natural areas along the Black Sea coast.

From the beginning of the 21st century to the 2008 world economic crises, the region had sustained growth, with high levels of trade and investment, but following the collapse of financial markets the growth of the Black Sea region was interrupted sharply (Gavras, 2010).

All of the port cities are situated in naturally protected bays and their favorable geographic position gives the cities significant dynamics. Some ports like Burgas, Mangalia, Sochi, and Sevastopol are attractive resorts with transport and commercial importance, while others like Constanta, Odessa, Novorossiysk, Samsun, Varna are trade ports with facilities for crude oil refining, gas stocking capacity (Zygiaris, 2012), and are hubs for container traffic for cereals and grains (Martin, 2002). The port of Constanta enjoy a special position on several Pan-European Corridors and its water depth of up to 19 m can accommodate tankers with capacity of 165,000 dwt (deadweight) and bulkcarriers of 220,000 dwt (www.portofconstantza.com).

Measures such as activities to facilitate trade, elimination of dual taxation, and agreements for investments could work to benefit mutually the different countries, some of them being EU members, while others share historical connections.

8.6.2 Marine-Based Pollution; Pollutants and Pollution Hotspots

Land-based sources account for >70% of pollution entering the sea through rivers, one of the most important groups being nutrients. They have, however, showed a decline since the 1990s, although nutrients coming from the Danube River in recent years (mainly nitrates) remain significant but stable (ICPDR, 2010, Water Quality in the Danube river basin).

Pesticide concentrations in water have seldom been measured. In the frame of the international monitoring program 2004–2005 on the Black Sea (BSIMAP) very low-level pesticide pollution (DDT and lindane) was observed in coastal waters in general, with some occasional patches with very high pesticide concentrations related to large freshwater discharge into the sea after floods. Unexpectedly, the entire coastline contained a very high level of DDTs in bottom sediments without any clear indication of reduction, while other pesticides were close to their detection limits for all costal zones (Koroshenko, n.d., SER 2001–2006/7).



FIG. 8.5 Tourism increases. Sozopol Marina, photo by Miroslav Rangelov IOCCP-BAS.

Decreasing eutrophication measured as N and P discharges continue, but their 2000–2005 average values are still 1.5 times higher than their levels in 1955–1965, with P-PO4 flux supplied by the Danube maintaining a steady level between 10 and 20 kt year^{-1} at the Sulina discharge point to the sea. Hypoxia has decreased in Romanian coastal waters compared to the previous decade, and no hypoxia cases were observed in Bulgarian waters in 2001–2005. Relatively low oxygen concentrations tend to occur more predominantly in the northern sector upstream of the Danube delta region (Oguz, 2007).

The coastal regions face increasing development pressures due to high urbanization, population increase, and tourism, as climatic conditions are favorable in the whole Black Sea coastal belt (Guclu, 2011). Although tourism is considered a generally environment-friendly sector (Fig. 8.5), its uncontrolled development and excessive use of natural resources could become a crucial factor in environmental degradation (Dimadama & Chantzi, 2014), with tourism investment in almost all countries expected to rise by 2022 (Kereselidze, 2013).

The Black Sea has been subject also to (as of May 2010) >234 recorded exotic species (Daskalov, 2002; Zaitsev & Mamaev, 1997).

8.6.3 Coastal Hydrocarbons

Petroleum pollution is a major problem for the whole sea, with levels that usually exceed standard Maximum Allowed Concentration (0.05 mg L^{-1}), almost everywhere in the open sea. Very high spatial heterogeneity of total petroleum hydrocarbons (TPH) distribution is observed, such that about half of samples can be considered pollution-free. During a survey in the period 2005–2007, TPH content in bottom sediments were taken and analyzed, with the average concentration of TPH being about 0.05 mg g^{-1} at most sites. However, some samples from extremely polluted sites near large ports, oil refineries, or oil terminals in Romania, Turkish, and Russian waters exceeded the threshold 13–16 times. Higher concentrations were also detected in bottom sediments close to big cities, where municipal and manufacturing waste and the discharges from rivers play a substantial role (Koroshenko, n.d., SER 2001–2006/7). Heavy fractions of TPH, polycyclic aromatic hydrocarbons (PAH), some of them being carcinogens and threats to human health, tend to persist in bottom sediments close to their source point, with no clear legislation relating to their monitoring, and their elimination is exclusively performed by prokaryotic communities (Todorova, Mironova, & Karamfilov, 2014). Based on 16 priority PAH, bottom sediments near big cities and ports, such as Odessa, Sochi, Istanbul, Danube delta, the Bosphorus strait and some places on the Romanian and Bulgarian coast, tend to be classified as being highly polluted (Tiganus, Coatu, Lazar, Oros, & Spinu, 2013) (see Box 8.1).

BOX 8.1 Case Study/Sevastopol Bay: Long-Term Anthropogenic Impact

Being a regional center, the city of Sevastopol (southern-western part of the Crimean Peninsula) is one of the most urbanized areas of the Crimea because of its big commercial and industrial port. Its coastal area is a series of enclosed bays among which Sevastopol Bay is one of the largest in the Black Sea and, as a consequence, is most heavily subjected to human impact. Long-term anthropogenic loads have already caused adverse changes in the environment, affected marine organisms at every taxonomic level and, beginning at the end of the 1980s, Sevastopol Bay has been classified as an impacted zone with a wide spectra of contaminating substances among which oil hydrocarbons dominate (Mironov, Kirjukhina, & Alymov, 2003; Osadchaya, Alyomov, & Shadrina, 2004).

Persistent sources of the pollution (Fig. B.8.1) shape its zones and inhabiting biota. Long-lasting pollution determines the different status of all benthic habitats along established gradients of oil pollution. The recorded spread of pollution to the areas previously considered as environmentally being in good condition is accompanied by deterioration of biological (macrobenthic) quality (Fig. B.8.2).

Evaluation the bottom macrofauna quality using the index M-AMBI (Borja, Josefson, Miles, et al., 2007) has shown a detectable deterioration of overall environmental status in Sevastopol Bay: by 2009, number the sites with "good ecological status" decreased up to 7% compared with 26% in 2000, and the area with "poor" environmental conditions has expanded up to 33% from 20%.

The natural remediation period by the benthic organisms in these polluted marine ecosystems is estimated to be 10–20 years.

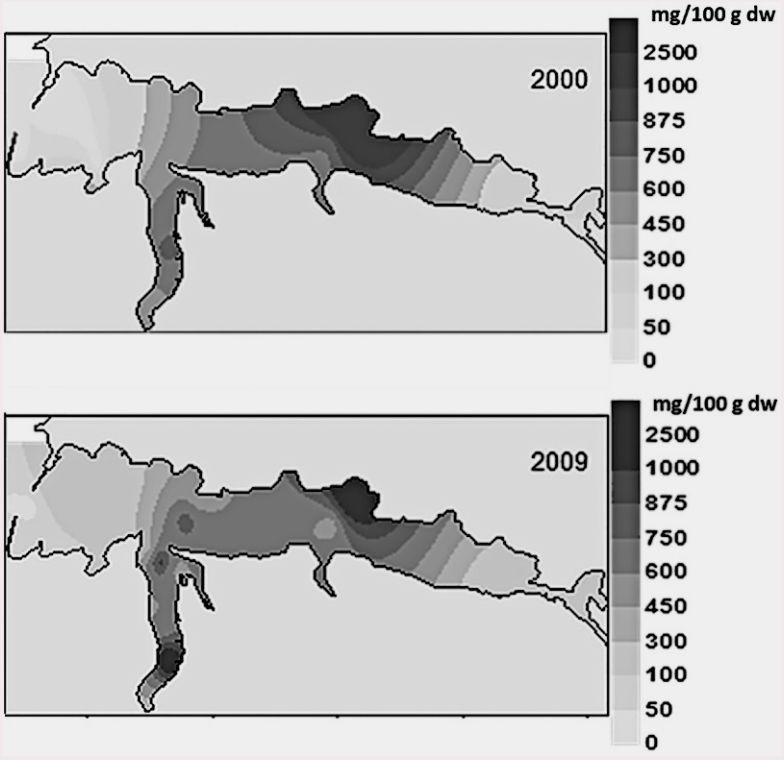


FIG. B.8.1 Patterns of oil hydrocarbon distribution in Sevastopol Bay, mg per 100 g of sediment dry weight (Osadchaya, 2017, current article).

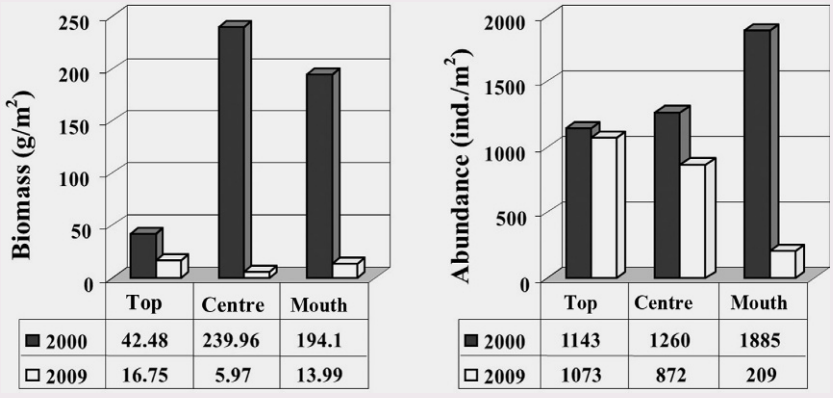


FIG. B.8.2 Long-term changes of the biomass and abundance of macrozoobenthos in different regions of the Sevastopol Bay (Osadchaya, 2017, current article).

8.6.4 Oil Pollution in Open Waters, Pollution From Ships

Marine oil spills, from illegal bilge water discharges or from accidents, pose serious risks of ecological damage and socio-economic losses (ClearSeaNet).

The Black Sea is vulnerable due to intense transportation of oil products and its semi-enclosed nature. Pipelines and tankers for oil and gas from the Caspian basin and Russia to the West cross the region (Lyratzopouoou & Zarotiadis, 2014). CleanSeaNet, a satellite-based pan-European oil spill and vessel monitoring service has been available since 2007 from the European Maritime Safety Agency. This service aims to provide information about oil spills and pollution alerts (and related data) to national authorities in 27 coastal states in near real-time (Fig. 8.6).

Maritime accidents caused by severe weather phenomena.

Storms in the Black Sea are frequent from November to March, being stronger in the NW. Along the Romanian coast they have been defined using two parameters: wind speed $>12\,m\,s^{-1}$ for at least 12 consecutive hours and sea state 4 near the coast (wave height between 1.25 and 2.50 m). The highest number of accidents at sea caused by severe weather phenomena for a 26-year period occurred in Romanian waters in winter, between October and March, with a maximum in January and December (Chiotoroiu & Ciuchea, 2009).

8.6.5 Invasive Species

Exotic species brought by ships through exchange of ballast waters or other wastewaters affect the Black Sea ecosystem, since they tend to proliferate due to lack of natural predators, and among them new invasive species are regularly discovered.

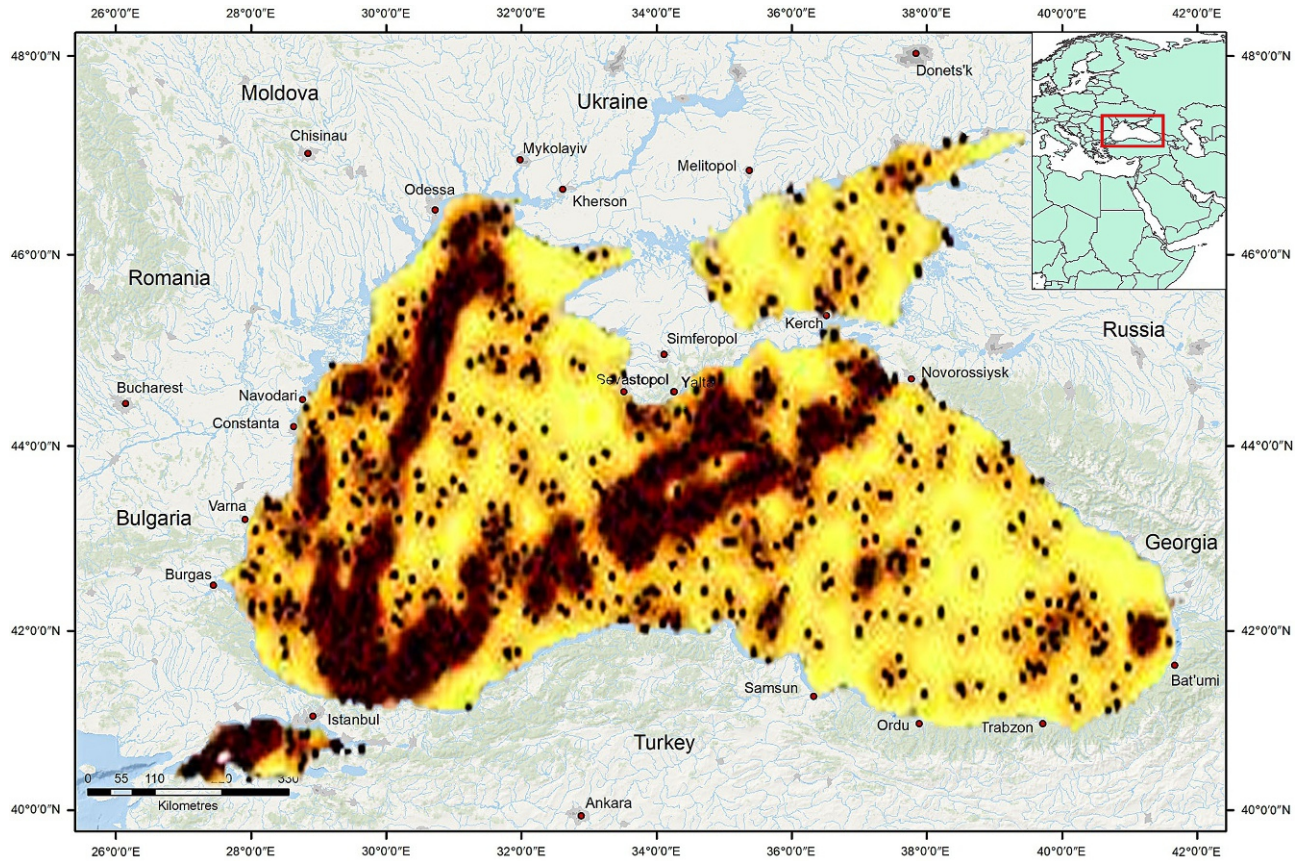


FIG. 8.6 The oil spills in the Black Sea for period 2000–2004. Map of oil spills based on images taken by synthetic aperture radars (SARs) of European satellites ERS-2 and Envisat (State of Environment Report 2001–2006/7).

8.7 RESOURCES

8.7.1 Oil and Gas

There are considerable stocks of hydrogen sulfide, gas, and oil available in the Black Sea and the full-scale extraction of some of these resources will require the development of new and complex technologies (www.eea.europa.eu). Most exploitation occurs in the shallow NW shelf, with Ukraine and Romania being traditional oil and gas producers and exporters (Popovici, 2009). The first deep-water well drilled in 2012 in the Black Sea has a potential gas production of approximately $17.8 \times 10^6\,m^3\,day^{-1}$ (ROPEPCA, 2016).

There is a need for renovating gas distribution systems and operational environmental protection, as the long-term impacts of such large-scale activities will have to be carefully assessed given the potential consequences on the marine ecosystem.

8.7.2 Fisheries

The Black Sea does not have an ecosystem-wide management authority, and the exploitation of resources is largely regulated by national commitment. There are attempts at bilateral mechanisms for regional fishery cooperation as a semienclosed sea that is party to UNCLOS (IP/B/PECH/IC/2012–069). All Black Sea countries exhibit similar trends in their industrial fish catch as most of the assessed stocks are overfished. In the late 1960s and early 1970s, Atlantic mackerel (*Scomber scombrus*), bonito (*Sarda sarda*), and bluefish (*Pomatomus saltatrix*) catches dramatically decreased, followed by turbot (*Scophthalmus maximus*), one of the most important commercial species, whose catch also had declined by the 1980s (Zaitsev & Mamaev, 1997). In the 1970s, overexploitation of larger pelagic predators, combined with increased eutrophication in the NW led to a dramatic increase in the catches of small pelagics such as sprat (*Sprattus sprattus*), anchovy (*Engraulis encrasicolus*), and Mediterranean horse mackerel (*Trachurus mediterraneus*), which was thought to be sustained by the extensive eutrophication that caused the ecosystem to be overproductive (STECF, 2015).

In the late 1980s, an alien invasive species, the ctenophore *Mnemiopsis leidyi* reached its maximum abundance in the Black Sea, and became a powerful food competitor of adult planktivorous fish (the anchovy fishery in the entire Black Sea collapsed in 1989/90), and a significant predator of their eggs and larvae (Keskin et al., 2015). After the collapse, the eastern region became the only region sustaining a relatively high anchovy catch (400,000 t), whereas the total catch within the rest of the sea was reduced to nearly one-third (Oguz, 2017). Today the most abundant and commercially important target species are anchovy and sprat (*Sprat sprattus*) (STECF, 2015). The most commonly caught species in the western Black Sea are European sprat (56%) targeted mainly by large-scale pelagic trawls from February to November. Anchovy in the Black Sea exhibits migration behavior mainly driven by the ambient temperature (Shulman et al., 2008). When cold temperatures approach in fall, anchovy adults and juveniles aggregate to form dense schools and start their wintering migration toward warmer waters in the southern Black Sea. A return migration commences in spring when water temperatures rise again (Fig. 8.7).

The coastal fishery has traditionally been carried out by small vessels (<12 m), which use mainly passive types of fishing gear, such as trap nets (uncovered pound nets), and beach seines in the inshore area, while target species vary according to season. In Bulgaria and Romania the bottom trawl fishery was banned, due to protection of vulnerable benthic biotic communities (Keskin et al., 2015). The Turkish fishery uses purse seiners to fish schools of overwintering anchovy along the southeastern Turkish coast during winter time (September to mid-April) after which industrial fishing is banned for 4.5 months. To control harvest, fishing is restricted to night time only, however there is no total allowable catch (TAC) in place. In an effort to reduce fishing pressure, the licensing of new fishing boats has been halted since 2015 and a periodic, voluntary fishing vessel decommissioning program has been applied since 2012 (Gucu et al., 2017).

Sustainable fishing in the Black Sea is under serious threat by illegal, unreported, and unregulated (IUU) fishing, which includes ghost fishing, and by destruction of the benthic ecosystem. A total of 65 illegal fishing cases have been reported in various exclusive economic zones (EEZs) in the Black Sea from 1992 to 2012 (Ozturk, 2013).

The Black Sea is still in an unstable condition, with a serious overfishing/recovery problem. Unfortunately, the quotas are enforced under political and social pressures to support short-term fishing prospects instead of the long-term sustainability. A variety of fisheries management actions such as quotas, effort reduction, area, and season closure of fisheries, can be applied by the authorities to improve the situation. Therefore, more straightforward management actions against overcapacity and overexploitation of fish stocks are urgently needed (Oguz, 2017).

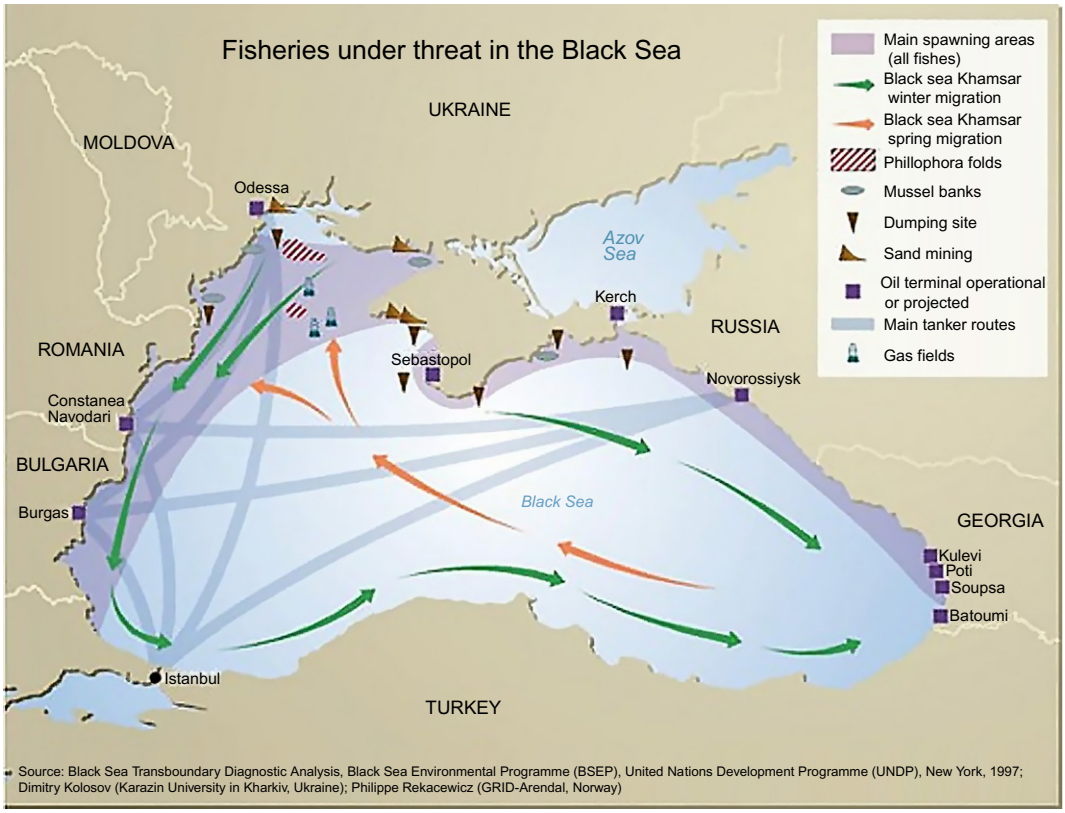


FIG. 8.7 Main routes of anchovy migration (according to Rekacewicz, 2006, http://www.grida.no/resources/6522).

8.8 THREATS AND MANAGEMENT

The main threats for the Black Sea ecosystem are water pollution, notably nutrients from land-based sources and by inputs of other harmful substances, including oil from vessels or land-based sources; invasive species from deballasting of vessels; overfishing and IUU fishing; erosion driven by sea level rise, extreme storm events, diminishing sediment supply from the heavily managed rivers; coastal development and poorly designed coastal protection schemes; river, coastal, and near-shore sediment mining; uncontrolled urban, tourist, and industrial development; and discharge of wastes straight into the waterways without treatment.

Thus, the Black Sea is a subject to multiple stressors, whose cumulative effects are neither well understood nor are they easy to be modeled for future prognosis. No sign of appreciable ecosystem rehabilitation is obvious (Oguz, 2017) and there is scientific uncertainty as to whether a more desirable equilibrium state is even possible, or when it might be reached. Real assessment of the current state, needed for management development, is hindered by the lack of systematic time series.

8.8.1 Protection and Conservation Measures, Deficiencies

The marine strategy framework directive (MSFD), is a long-awaited EU instrument central to the Integrated Maritime Policy, despite the lack of an EU Black Sea strategy. It requires EU Member States to reach or maintain good environmental status (GES) in the marine environment by 2020 (Lyons, Thain, Hylland, Davies, & Vethaak, 2010). Marine protected areas (MPAs) have been identified as crucial components of the program of measures to achieve GES.

Mapped classifications of biodiversity patterns are an important tool in conservation planning. Marine Ecoregions as defined by Spalding et al. (2007) are the smallest unit of their classification system. They are areas of relatively homogeneous species composition that are clearly distinct and are strongly cohesive units, sufficiently large to encompass ecological or life history processes for most sedentary species. The Black Sea has been defined as one ecoregion in that

classification. Ozturk et al. (2017), however, suggest that there are four subregions based on biodiversity characteristics, which are the Pre-Bosphoric Region reaching from the Romanian border to Sile, the NW Shelf, Kerch Strait, and the Southern Black Sea.

To enable the MPA network to fulfill its critical role in the delivery of GES, both national progress and transboundary agreements toward designation of adequate MPAs will be required, as well as coordination at a regional scale and cooperation between Member State governments.

8.8.2 Marine Protected Areas

Oguz (2017) described the Black Sea as one of the most polluted and mismanaged semienclosed seas in the world. The adoption of appropriate management strategies requires an understanding of the potential response of the system to individual drivers of change.

Establishing MPAs is a key element toward the ecosystem-based approach of marine management in order to maintain ecological integrity and a sustainability (Fig. 8.8).

Bulgaria, Romania, and Turkey have established MPAs with similar categories of protection. Natura 2000 in Bulgaria and Romania and the Emerald Network and RAMSAR Convention in Turkey have been the basis of their MPAs. Bulgaria has 15 MPAs both marine and terrestrial, Romania has two with the largest being the marine part of the Danube Delta Biosphere (Begun et al., 2012). Ozturk et al. (2013) proposed five ecologically important regions along the Turkish Black Sea coast, containing the internationally important wetland of Kizilirmak Delta, a Ramsar Site since 1998, and Yesilirmak Delta in the Samsun region. These sites were proposed taking into account the criteria of the Convention on Biological Diversity and modeling studies of larval dispersal within the Black Sea (Fach, Arkin, & Salihoglu, 2016), confirming connectivity between each of the regions to form a network of protected areas. Other counties in the region, Georgia, Russia, Ukraine, although also not EU members, try to harmonize their protected zones with the European Directives (Milchakova et al., 2015).

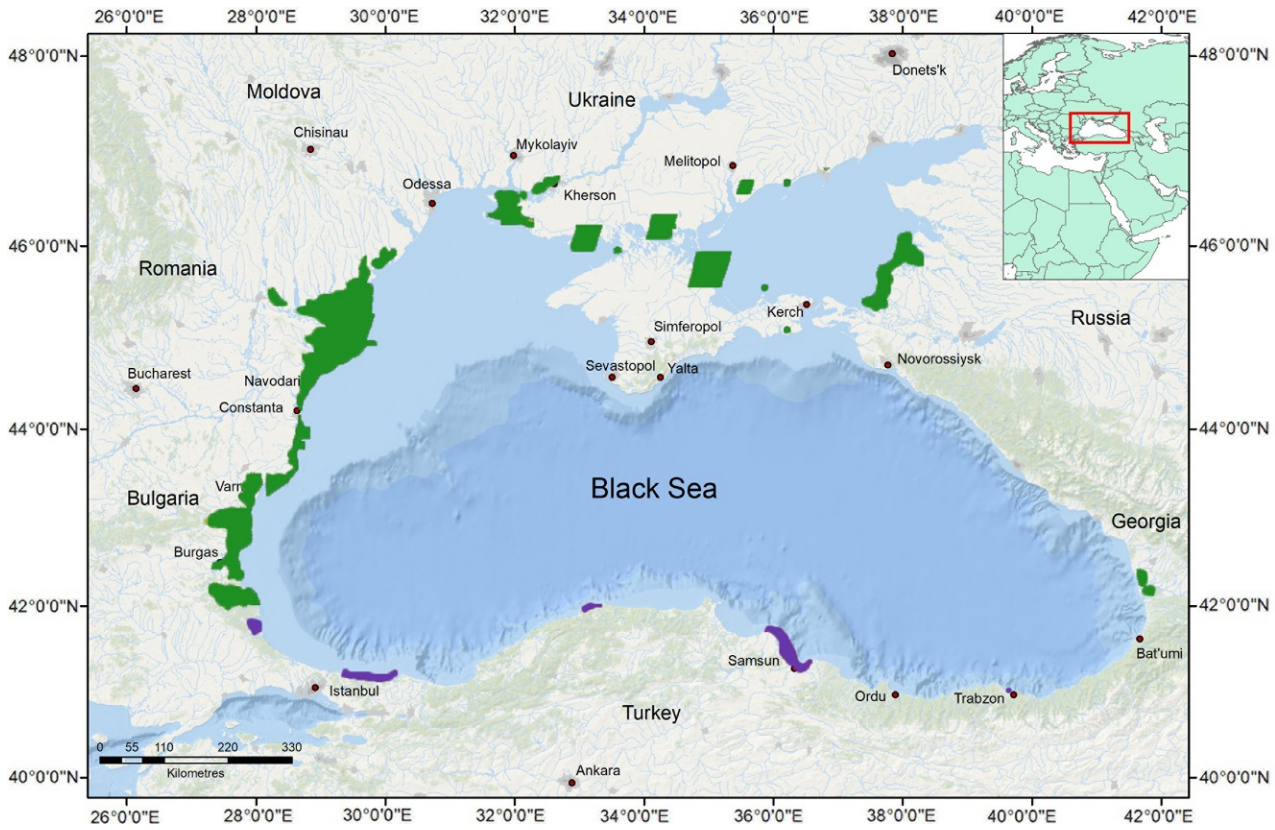


FIG. 8.8 MPA in Black Sea region (in blue proposed MPA) (according to CoCoNet and Ozturk et al., 2013).

8.9 SUMMARY, PROGNOSES, OR NEEDS

The present Black Sea ecosystem is undergoing a slow recovery from its degraded state of the 1970s. The low rate of recovery may be related to inappropriate management as well as to continuing impacts. Additional ecosystem-level planning and integrated assessments are urgently needed, including reducing eutrophication, reducing fleet capacity, and banning fisheries for particular stocks or regions.

Due to decades of unsustainable fishing efforts, with the exception of the southeastern part, the Black Sea does not support much fish. This is a unique case among the large marine ecosystems in the world and represents an almost collapsed ecosystem whose size is ~400,000 km^2 (Oguz, 2017). The implementation of ecosystem-based management strategies requires tools that are being developed collaboratively and which will lead to a more stable and sustainable Black Sea functional ecosystem.

REFERENCES

Agirbas, E., Feyzioglu, A. M., Aytan, U., Valente, A., & Yildiz, I. (2015). Are trends in SST, surface chlorophyll-a, primary production and wind stress similar or different over the decadal scale in the south-eastern Black Sea? *Cahiers de Biologie Marine*, *56*, 329–336.

Agirbas, E., Koca, L., & Aytan, U. (2017). Spatio-temporal pattern of phytoplankton and pigment composition in surface waters of south-eastern Black Sea. *Oceanologia*, *59*, 283–299.

Akpinar, A., Fach, B. A., & Oguz, T. (2017). Observing the subsurface thermal signature of the Black Sea cold intermediate layer with Argo profiling floats. *Deep-Sea Research Part I*, *124*, 140–152.

Allenbach, K., Garonna, I., Herold, C., Monioudi, I., Giuliani, G., Lehmann, A., et al. (2015). Black Sea beaches vulnerability to sea level rise. *Environmental Science & Policy*, *46*, 95–109.

Arashkevich, E. G., Stefanova, K., Bandelj, V., Siokou, I., Kurt, T. T., Orek, Y. A., et al. (2014). Mesozooplankton in the open Black Sea: Regional and seasonal characteristics. *Journal of Marine Systems*, *135*, 1–96.

Avsar, N. B., Jin, S., Kutoglu, H., & Gurbuz, G. (2016). Sea level change along the Black Sea coast from satellite altimetry, tide gauge and GPS observations. *Geodesy and Geodynamics*, *7*(1), 50–55.

Balan, S., Fach, B., Grayek, S., Poulain, P.-M., Stanev, E., & Storto, A. (2017). Argo activities in the Black Sea. Euro-Argo RI, on-line at: http://www.euro-argo.eu/News-Meetings/News/Argo-activities-in-the-Black-Sea.

Begun, T., Muresan, M., Zaharia, T., Dencheva, K., Sezgin, M., Bat, L., et al. (2012). Conservation and protection of the Black Sea biodiversity. Review of the existing and planned protected areas in the Black Sea (Bulgaria, Romania, Turkey) with a special focus on possible deficiencies regarding law enforcement and implementation of management plans. EC DG Env. MISIS Project Deliverables. www.misisproject.eu.

Berseneva, G. P., Churilova, T. Y., & Georgieva, L. V. (2004). Seasonal variability of chlorophyll and phytoplankton biomass in the western part of the Black Sea. *Oceanology*, *44*(3), 389–398.

Borja, A., Josefson, B., Miles, A., et al. (2007). An approach to the intercalibration of benthic ecological status assessment in the North Atlantic ecoregion, according to the European Water Framework Directive. *Marine Pollution Bulletin*, *55*, 42–52.

Capet, A., Stanev, E. V., Beckers, J.-M., Murray, J. M., & Grégoire, M. (2016). Decline of the Black Sea oxygen inventory. *Biogeosciences*, *13*, 1287–1297.

Chiotoroiu, B., & Ciuchea, V. (2009). Severe weather conditions and maritime accidents along the Romanian Black Sea coast. In L. Gucma (Ed.), *Proceedings of the XIII International Scientific and Technical Conference on Marine Traffic Engineering* (pp. 35–39). Malmo, Sweden: Institute of Marine Traffic Engineering.

Croitoru, A. E., & Piticar, A. (2013). Changes in daily extreme temperatures in the extra-Carpathians regions of Romania. *International Journal of Climatology*, *33*(8), 1987–2001.

Daskalov, G. M. (2002). Overfishing drives a trophic cascade in the Black Sea. *Marine Ecology Progress Series*, *225*, 53–63.

Daskalov, G. M., Grishin, A. N., Rodionov, S., & Mihneva, V. (2007). Trophic cascades triggered by overfishing reveal possible mechanisms of ecosystem regime shifts. *Proceedings of the National Academy of Sciences*, *104*, 10518–10523.

Dimadama, Z., & Chantzi, G. (2014). A new era for tourism in the Black Sea area. *International Journal of Cultural and Digital Tourism*, *1*(2).

Dorofeyev, V. L., Oguz, T., Sukhikh, L. I., Knysh, V. V., Kubryakov, A. I., & Korotaev, G. K. (2012). Modeling long-term changes of the Black Sea ecosystem characteristics. *Ocean Science Discussions*, *9*, 2039–2080.

Duarte, C. M. (2002). The future of seagrass meadows. *Environmental Conservation*, *29*(2), 192–206.

Esin, N. V., Yanko-Hombach, V., & Kukleva, O. N. (2010). Mathematical model of the late Pleistocene and Holocene transgressions of the Black Sea. *Quaternary International*, *225*(2), 180–190.

EUNETMAR 2014, Black Sea. http://www.msp-platform.eu/sea-basins/black-sea-0.

Fach, B. A., Arkin, S. S., & Salihoglu, B. (2016). Modeling ecological connectivity and dispersal in the Black Sea: Seasonal and interannual variability. In F. Briand (Ed.), *CIESM Workshop Monographs n°48 Marine Connectivity—Migration and Larval dispersal* (pp. 105–114). Monaco: CIESM Publisher.

Friedrich, J., Dinkel, C., Friedla, G., Pimenov, N., Wijsman, J., Gomoiu, M.-T., et al. (2002). Benthic nutrient cycling and Diagenetic pathways in the north-western Black Sea. *Estuarine, Coastal and Shelf Science*, *54*(3), 369–383.

Garnier, J., Billen, G., Hannon, E., Fonbonne, S., Videnina, Y., & Soulie, M. (2002). Modelling the transfer and retention of nutrients in the drainage network of the Danube River. *Estuarine, Coastal and Shelf Science*, *54*, 285–308.

Gavras, P. (2010). The current state of economic development in the Black Sea region. *Southeast European and Black Sea Studies*, *10*(3), 263–285.

Gavrilova, N., & Dolan, J. (2007). A note on species lists and ecosystem shifts: Black Sea tintinnids, ciliates of the microzooplankton. *Acta Protozoologica, Jagiellonian University*, *46*, 279–288.

Georgescu, F., Tascu, S., Caian, M., & Banciu, D. (2009). A severe blizzard event in Romania—A case study. *Natural Hazards and Earth System Sciences*, *9*, 623–634.

Gippius, F. N., Arkhipkin, V. S., & Surkova, G. V. (2012). Analysis of storm waves on the Black Sea, Plinius Conference abstracts 14, Plinius 14-32, 2012. In *14th EGU Plinius conference on Mediterranean storms and MEDEX final conference*.

Gregg, M. C., & Yakushev, E. (2005). Surface ventilation of the Black Sea's cold intermediate layer in the middle of the western gyre. *Geophysical Research Letters*, *32*, L03604.

Guclu, Y. (2011). The determination of sea tourism season with respect to climatical conditions on the black sea region of Turkey, the 2nd international Geography symposium GEOMED 2010. *Procedia—Social and Behavioral Sciences*, *19*, 258–269.

Gucu, A. C., Genc, Y., Dagtekin, M., Sakinan, S., Ak, O., Ok, M., et al. (2017). On Black Sea anchovy and its fishery. *Reviews in Fisheries Science & Aquaculture*, *25*, 230–244.

Gulin, S. B., Aarkrog, A., Polikarpov, G. G., Nielsen, S. P., & Egorov, V. N. (1997). Chronological study of 137Cs input to the Black Sea deep and shelf sediments. In P. Germain, J. C. Guary, P. Guéguéniat, & H. Métivier (Eds.), *Radionuclides in the oceans. RADOC 96-97. Proceedings. Part 1: Inventories, behaviour and processes* (no. C2, vol. 32, pp. 257–262). Les Editions de Physique, Les Ulis Cedex, Radioprotection.

IPCC, Pachauri, R. K., & Reisinger, A. (Eds.). (2007). *IPCC 4th Assessment Report AR4, Climate Change 2007: Synthesis Report, Contribution of Working Groups I, II and III to the Fourth Assessment Report of the Intergovernmental Panel on Climate Change Core Writing Team* (p. 104). Geneva, Switzerland: IPCC.

Ivanov, V. A., & Belokopytov, V. N. (2013). *Oceanography of the Black Sea*. Sevastopol: Marine Hydrophysical Institute of National Academy of Science of Ukraine, ECOSY-Gidrofizika.

Jaoshvili, S. (2002). The rivers of the Black Sea. European Environmental Agency 58, Technical report 71.

Karaca, M., & Nicholls, R. J. (2008). Potential implications of accelerated sea level-rise for Turkey. *Journal of Coastal Research*, *24*(2), 288–298.

Kereselidze, D. (2013). *A perspective on tourism in the BSEC countries*. Policy Brief No. 27 ICBSS: Athens.

Keskin, C., Ulman, A., Raykov, V., Daskalov, G. M., Zylich, K., Pauly, D., et al. (2015). Reconstruction of fisheries catches for Bulgaria: 1950–2010. Fisheries Centre The University of British Columbia, Working Paper #2015–20.

Koroshenko, A. (n.d.). Chapter 3 The State of chemical pollution, State of Environment Report (SER) 2001–2006/7. http://www.blacksea-commission.org/_publ-SOE2009-CH3.asp.

Korotaev, G., Oguz, T., Nikiforov, A., & Koblinsky, C. (2003). Seasonal, interannual, and mesoscale variability of the Black Sea upper layer circulation derived from altimeter data. *Journal of Geophysical Research*, *108*(C4), 3122. https://doi.org/10.1029/2002jc001508.

Korotaev, G. K., Oguz, T., & Riser, S. (2006). Intermediate and deep currents of the Black Sea obtained from autonomous profiling floats. *Deep Sea Research*, *11*(53), 1901–1910.

Kubryakov, A. A., & Stanichny, S. V. (2015). Mesoscale eddies in the Black Sea from satellite altimetry data. *Oceanology*, *55*(1), 56–67.

Langmead, O., McQuatters-Gollop, A., Mee, L. D., Friedrich, J., Gilbert, A. J., Gomoiu, M. T., et al. (2009). Recovery or decline of the Black Sea: A societal choice revealed by socio-ecological modeling. *Ecological Modelling*, *220*(21), 2927–2939.

Lehmann, A., Guigoz, Y., Ray, N., Mancosu, E., Abbaspour, K. C., Freund, E. R., et al. (2017). Data descriptor: a web platform for landuse, climate, demography, hydrology and beach erosion in the Black Sea catchment. *Scientific Data*, *4*, 170087.

Llope, M., Daskalov, G. M., Rouyer, T. A., Mihneva, V., Chan, K.-S., Alexander, N., et al. (2010). Overfishing of top predators eroded the resilience of the Black Sea system regardless of the climate and anthropogenic conditions. *Global Change Biology*, *17*, 1251–1265.

Lopatoukhin, L., Boukhanovsky, A., & Chernysheva, E. (2009). In E. Ozhan (Ed.), *Statistics of Black Sea extreme storms Proceedings of the ninth international conference on the Mediterranean coastal environment, MEDCOAST 09, Sochi, Russia*.

Ludwig, W., Dumont, E., Meybeck, M., & Heussner, S. (2009). River discharges of water and nutrients to the Mediterranean and Black Sea: Major drivers for ecosystem changes during past and future decades. *Progress in Oceanography*, *80*(3–4), 199–217.

Lyons, B. P., Thain, J. E., Hylland, K., Davies, I. M., & Vethaak, A. D. (2010). Using biological effects tools to define good environmental status under the European Union marine strategy framework directive. *Marine Pollution Bulletin*, *60*, 1647–1651.

Lyratzopouoou, D., & Zarotiadis, G. (2014). The economies of Balkan and Eastern Europe Countries in the Changed World (EBEEC 2013) Black Sea: Old trade routes and current perspectives of socioeconomic co-operation. *Procedia Economics and Finance*, *9*, 74–82.

Martin, E. (2002). In *International Waterway in Crisis: the case of the River Danube IAME Panama 2002 Conference Proceedings, Panama, USA*.

Mikaelyan, A. S., Chasovnikov, V. K., Kubryakov, A. A., & Stanichny, S. V. (2017). Phenology and drivers of the winter–spring phytoplankton bloom in the open Black Sea: The application of Sverdrup's hypothesis and its refinements. *Progress in Oceanography*, *151*, 163–176.

Miladinova, S., Stips, A., Garcia-Gorriz, E., & Macias Moy, D. (2016). *Changes in the Black Sea physical properties and their effect on the ecosystem. JRC technical reports*. Publications Office of the European Union.

Milchakova, N. A., Aleksandrov, V. V., Bondareva, L. V., Pankeeva, T. V., & Chernysheva, E. B. (2015). Marine protected areas of the Crimea. Scientific handbook, Ed. Dr. Milchakova, NA, Simferopol, N. Orianda [original in Russian].

Milchakova, N. A., & Phillips, R. C. (2003). Black Sea seagrasses. *Marine Pollution Bulletin*, *46*(6), 695–699.

Mironov, O. G., Kirjukhina, L. N., & Alymov, S. V. (Eds.). (2003). *Sanitary-biological aspects of the Sevastopol bays ecology in XX century* (p. 185). Sevastopol: IBSS NAS of Ukraine.

Oguz, T. (2007). Chapter 1A—general oceanographic properties: physico-chemical and climatic features. State of Environment Report 2001–2006/7. (http://www.blacksea-commission.org/_publ-SOE2009-CH1A.asp).

Oguz, T. (2017). Controls of multiple stressors on the Black Sea fishery. *Frontiers in Marine Science*, *4*(110).

Oguz, T., & Besiktepe, S. (1999). Observations on the rim current structure, CIW formation and transport in the Western Black Sea. *Deep-Sea Research Part I*, *46*, 1733–1753.

Oguz, T., Deshpande, A. G., & Malanotte-Rizzoli, P. (2002). On the role of Mesoscale processes controlling biological variability in the Black Sea: Inferrences from SeaWIFS-derived surface chlorophyll field. *Continental Shelf Research*, *22*, 1477–1492.

Oguz, T., Dippner, J. W., & Kaymaz, Z. (2006). Climatic regulation of the Black Sea hydro-meteorological and ecological properties at interannual-to-decadal time scales. *Journal of Marine Systems*, *60*, 235–254.

Oguz, T., & Merico, A. (2006). Factors controlling the summer Emiliania huxleyi bloom in the Black Sea: A modeling study. *Journal of Marine Systems*, *59*(3–4), 173–188.

Oral, N. (2013). Chapter II State of the Black Sea: The making and unmaking of a sea. In *Regional cooperation and protection of the marine environment under international low*: IDC Publishers and Martinus Nijhoff Publishers.

Osadchaya, T. S., Alyomov, S. V., & Shadrina, T. V. (2004). Ecological quality of Sevastopol Bay bottom sediments: retrospective and present-day state. *Ekology of the Sea, Sevastopol*, *66*, 82–87.

Ostrovskii, A. G., & Zatsepin, A. G. (2016). Intense ventilation of the Black Sea pycnocline due to vertical turbulent exchange in the rim current area. *Deep-Sea Res Part I*, *116*, 1–13.

Ozsoy, E., & Unluata, U. (1997). Oceanography of the Black Sea: A review of some recent results. *Earth-Science Reviews*, *42*, 231–272.

Ozturk, B. (2013). Some remarks of illegal, unreported and unregulated (IUU) fishing in Turkish part of the Black Sea. *Journal of the Black Sea/Mediterranean Environment*, *19*(2), 256–267.

Ozturk, B., Fach, B. A., Keskin, C., Arkin, S., Topaloglu, B., & Ozturk, A. A. (2017). Prospects for marine protected areas in the Turkish Black Sea. In P. D. Goriup (Ed.), *Management of Marine Protected Areas: A Network Perspective* (p. 247): Wiley and Sons Ltd.

Ozturk, B., Topaloglu, B., Kıdeys, A., Bat, L., Keskin, C., Sezgin, M., et al. (2013). A proposal for new marine protected areas along the Turkish Black Sea coast. *Journal of the Black Sea/Mediterranean Environment*, *19*(3), 365–379.

Polonsky, A. (2012). Had been observing the acidification of the Black Sea upper layer in XX century? *Turkish Journal of Fisheries and Aquatic Sciences*, *12*, 391–396.

Popovici, V. (2009). Black Sea region stands at energy crossroads. *Oil & Gas Journal*.

Rekacewicz, P. (2006). UNEP/GRID-Arendal. http://www.grida.no/resources/6522.

Robertson, A., Parlak, O., Ustaömer, T., Taslı, K., İnan, N., Dumitrica, P., et al. (2014). Subduction, ophiolite genesis and collision history of Tethys adjacent to the Eurasian continental margin: New evidence from the eastern Pontides, Turkey. *Geodinamica Acta*, *26*, 230–293.

ROPEPCA website. (2016). Romanian Petroleum Exploration and Production Companies Association. http://www.ropepca.ro/en/articole/black-sea-energy-resources-and-economic-potential/215/.

Shaltout, M., & Omstedt, A. (2014). Recent sea surface temperature trends and future scenarios for the Mediterranean Sea. *Oceanologia*, *56*(3), 411–443.

Shiganova, T. A. (1998). Invasion of the Black Sea by the ctenophore Mnemiopsis Leidyi and recent changes in pelagic community structure. *Fisheries Oceanography*, *7*(3/4), 305–310.

Shillington, D., White, N., Minshull, T. A., Edwards, G. R. H., Jones, S. M., Edwards, R. A., et al. (2008). Cenozoic evolution of the eastern Black Sea: A test of depth-dependent stretching models. *Earth and Planetary Science Letters*, *265*(3–4), 360–378.

Shulman, G. E., Nikolsky, V. N., Yuneva, T. V., Shchepkina, A. M., Bat, L., & Kideys, A. (2008). Significance of physiological and biochemical approaches for Black Sea fishery investigations. *International Journal of Natural and Engineering Sciences*, *2*, 107–112.

Spalding, M. D., Fox, H. E., Allen, G. R., Davidson, N., Ferdana, Z. A., Finlayson, M., et al. (2007). Marine ecoregions of the world: A bioregionalization of coastal and shelf areas. *Bioscience*, *57*(7), 573–583.

Stanev, E. V., Bowman, M. J., Peneva, E. L., & Staneva, J. V. (2003). Control of Black Sea intermediate water mass formation by dynamics and topography: Comparison of numerical simulations, survey and satellite data. *Journal of Marine Research*, *61*, 59–99.

STECF. (2015). Scientific, technical and economic committee for fisheries—Black Sea assessments (STECF-15-16). Luxembourg, EUR 27517 EN, JRC 98095: Publications Office of the European Union, 284 p.

Tiganus, D., Coatu, V., Lazar, L., Oros, A., & Spinu, A. D. (2013). Identification of the sources of polycyclic aromatic hydrocarbons in sediments from the Romanian Black Sea sector. *Cercetări Marine*, *43*, 187–196.

Todorova, N., Mironova, R., & Karamfilov, V. (2014). Comparative molecular analysis of bacterial communities inhabiting pristine and polluted with polycyclic aromatic hydrocarbons Black Sea coastal sediments. *Marine Pollution Bulletin*, *83*, 231–240.

Trifonova, E., Valchev, N., Andreeva, N., & Eftimova, P. (2012). Critical storm thresholds for morphological changes in the western Black Sea coastal zone. *Geomorphology*, *143–144*, 81–94.

Tsimplis, M. N., Josey, S. A., Rixen, M., & Stanev, E. V. (2004). On the forcing of sea level in the Black Sea. *Journal of Geophysical Research*, *109*, C08015.

Valchev, N., Trifonova, E. V., & Andreeva, N. K. (2012). Past and recent trends in the western Black Sea storminess. *Natural Hazards and Earth System Sciences*, *12*, 961–977.

Vandenbulcke, L., Capet, A., & Grégoire, M. (2017). Recent evolution of the Black Sea cold intermediate layer. *Geophysical Research Abstracts*, *19*, EGU2017–10778.

Vespremeanu-Stroe, A., & Tatui, F. (2005). The influence of North Atlantic Oscillation on Romanian Black Sea coast wind regime. *Annals of the University of Bucharest—Geography Series*, *LIV*, 17–25.

von Schuckmann, K., et al. (2017). The Copernicus marine environment monitoring Service Ocean state report. *Journal of Operational Oceanography*, *9*(S2), s235–s320.

Vorosmarty, C. J., Sharma, K., Fekete, B. M., Copeland, A. H., Holden, J., Marble, J., et al. (1997). The storage and aging of continental runoff in large reservoir systems of the world. *Ambio*, *26*, 210–219.

Yucel, M., Moore, W. S., Butler, I. B., Boyce, A., & Luther, G. W., III. (2012). Recent sedimentation in the Black Sea: New insights from radionuclide distributions and sulfur isotopes. *Deep-Sea Research Part I*, *66*, 103–113.

Zaharia, T., Micu, D., Todorva, V., Maximov, V., & Nita, V. (2008). The Development of an indicative ecologically coherent network of marine protected areas in Romania, Romart Design—2008.

Zainescu, I. F., Tatui, F., Valchev, N., & Vespremeanu-Stroe, A. (2017). Storm climate on the Danube delta coast: Evidence of recent storminess change and links with large-scale teleconnection patterns. *Natural Hazards*, *87*(2), 599–621.

Zaitsev, Y. P., & Mamaev, V. (1997). *Marine biological diversity in the Black Sea: a study of change and decline*. GEF Black Sea Environmental Programme New York: United Nations Publications.

Zatsepin, A. G., Ginzburg, A. I., Kostianoy, A. G., Kremenetskiy, V. V., Krivosheya, V. G., Stanichny, S. V., et al. (2003). Observation of Black Sea mesoscale eddies and associated horizontal mixing. *Journal of Geophysical Research*, *108*, 1–27.

Zygiaris, S. (2012). Lending dynamism to innovative capacity in the periphery of Europe. *The Innovation Journal: The Public Sector Innovation Journal*, *17*(2), 1–15.

FURTHER READING

CleanSeaNet. (n.d.). A tool for the protection of our seas. (http://newsletter.copernicus.eu/article/cleanseanet-tool-protection-our-seas).

Daskalov, G. M., Prodanov, K., & Zengin, M. (2004). The Black Sea fisheries and ecosystem change: Discriminating between natural variability and human-related effects. In *Review proceedings of the fourth world fisheries congress, American fisheries society books* (*4th world fisheries congress*, Vancouver, May 2004).

Oguz, T. (2009). Chapter 1A—General Oceanographic Properties: Physico-chemical and Climatic Featuers, State of Environment Report 2001–2006/7. http://www.blacksea-commission.org/_publ-SOE2009-CH1A.asp.

Oguz, T., Latun, V. S., Latif, M. A., Vladimirov, V. V., Sur, H. I., Makarov, A. A., et al. (1993). Circulation in the surface and intermediate layers of the Black Sea. *Deep-Sea Res Part I*, *40*, 1597–1612.

Доклади на Българската академия на науките
Comptes rendus de l'Académie bulgare des Sciences

Tome 71, No 6, 2018

CHEMISTRY

Analytical chemistry

APPLICATIONS OF SOIL PHOSPHATE ANALYSIS FOR IDENTIFICATION OF ACTIVITY AREAS AT DOSCHKERE, SE BULGARIA

Boika Zlateva, Boyan Dumanov*, Miroslav Rangelov**

(*Submitted by Corresponding Member D. Tsalev on March 3, 2018*)

Abstract

Human occupation enriches soils with phosphorus, which may provide an useful chemical tracer for site delineation in archaeological studies. In the present paper we use "spot-method" as well as extractible phosphorous soil content to estimate site boundaries and the activity areas at the region "Doschkere", situated near Malko Tranovo, Chirpan, SE Bulgaria.

Key words: phosphate soil analysis, site boundaries, human activity area, archaeometry, Bulgaria

1. Introduction. Phosphorus (P) is unique among the elements in being a sensitive and persistent indicator of human activity. It has long been of interest to archaeologists because of its potential to inform them about the presence of past human occupation and to offer clues regarding the type and intensity of human activity. A wide variety of methods have been developed in both soil science and in archaeology to extract and measure phosphate content in soil, resulting in a tremendous amount of data and a wide array of interpretations, but also considerable confusion over appropriateness of methods and terminology. The reconstruction of the human activities areas of archaeological sites using soil phosphate analysis is a well-known technique [1–6]. The purpose of the technique is the detection and delineation of archaeological sites, identification of the activity area, through the measurement of the quantity of phosphates present in the soil [3, 4, 7, 8].

DOI:10.7546/CRABS.2018.06.04

Phosphates are chemical substances indicating specific human activities, such as the preparation and conservation of food, the deposit of liquid and solid wastes and burial. The detection can be executed directly in the field ("spot method") [9] or else in the laboratory on soil samples. In the latter case, the total or available phosphate content is normally measured. The main advantage of the technique in the field ("spot method") is the immediate response to traces of specific organic materials.

The aim of this investigation is to indicate activity areas in the archaeological excavation as well as to find the areas of habitation close to the archaeological complex. The excavation was in the field Doschkere, close to Malko Tranovo, south-eastern Bulgaria, where evidence of ancient occupancy is absent. The territory of south-west direction, situated in the modern forest in distance at 500 m of the excavated archaeological complex was investigated for human activities using soil phosphate data.

2. Archaeological background. The archaeological site is situated near village Malko Tranovo, (SE Bulgaria) and it is registered for archaeological investigations at the 2000 year. Because the place is located on highway under construction the excavations were carried out in the Autumn of 2003 year. The archaeological excavations have taken only the territory of the highway "Trakia", 15 km to the east of Chirpan (see Fig. 1). The primary data indicated different ceramic remains, which had been hand produced as well as using ceramic wheel. The most ceramics remains are dated from the Roman period.

The archaeological region is with slope in south-southeast direction and cov-



Fig. 1. Map of the investigated area

ers area of about 3000 m^2. After the preliminary researches a wall in the north-south direction was found preserved in one, two lines. Subsequent excavations revealed the boundaries of the complex, which is located partially within highway. The complex consists of five chain buildings incorporated around central inner courtyard. The found archaeological troves are building ceramics, tiles (tegulae and imbreces), and glass windows. The storage vessels (dolium) as well as the fragments of pitos represent the ceramics of everyday use, and generally were dated 3rd–4th c. AD. Flints, iron nails, and different small archaeological fragments were also found. Outside the investigated field of excavations nearest to the wall of the complex was found buckle of the type mostly circulated at the second half of 4th c. AD. More accurate dating was done by found coins; the earliest of them were from the serial of Emperor Constantine I and the oldest are from Emperor Valentinian I (also known as Valentinian the Great – 364 to 375 or 378 AD). The complex to reveal outside the archaeological excavation area consists probably of several buildings, a rural area or perhaps it is part of a larger complex. The coins found there show the end of the complex's life in the 70s of the 4th century AD, which are related to the Gothic invasions of this region.

3. Materials and methods. There are many investigations of the soil phosphate chemistry in archaeology (described clearly in [10]); here the field classical "spot method" [11] modified by Perrson [9] was used and laboratory measurement of the available phosphate-content was performed [12].

A stratified sampling was performed over the excavation areas and the outside region of interest. A total number of 172 soil samples were collected along predetermined transect lines. After using the "spot-method" in the field, 70 samples (about 0.5 kg each) with highest phosphate content (i.e. highest intensive blue colour) were collected from the archaeological layer (in depth 30–40 cm) for instrumental analysis of P concentration. The taken samples for laboratory measurement included samples from the archaeological excavation area as well as from the territory in SW direction, situated in the modern forest at a distance of 500 m of the excavated archaeological complex to find settlement boundaries. Control samples from an off-site area were also collected. Sub-samples of 20 g from the collected soil samples were dried to constant weight (48 h, 30 °C) and were cleaned up carefully from stones and rootlets. Subsequently the samples were ground in an agate mortar and the powder was passed through a 2 mm sieve and then 0.1 mm sieve.

The analysis was performed as follows: about 0.4 g of sample was extracted for 20 min with 2M HCl and 3% citric acid. The use of citric acid is suitable for the podzolic soils with high contents of Fe^{3+} (typical for the region of interest) because there is strong tendency of forming citric complexes with Fe^{3+}, without extensively releasing organically bound phosphorus. Finally about 0.01g $SnCl_2$ was added to reduce Fe^{3+} to Fe^{2+}. The colour strength is proportional to P content and is measured by spectrophotometer Spekol 11 at 815 nm (blue colour).

The percentage intensity was converted to mg/L by means of calibration curve, and appropriate dilution factors were used to convert the concentration values to mg P/kg soil.

4. Results and discussion. The results from the chemical analyses are displayed as scatter plots, describing the P content vs sampling location. Figure 2 presents the results of phosphate content for the excavation archaeological complex with marked points corresponding to the sampling places. Figure 3 provides the data for the investigated field in SE direction from the archaeological complex.

Part of the samples were taken in the opposite direction to obtain background level of phosphorus at the undisturbed natural soils. Although the field had been fertilized in the 60s–70s of 20th c., we tried to estimate the level of the archaeological phosphate content using collected data of the disturbed and undisturbed regions and statistical treatment after z-normalization. Obviously there is a serious lack of compromising of the data but on the basis of ANOVA statistical treatment the total variances between the groups (Statistica 8.0) are below the accuracy of the used method (below 0.1%) which is an evidence of the relevance of the procedure.

The distribution of phosphorous concentrations from the different locations illustrates the variability quite well (Fig. 3). These patterns of P concentration variations in the soils provide the basis for numerical classification. The samples from excavation site are compared to and matched with the samples from site of interest and off-site samples to identify the activity areas as well as the site boundaries.

Activity areas. At the excavation site 3 groups can be identified (see Fig. 3) which match well to ethnoarchaeologically defined activity areas. The first group is characterized by relatively low concentration of phosphorus but higher than off-site control and corresponds to samples collected close to walls, broken tiles and stone aggregations. These results may suggest zones with high traffic or very low activity, or that this area may have been reserved for any activities that did not involve using of organic substances. The concentrations of the second and third groups are much higher than all of the other samples although there are significant differences between the groups. Group 2 is connected with a general occupation and it is characterized by highest concentration of phosphorus in area of archaeological excavation. The highest concentration of phosphorus is obtained around the pit in northeast edge of the excavation area, in House 3 and 4, and to the south of House 4.

Together with archaeological finds – jars and vessels, this suggests that these buildings were connected with activities related to the preparation and consumption of food and perhaps beverages. The high concentration of phosphate content to the south of House 4 as well as around the pit in the northeast edge of the area may be connected with human waste. The third group consists of the samples,

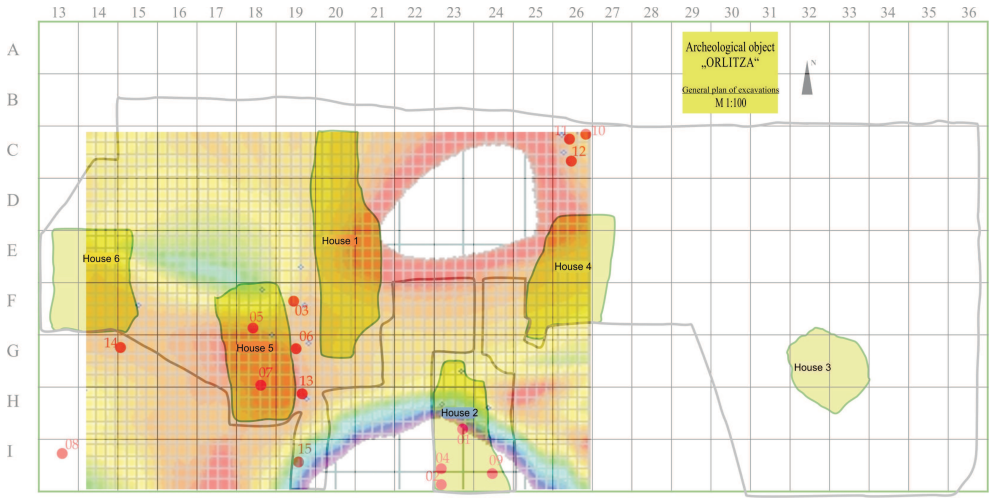


Fig. 2. Plan of the archaeological complex 13 A with excavated structures and mapping of the phosphate concentration (g/kg)

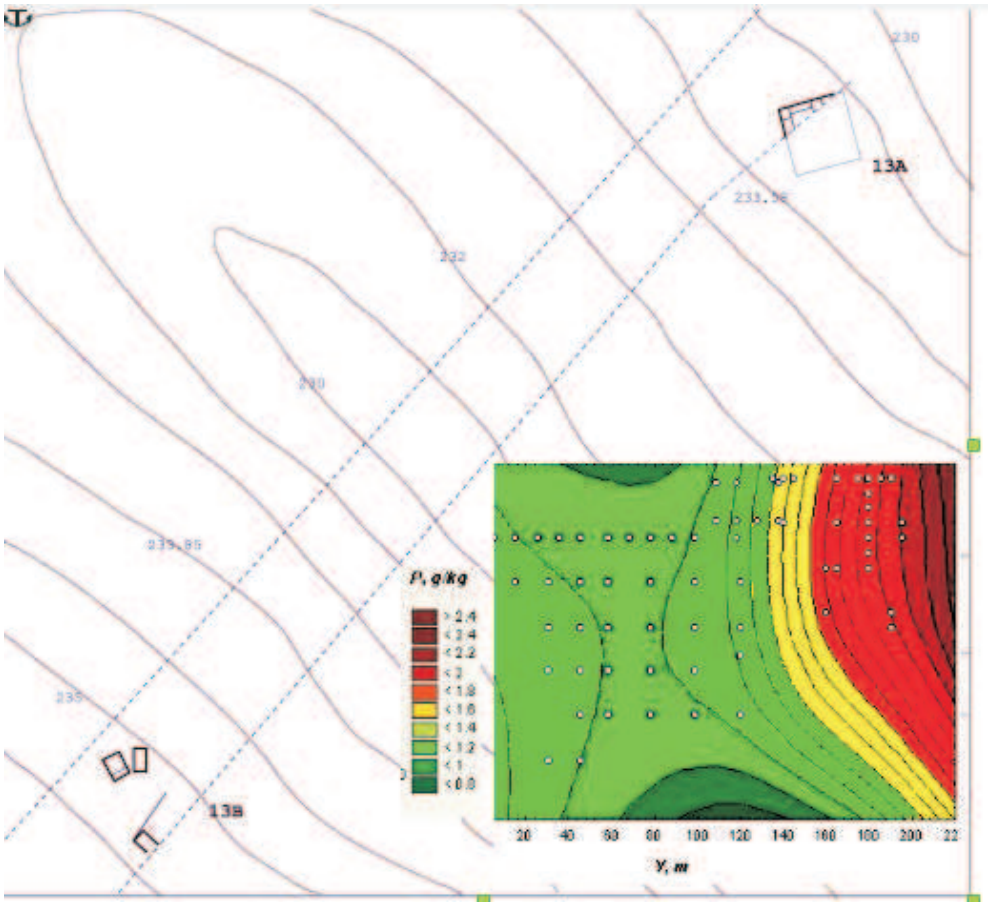


Fig. 3. Scatter plot of the data of phosphate content and sampling points in the SW area to the excavation archaeological complex. The isoplethe lines represent aviable phosphate concentration (g/kg) of the SW area and the direction of potential site borders are indicated (marked with black line)

collected close to eastern part of House 6, and in House 1. The relatively low phosphate-content compared to the second group and at the same time higher concentration compared to the first group samples, may be associated with domestic activities – grinding stones, stone tools, etc., or craft manufactures.

Settlement boundaries. At a distance of 500 m to the south-west of the excavation area region of about 150 m^2 had been exploited for eventually defining settlement boundaries by laboratory measurements of P content. The data of used in the field "spot method" shows that there is enrichment in soil phosphate in north-eastern edge of the investigated area and the collected samples were additionally analyzed in the laboratory to clarify the results.

The changes of phosphate content in north-eastern edge are smooth and show a slight increase in direction to the archaeological complex. The level of phosphate in this region is in the same concentration ratio as determined for the second group in the archaeological complex (i.e. medium high concentration of P content). On this basis, we can assume that (probably) in this area there had been human activity. Unfortunately, on the basis of he limited number of the samples and the presence of modern forest, road and farmlands in the area, would be difficult to conclude that we found south-west settlement boundary. There is no doubt, however, that experimentally found higher phosphate concentrations are a result of human activities in the past which is also supported by archaeological ceramics finds.

5. Conclusion. The results of our analyses indicate that soil chemical signatures of midden materials may be very important in decoding the various waste deposits of the ancient people. The obtained results from this investigation despite the limited number of the samples and the impossibility to clarify the settlement boundaries is an example for the applicability of soil phosphate method in archaeology. The combination between the "spot method" using in the field and laboratory measurement of P content can be used to identify areas of prior human occupation. In field situations where vegetation is dense and surface visibility is poor, this technique can offer a quick and inexpensive assessment of P content in the soil and ancient site presence when other investigative approaches are not feasible. The data demonstrate the possibilities of the method for reconstruction of the activity area, the way of the utilization of the areas, settlement boundaries and could be useful in providing guidelines for future studies.

REFERENCES

[1] Bethell Ph., I. Mate (1989) The use of soil phosphate analyses in archaeometry: Acritique. In: Scientific Analyses in Archaeology and its interpretation (ed. J. Henderson), Exeter, Short Run Press, 1–29.

[2] Cañabate Sánchez A. M. L., R. Lizcano (1996) Phosphorus analysis at archaeological sites: an optimization of the method and interpretation of the results, Arch., **38**(1), 151–164.
[3] Middelton W. D. (2004) Identifying chemical activity residues on prehistoric house floors: a methodology and rationale for multi-elemental characterization of a mild acid extract of anthropogenic sediments, Arch., **46**(1), 47–65.
[4] Parnell J. J., R. E Terry, Z. Nelson (2002) Soil chemical analysis applied as an interpretive tool for ancient human activities in Piedras Negras, Guatemala, J. Arch. Sci., **29**(4), 379–404.
[5] Wells E. C. (2004) Investigating activity patterns in prehispanic plazas: weak acid-extraction ICP-AES analysis of anthrosols at Classic period El Coyote, Northwestern Honduras, Arch, **46**(1), 65–84.
[6] Wells E. C., R. E. Terry, J. J. Parnell, P. J. Hardin, M. W. Jackson, St. D. Houston (2000) Chemical analyses of ancient anthrosols in residential areas at Piedras Negras, Guatemala, J. Arch. Sci., **27**(2), 449–462.
[7] Bjelajac V. E., R. Lubyrose (1996) Validation test of a field-based phosphate analysis technique, J. Arch. Sci., **23**(2), 243–248.
[8] Cabanes D., Y. Gadot, M. Cabanes, I. Finkelstein, S. Weiner, R. Shahack-Gross (2012) Human impact around settlement sites: a phytolith and mineralogical study for assessing site boundaries, phytolith preservation, and implications for spatial reconstructions using plant remains, J. Arch. Sci., **39**(8), 2697–2705.
[9] Perrson K. B. (1997) Soil phosphate analysis: a new technique for measurement in the field using a test strip, Arch., **39**(2), 441–443.
[10] Holliday V. T. A., W. G. Gartner (2007) Methods of soil P analysis in archaeology, J. Arch. Sci., **34**(3), 301–333.
[11] Eidt R. C. (1977) Detection and examination of anthrosols by phosphate analysis, Science, **197**, 1327–1333.
[12] Kuleff I. (2012) Archaeometry, Sofia, Sofia University Press St. Kl. Ohridski (in Bulgarian).

Faculty of Chemistry and Pharmacy
Sofia University "St. Kliment Ohridski"
1, J. Bourchier Blvd
1164 Sofia, Bulgaria,
e-mail: ahbz@chem.uni-sofia.bg

Department of Archaeology
New Bulgarian University
21, Montevideo St
1618 Sofia, Bulgaria
e-mail: bdumanov@nbu.bg

**Institute of Organic Chemistry*
with Centre of Phytochemistry
Bulgarian Academy of Sciences
Acad. G. Bonchev St, Bl. 9
1113 Sofia, Bulgaria
e-mail: marangelov@gmail.com